

## Component control for the Zero Inertia powertrain

**Citation for published version (APA):**

Vroemen, B. G. (2001). *Component control for the Zero Inertia powertrain*. [Phd Thesis 1 (Research TU/e / Graduation TU/e), Mechanical Engineering]. Technische Universiteit Eindhoven.  
<https://doi.org/10.6100/IR549999>

**DOI:**

[10.6100/IR549999](https://doi.org/10.6100/IR549999)

**Document status and date:**

Published: 01/01/2001

**Document Version:**

Publisher's PDF, also known as Version of Record (includes final page, issue and volume numbers)

**Please check the document version of this publication:**

- A submitted manuscript is the version of the article upon submission and before peer-review. There can be important differences between the submitted version and the official published version of record. People interested in the research are advised to contact the author for the final version of the publication, or visit the DOI to the publisher's website.
- The final author version and the galley proof are versions of the publication after peer review.
- The final published version features the final layout of the paper including the volume, issue and page numbers.

[Link to publication](#)

**General rights**

Copyright and moral rights for the publications made accessible in the public portal are retained by the authors and/or other copyright owners and it is a condition of accessing publications that users recognise and abide by the legal requirements associated with these rights.

- Users may download and print one copy of any publication from the public portal for the purpose of private study or research.
- You may not further distribute the material or use it for any profit-making activity or commercial gain
- You may freely distribute the URL identifying the publication in the public portal.

If the publication is distributed under the terms of Article 25fa of the Dutch Copyright Act, indicated by the "Taverne" license above, please follow below link for the End User Agreement:

[www.tue.nl/taverne](http://www.tue.nl/taverne)

**Take down policy**

If you believe that this document breaches copyright please contact us at:

[openaccess@tue.nl](mailto:openaccess@tue.nl)

providing details and we will investigate your claim.

Component Control for  
The Zero Inertia Powertrain

CIP-DATA LIBRARY TECHNISCHE UNIVERSITEIT EINDHOVEN

Vroemen, Bas G.

Component control for the Zero Inertia Powertrain / by Bas G. Vroemen. –

Eindhoven : Technische Universiteit Eindhoven, 2001.

Proefschrift. – ISBN 90-386-2593-6

NUGI 834

Trefwoorden: aandrijflijn voor personenvoertuig / voertuig transmissie / continu variabele transmissie / CVT / duwband / verbrandingsmotor / brandstofverbruik / driveability / aandrijflijn ; vliegwiel / hybride voertuigen / Zero Inertia aandrijflijn / CVT ; hydrauliek regeling / CVT ; modellering / CVT ; efficiëntie / Stop-Go

Subject headings: passenger car powertrain / vehicular transmission / continuously variable transmission / CVT ; pushbelt / internal combustion engine / fuel economy / driveability / powertrain ; flywheel / hybrid vehicles / Zero Inertia powertrain / CVT ; hydraulic control / CVT ; modeling / CVT ; efficiency / Stop-Go / engine idle shutdown

This thesis was prepared with the L<sup>A</sup>T<sub>E</sub>X 2<sub>ε</sub> documentation system.

Printed by University Press Facilities, Eindhoven, The Netherlands

Cover Design by Dirk Vroemen and Nanne Verbruggen

Copyright © 2001 by B. G. Vroemen

All rights reserved. No parts of this publication may be reproduced or utilized in any form or by any means, electronic or mechanical, including photocopying, recording or by any information storage and retrieval system, without permission of the copyright holder.

This work forms a part of the EcoDrive project, subsidized by the Dutch program EET (Economy, Ecology and Technology).

# **Component Control for The Zero Inertia Powertrain**

PROEFSCHRIFT

ter verkrijging van de graad van doctor  
aan de Technische Universiteit Eindhoven  
op gezag van de Rector Magnificus, prof.dr. R. A. van Santen,  
voor een commissie aangewezen door het College voor Promoties  
in het openbaar te verdedigen op  
dinsdag 27 november 2001 om 15.00 uur

door

**Bas Gerard Vroemen**

geboren te Breda

Dit proefschrift is goedgekeurd door de promotoren:

prof.dr.ir. M. Steinbuch  
en  
prof.ir. N. J. J. Liebrand

Co-promotor:

dr.ir. F. E. Veldpaus

# Contents

<b>Summary</b>	<b>ix</b>
<b>I General Introduction</b>	<b>1</b>
<b>1 Introduction and Project Goals</b>	<b>3</b>
1.1 Project chronology . . . . .	5
1.2 Problem description . . . . .	6
1.3 Research objectives . . . . .	7
1.4 Main contributions and outline of this thesis . . . . .	9
<b>2 Fuel Saving Principles</b>	<b>11</b>
2.1 Introduction . . . . .	11
2.2 Improving component efficiency . . . . .	12
2.2.1 Engine efficiency . . . . .	12
2.2.2 Transmission efficiency . . . . .	15
2.2.3 Power take-off . . . . .	15
2.3 Reducing the external load . . . . .	16
2.3.1 Vehicle mass . . . . .	16
2.3.2 Rolling resistance . . . . .	16
2.3.3 Air drag . . . . .	17
2.4 Alternative powertrain operation . . . . .	18
2.5 Non-vehicle technology . . . . .	19
2.5.1 Driving behaviour . . . . .	19
2.5.2 Infrastructure and traffic management . . . . .	19
2.5.3 Law, policy and legislation . . . . .	20
<b>3 Normalized Innovation Values</b>	<b>21</b>
3.1 Hybrid powertrains . . . . .	21
3.2 Innovation values: fuel economy . . . . .	23
3.2.1 Reference vehicle . . . . .	24
3.2.2 Influence of driving cycles . . . . .	25
3.2.3 Fuel economy . . . . .	26
3.3 Innovation efforts . . . . .	28
3.3.1 E-line tracking . . . . .	29
3.3.2 Stop-Go operation . . . . .	35
3.3.3 Start-Stop operation . . . . .	36

---

3.3.4	Brake energy recovery . . . . .	41
3.4	Innovation value versus effort . . . . .	41
<b>4</b>	<b>The Zero Inertia Powertrain</b>	<b>45</b>
4.1	Zero Inertia principle . . . . .	45
4.2	ZI Concept design . . . . .	48
4.2.1	Resulting configuration . . . . .	48
4.3	ZI Stop-Go . . . . .	49
4.4	Further reading . . . . .	50
<b>II</b>	<b>CVT Modeling and Control</b>	<b>51</b>
<b>5</b>	<b>The CVT in the ZI Powertrain</b>	<b>53</b>
5.1	The pushbelt variator . . . . .	54
5.2	The pushbelt construction in detail . . . . .	55
5.2.1	Segment design . . . . .	56
5.2.2	Band design . . . . .	57
5.2.3	Pulley design . . . . .	57
<b>6</b>	<b>CVT Modeling and Validation</b>	<b>59</b>
6.1	Introduction . . . . .	59
6.2	Description of the test platform . . . . .	59
6.3	Static variator models . . . . .	60
6.3.1	Geometry and definitions . . . . .	61
6.3.2	Variator models based on Coulomb friction . . . . .	62
6.3.3	Variator model based on viscous shear . . . . .	68
6.4	Transient variator models . . . . .	69
6.4.1	Validation of transient variator models . . . . .	71
6.5	Hydraulics . . . . .	71
6.5.1	Hydraulic circuit . . . . .	72
6.5.2	Proportional solenoid valves . . . . .	74
6.5.3	Roller vane pump . . . . .	78
6.5.4	Alternative hydraulic actuation . . . . .	78
6.6	ZI powertrain . . . . .	79
6.6.1	Planetary gear . . . . .	80
6.6.2	Flywheel . . . . .	81
6.6.3	Combined model for primary side of powertrain . . . . .	81
6.7	CVT efficiency analysis and measurements . . . . .	81
6.7.1	Power transmission in the variator . . . . .	82
6.7.2	Speed and torque losses . . . . .	83
6.7.3	Efficiency measurements . . . . .	85
6.7.4	Empirical efficiency model . . . . .	89
6.8	ZI-CVT load envelope . . . . .	90
6.8.1	Impact on transmission and powertrain controller design . . . . .	90
6.8.2	Impact on CVT controller design . . . . .	93

---

<b>7</b>	<b>Hydraulic CVT Control</b>	<b>97</b>
7.1	To-be-controlled quantity . . . . .	97
7.2	Control objectives . . . . .	101
7.3	Inputs and outputs of the controller . . . . .	101
7.4	Constraints and integral windup . . . . .	101
7.4.1	Conditional anti-windup . . . . .	102
7.5	Control strategy . . . . .	103
7.6	Literature on CVT control . . . . .	104
7.7	Controller design . . . . .	104
7.7.1	Pressure control . . . . .	106
7.8	Simulations . . . . .	106
7.9	Experimental control results . . . . .	109

### **III ZI Stop-Go 115**

<b>8</b>	<b>Introduction to Stop-Go</b>	<b>117</b>
8.1	Commercial Stop-Go concepts . . . . .	117
8.1.1	Stop-Go configurations . . . . .	118
8.1.2	Additional functions of Stop-Go systems . . . . .	121
8.1.3	Ways to gain acceptance . . . . .	122
8.2	Mechanical solution: ZI Stop-Go . . . . .	123
8.2.1	ZI Stop-Go operation . . . . .	123
<b>9</b>	<b>ZI Stop-Go Modeling</b>	<b>127</b>
9.1	Model of the ZI Stop-Go Powertrain . . . . .	127
9.1.1	Torque converter . . . . .	128
9.1.2	Clutch model . . . . .	128
9.1.3	Abbreviations . . . . .	130
9.1.4	Differential equations for the launch sequence . . . . .	130
9.2	Minimum flywheel speed . . . . .	132
9.3	Pedal interpretation . . . . .	136
9.3.1	Torque interpretation . . . . .	137
9.3.2	Power interpretation . . . . .	138
9.3.3	Transition between torque and power interpretation . . . . .	138
9.3.4	CVT and TC operation . . . . .	139
<b>10</b>	<b>ZI Stop-Go Control</b>	<b>141</b>
10.1	General ideas for controlling ZI Stop-Go . . . . .	141
10.2	Control strategy for the Start phase . . . . .	145
10.3	Control strategy for the Brake phase . . . . .	145
10.3.1	Unlocking the torque converter . . . . .	146
10.3.2	Braking the primary pulley . . . . .	147
10.3.3	Synchronizing the drive clutch . . . . .	148
10.4	Control strategy for the Sync phase . . . . .	149
10.4.1	Accelerating the secondary pulley . . . . .	149
10.4.2	Synchronizing the secondary pulley clutch . . . . .	149
10.5	Control strategy for the End phase . . . . .	150
10.6	Controller implementation . . . . .	150



---

10.7 Simulation results . . . . .	151
10.8 Preliminary experimental results . . . . .	154
<b>IV Closure</b>	<b>157</b>
<b>11 Conclusions</b>	<b>159</b>
11.1 Overall conclusions . . . . .	159
11.2 Modeling and control of powertrain components . . . . .	160
11.3 Directions for future research . . . . .	161
<b>References</b>	<b>163</b>
<b>A Test Rig Description</b>	<b>171</b>
A.1 Electric motors . . . . .	172
A.2 Miscellaneous components . . . . .	173
A.3 Sensors and actuators . . . . .	173
A.4 dSPACE . . . . .	174
A.5 Hydraulics . . . . .	175
A.6 Additional ZI Stop-Go clutches . . . . .	177
<b>B Metal V-belt Model</b>	<b>179</b>
B.1 Elaboration of the Coulomb model . . . . .	179
B.1.1 Calculation procedure . . . . .	182
B.2 Elaboration of the viscous shear model . . . . .	183
B.2.1 Minimal pulley clamping force . . . . .	184
<b>C Alternative Hydraulic Actuation</b>	<b>187</b>
C.1 Hydraulic circuit design . . . . .	187
C.1.1 VDT layout . . . . .	187
C.1.2 Alternative layout . . . . .	188
C.1.3 Cylinder dimensioning . . . . .	190
C.2 Simulation results . . . . .	190
C.2.1 Safety in case of pressure breakdown . . . . .	190
C.2.2 Shifting speed . . . . .	191
C.2.3 Shifting while coasting . . . . .	193
<b>D CVT and TC Operation</b>	<b>195</b>
D.1 Efficient driveline operation . . . . .	195
D.1.1 Torque converter logic . . . . .	195
D.1.2 E-line operation . . . . .	196
<b>Nomenclature and Acronyms</b>	<b>199</b>
<b>Samenvatting</b>	<b>207</b>
<b>Acknowledgments</b>	<b>209</b>
<b>Curriculum Vitae</b>	<b>211</b>

# Summary

The fuel economy of passenger cars can be improved in various ways. One can think of reducing the external load, for instance by lowering the weight and air drag of the vehicle. Another possibility is to improve the propulsion system, *i.e.*, the *powertrain*. Increasing the efficiency of the different powertrain components, such as the engine and the transmission, is one way to do so. Another approach is to operate the powertrain as a whole in a more fuel-optimal way. Especially the operating point in which the engine delivers the required energy is of vital importance to the fuel consumption. While the efficiency of the modern combustion engine is thought to be close to what can be achieved, the field of *alternative powertrain operation* is by no means fully cultivated.

In the EcoDrive project underlying this thesis it was therefore chosen to concentrate on technologies in this field as means to save fuel. Based on a survey of fuel saving methods related to alternative powertrain operation, two of these methods were selected due to their high fuel saving potential relative to the additional weight, cost and complexity as compared to a conventional vehicle. The first of these methods, called *E-line tracking*, can save fuel by delivering requested stationary wheel powers in fuel-optimal engine operating points. The second method, called *Stop-Go*, improves the fuel economy by eliminating the idle fuel consumption of the engine at vehicle standstill. The actual difficulty in both approaches is to achieve the fuel savings *without* impairing the vehicle response to the accelerator pedal, also known as *driveability*. The project target was therefore set at saving 25% fuel with respect to a 4-speed automatic transmission on the NEDC driving cycle, *without* compromising the driveability.

For that purpose, a flywheel is connected in parallel to the transmission via a planetary gear stage. In case of *E-line tracking*, the flywheel operates as a power assist source during transients when the vehicle is to be accelerated starting from a fuel efficient, hence low engine speed. Because the resulting vehicle response appears as if the engine inertia is absent, the resulting powertrain is referred to as the *Zero Inertia (ZI) powertrain*. For *Stop-Go*, the flywheel can also be used to launch the vehicle from standstill, provided it is decoupled from the powertrain some time before standstill. In the proposed design, called *ZI Stop-Go*, the vehicle and the engine can be accelerated *simultaneously*, enabling a *Stop-Go* functionality without a noticeable delay between pedal depression and vehicle launch.

The smooth exchange of energy between the flywheel and the rest of the powertrain during transient operation is possible through the use of a Continuously Variable Transmission (CVT). Furthermore, the CVT enables exact matching of the fuel-optimal engine operating points to the vehicle speed. This thesis is concerned with the development of the (*pushbelt*) CVT controller, and of the models required for that. The presented models are also useful for gaining insight into the operation of the CVT and for explaining empirical observations, such as power loss in the transmission. Special consideration is given to dealing with constraints

---

like actuator and system saturations. The CVT controller is evaluated experimentally on a test rig and in a test vehicle, in conjunction with the setpoint generator derived in [Serrarens, 2001]. In stationary situations, the CVT controller achieves a close to maximal transmission efficiency without slip of the pushbelt, while highly dynamic transients are performed with acceptable tracking errors.

The second part of this thesis elaborates on the ZI Stop-Go powertrain. Several existing Stop-Go solutions are presented, and the potentials and operational difficulties of this technology are shown. The proposed ZI Stop-Go concept requires the introduction of two extra clutches. This solution is mechanically simple, but nevertheless complex to operate. It places heavy demands on its controls, both on the supervisory level and on the component control level. For that purpose, (hybrid) models of the powertrain are derived for developing a (hybrid) controller. The controller is evaluated using a more elaborate version of the mentioned model. Simulations of a kickdown vehicle launch show a response which is comparable to that of a conventional CVT vehicle. The ZI Stop-Go transmission was realized and the CVT hydraulics were modified to enable the actuation of the clutches, also during engine shutdown. This transmission was mounted on the test rig and first tests yield promising results.

The contributions of the research covered in this thesis helped to largely achieve the project target, *i.e.*, a fuel saving of 18% was realized, while the driveability was even improved.

## **Part I**

# **General Introduction**



# Chapter 1

## Introduction and Project Goals

The focus of this thesis is the modeling and control of components that play a vital part in the innovative automotive transmission concept, designated the *Zero Inertia (ZI) powertrain*. This powertrain combines a Van Doorne Continuously Variable Transmission (CVT), a low-speed flywheel and a planetary gear stage, targeting for 25% fuel saving without compromising the vehicle's longitudinal response. The modeling and control of the CVT and the experimental validation of the CVT controller—on a test rig as well as in a test vehicle—is the subject of the first half of this thesis. The generation of the setpoints for the CVT controller is covered in [Serrarens, 2001], and is outside the scope of this thesis. The connection with [Serrarens, 2001] is elucidated further on. The second half of this thesis is concerned with the modeling and supervisory control of the *Stop-Go* facility in the ZI powertrain. The Stop-Go extension enables shutdown of the engine during vehicle standstill, and should yield about half the projected fuel saving of 25%. The Stop-Go design is specifically laid out as an add-on to the ZI transmission, which doesn't interfere with the ZI functionality. Consequently, the ZI Stop-Go transmission has two additional clutches, which must be controlled in conjunction with the existing clutches, engine and CVT speed ratio controllers.

This work is one out of three theses that describe different topics of the ZI powertrain. In [van Druten, 2001] the mechanical design and construction of the ZI transmission is focused on. The setpoint generation for CVT and engine (coordinated powertrain control) and modeling and testing of the ZI powertrain is subject of [Serrarens, 2001].

The ZI and ZI Stop-Go transmissions are materializations of the goals set in the *EcoDrive* project. EcoDrive is a cooperation between Van Doorne's Transmissie (VDT) in Tilburg, the Technische Universiteit Eindhoven (TU/e) and TNO Automotive in Delft. The project was initiated by VDT and subsidized by the Dutch governmental program EET (Economy, Ecology and Technology). The ZI powertrain is the result of the EcoDrive assignment to achieve considerable fuel saving with a CVT and an additional power source in a driveline for passenger cars. The properties of the CVT can be exploited to save fuel by having the engine run in operating points with better fuel economy. This should occur without deteriorating the vehicle's longitudinal dynamic response, in other words, without compromising *driveability*. For that purpose, the additional power source is used, which will be embodied as a flywheel.

The formulation of this assignment has a historical background at the Technische Universiteit Eindhoven. In the late 1970s a project was initiated to integrate a high speed flywheel in a powertrain enabling the engine to operate intermittently as a constant speed aggregate in its most efficient operating point. This led to the materialization of an optimized Fly-

---

wheel Hybrid<sup>1</sup> Driveline (FHD-III) and its fuel economy was demonstrated in [Kok, 1999]. The driveability was never assessed, nevertheless interest in this area began to increase.

## EcoDrive

The main goal of the EcoDrive project is twofold. One part of the project concentrated merely on improving the efficiencies of the engine and the CVT, aiming at an increased total driveline efficiency (System Integrated driveline, SI). The second part (HYbrid driveline, HY) was to design the hard- and software of a new powertrain with CVT and additional power source that saves 25% fuel on the New European Drive Cycle (NEDC) compared to a 5-speed manual transmission (5-MT) vehicle and that has a driveability level comparable to commercially available mid-sized passenger cars. The EcoDrive SI project was primarily a cooperation of VDT and TNO Automotive, whereas in the EcoDrive HY part VDT and TU/e worked together. The EcoDrive project started back in 1997 and is finalized at the end of 2001.

A year after kicking-off the EcoDrive HY project, it was reformulated into the 'EcoDrive ZI' project, for reasons that will be explained further on. Figure 1.1 elucidates the organization and the resulting concepts of the EcoDrive project.

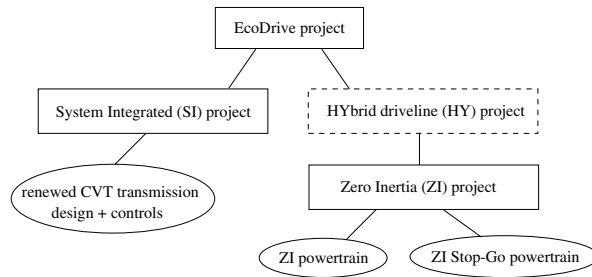


Figure 1.1: EcoDrive project organization

In this thesis and in [van Druten, 2001] and [Serrarens, 2001], the findings of the EcoDrive ZI project are described. Results of the renewed CVT transmission design and control achieved in EcoDrive SI can be found in [Veenhuizen and van Spijk, 2000].

## Zero Inertia powertrain

Choosing for the materialization of a certain powertrain concept starting from a problem description depends for the larger part on the conclusions of a preliminary investigation. In the case of EcoDrive HY, such a preliminary investigation lead to a simple configuration and operation principle of a hybrid powertrain with internal combustion engine, CVT, flywheel and a few clutches based on the findings of the FHD-III, [Serrarens and Veldpaus, 1998].

Along with the search for the 'ideal' flywheel hybrid powertrain, interest was put in the functional problems of basic CVT powertrains. A basic CVT powertrain is afflicted with the paradox that it can realize a high fuel economy and driveability, but hardly at the same time. Triggered by this phenomenon, the idea came up to try and find a way to break up this paradox with a flywheel inertia. This lead to the aforementioned Zero Inertia powertrain. The ZI

---

<sup>1</sup>The definition of *hybrid vehicles* will be presented in Section 3.1.

concept is based on the notion that some unwanted inertial effects of the powertrain can in principle be nullified by exchanging kinetic energy between an additional flywheel and the engine sided inertias. As such, high fuel economy obtained by optimizing the engine operating points is no longer penalized by reduced driveability. It was decided to elaborate further on the ZI powertrain leading to a reformulation of the EcoDrive HY into the EcoDrive ZI project.

### outline of this chapter

The remainder of this chapter is organized as follows. Section 1.1 describes the chronology of the project. In Sections 1.2 and 1.3 the problem description underlying this thesis is described. The main contributions of the present research and the outline of this thesis are presented in Section 1.4.

## 1.1 Project chronology

In Figure 1.2, the chronology of the EcoDrive ZI project is displayed. The decision to concentrate on the ZI and the ZI Stop-Go powertrains, required some organizational and financial reformulations of the goals first set in EcoDrive HY. It was decided to design and build a prototype ZI transmission, develop control software and conduct fuel consumption and driveability tests. The ultimate project goal, *i.e.*, demonstrating 25% fuel consumption reduction on the NEDC, could not be reached by ZI alone. Therefore the Stop-Go extension upon the ZI powertrain was introduced. The feasibility of the original project goal was questioned and a new goal was set, being 25% reduction of fuel consumption of a 1.6 ℓ petrol engine with ZI Stop-Go compared to the same engine in conjunction with a 4-speed automatic transmission (4-AT), or a CVT in ‘performance mode’. Due to the limited time schedule and the desire to investigate systems step-by-step it was decided to implement ZI in a test vehicle and to test the feasibility of ZI Stop-Go on a test rig only.

Regarding Figure 1.2, the main observation is that the time span between the invention of the ZI powertrain and first successful road testing covers just over three years. Conceiving and designing the ZI concept for a vehicle implementation took just over half a year. The materialization and mounting on the test rig of the first ZI transmission required around one year, whereas the testing of the transmission and its controls on a test rig and in a vehicle required an additional one and a half year. Reasons for the relatively short development time appear to be:

- the fact that the ZI idea itself hardly necessitates research on components, enabling the use of proven technology;
- the control system hardware requires no major adaptations compared to a standard CVT powertrain, instead new developments in software are achieved;
- prompt freezing of the mechanical layout through reasoning according to first principles;
- the use of simple kinematic, dynamic and energy models to gain quick insight in the mechanisms and to optimize the system parameters of the prototype ZI transmission;
- the use of an available CVT and other available transmission components to make the extension towards a ZI transmission;



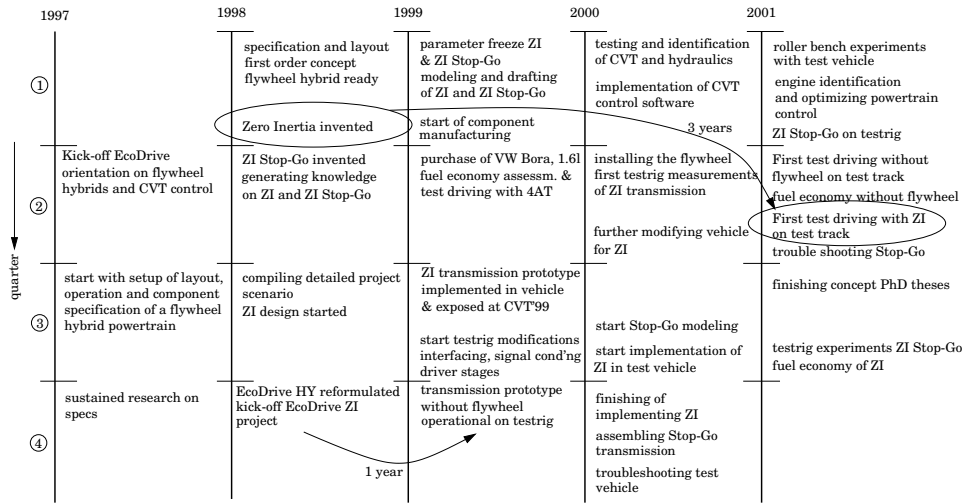


Figure 1.2: EcoDrive ZI project chronology

- step-by-step testing of the ZI powertrain, by consecutively testing the available CVT transmission on a test rig, followed by the ZI transmission on the test rig and finally in the vehicle. This way, inevitable setbacks could be handled reasonably quickly;
- the use of flexible and state-of-the-art test rig facilities, which were developed within the EcoDrive project;
- the modest modifications required within the engine compartment in order to make the ZI powertrain fit into the test vehicle;
- coordinated teamwork, frequent team meetings and ticking off achieved milestones.

## 1.2 Problem description

As explained, the main project goal for EcoDrive ZI is 25% fuel economy improvement on the NEDC cycle compared to 4-AT, under the constraint of uncompromized driveability. In general there are different ways to achieve this, when altering the powertrain only. Four of them are mentioned:

- a) matching fuel-optimal engine operating points that fulfill the momentary power demand, to the actual vehicle speed;
- b) shutting down the engine at full vehicle stops to save the fuel normally consumed during idling;
- c) matching the engine operating point with the highest efficiency to the average power request, requiring an additional power source, and
- d) effective reuse of the vehicle's kinetic energy.

In the initial assignment of EcoDrive HY all off the above principles were combined into one versatile but rather impractical concept. In the EcoDrive ZI project only the principles a) and b) are chosen, materialized as the ZI and ZI Stop-Go powertrains, respectively. From Figure 1.3,

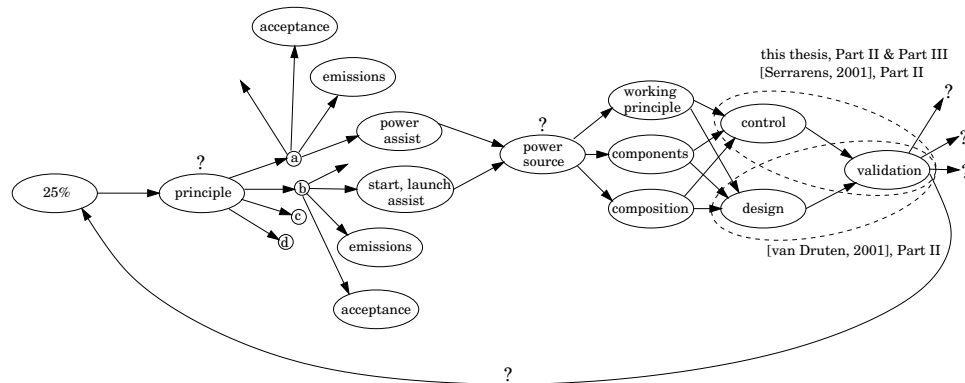


Figure 1.3: Research trajectory for EcoDrive ZI

three problem descriptions are identified. The first is how to motivate the choice for fuel saving principles a) and b). Both principles need a power assist system in order to meet the driveability objective. This will be explained in more detail in Chapters 3 and 4. The second problem then is how to motivate the choice for the power source, being a flywheel for both ZI and ZI Stop-Go. The third question is up to what extent the main project target of 25% is met, and the reasons for that. Naturally, a number of research questions evolve when developing, examining and validating the new concepts. This may be regarded as scientific or engineering spin-off from the project.

In this thesis, the first and second research questions are answered in Chapter 3. Answers to the third research question, and directions for future research are presented in Chapter 11, Part IV.

### 1.3 Research objectives

Part II of this thesis is concerned with the CVT in the ZI powertrain, which is of the metal pushbelt type. In order to develop a CVT speed ratio controller, models of the CVT and its hydraulics are required to develop model-based control laws and to evaluate the controller performance in a simulation environment. Research on the modeling of metal pushbelt CVTs has been extensively reported in literature, mostly numerical-experimentally flavoured [Kuwabara *et al.*, 1998, 1999; Fushimi *et al.*, 1996; Ide *et al.*, 1994; Kitagawa *et al.*, 1995; Kanehara *et al.*, 1999; Kobayashi *et al.*, 1998; Yoshida, 1995], though sometimes more analytical ('white-box') in nature [Asayama *et al.*, 1995; Becker, 1987; Gerbert, 1984; Karam and Play, 1992; van Rooij and Schaeerlaeckens, 1993; Carbone *et al.*, 2000; Shafai *et al.*, 1995; Mickle *et al.*, 1994]. Most of these contributions are useful for gaining insight in the CVT mechanics, but are hardly suited for developing a model suitable for control applications. Moreover, publications on local CVT control are rare and often somewhat concealing. In this thesis, an overview of the aforementioned models is presented, mainly to develop a framework to facilitate the explanation of

phenomena encountered in the experimental validation of CVT models and controllers. From this overview, a model useful for simulation purposes and for controller development is selected and customized for the intended implementation.

To validate the models of the CVT and of its hydraulics and to eventually test the CVT controller, a high-power test rig has been realized within the EcoDrive project. Using this experimental platform, some CVT parameters are further identified and the performance of the CVT controller in conjunction with the coordinated powertrain controller [Serrarens, 2001] is evaluated. Proceeding as such, the CVT controller and most of the associated overhead were more or less crystallized by the time the ZI transmission was transferred to the test vehicle, also developed within the EcoDrive project.

After this milestone, the attention was shifted to the second part of the EcoDrive ZI project: the Stop-Go facility. As mentioned earlier it was decided to develop ZI Stop-Go up to the test rig phase, at least within the EcoDrive project. To arrive at that goal, elaborate hybrid models have been developed as well as supervisory control strategies to operate the various clutches in conjunction with the CVT and engine. The two additional clutches needed for Stop-Go were designed and mounted into a second ZI transmission, and the hydraulics were modified to enable the actuation of the clutches, also during engine shutdown. The controllers are validated in a simulation environment and in part experimentally. The extent of experimental results is limited, though, due to the fact that the revised test rig and transmission were fully functional just prior to the moment of writing. Nevertheless, the results of simulations and first experiments are promising and justify further research.

Summarizing, the objectives of this research are:

1. develop experimentally validated models for the CVT and its hydraulic actuation;
2. use the model information to arrive at a model-based CVT speed ratio controller;
3. design and realize a high-power fully programmable test rig, for testing of automotive components, and transmissions in particular;
4. evaluate the CVT controller performance and robustness, both in simulations and experiments;
5. assess the performance and robustness of the latter controller in conjunction with the aforementioned coordinated powertrain controller, first on the test rig and next in the test vehicle;
6. develop models of the ZI Stop-Go powertrain, suited for simulation purposes and for controller development;
7. design and evaluate a supervisory controller for the various clutches, the engine and the CVT;
8. modify the hydraulic system of the CVT to enable the actuation of the clutches;
9. develop local clutch pressure controllers;
10. experimentally validate the supervisory and local controllers, and show the feasibility of the Stop-Go facility, as a means for saving fuel without compromising performance, driveability and predictability of the vehicle.

Besides, in cooperation with the authors of [van Druten, 2001] and [Serrarens, 2001] a thorough overview of fuel saving principles, and the associated efforts (development, cost, packaging, *etc.*) is given.

## 1.4 Main contributions and outline of this thesis

The main contributions of this thesis and the underlying research are listed below, at the same time indicating the outline of this thesis:

- a rather complete survey of fuel saving principles and associated efforts is provided, especially with respect to the powertrain (Chapters 2 and 3). Moreover, a *hybridization factor* is introduced, and a lower bound for the level of hybridization (see Chapter 3) is obtained, resulting in an upper bound for the associated fuel savings;
- a novel transmission concept, referred to as the Zero Inertia powertrain, is presented (Chapter 4). This transmission concept for automotive application combines a CVT and a low-speed flywheel, in a way that is unprecedented (see [van Druuten *et al.*, 2000b,a]);
- the operation of CVTs and related design issues are introduced in Chapter 5;
- an overview of CVT models, describing stationary and transient behaviour, is provided, as well as a model for the CVT hydraulics, see Chapter 6 and Appendix B. Furthermore, an alternative hydraulic actuation scheme is suggested, capable of faster shifting with increased robustness with respect to gross belt slip (Appendix C);
- the power losses in the CVT are elucidated in a way that is believed to give more physical insight. In the implementation, these losses are taken into account using an additive torque loss model (Chapter 6);
- a CVT speed ratio controller is proposed, which aims at minimizing the tracking error as well as the transmission losses, subject to the constraint that gross belt slip is to be prevented at all times (Chapter 7). Much attention is paid to properly deal with several operational constraints, in conjunction with integral controller action (anti-windup);
- existing approaches to implement a Stop-Go functionality are listed in Chapter 8, succeeded by an introduction to the mechanical Stop-Go solution, indicated as ZI Stop-Go. This system should enable simultaneous acceleration of the vehicle and engine without noticeable delays;
- a hybrid model for the (different stages in the) ZI Stop-Go system is presented (Chapter 9). Using some simplifying assumptions, an analytical expression for the minimally required flywheel speed is obtained. To translate the accelerator and brake pedal positions into setpoints for the supervisory controller, a pedal interpretation is devised which is useful for (CVT) powertrains in general. This interpretation switches from a torque to a power interpretation in a continuous way, while aiming for maximal drive-line efficiency (Appendix D);
- general ideas for controlling the ZI Stop-Go transmission are explained using nomographs (Chapter 10). The supervisory Stop-Go controller is designed and evaluated in simulations, and experimental evaluation of the controller and of the concept has commenced, yielding promising results;
- a fully programmable high-power test rig was designed and realized, providing an experimental platform for testing both the ZI and the ZI Stop-Go transmission (Appendix A).

Finally, Chapter 11 summarizes the outcome of this thesis and gives directions for future research.



## Chapter 2

# Fuel Saving Principles

### 2.1 Introduction

Modern passenger cars represent a technologically advanced form of flexible personal mobility. They are comfortable, high performing and relatively safe. Imagining global society without passenger cars is simply impossible. Despite all efforts, the passenger car is still a fairly inefficient means of individual transportation. Figure 2.1(a), from [Delsey, 1991], shows the distribution of fuel energy to the various heat producing processes involved with driving a passenger car. A more realistic graph might be the pie-chart of Figure 2.1(b), from [DOE

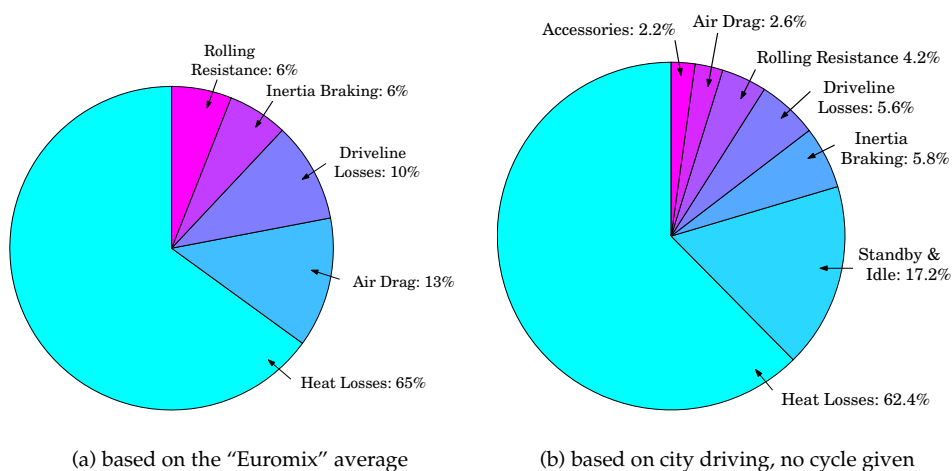


Figure 2.1: Typical energy distributions for a passenger car

and EPA, 2001] (measured drive cycle is not given). From both figures it follows that only between 15% and 25% of the energy in the gasoline is actually used to propel the vehicle—that

is to overcome vehicle inertia, aerodynamic drag and rolling resistance—and to power accessory systems like airconditioning. The rest of the energy is lost in the form of heat transfer to coolant and ambient air, friction within the engine and transmission, and pumping of air into and out of the cylinders (*e.g.*, during idling).

Regarding these figures, insight can be gained into how fuel economy might be improved. In general, methods for reducing the fuel consumption can be divided into four categories:

1. improving the efficiency of the individual powertrain components, *i.e.*, engine, transmission and power take-off;
2. reducing the external load of the powertrain, *i.e.*, vehicle mass, rolling resistance and air drag;
3. alternative powertrain operation, *i.e.*, E-line<sup>1</sup> tracking, Stop-Go<sup>1</sup>, Start-Stop<sup>1</sup> and Brake Energy Recovery (BER)<sup>1</sup>;
4. non-vehicle technology, *i.e.*, driving behaviour, infrastructure and traffic management, law, policy and legislation.

In this chapter, all four categories are briefly discussed. The following chapter concentrates on alternative powertrain operation in more detail. Engine emissions are only briefly treated.

## 2.2 Improving component efficiency

A conventional passenger car driveline basically comprises an internal combustion engine, a launching device (friction plate clutch, torque converter, magnetic powder coupling, *etc.*), a torque amplifying transmission (any kind), differential and driveshafts, see Figure 2.2. The fuel tank, cooling system, battery, electric starter motor and various Power Take-Off (PTO) components, such as the alternator, fuel pump, water pump, power steering pump, and ignition, draw up the indispensable but fuel consuming periphery of the driveline. Part of the mechanical power generated by the engine is lost in the transmission and to the PTO. The net torque in the drive shafts propels the wheels. Ways for decreasing the driving resistance are discussed further on. First, various methods and potentials for fuel economy improvement by enhancing the efficiency of individual driveline components are discussed.

### 2.2.1 Engine efficiency

The engine efficiency has been strongly improved in the recent past, although it is still the least efficient component in the powertrain. Despite its disappointing efficiency, the modern combustion engine, the prime mover of road-going vehicles, is a more or less optimal combination of low manufacturing cost and -energy, power density, volume, efficiency, durability, maintainability, recycleability and controllability. A point of concern about this machinery is the load-dependent efficiency characteristic. Without employing more advanced powertrain concepts this dependency hampers the most fuel-optimal utilization of the combustion engine.

The fluctuating power requests needed for the vehicle's motion, demand the operating conditions of the engine to be changed accordingly. In this respect, there are two main reasons why fuel consumption may be larger than theoretically achievable, namely:

---

<sup>1</sup>To be defined in Section 3.2

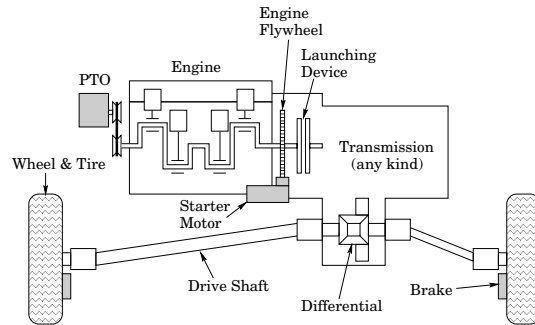


Figure 2.2: Basic (front wheel) driveline

- the energy-specific fuel consumption [ $\text{g/kWh}$ ], also known as *Brake Specific Fuel Consumption (BSFC)*, depends on the operating point, defined by the engine torque and speed, that fulfill the requested power;
- the BSFC varies with the power demand itself.

The BSFC is best viewed in a so called engine map. In this map various quantities may be visualized by iso-curves being a function of static engine speed and engine output torque. In the map of Figure 2.3 the BSFC curves of a 1.6  $\ell$ , multi-point injection petrol engine are sketched. Also hyperbolas graphing constant engine power are drawn. The BSFC varies

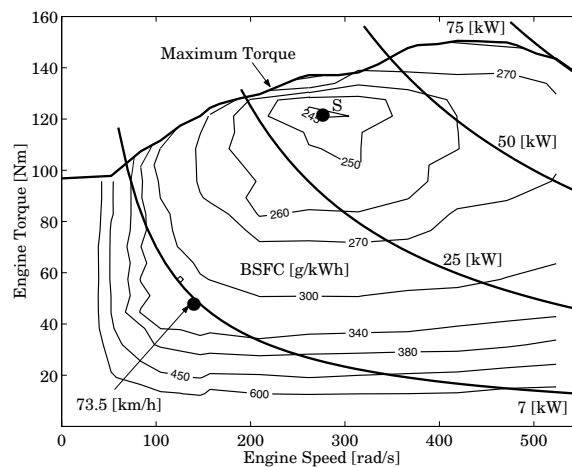


Figure 2.3: Energy specific fuel consumption (BSFC) in engine map

substantially along and between the power hyperbolas. The operating point with the lowest BSFC, indicated in Figure 2.3 by 'S', is termed the *sweet spot*.



The influence of the chosen operating point on the fuel economy is substantial. In an illustrative example a mid-sized passenger car runs at 73.5 [km/h], indicated by the dots in Figures 2.3, 2.4(a) and 2.4(b). Figure 2.4(a) displays the fuel consumption per traveled kilometer (DSFC) as a function of constant vehicle and engine speed. The fuel consumption per second (TSFC) as a function of engine output power is plotted in Figure 2.4(b).

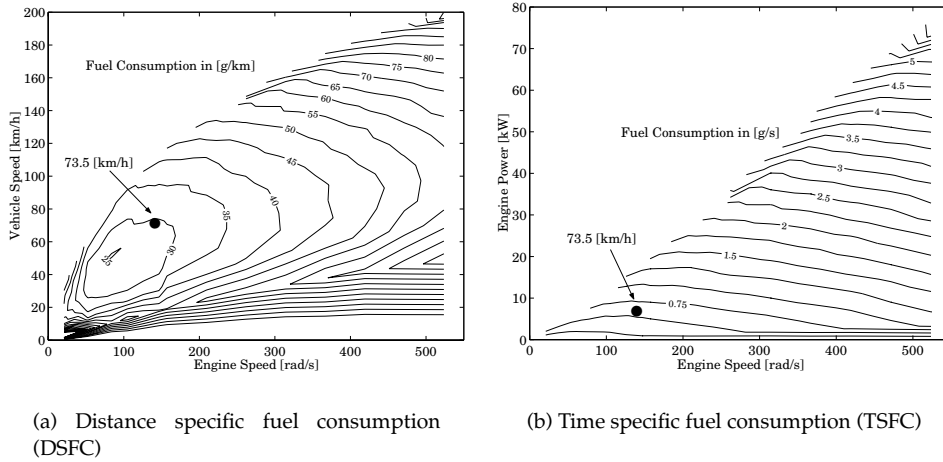


Figure 2.4: Alternative representations of the fuel consumption

Maintaining the constant vehicle speed at higher engine speeds substantially raises the fuel consumption per traveled kilometer, *cf.* Figure 2.4(a). For instance, up to twice as much fuel is consumed if the vehicle speed is kept at 73.5 [km/h] with an engine speed of 500 [rad/s]. Regarding Figure 2.4(b), a full acceleration (exploiting maximum engine power) from 73.5 [km/h] would consume about ten times more fuel!

### engine improvements

In trying to improve driveline component efficiency, the internal combustion engine has been given the most attention, leading to a multitude of solutions which improve the combustion efficiency, along with the emissions. Treating them all would go far beyond the scope of this thesis. However, the most important solutions for the petrol engine, being the engine type considered in the EcoDrive project, should receive some attention.

*Variable valve timing* has improved the efficiency, performance and emission quality. Advancing the intake valve timing for higher engine speeds improves the homogeneity of the air/fuel mixture and in general improves the combustion performance. This increases the engine torque or alternatively provides the same torque using less fuel. Furthermore, retarding the closing of the exhaust valve for higher engine speeds leaves part of the exhaust gases in the cylinder while the new air/fuel mixture is already entering the cylinder (overlapping of intake and exhaust period). Consequently, the mixture can be leaner resulting in further combustion of unburned constituents and hence lower emissions. *Exhaust Gas Recirculation (EGR)*

further exploits this technique by actively recirculating the exhaust gases through a by-pass channel controlled by a valve. Through the combination of *variable spark timing* and metered *fuel-injection*, complete combustion (stoichiometric operation) is possible for varying engine speed, load and temperature, further reducing fuel consumption and emissions.

The fuel consumption, the emissions and the engine performance are often conflicting targets. Especially emission standards hinder the further improvement of the engine efficiency [Oppenheim *et al.*, 1994]. This is caused by the fact that engine operating conditions are often shifted to regions with less  $\text{NO}_x$ , HC and/or CO emissions, but increased specific fuel consumption (also leading to higher  $\text{CO}_2$ ).

Techniques related to engine technology as described may result in a lower fuel consumption for *equal engine power* demands. On the other hand improving the efficiency of other driveline components such as the transmission and PTO will reduce the energy demand for *equal covered vehicle distance*.

## 2.2.2 Transmission efficiency

Only recently, improving the efficiency of stepped transmissions (MT and AT) has been given more attention, whereas that of the CVT has been a concern since *mature* versions of the push-belt CVT started to be commercially produced (early nineties). From [Kluger and Long, 1999] it is concluded that manual transmissions have overall efficiency values of 96.2% and leave little room for improvement (up to 96.7% at most). Kluger and Long furthermore evaluate the overall efficiency of ATs at 85.3%, whereas the efficiency of the best current AT could be improved up to 86.3%. Finally, the overall efficiency of belt type CVTs is estimated at 84.6%, and may be improved towards 88.4% by reducing the pump losses. These hydraulic pump losses for the larger part determine the efficiency of CVTs and of ATs, and are relatively high at low transmission loads. Improved pump and hydraulic circuit design can substantially increase the efficiency of CVT and AT. The design of the pump, friction fluids and mechanical part of the CVT is subject of ongoing research. Alternatively, the actuation of the clutches and of the CVT may be (partly) electrical, thus replacing the hydraulic losses by potentially lower electrical losses. For instance, in [van Tilborg, 2001], it is shown that the pump losses in the CVT can be reduced by applying part of the pulley clamping force electro-mechanically.

Finally, the overall efficiency of toroidal or traction drive CVTs (*e.g.*, see [Machida, 1999]) is estimated by [Kluger and Long, 1999] at around 91%, and may be improved by 1.8% through the implementation of more advanced traction fluids. This type of transmission holds good promise since it is well suited for high power applications, though production numbers are still limited.

## 2.2.3 Power take-off

The fuel consumption could be further reduced if also the power demand by the PTO is somehow lowered. For example, methods to improve the efficiency of the alternator are discussed in [Bürger *et al.*, 1994]. They projected a potential fuel saving of 1% when the alternator efficiency is improved by 5%. Enhancing the efficiency of all auxiliary systems is possible by increasing the on-board voltage level, giving rise to the recent development of a 42 Volt on-board grid. The alternator and starter can then be re-engineered into an integrated unit referred to as *starter-alternator (SA)*. A higher voltage leads to lower currents and reduced electric transmission losses. This is necessary for operating the increasing number of on-board electric systems, which in turn does not guarantee a lower fuel consumption altogether.

## 2.3 Reducing the external load

### 2.3.1 Vehicle mass

The increase of vehicle mass is mainly caused by higher safety and comfort standards. A better crash protection usually results in higher vehicle weight and thus fuel consumption. Vehicle weight is also increased due to the expanding amount of on-board auxiliary systems such as airconditioning, power-assisted steering, electrically operated windows, sunroofs, mirrors, seats, door-locking, in-car entertainment, *etc.* Furthermore, these systems claim supplementary power to operate. Besides the growing demands for more safety and comfort, drivers also claim an unspoilt driving pleasure. For that reason, the enhanced engine efficiency may well be overshadowed by an increased power demand. This can also be seen in Figure 2.5 (sources

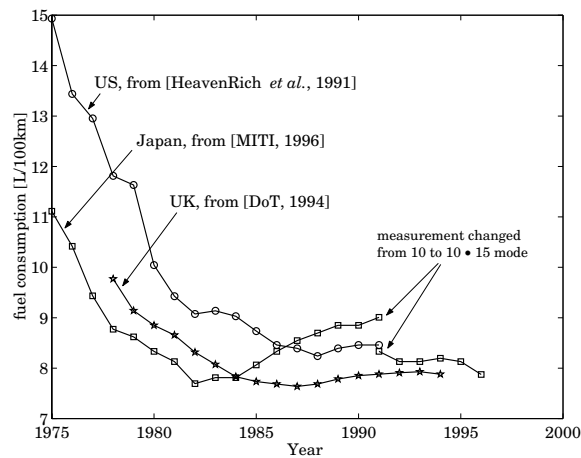


Figure 2.5: Average fuel consumption of new-sold passenger car fleet in UK, US and Japan from 1975 to 1996

from [Heavenrich *et al.*, 1991], [MITI, 1996], and [DoT, 1994]) where the fuel consumption of the average *new-sold passenger car* is shown between 1975 and 1996 for US, UK (assumed to be representative of Europe) and Japan. The absolute fuel consumption indicated by the curves can not be directly compared as such because the curves are obtained with different test driving cycles. The increase of fuel consumption after 1980 for Japan, which is not seen for the US and the UK, is explained by the increased use of rather inefficient vehicle electronics (for in-car convenience) and weight of the average Japanese car. The improvements in engine efficiency on the one hand, and especially the increase of the auxiliary power demand on the other, start to even out in the US and the UK during the late 1980s, flattening the average fuel consumption.

### 2.3.2 Rolling resistance

The rolling resistance of a vehicle is predominantly due to the tires, apart from negligibly small wheel bearing losses. The actual tire rolling resistance consists for a very small part of tire-road friction and for the larger part of tire deformation losses. The magnitude of these losses is

determined by what might be termed ‘internal’ and ‘external’ factors. The internal factors such as the tire material, the tire shape, and the tire size (width especially), substantially influence the rolling resistance. For example, two tire designs of the same overall size, but with different shapes and materials may differ in rolling resistance by a factor of two [Junio *et al.*, 1999]. External conditions influencing the tire rolling resistance are the tire pressure, tire load, road surface conditions, (internal and ambient) temperature, speed, dynamic conditions (wheel torque, cornering) and the wheel alignment (toe-in and camber). For instance, an additional 0.3 [bar] of tire pressure lowers the tire rolling resistance by about 7% [Junio *et al.*, 1999].

Reductions of tire rolling resistance may be accomplished by using better materials especially, and to a lesser extent by applying ‘smart’ tires (*e.g.*, monitoring and controlling the tire pressure) as well as active suspension (decreased dynamic tire load). The application of these technologies is limited by requirements for wet skid conditions, high speed driving, tire damping (noise and comfort) and cost. Nevertheless, a reduction of rolling resistance of 50% for 2006 (compared to 1999) is projected by Good Year [Junio *et al.*, 1999].

The rolling resistance is the dominant external load for vehicle speeds below circa 60 [km/h]; above that speed air drag is the most important.

### 2.3.3 Air drag

The shape and size of the passenger vehicle body have changed during one hundred years of automotive technology. Frontal area and shape directly influence fuel consumption through friction with the ambient air. The car designers’ utmost challenge is to mediate between interior space and exterior aerodynamical shape and size. The air resistance is made up of the pressure drag including pressure induced turbulence drag, surface resistance and through-flow resistance. The longitudinal aerodynamical drag force on the vehicle is approximately proportional to the frontal area, the square of vehicle speed and a characteristic value  $c_d$ —better known as the air drag coefficient—depending on the body shape. Increasing comfort demands and occupants’ stature do not allow a significant further decrease of the average vehicle frontal area. For instance, the growing popularity of the Multi Purpose Vehicle (MPV), has even increased the average frontal area.

Nonetheless, continuous re-fashioning of the vehicle shape has reduced the  $c_d$ -coefficient tremendously, see Figure 2.6. The theoretical minimum of  $c_d$  lies somewhere around 0.15. The General Motors’ Precept concept vehicle, reaching  $c_d = 0.163$ , comes close to this minimum. For normal passenger cars, a number of important measures influence the aerodynamics. The most important measures are the decrease of the rear window angle with the horizontal axis, the smoothness and rounding of the rear window stile (C-stile) and a high but short trunk with a sharp transition down at the end. Taking such measures may lead to a higher vehicle mass because of the unfavourable ratio between surface and volume. This might be compensated by lighter materials or by improved constructional design.

The lower air resistance due to a smaller air drag coefficient leads to a higher maximum speed of the vehicle, hence requiring an increased speed ratio coverage of engine and/or transmission. The latter demands for a higher overdrive bringing the engine operating point towards lower engine speeds at virtually equal engine torque. Fuel economy can be improved by about 1% for 3% air drag reduction, [Seiffert and Walzer, 1989]. Naturally, this number depends on the combination of the specific vehicle and engine and should therefore be interpreted with care.

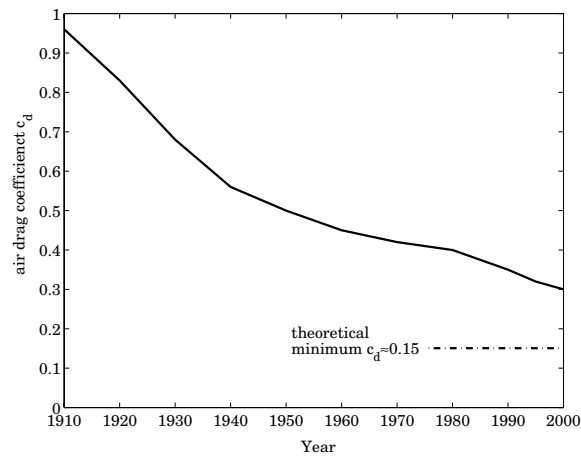


Figure 2.6: Historical trend for the average air drag coefficient

## 2.4 Alternative powertrain operation

Fuel economy can be improved by more optimal operation of the existing powertrain components or by extending the powertrain with more components to enhance its functionality. By such means operating regions with poor engine efficiency can be avoided. In this section, four principles which aim at more efficient engine operation, or at avoiding excessive fuel consumption otherwise, are briefly discussed. In Chapter 3, these fuel saving principles will be given more attention.

- *E-line tracking* amounts to controlling the engine in such a way that for each requested engine power the fuel consumption is minimal. For modest driving this comes down to restraining the engine speed to extremely low values.
- *Stop-Go (SG)* systems halt the engine during full vehicle stops and facilitate a new vehicle launch either by first restarting the engine and then launching the vehicle, first launching the vehicle and then restarting the engine, or launching and restarting at the same time. Clearly, the fuel otherwise consumed during engine idling can be saved.
- *Start-Stop (SS)* refers to delivering the required energy by intermittently operating the engine in the sweet spot (defined in Section 2.2.1). Because the engine power delivered in the sweet spot will generally be different (usually higher) than the demanded wheel power, some sort of energy buffer is needed, as well as a generator and motor to compensate for the momentary power surplus (while the engine is on) and power deficit (while the engine is off), respectively.
- *Brake Energy Recovery (BER)*. The mechanical energy stemming from the engine is partly accumulated in the vehicle's inertia. This energy can be recuperated whenever decelerations of the vehicle are requested by the driver. Reusing this energy for vehicle propulsion or to power auxiliary functions, in principle decreases the net fuel consumption.

In designing an alternative powertrain for the sake of a higher fuel economy, the drawbacks of such a redesign should have minor influence on the final vehicle concept, at least in proportion to the gained reduction of fuel consumption. A method for rating the fuel reduction against additional efforts and penalties is discussed in the next chapter. The following section lists some developments potentially leading to a better fuel economy, but not directly linked to vehicle technology.

## 2.5 Non-vehicle technology

There are a number of measures that are not directly related to powertrain or vehicle technology but are rather driven by external factors such as driving behaviour, legislation, policies, traffic management, infrastructure, *etc.* These factors are briefly illustrated in this section.

### 2.5.1 Driving behaviour

The behaviour of the driver and the traffic conditions strongly influence the fuel consumption. In [An and Ross, 1993] the fuel consumption as a function of *average* trip speed is measured, showing that minimal fuel consumption is reached between 65 and 80 [km/h]. On the other hand, if the fuel consumption is measured for *constant* vehicle speed this optimum lies around 50 [km/h], as will be shown in [Serrarens, 2001].

Average vehicle speed but also the number and intensity of accelerations and decelerations are highly related to the traffic conditions and the drivers' state-of-mind during a trip. Without increasing the travel time, a significant decrease of fuel consumption can be reached if the driver alters his or her driving behaviour. Theoretical studies by [Evans, 1979] and [Waters and Laker, 1980] showed that around 15% fuel reduction is possible. The evaluation of a driver-friendly fuel efficiency support tool as in [van der Voort *et al.*, 2001] showed that with a 5-speed manual transmission even 20% fuel can be saved in rural areas. Essentially, the support tool gives advice to the driver when to shift gears according to measurements of the vehicle conditions and of the actual accelerator pedal deflection.

### 2.5.2 Infrastructure and traffic management

Fuel consumption is closely related to the vehicle speed, which in turn is strongly influenced by the road infrastructure. In city driving the traffic flow is often hampered by frequent stop-and-go actions due to crossings, different speed of the traffic participants, *etc.*

Active control of traffic flow, also termed *traffic management* can decrease the congestion through leveling the traffic speed. Reducing the average speed by such means can also reduce the fuel consumption. Personal mobility is still the most favourable way of human transportation. On the other hand, when active control of traffic implies that traffic flow is homogenized, the distinction with public transportation becomes somewhat smaller. Traffic management therefore also requires a change in attitude of the traffic participants.

Recent investigations in intelligent vehicle guidance, platooning and automated highways look ahead in this direction. Through tight intercommunication between vehicles or indirectly through in-road sensors, active distance control between vehicles can minimize congestion and homogenize traffic density. Moreover, the safety can be increased but at the cost of individual vehicle control. Developments in this area are ongoing, mostly still encountering problems with robustness and safety.

Along with adapting traffic systems, vehicle technology itself should continuously reiterate to find a new optimum between fuel economy and the changing vehicle utilization. Governments can be effective in helping these actors to bring their influence in tune.

### **2.5.3 Law, policy and legislation**

Speed limits set by law can manipulate the average speed in urban, rural and highway driving. On the other hand, a substantial decrease of speed limits is hardly accepted by society. Governmental legislation in the area of emissions and fuel consumption stimulate car manufacturers and research institutes in their search for new vehicle propulsion and fuel technologies. One can think of fuel taxes, emission standards and categorization of vehicles with respect to fuel consumption (using labels). Also subsidizing research initiatives in this area helps to find new ways for improving fuel economy and reducing emissions. Through educational programs, governments can make new generations more aware of the limited fossil fuel resources and the environmental impact of transportation. This way the social basis for spending money and capacity of society into the improvement of fuel economy and reduction of emissions will get broader.

## Chapter 3

# Normalized Innovation Values

In practice, the most promising fuel saving principle is the one that achieves the highest ratio between fuel economy on the one hand and additional costs, size, weight, *etc.* on the other. The fuel economy obtained by exploiting an innovative idea may be termed *innovation value* whereas the mentioned penalties besides those related to development risks, complexity and driveability are termed *innovation efforts*. Hence, the most promising innovation is the one with the highest innovation values demanding the least innovation efforts. In this chapter, an attempt is made to judge the values over the efforts for the powertrain-related fuel saving principles mentioned in Section 2.4 or combinations thereof. This is defined as the *normalization* of the innovation values. Based on the normalization, the ZI powertrain proves to be the second best solution for saving fuel. The eventual decision to develop the ZI powertrain is supported by additional constraints overruling the outcome of the normalization. These constraints are set by the project target aiming at a fuel saving of 25% (the optimal solution can potentially save more) in combination with the limited project resources.

The remainder of this chapter is organized as follows. Throughout this chapter, examples of so-called *hybrid* vehicles are presented. For completeness, first a number of definitions related to hybrid vehicles are given in the next section. In Section 3.2 the theoretical fuel saving potentials are calculated and the results are analyzed. Next, in Section 3.3 the corresponding efforts, such as component efficiency, weight, driveability penalties and production costs, are discussed. In Section 3.4 the actual normalization of the innovation values is performed and conclusions are drawn with respect to the value of the ZI powertrain as a purely mechanical solution for saving fuel.

### 3.1 Hybrid powertrains

A *hybrid* powertrain uses different types of power sources to propel the vehicle. The power source which primarily determines the range of the vehicle, is called the *primary* source. Additional power sources are referred to as *secondary* sources.

Hybrid vehicles can be operated in four different *modes*. The *conventional* mode applies when the primary source is *mechanically* connected to the wheels and moreover is the only active power source. If besides the primary source, a secondary source is mechanically connected to the wheels and active, the *parallel* mode applies. The *series* mode refers to the situation where the primary source is *not* mechanically connected to the wheels, hence all wheel



power is delivered by a secondary power source that acquires its energy non-mechanically from the primary source. Finally, the parallel mode and the series mode can occur at the same time. That case is referred to as the *combined* mode.

It is chosen to indicate the different types of operation as *modes*, instead of reverting to the commonly used terms *series, parallel and combined hybrids*, since a hybrid vehicle can generally be operated in either of the four mentioned modes. In practice, the combined mode is mostly encountered in so-called 'power-split' configurations, involving a planetary gear set.

Figure 3.1 schematically depicts a generic hybrid vehicle, capable of operating in all discussed modes. The component E represents the primary power source, whereas the wheel W on the right side of the figure represents the vehicle load. In between are a transmission T, a generator G, an accumulator A, and a motor M. The transmission T strictly has a variable transmission ratio, and possibly incorporates a planetary gear set. Fixed reductions are omitted for clarity, but may be present in any of the connections. All components may be separated by connecting interfaces, *e.g.*, mechanical (clutches) or electrical (actuation, wiring). The generator and motor can be separate devices but may also be combined into one component. In case of a flywheel as the secondary source, the motor, the generator and the accumulator are in fact all combined into a single device.

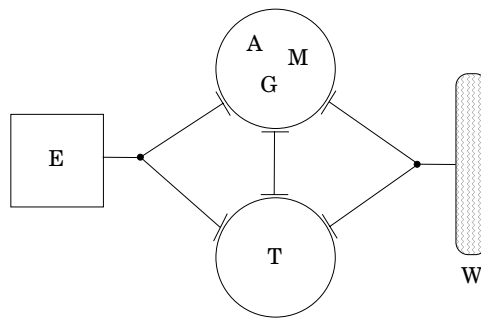


Figure 3.1: Generic hybrid powertrain configuration

As an example, the Toyota Prius powertrain is shown in Figure 3.2. Here the transmission T is a planetary gear set. The primary source E, a gasoline engine, is connected to the carrier of the planetary gear. The annulus gear is connected to the load W as well as to a secondary power source M1/G1, while the sun gear is connected to yet another secondary power source M2/G2. Both M1/G1 and M2/G2 can be operated as motor or as generator and are connected to the accumulator A. Because M1/G1 is directly connected to the wheels, it can be used as sole mover, hence the Prius is operated in series mode then. In all other cases, either the parallel or the combined mode applies. Charging the accumulator is possible using either parallel or combined mode. If the engine is delivering power, the secondary power source M2/G2 *must* always be active (motor or generator mode) to maintain a torque balance over the planetary gear set. Furthermore, the secondary source M1/G1 should always operate as a motor (either in series or combined mode) if the accumulator is fully charged.

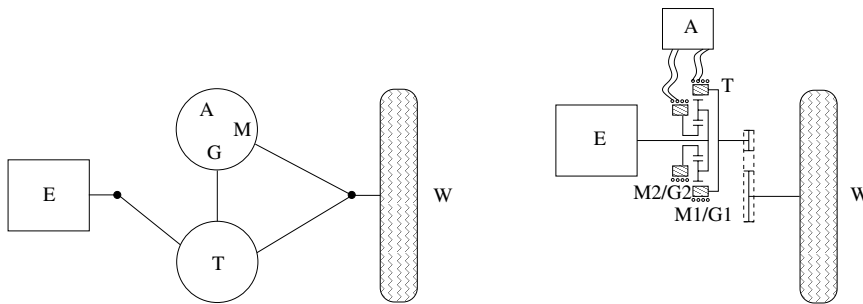


Figure 3.2: Toyota Prius powertrain

### 3.2 Innovation values: fuel economy

First insights in fuel saving potentials are gained when mapping certain driving cycles directly onto the specific fuel consumption characteristics of the internal combustion engine. The innovation value (fuel economy) of each fuel saving principle is analyzed for the rural, city and highway driving cycle within the HYZEM (HYbrid technology approaching efficient Zero Emission Mobility) envelope and the NEDC. A driving cycle is a time representation of a requested vehicle speed trajectory, used for generating fuel consumption figures on a roller-bench with controllable brake facility (chassis dynamometer). In practice, a human driver has to follow the speed trajectory within a certain margin. Measuring the fuel consumption as such appears to be somewhat deceptive, depending on the type of powertrain. For powertrains with manual transmissions, the gear changes are prescribed during the drive cycle. This is not true for (all kinds of) automatic transmissions, for which in principle the gear shift strategies—or equivalently the engine operating points—may be chosen freely.

In the calculations underlying this chapter, for simplicity the vehicle is assumed to track the reference speed exactly. Furthermore, the freedom of choosing the engine operating points is adopted here in order to fully exploit the fuel saving principles. These assumptions provide a clear understanding in the mechanisms of the four fuel saving principles.

The influence of the transmission and conversion efficiencies on the fuel saving principles is regarded separately. The efficiency is unknown a priori and maximizing it is seen as one of the developing efforts to be undertaken. The underlying computations of this section hence assume a transmission efficiency of 100%. This assumption implies that the computed fuel consumption over a particular drive cycle and according to a certain fuel saving principle will be a theoretical minimum. It is therefore interesting to investigate how close this minimum can be reached in practice.

Using the outcome of this section, the innovation values will be corrected for efficiency and for increased weight and subsequently normalized in Section 3.4 using the efforts of various materializations presented in Section 3.3. The fuel saving of the four principles, mentioned earlier in Section 2.4, is determined as follows:

- E-line tracking. The fuel saving of E-line tracking is determined with respect to operating lines roughly resembling operating lines seen in practice, see Section 3.2.1. Such lines are always a compromise between driveability and fuel economy;
- Stop-Go. The fuel saving due to Stop-Go operation is determined by subtracting the

- total amount of fuel otherwise consumed during engine idling at vehicle halt;
- Start-Stop. The fuel economy potential can be computed by assuming that the required energy is generated intermittently in the sweet spot if the momentary drive power is below or equal to the sweet spot power  $P_{ss}$ . Above  $P_{ss}$ , E-line tracking is performed;
  - brake energy recovery. The recovered energy can be used in a number of ways making it hard to determine the fuel saving potential unambiguously. In this section, the accumulated fuel required to deliver the energy needed for vehicle acceleration is assumed to be delivered in the sweet spot and is in Section 3.2 assumed to be fully recovered.

### 3.2.1 Reference vehicle

The vehicle that will be used as a reference in all the comparisons throughout this chapter is a mid-size passenger car, that weighs 1360 [kg] (including two occupants), has a rolling resistance of 55 [Nm] and a  $c_d$  value of 0.31. It is termed the *reference vehicle*. The engine is a 1.6 l 4-cylinder petrol engine with a maximum power rating of 75 [kW] at 540 [rad/s], and is assumed to be operated on the *reference operating line*, that is defined further on. The E-line collects the engine operating points which are fuel-optimal for a given power level, and can be uniquely determined for any engine. Figure 3.3 depicts the E-line and operating lines  $OL_{x\%}$  comprising operating points with  $x\%$  higher fuel consumption compared to the E-line. Also depicted is the *Wide Open Throttle (WOT) line*, which represents the maximum engine torque as a function of the engine speed. The E-line is jagged because of the limited number

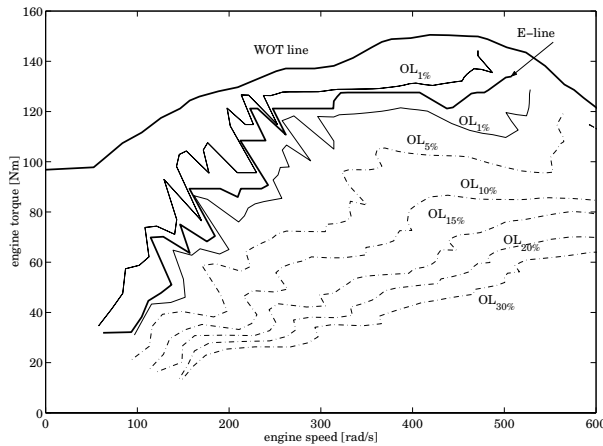


Figure 3.3: E-line and operating lines with  $x\%$  more fuel consumption

of measurements combined with the small differences in fuel consumption around the E-line, as is shown by the two lines indicating a margin of 1% extra fuel consumption with respect to the E-line. In practical implementations, a smoothed version of the E-line is used.

In today's passenger cars, if equipped with either a CVT or AT, an operating line roughly between the  $OL_{15\%}$  and  $OL_{20\%}$  lines is applied for stationary situations. Using such an operating line results in an acceptable driveability but clearly penalizes the fuel economy, as

compared to the E-line. Here, the  $OL_{15\%}$  is chosen as the reference operating line for computing the fuel saving potentials. This operating line is highly similar to those used in 4-AT and CVT in ‘performance mode’.

### 3.2.2 Influence of driving cycles

There exists a wide variety of certified driving cycles, showing large differences in power requests, dynamics, average speed, *etc.* From these cycles, the HYZEM and NEDC are chosen to determine the innovation values. The HYZEM cycle consists of three subcycles, namely the urban (city), rural and highway cycle. Since the HYZEM was obtained by averaging typical vehicle usage in Europe it is thought to be a good representation of everyday driving. The potentials of the four fuel saving principles depend highly on the considered cycle.

In Figure 3.4 power histograms of the HYZEM (urban, rural, highway) and NEDC cycles are shown. The required power is calculated using a model of the reference vehicle. The power histograms are obtained using steps of 1 [kW]. Especially for the NEDC and the urban drive cycle, the time fraction spent at zero power (vehicle halts) is remarkably large. Furthermore, power demands larger than half the maximum engine power are rare on the depicted driving cycles.

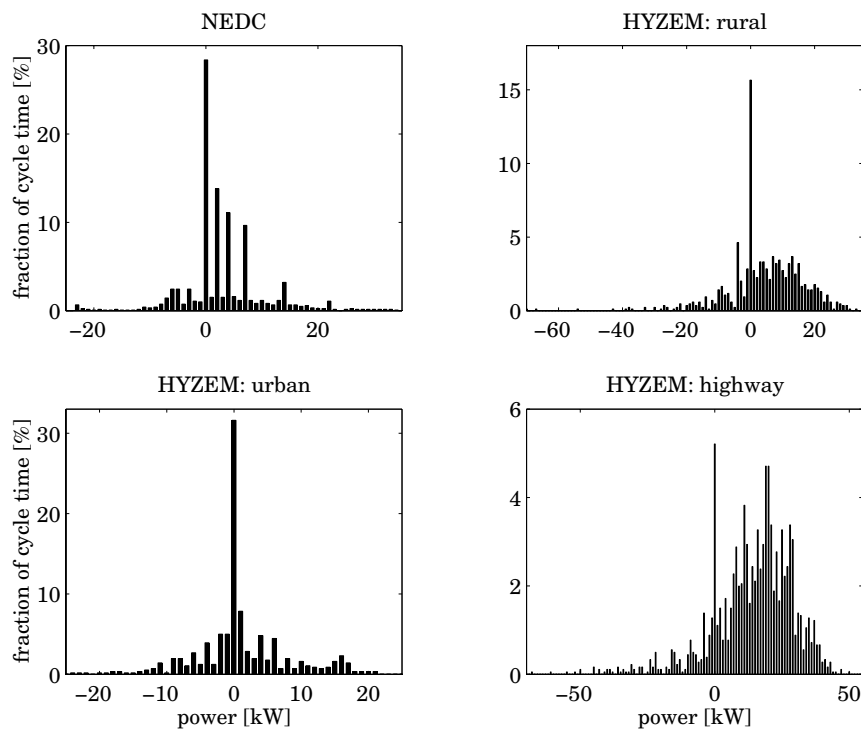


Figure 3.4: Time histograms of power distribution over the drive cycles

### 3.2.3 Fuel economy

In this section, the fuel savings with respect to the reference operating line  $OL_{15\%}$  are evaluated, using the mentioned drive cycles, for each of the four fuel saving principles.

#### E-line tracking

The accumulated fuel consumption in [g] and the percentage of fuel consumption reduction for the four driving cycles are shown in Table 3.1. From this table it is apparent that the

CYCLE	$OL_{15\%}$ [g]	E-LINE [g]	E-LINE FUEL SAVING [%]	IDLE [g]	STOP-GO FUEL SAVING [%]
NEDC	556.7	493.5	11.4	64.4	11.6
rural	568.4	498.0	12.4	19.0	3.3
urban	205.1	183.5	10.5	30.5	14.9
highway	2460.3	2142.1	12.9	13.0	0.5

Table 3.1: Fuel savings using E-line tracking and Stop-Go

fuel consumption reduction for E-line tracking is between 10 and 13.0%, approximating the maximally achievable fuel saving  $((1 - 1/1.15) \times 100 = 13\%)$  of E-line tracking with respect to the  $OL_{15\%}$ . The 13% fuel saving is reached when the contribution of engine idling converges to zero, which is almost the case on the highway subcycle, where a relatively short standstill time applies (5.5% of the total cycle time). Furthermore, the average power level on this cycle is high compared to the other cycles.

#### Stop-Go

The fuel savings when using Stop-Go (also see Table 3.1) can amount up to 15% on the urban subcycle, assuming that the restarts of the engine require no additional energy. Also, incomplete combustions during starting, leading to a slight increase in fuel consumption and emissions are not treated here. Hence it is assumed that the fuel saving exactly equals the accumulated idle fuel consumption (where the time-specific idle fuel consumption is taken to be 0.23 [g/s]). The impact of Stop-Go on the highway subcycle is obviously limited, again due to the limited contribution of engine idling.

#### Start-Stop

The Start-Stop principle can be best explained looking at the specific fuel consumption (BSFC) of the engine as a function of the output engine power. For the E-line and the  $OL_{15\%}$  this BSFC characteristic is plotted in Figure 3.5. From this figure it can be concluded that around  $P_{ss}=32$  [kW] there is a minimum, previously called the sweet spot. Consequently, fuel can be saved when for all requested powers below  $P_{ss}$ , the drive energy is delivered in the sweet spot operating point. Operating the engine in the sweet spot requires intermittent (duty-cycled) operation of the engine to match the generated energy to the required drive energy. Furthermore, an accumulator is required to store the generated energy. Apart from that, Start-Stop necessitates an extra motor and generator to compensate for the momentary power deficit and surplus, respectively. For power requests beyond  $P_{ss}$  the engine must be operated on a regular operating line. In this case, the E-line is chosen.

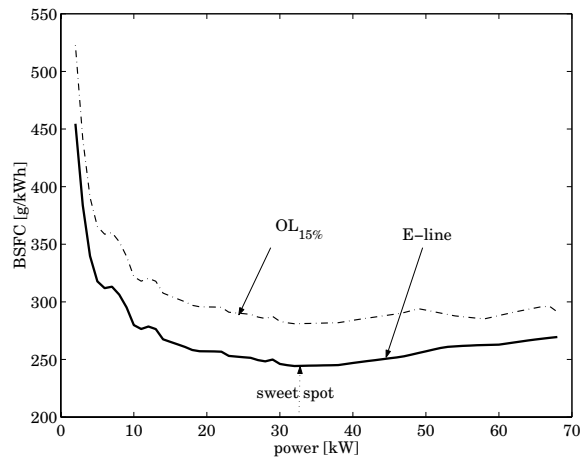


Figure 3.5: Brake specific fuel consumption for the  $OL_{15\%}$  line and the E-line

The maximum fuel saving potential for the Start-Stop principle with respect to  $OL_{15\%}$  and with respect to E-line+Stop-Go, is shown in Table 3.2. The latter fuel savings (last column) are included to show the merit of Start-Stop for requested power levels larger than zero and smaller than  $P_{ss}$ . Note that Stop-Go and E-line tracking for power levels beyond  $P_{ss}$  were chosen to be an integral part of the Start-Stop principle.

CYCLE	$OL_{15\%}$ [g]	START-STOP [g]	FUEL SAVING [%]	FUEL SAVING W.R.T. E-LINE + STOP-GO [%]
NEDC	556.7	347.5	37.6	14.6
rural	568.4	419.4	26.2	10.5
urban	205.1	119.8	41.6	16.2
highway	2460.3	2018.4	18.0	4.6

Table 3.2: Fuel savings using Start-Stop

A number of observations are made. First, the saving potential is especially high for city driving (urban and NEDC). This can be explained by the poor engine efficiency at low output power levels even in case of E-line tracking, in combination with the large share of required power levels beneath  $P_{ss}$  for such cycles. Second, the improvement of fuel economy over E-line+Stop-Go is rather limited for the highway cycle. For such a cycle, the power histogram is largely concentrated around  $P_{ss}$  and beyond. Moreover, around the sweet spot the specific fuel consumption is already quite low and rather insensitive for the power level, *cf.* Figure 3.5. The resemblance between the fuel savings for urban and NEDC with respect to E-line+Stop-Go may become clear when observing the similarity between the power histograms of the two (see Figure 3.4).

### brake energy recovery

In principle, the kinetic energy of the vehicle that is normally dissipated at the wheel brakes can be recovered. In this section, a number of rigorous assumptions underlie the calculated fuel saving potentials of brake energy recovery:

- all vehicle braking is performed by a generator. This assumption implies radical demands on the maximum power of the generator and control periphery as well as its reliability and safety;
- the kinetic energy is completely re-used for propulsion of the vehicle;
- all transmission and conversions involved occur with 100% efficiency.

In Section 3.3, these assumptions are partly released. Table 3.3 lists the computed savings using these assumptions. The first (numerical) column repeats the fuel consumption figures for  $OL_{15\%}$ . The above assumptions imply that the required drive energy exactly equals the energy which is dissipated by the road load. The fuel needed for delivering this energy is calculated operating the engine in the sweet spot, and hence is the minimal fuel consumption theoretically possible with the reference vehicle and the adopted engine. Delivering the road load energy using other strategies than sweet spot poses problems of ambiguity. The recovered brake energy can be reused for assisting the engine in a number of ways. The strict relationship between the requested drive power and specific fuel consumption may then disappear. This ambiguity does not occur when persistently delivering the cycle energy in the sweet spot. This implies that the computations assume that the Start-Stop principle is integrated in brake energy recovery.

Note that such operation is impossible during prolonged driving at power levels higher than  $P_{ss}$ . However, in the highway cycle, the power levels above  $P_{ss}$  (32 [kW]) are linked to short term vehicle accelerations, while the average power level on this cycle still is below  $P_{ss}$ . Also, in the computations it was implicitly assumed that the surplus of requested power beyond  $P_{ss}$  is delivered by the additional accumulator, in order to keep the engine in the sweet spot.

CYCLE	$OL_{15\%}$ [g]	ROAD LOAD IN SWEET SPOT [g]	FUEL SAVING [%]
NEDC	556.7	269.8	51.5
rural	568.4	284.8	49.9
urban	205.1	65.6	68.0
highway	2460.3	1823.2	25.9

Table 3.3: Fuel savings using brake energy recovery and Start-Stop

### 3.3 Innovation efforts

In this section a number of innovation efforts is defined and evaluated for the fuel saving principles. Somehow quantifying these efforts—often just using relative ranks such as ‘high’, ‘low’, ‘average’—provides ways to compare the saving principles. Efforts, when applicable, treated for each principle are:

- additional fuel economy penalties depending on the specific technology and configuration (transmission and conversion efficiencies, supplementary weight, *etc.*);
- driveability aspects such as instant power reserve, engine restarts, noise-vibration-harshness (NVH), comfort, predictability;
- impact on total vehicle design, for example packaging, vehicle dynamics, safety;
- additional costs of development, manufacturing, materials;
- complexity leading to penalties for robustness, durability, maintenance, control development;
- environmental aspects such as recyclability, emissions.

### 3.3.1 E-line tracking

#### transmission efficiency

The fuel economy for E-line tracking is influenced by the limited transmission efficiency  $\eta_T$ . Especially in the case of cycles showing insignificant idling phases, the influence of the transmission efficiency on the fuel economy is near to linear. For instance, increasing  $\eta_T$  from 80 to 100%, reduces the fuel consumption of the reference vehicle (at the OL<sub>15%</sub>) on the urban cycle by 13.6%. For the highway cycle this fuel economy improvement is 18.6%, that is almost the transmission efficiency difference, 20%. Lowering the efficiencies of two identical vehicles, one controlled at the OL<sub>15%</sub> and the other at the E-line, hardly influences the *relative* fuel saving (less than 0.5% when altering  $\eta_T$  from 80 to 100%).

#### driveability

Driveability is for the larger part determined by the instant availability of power when pressing the accelerator pedal. The so-called *power reserve* is the product of the actual engine speed and the *torque reserve*, where the torque reserve is defined as the difference between the actual and maximum (WOT) engine torque. As can be seen in the engine map (Figure 3.3), when for a given power level the engine is operated at a higher engine speed and a larger torque reserve, a much larger power reserve results at the expense of fuel economy. This observation is more exemplified in Figure 3.6, where the *power reserve* is plotted against the actually delivered engine power. The driveability is improved tremendously when leaving the E-line for an operating line below it. For instance, choosing OL<sub>15%</sub> degrades fuel efficiency by 15% but increases the power reserve by a factor 4 to 7. The dashed line indicates the maximum power reserve possible, truncated by the engine speed that corresponds to maximum engine power. All operating lines coincide at this line, tending to zero power reserve when approaching the maximum engine power (75 [kW]).

In the previous reasoning it was assumed that the engine torque can be changed instantaneously and without penalty. Changing the engine speed could (eventually) increase the output power as well, though the dynamic response of the vehicle—and thus its driveability—is penalized greatly when the engine acceleration is too large.

The physical background for this can be found in the primary-sided or, for short, *primary inertia*, *i.e.*, the total inertia of the components directly connected to and including the engine. Although the primary inertia is relatively small compared to the vehicle inertia, for good driveability it is of great relevance that the engine can be swiftly accelerated by *shifting down*



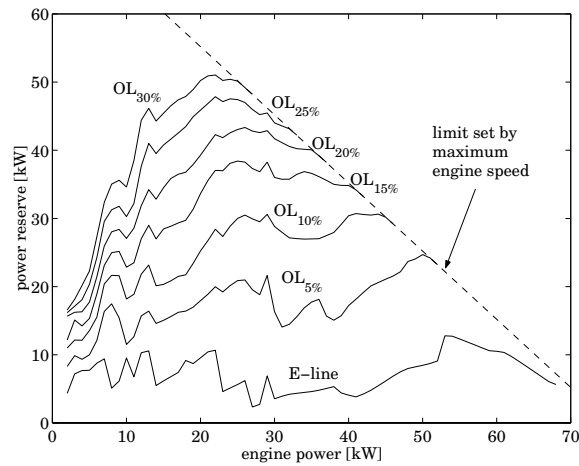


Figure 3.6: Power reserve as a function of stationary power for various operating lines

the transmission, *i.e.*, lowering the transmission ratio (defined as output speed divided by input speed). The engine power reaches its maximum at a fairly high engine speed. If the transient to this maximum power is required to be fast, the acceleration of the primary inertia (shortly) requires a power level similar to the power needed for the actual propulsion of the vehicle. When in such a case the engine was operating at low speed and high torque, *i.e.*, with a small power reserve, fulfilling an acceptable power transient is deemed impossible. Instead, to facilitate the acceleration of the primary inertia, power flows from the vehicle to the engine, consequently shortly decelerating the vehicle instead of accelerating it.

When shifting down the transmission more slowly, the increase of wheel power might show a latency as the available power reserve is just enough to accelerate the primary inertia and cannot be used for a prompt increase of wheel power. This degrades the sensitivity of the accelerator pedal as the requested higher power is delivered after the primary inertia has accelerated. This phenomenon is referred to as *jet start* (also known as *shift-shock*, *rubber belt effect*, *torque hole*, *worn clutch effect*). Jet start behaviour is known from aircraft propulsion, where initially all combustion power must be used to accelerate the turbines before the increased engine power can be used to propel the aircraft. For pedal back-out the phenomenon also occurs but then reversely, because the instant decrease of power is counteracted as the engine speed decreases.

Jet start can be minimized by persistently operating the engine at high speeds at the expense of fuel economy, for example using the line OL<sub>15%</sub>. Even then, the transmission ratio shift speed cannot be arbitrarily high, so an advanced control strategy is required to yield an acceptable compromise between fuel economy and driveability. The advantage of using controls (software) to counteract the driveability problem is that such a solution can be flexible and cheap, as opposed to rigid and generally more expensive hardware solutions. On the other hand, pure hardware solutions will be more robust and often inherently stable, whereas software solutions cannot extend physical system limitations. The additional costs for modified hardware (and to a lesser extent, software) largely depend on production numbers.

An example of a pure hardware solution is lowering the primary (engine) inertia while simultaneously increasing the number of cylinders in order to compensate for the lack in torsional damping, as suggested, *e.g.*, in [Guo *et al.*, 1988]. Such a solution is quite expensive and moreover rather ineffective, since the remaining inertia can still adversely influence driveability. If the primary inertia were zero, the engine output torque would be independent of the engine acceleration. The ‘Zero Inertia’ solution, to be elucidated in Chapter 4, will be shown to partly realize this.

If the compromise between fuel economy and driveability is considered unacceptable, E-line tracking demands an additional power source. The additional power source has to fill up the power gap between the actual power level and a (higher) requested power level. This should be done as long as the engine itself has not reached the requested power level yet, *i.e.*, during acceleration of the engine by altering the transmission gear ratio.

Figure 3.7 shows an illustrative example of this mechanism. In the example, it is assumed that the driveability level reached with the  $OL_{15\%}$  is acceptable in practice. In other words, the additional power source should at least raise the power reserve of E-line tracking up to the power reserve reached when tracking the  $OL_{15\%}$ , see Figure 3.6. The left plot in Figure 3.7 depicts the engine combustion power  $P_{\text{combustion}}$ , the power from the primary inertia  $P_{\text{inertia}}$ , and their combined total  $P_{\text{e,total}} = P_{\text{combustion}} + P_{\text{inertia}}$ . The right plot shows the wheel power  $P_{\text{desired}}$  as it is assumed to be desired. To arrive at the desired power, an additional power, depicted in the middle as  $P_{\text{assist}}$ , is needed. In this example, a stepwise power transient from 20 [kW] (roughly corresponding to a stationary vehicle speed of 110 [km/h]) to 50 [kW] is desired. Operating on the  $OL_{15\%}$ , this step can be performed without increasing the engine speed, see Figure 3.6. When starting from the E-line, the engine power reserve is only 10 [kW], hence a power assist source of at least 20 [kW] is needed. However, for a prolonged increase of wheel power, the engine must be accelerated to arrive at a speed where it can maintain the desired power level of 50 [kW]. In this example the engine speeds up from 230 [rad/s] to 330 [rad/s] (corresponding to 20 and 50 [kW] on the E-line, respectively) in a time interval  $\Delta t = 0.8$  [s]. Hence, an additional power  $P_{\text{inertia}}$  between 7 and 10 [kW] is required to perform the acceleration of the engine inertia. As a result, the necessary power level  $P_{\text{assist}}$  of the assist source amounts up to 27 [kW], such that  $P_{\text{e,total}} + P_{\text{assist}} = P_{\text{desired}}$ .

### power assist sources

Examples of power assist solutions are:

- electric motor + battery;
- electric motor + battery + ultracapacitor;
- flywheel + transmission;
- flywheel + electric motor.

Table 3.4 lists some relevant weight-specific ( $[\cdot/\text{kg}]$ ) quantities for a number of power source technologies and related components. In this table, PM refers to permanent magnet, EM means electric motor (synchronous and asynchronous), NiMH is Nickel Metal Hydride, Li-ion means Lithium-ion, FESS refers to Flywheel Energy Storage Systems and embodies high speed flywheels (carbon-glassfiber composites) in vacuum casing combined with a directly connected electric motor. The ZI flywheel refers to the low speed, steel flywheel that is used in the ZI powertrain, and is discussed in [van Druten, 2001]. Gearing and clutches are included to show the possibly needed efforts for extracting power mechanically. The specific

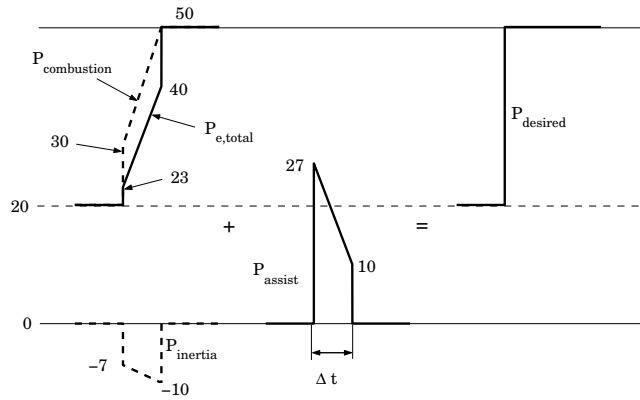


Figure 3.7: Realization of a power transient; power levels in [kW]

	P [kW/kg]	V [l/kg]	E [Wh/kg]	C [€/kg]	$\eta$ [%]	L [cyc.]
PM synch. EM	1	0.3	–	?	87–92	
asynch. EM	0.4	0.7	–	15–80	85	
NiMH battery	0.18–0.9	0.6–1.3	17–100	10–50	65–85	$1-2 \cdot 10^3$
Li-ion battery	0.15–1.4	0.6–0.7	30–120	15–100	90	$> 10^3$
ultra-capacitor	1–5.5	0.8	1–50	$> 10$	85–98	$> 5 \cdot 10^5$
flywheels (FESS)	0.75–1.5	0.4–1.0	2–50	30	83–90	$> 10^7$
ZI flywheel	1.5–3.5	0.14	0.2–2	10	98–99	$> 10^8$
(planetary) gearing	1–3	0.3–0.8	–	10	96–99	$> 10^7$
clutch (slipping)	1.5–2	0.3	–	10	50	$< 10^5$

Table 3.4: Specific values: P=specific (peak) output power, V=specific volume, E=specific (peak) energy, C=specific cost,  $\eta$ =conversion efficiency into mechanical power, L=lifespan

values for clutches are valid for a slipping clutch, since those situations are limiting the power density, especially. Values are taken from [Dietrich, 2000; Lehna, 1998; Paefgen and Lehna, 1997; Thoolen, 1993; Office of Technology Assessment, 1995; Kok, 1999] and include the corresponding power-electronics and cooling in case the energy domain is electrical. Some exceptions are not included in this table. For instance, [Dietrich, 2000] reports on *alu-elco* capacitors that reach specific power values of 10 [kW/kg] though always in combination with specific energies no higher than 0.01–0.1 [Wh/kg]. Furthermore, American Flywheel Systems, in conjunction with Honeywell claims energy densities which seem very high (over 130 [Wh/kg]) relative to other flywheels that have been built, though no official performance publications exist [Office of Technology Assessment, 1995]. The lifespan of the ZI flywheel is deemed higher than FESS because the material stress is far below the maximum allowable value, and moreover, the bearing speeds are lower. Considering this table the following observations are made:

- the ultra-capacitor and the ZI flywheel have the highest specific power. The latter shows

low energy density;

- batteries excel in energy density but are costly and lower in efficiency and lifespan;
- FESS possesses mediocre figures in every category; lifespan, however, is exceptional.

Some of the technologies are also graphically presented in a spider diagram, see Figure 3.8. Webs lying further outward indicate higher ranking, and thus lower efforts. For that purpose, specific cost and volume are inverted, whereas for the lifespan  $L$ , logarithmic values are used.

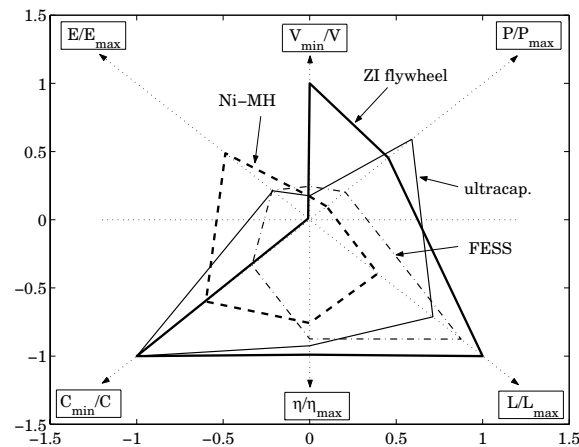


Figure 3.8: Spider diagram for comparison of innovation efforts related to various power sources, 'min' and 'max' correspond to the minimum and maximum value of the depicted components, respectively

An example power assist system is elaborated, for a power level of 27 [kW] and energy contents of 18 [Wh]. The power specification is based on the discussion in the above section, where a power assist level of 27 [kW] was concluded to be necessary for an acceleration from 110 [km/h], when operating the engine on the E-line. For lower vehicle speeds, the power requirements are smaller, mainly because the difference in engine power reserve between the E-line and the  $OL_{15\%}$  decreases. On the other hand, the mentioned difference in engine power reserve increases with higher vehicle speed, in principle yielding higher power assist demands. However, the acceleration performance from vehicle speeds far beyond 110 [km/h] is considered to be less relevant in practice. The energy contents specification is obtained as the sum of the kinetic energy increase for the maximum speed transient (approximately from 100 [rad/s] to 550 [rad/s]) and the combustion energy that is lacked during the transient time interval  $\Delta t$  (Figure 3.7).

For these specifications, a mechanical system with ZI flywheel is compared with two electrical power assist systems, one with a NiMH battery and one with an ultra-capacitor, see Table 3.5. The ZI flywheel system clearly outperforms the other two. The NiMH system is least attractive, especially with respect to weight and total efficiency. Furthermore, both electrical systems are more expensive by an order of magnitude. On the other hand, the electrical systems can potentially be used for other functions in a more flexible way. As a commercially

	mass [kg]	volume [l]	cost [€]	efficiency [%]
asynch. EM + NiMH	126	103	4970	41
asynch. EM + ultra-cap.	78	55	3330	60
ZI flywheel + gearing	34	16	340	91

Table 3.5: Comparison between three power assist systems for 27 [kW], 18 [Wh]

available example, the Honda Insight uses a 10 [kW] (peak) neodymium PM brushless DC motor weighing approximately 50 [kg], a 0.94 [kWh] NiMH battery-pack weighing 20 [kg], and an ultra-capacitor of circa 6 [kg]. Besides, a high-density inverter is present which operates as a DC-DC converter as well as a motor cooler. In total, the additional weight of the secondary power source of the Honda Insight, which is designed for power assist and Stop-Go operation, is around 75 [kg]. The additional weight adversely affects fuel economy. The combined effects of efficiency and weight are evaluated in Section 3.3.

An interesting (not commercially available) example of a hybrid system for application in the upper-size vehicle class is the so-called *E-Automat* developed at the University of Chemnitz [Tenberge, 2001], which combines an existing 6-AT with a circa 10 [kW] electric motor.

### miscellaneous efforts

Apart from the fact that an additional power source is needed to solve the driveability problem associated with E-line tracking, a CVT is required to exactly track the E-line. In case a stepped transmission is used, some penalty on the fuel consumption reduction is to be expected. On the other hand, the fact that the transmission efficiency of a CVT is generally lower than that of a stepped transmission (especially MT) will partly cancel out the obtained fuel reduction [Yamamoto and Aoki, 2000]. Moreover, for E-line tracking the transmission must be automatic (AT or CVT) or automated (Automated Manual Transmission, AMT). The ratio coverage of the transmission must generally be much larger than that of commercially available stepped transmissions and even CVTs. However, the penalty on fuel consumption reduction when using a 6-AT, 6-AMT or CVT (ratio coverage between 5 and 6) is comparatively small [Hofmann *et al.*, 1998]. Additionally, requiring the ratio coverage to be much higher necessitates significant modifications (*e.g.*, larger transmission size, '*i*<sup>2</sup>-transmissions' [Höhn, 1994, 2001]). Finally, an electronic throttle (drive-by-wire) is necessary, but is getting more common in modern passenger cars anyway and the additional cost is relatively small.

The remaining efforts are related to software development especially. Drive-by-wire poses additional safety and reliability issues. Furthermore, E-line tracking tends to decrease CO<sub>2</sub> emissions but increase NO<sub>x</sub>, thus new engine management strategies dedicated to E-line tracking are mandatory. For a CVT or a wide-spread 6-AT, manufacturing costs and complexity are relatively high. The production numbers for AT are much higher than for CVT and the latter is still maturing with regard to durability, robustness and maintenance infrastructure. Operating the engine at very low speeds and high torques may introduce additional problems with respect to NVH. On the other hand, cruising at low engine speeds is generally associated with high comfort.

The additional power source may be used for other functions as well, *e.g.*, as a starter-alternator. Such a machine is well equipped to meet the increasing electric power demands (such as airconditioning, power steering and brake assist), which are debit to the increased research into a 42 Volt on-board electrical net. Furthermore, a starter-alternator but also a low

speed flywheel may be used to implement a Stop-Go system, *i.e.*, engine shutdown at vehicle standstill. This is the topic of the following section.

### 3.3.2 Stop-Go operation

Stop-Go, like E-line tracking, requires an additional power source. Different technologies can be thought of to facilitate the frequent engine restarts, that is an electric motor, a flywheel, *etc.*

#### system requirements

The engine speed where combustion is resumed is a trade-off between starting-time and power demand on the one hand and emissions and noise on the other. Also, when the launching clutch is engaged after engine restart, the engine torque must be sufficient to propel the vehicle. When assuming the engine must be accelerated towards idle speed (around 800 [rpm]) within 0.15 [s], the power and energy requirements for Stop-Go are 12.6 [kW] and 0.26 [Wh], respectively. In case of an *impulse-start* (*i.e.*, using inertia force to start the engine, see Chapter 8), the power requirements can be lower, but the starting-time may be longer if the inertia has to be accelerated first.

#### efficiency

The efficiency of the additional power source is important for the absolute amount of energy needed for an engine restart. The additional losses (*e.g.*, due to an increased mass) when not using the extra power source deteriorate fuel economy. Depending on the way the energy required for Stop-Go is subtracted from the powertrain, the fuel saving potentials may vary. For instance, when combining Stop-Go with brake energy recuperation, the fuel savings due to Stop-Go are as large as indicated in Table 3.1. On the other hand, when the energy is generated by the engine running in arbitrary operating points, the absolute fuel saving is as large as the fuel required for idling minus the fuel required for generating the accumulated restart energy. If the restart energy is generated in the sweet spot an unambiguous upper limit for the fuel saving can be obtained. Incorporating this as well as 50% efficiency (average) for the Stop-Go system itself (see Table 3.6), the *deterioration of the fuel saving* amounts up to just 0.3% for the urban and the NEDC cycle, whereas for the other two cycles the difference is even less significant.

In Stop-Go, the efficiency of the transmission between engine and wheels does not influence the *absolute* fuel-savings, but the *relative* savings instead. A decrease in fuel-consumption due to an improved transmission raises the relative fuel-savings for Stop-Go. For example, the fuel consumed on the urban cycle decreases by 13.6% when improving the transmission efficiency from 80 to 100%, while the potential relative fuel-savings from Stop-Go increase from 12.8 to 14.9%.

Table 3.6 compares the three systems from Table 3.5, but now for Stop-Go application. The two electrical systems are assumed to use *direct-start* (starter-alternator directly connected to the crank shaft), the flywheel system naturally uses impulse-start. An impulse-start system, whether purely mechanical or 'semi-electrical' (*i.e.*, the rotor of the starter-alternator is used as inertia) always requires an additional clutch. Again the mechanical solution offers advantages over the two electrical systems, although the total efficiency is better for the ultra-capacitor variant.

	mass [kg]	volume [l]	cost [€]	efficiency [%]
asynch. EM + NiMH	56	46	2205	41
asynch. EM + ultra-cap.	35	25	1470	60
flywheel + gearing + clutch	20	9	200	49

Table 3.6: Comparison between three Stop-Go systems for 12 [kW], 0.26 [Wh]

### driveability

In commercially available Stop-Go systems, the vehicle response to accelerator pedal motions is delayed, because none of them simultaneously start the engine *and* launch the vehicle. The combined time needed for engine restart followed by possible clutch-actuation delays, should not exceed approximately 0.2 [s]. Longer delays are known to cause annoyance and lack of confidence by the driver. The ZI Stop-Go solution, as treated in Part III, is able to immediately launch the vehicle and meanwhile restart the engine. The potential for acceptance is expected to be higher this way. For Stop-Go systems in general, the frequent engine restarts should be more refined and silent, for reasons of comfort.

### miscellaneous efforts

The reliability of the engine start should be increased by an order of magnitude with respect to conventional starter systems, because of the more frequent engine restarts. Also, some dedicated type of (battery or flywheel) State-Of-Charge (SOC) management must anticipate for a possible energy deficit, and consequently decide not to shut down the engine.

The engine emissions can be lower than in a conventional engine start. They largely depend on the engine speed where combustion is resumed and on the engine temperature. More importantly, the temperature of the catalytic converter should not drop dramatically during engine shutdown. Straightforward solutions include heating and encapsulation of the catalyst (see, *e.g.*, [Kok, 1999]). The power take-off supply must be taken over by the secondary power source while the engine is shutdown.

A possible additional function of starter-alternators is active oscillation attenuation, for the driveline and for the engine especially, see [Zeyen and Pels, 1997]. Other than actively, the rotor of an electric machine will also attenuate oscillations in a passive way, mechanically and electrically. Because the additional power source can replace the conventional engine-flywheel, the impact on overall vehicle design may be relatively small, though larger than for E-line tracking due to the significant changes in vehicle operation.

### 3.3.3 Start-Stop operation

The efforts linked to duty cycled engine operation are related to the following three types of operation and the transitions between them:

- engine on: sweet spot operation;
- engine off: driving on secondary power source;
- conventional driving beyond sweet spot.

Start-Stop at least requires the earlier defined series mode. In terms of the definitions from Figure 3.1, the primary power source E then charges the accumulator A by the generator G while the motor M propels the wheels W. Depending on the accumulator's SOC, the primary source E is shut down intermittently. Start-Stop can also be realized using parallel mode, but then the series mode has to be incorporated as well. When E directly propels the wheels W, G diverts the surplus of power (delivered in the sweet spot) into A. When A is fully charged either M or E should propel the vehicle. The former then equals the series mode, whereas the latter in fact is conventional driving.

### component efforts

For sweet spot operation the surplus of power varying from zero to  $P_{ss}$  has to be stored in the accumulator. The transmission between the primary and secondary energy source has to be able to split  $P_{ss}$  into a varying power  $P_w$  to the wheels and a power  $P_{ss} - P_w$  to the accumulator. Hence the generator, accumulator and motor have to be dimensioned such that powers maximally up to  $P_{ss}$  can be dealt with. The primary source must be shut down when either the SOC of the accumulator has reached its upper limit, or when the power request is below  $P_{ss}$  and the SOC has not reached its lower limit yet. The primary source must be restarted whenever the SOC drops below the lower limit or when the power request is higher than  $P_{ss}$ . This manner of engine operation requires sophisticated controls in order not to impair driveability under the constraint that fuel economy should be optimized. This is not always as straightforward as it seems. For instance, consider a stationary situation where the primary power source is shutdown and the secondary source is delivering a power slightly below  $P_{ss}$ . If the driver suddenly asks for a large increase in power, the primary power source must be restarted quickly. Clearly, the power reserve to restart the primary source is close to zero, and hence insufficient. In order not to withdraw this power from the vehicle, yet another secondary source is needed. The Nissan Tino [Matsuo *et al.*, 1999] operates as such. The situation is even worse in the Toyota Prius (recall Figure 3.2), where electric motor M2/G2 is responsible for restarting the engine E, and in doing so actually exerts a negative torque at the wheels through the planetary gear. Moreover, to enable the switching between the sources, clutches or some kind of infinitely variable transmissions are needed.

### efficiency

The efficiencies of the conversion and transmission of energy greatly influence the fuel saving potential. Let  $E_{cyc}^+$  be the energy needed at the wheels for driving a certain cycle, and  $E_{cyc}^-$  the potentially recoverable energy which is normally (*i.e.*, in a conventional vehicle) dissipated at the brakes or in the engine. The actually recovered energy  $E_{BER}$  will generally be smaller than  $E_{cyc}^-$  if the generator power is limited. The net energy that is minimally needed for all but the vehicle's kinetic energy is  $E_{cyc} = E_{cyc}^+ - E_{cyc}^-$ . If part of this energy is drained from the accumulator and not *replenished* before the end of the driving cycle, the type of operation is called *charge depleting* [Müller and Köhle, 2000]. If on the other hand no charging from outside the vehicle takes place during the driving cycle, the vehicle is said to be *charge sustaining*. If the vehicle is charge sustaining and, moreover, the accumulator's SOC at the start and at the end of the driving cycle are equal, all the required energy must be supplied by the primary power source. This situation is depicted in Figure 3.9, where  $\eta_T$  and  $\eta_{II}$  are the efficiencies of the transmission and of the *secondary path*, respectively. The latter efficiency at least comprises the efficiencies  $\eta_G$ ,  $\eta_A$  and  $\eta_M$  of the generator, accumulator and motor, respectively, and also the mutual conversion efficiencies  $\eta_{G \rightarrow A}$ ,  $\eta_{A \rightarrow M}$ ,  $\eta_{M \rightarrow W}$ , and either  $\eta_{E \rightarrow G}$  or  $\eta_{W \rightarrow G}$ , depending



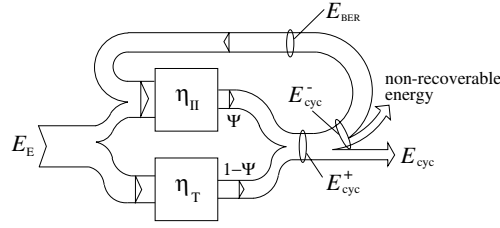


Figure 3.9: Energy flows

on the direction of the energy flow. If the secondary sources are directly connected to the primary source and the wheels,  $\eta_{E \rightarrow G}$  and  $\eta_{M \rightarrow W}$  are both equal to 1. The accumulator efficiency  $\eta_A$  is included to somehow reflect the effect of (time-dependent) self-discharge. For flywheels,  $\eta_A$  accounts for air drag induced self-discharge, while  $\eta_G$  and  $\eta_M$  are 1, since no energy conversion is required. For a hybrid vehicle like the Nissan Tino [Matsuo *et al.*, 1999], the power of both secondary power sources must pass through the transmission, hence the transmission efficiency  $\eta_T$  would appear twice in  $\eta_{II}$ . On the other hand, part of the secondary power may not always have to pass through the accumulator, thus increasing  $\eta_{II}$ . The total energy  $E_E$  that is to be delivered by the primary source, is given by

$$E_E = E_{cyc}^+ \left( \frac{1 - \Psi}{\eta_T} + \frac{\Psi}{\eta_{II}} \right) - E_{BER} \quad (3.1)$$

where the term  $E_{BER}$  is only present if brake energy can be recovered. Else, all energy  $E_{cyc}^-$  is non-recoverable.

The factors  $\Psi$  and  $1 - \Psi$  represent the relative parts of  $E_{cyc}^+$  that pass through  $\eta_{II}$  and  $\eta_T$ , respectively.  $\Psi$  depends on the duty-cycle strategy of the engine, as well as on the driving cycle, and is not known a priori for a given hybrid powertrain or arbitrary journey, except for a pure series hybrid, where  $\Psi = 1$ . If the engine is intermittently operated only in the sweet spot,  $\Psi$  must be larger than 0, in order to meet power demands below  $P_{ss}$ . In fact,  $\Psi$  can be viewed as a *hybridization factor*, although other definitions are encountered in literature. For instance, [Baumann *et al.*, 1998] defines the Degree Of Hybridization *DOH* for a hybrid vehicle operating in two different Energy Domains (ED), as

$$DOH = 1 - \frac{|P_{max,ED1} - P_{max,ED2}|}{P_{max,ED1} + P_{max,ED2}} \quad (3.2)$$

For  $DOH = 1$  the hybridization is maximal, whereas  $DOH = 0$  for a conventional vehicle and also for a purely electric vehicle. In [Müller and Köhle, 2000], hybrid vehicles are classified depending on the relative share of the battery in the total energy storage on the one hand, and of the electric motor in the total output power on the other.

In Figure 3.10 contour lines of the *relative fuel consumption*  $\mathcal{F}(\Psi) = f / f_{OL_{15\%}}$  are drawn as a function of  $\Psi$  and  $\eta_{II}$ . Here,  $f$  represents the actual fuel consumption of the Start-Stop system with mechanical efficiency  $\eta_T$ , whereas  $f_{OL_{15\%}}$  is the fuel consumption, when driving along the  $OL_{15\%}$  operating line, with the same mechanical efficiency  $\eta_T$ . Realistic values  $\eta_{II} = 0.44$  ( $= \eta_G \cdot \eta_{G \rightarrow A} \cdot \eta_{A \rightarrow M} \cdot \eta_M = 0.88 \times 0.75 \times 0.88 \times 0.75$ ) for an *electrical* secondary power source and  $\eta_T = 0.85$  for a CVT, are indicated in the figure by dashed lines. The increased

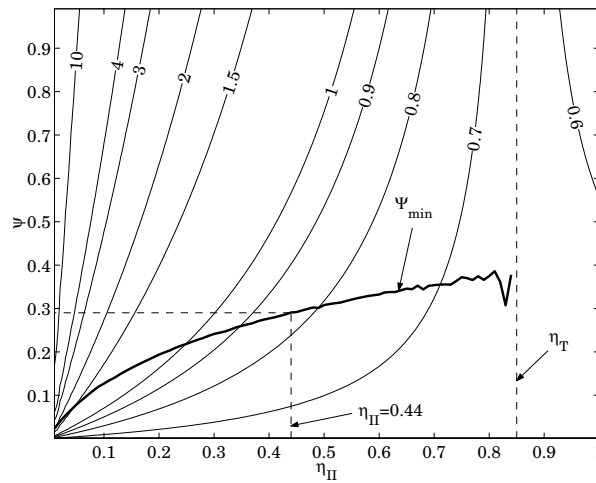


Figure 3.10: Hybridization factor and potential fuel savings as a function of total secondary source efficiency for the urban drive cycle

weight of such a hybrid vehicle (around 120 [kg], see Section 3.4) is also taken into account. The bold line  $\Psi_{\min}$  indicates the minimal hybridization factor that is required if it is assumed that the engine is running *only* for power demands *above* some threshold power level  $P_{\text{th}}$ , that is yet to be determined. Below  $P_{\text{th}}$  the secondary power source, that is the motor M, is activated for vehicle propulsion. Furthermore, for wheel power demands higher than  $P_{\text{th}}$ , but below  $P_{\text{ss}}\eta_{\text{T}}$  (*i.e.*,  $P_{\text{ss}}$  corrected with transmission efficiency), the engine E is running in sweet spot and the excessive energy is stored in the accumulator A by the generator G. Finally, for wheel power demands above  $P_{\text{ss}}\eta_{\text{T}}$ , the engine is assumed to operate as the sole mover (conventional mode) along the E-line. The activity of the engine E, the motor M and the generator G as a function of the wheel power is schematically displayed in Figure 3.11. For

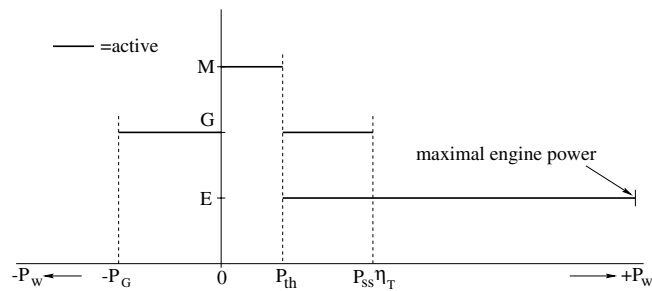


Figure 3.11: Activation of primary and secondary sources as a function of the (requested) wheel power

negative wheel power the generator G could be used for regenerative braking up to a level equal to the maximal generator power  $P_G$ . This will be elaborated further in Section 3.3.4.

The threshold  $P_{th}$  is determined assuming that the total amount of energy accumulated in the intervals where  $P_{th} < P_w < P_{ss}\eta_T$  should be just enough to supply the energy necessary for vehicle propulsion whenever  $0 \leq P_w \leq P_{th}$ . For an arbitrary journey,  $P_{th}$  can in principle not be known beforehand. Instead, the standardized drive cycles are taken in order to obtain some practical indication for  $P_{th}$ . Thus  $P_w = P_{cyc}$  and by solving the energy balance for  $P_{th}$  given the above assumption:

$$\int_{t_0}^{t_f} (P_{th} < P_{cyc}(t) < P_{ss}\eta_T) \cdot \left( P_{ss} - \frac{P_{cyc}(t)}{\eta_T} \right) dt = \int_{t_0}^{t_f} (0 \leq P_{cyc}(t) \leq P_{th}) \cdot \frac{P_{cyc}(t)}{\eta_{II}} dt \quad (3.3)$$

the threshold power can be determined. In Equation (3.3)  $t_0$  and  $t_f$  are, respectively, the start and end time of the driving cycle. The Boolean expressions inside the integrands are included to set the appropriate interval of power levels which must actually be integrated. For the four cycles used here it appeared that the threshold power levels  $P_{th}$  do not differ that much, see Table 3.7. In practice  $P_{th}$  may be chosen at 10 [kW]. With  $P_{th}$ , Equation (3.1) can be solved for

CYCLE	$P_{th}$ [kW]
NEDC	8.6
rural	11.0
urban	8.3
highway	12.2

Table 3.7: Drive cycle power threshold beyond which the engine must be running, for  $\eta_T = 0.85$  and  $\eta_{II} = 0.44$

$\Psi$ . Proceeding as such for every  $\eta_{II}$ , the line  $\Psi_{min}$  emerges. For  $\eta_{II} = 0.44$  the fuel saving of Start-Stop is highest for  $\Psi = \Psi_{min}$  and then equals 16.8%, for the urban drive cycle.

The strategy of Start-Stop operation underlying the given analysis can not be pursued in all situations given a maximum and minimum SOC of the accumulator. For instance, when the accumulator is fully charged and the cycle power demand is still above  $P_{th}$ , either the secondary source must also be running to discharge the accumulator or the engine must supply the exact cycle power in the appropriate operating point below  $P_{ss}\eta_T$ . Note that for power demands larger than  $P_{ss}\eta_T$ , the engine is always running on its own to deliver the actual cycle power. Vice versa, if the SOC is down to its minimum, the engine must be running even though the demanded cycle power may be below  $P_{th}$ . These operational constraints are not considered here but are regarded as one of the main efforts in developing the energy management. Furthermore, the powertrain component controls must ensure the driveability, comfort and reliability. Also the cooling system of the engine (engine runs at  $P_{ss} = 32$  [kW] when on) has to be reconsidered for low speed driving.

The size of the motor, accumulator and the generator partly determine the potential for fuel saving. The proposed strategy is not only favourable with respect to the combined efficiency of the primary and secondary path, but also reduces the power requirements for the generator G and the motor M to an absolute minimum. Consequently, in the case where  $P_{ss} = 32$  [kW],  $P_{th} = 10$  [kW] and  $\eta_T = 100\%$  the necessary generator power is 22 [kW], whereas the required motor power is 10 [kW]. A lower transmission efficiency  $\eta_T$  will lower these demands even further. For instance, if  $\eta_T = 0.85$ , the engine can operate in the sweet spot already when  $P_w = \eta_T \cdot 32 \approx 27$  [kW]. Hence, a generator size of 27-10=17 [kW] is sufficient. If the motor and generator are combined in one machine, the size of the generator determines the actual

size of the secondary power source. Downsizing the secondary power source means that the engine operating point—which should ideally be in the sweet spot—moves towards a lower power level on the E-line. According to Figure 3.5, the penalty on specific fuel consumption is relatively low. For example, when shifting the intermittent engine operating point to 20 [kW], the BSFC rises by a mere 5%. On the other hand, the power requirement for the generator drops from 22 to 10 [kW]. Table 3.8 compares the efforts for two systems with generator sizes of 10 and 22 [kW], respectively. The cost saving due to a smaller generator is likely to out-

G [kW]	mass [kg]	volume [l]	cost [€]	fuel [%]
10	44	17	1740	105.2
22	96	36	3830	100

Table 3.8: Comparison of efforts for two Start-Stop generator (G) sizes

weigh the decrease of fuel saving in practice. On the other hand, if Start-Stop is combined with brake energy recovery, the fuel saving penalty associated with downsizing the generator will be more significant.

### 3.3.4 Brake energy recovery

Brake energy recovery must always be combined with some strategy that re-uses the recovered energy. In the following example it is chosen to combine this fuel saving principle with a Start-Stop system that operates the engine at  $P_{ss} = 32$  [kW] and uses a generator of 22 [kW]. The energy balance (3.3) is augmented with the recovered energy yielding

$$\int_{t_0}^{t_f} (P_{th} < P_{cyc}(t) < P_{ss}\eta_T) \cdot \left( P_{ss} - \frac{P_{cyc}(t)}{\eta_T} \right) dt = \int_{t_0}^{t_f} (0 \leq P_{cyc}(t) \leq P_{th}) \cdot \frac{P_{cyc}(t)}{\eta_{II}} + \int_{t_0}^{t_f} (-P_G \leq P_{cyc}(t) < 0) \cdot P_{cyc}(t) dt \quad (3.5)$$

where it is seen that the energy demand from the engine (left hand side) lowers due to the (last) recovery term ( $P_{cyc} < 0$ ). For brake energy recovery, a plot similar to Figure 3.10 can be made (not shown), where for a given  $\eta_{II}$  and  $\Psi$ , the potential fuel savings increase, but also the locus of minimal hybridization factors  $\Psi_{min}$  tilts towards higher values. Still, again for the urban drive cycle, the fuel saving at  $\Psi = \Psi_{min}$  (for  $\eta_T = 0.85$ ) increases significantly up to 36.6% for an electrical system and to 53.3% for a mechanical system, as will be summarized in Section 3.4. If it is decided not to increase the power level of the generator, the additional efforts for brake energy recovery are relatively small, and limited to a revision of the energy management system. Because this fuel saving principle in fact constitutes brake-by-wire, safety issues must be taken into account. Moreover, the brake feel and performance should not be different from a normal vehicle. Since the generator power is limited and dependent on battery state (SOC, temperature, age), conventional disc brakes are still indispensable.

## 3.4 Innovation value versus effort

In this section, the innovation values are weighed against the corresponding efforts, for all four fuel saving principles. These *normalized* innovation values are evaluated for a system with

a mechanical secondary power source and compared to those of a system with an electrical secondary power source. To give an indication for city and highway driving, the comparison is performed for the urban and the highway cycle.

The normalized innovation values are obtained simply as the quotient of the percentage of fuel saving and the effort (be it cost, weight or volume), always with respect to the reference vehicle. The additional weight, volume and cost are determined for the mechanical and electrical system, based on output power demands taken from the sections corresponding to the various fuel saving principles.

Additionally, the power demand for the accumulator using Start-Stop was set at 26 [kW] ( $\approx 22/\eta_G$ ). For the electrical system, these *power* requirements are normative, but not for the mechanical system, where the *energy* demand is normative and is set at 200 [Wh], taken from [van Druten, 2001]. The additional weights are then obtained using Table 3.4, where the specific values for the electrical system are taken from the asynchronous EM combined with an ultracapacitor. For the mechanical system, values between those of the ZI flywheel and FESS are taken. In practice, the electrical system may additionally require a battery.

The fuel savings presented in this section are obtained taking all the relevant efficiencies as well as the increased weights into account. Figures 3.12 and 3.13 depict the normalized innovation values for the mechanical and the electrical system, being the fuel saving relative to the additional cost [% per €], the fuel saving relative to the increased weight [% per kg] and the fuel saving relative to the additional volume [% per dm<sup>3</sup>].

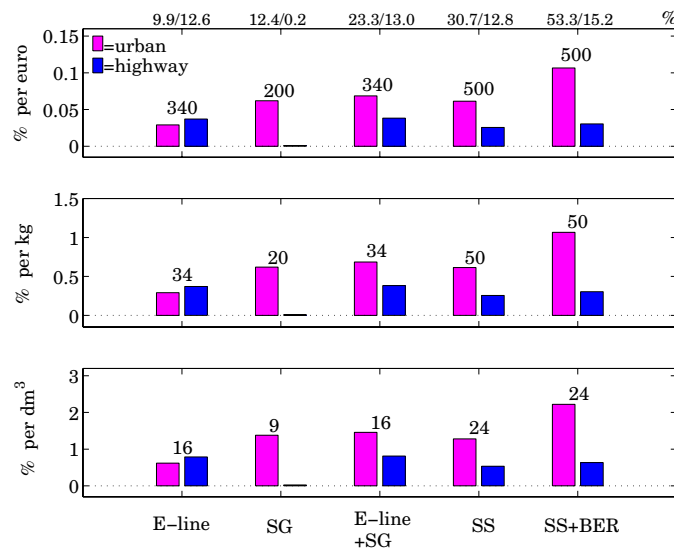


Figure 3.12: Normalized innovation values for a *mechanical* secondary source. At the abscissa are the four saving principles (E-line; SG=Stop-Go; SS=Start-Stop; BER=Brake Energy Recovery) and combinations thereof. On top of the bars is the corresponding increase of cost [€], weight [kg] and volume [dm<sup>3</sup>], respectively. Above the figure are the fuel saving percentages, corresponding to the two driving cycles and the different fuel saving principles

At the abscissa are the four saving principles (where ‘SG’ means Stop-Go, ‘SS’ is Start-

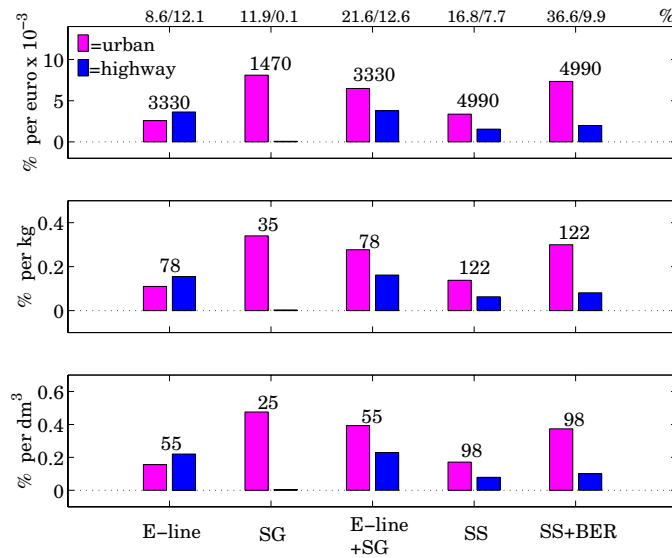


Figure 3.13: Normalized innovation values for an *electrical* secondary source. At the abscissa are the four saving principles (E-line; SG=Stop-Go; SS=Start-Stop; BER=Brake Energy Recovery) and combinations thereof. On top of the bars is the corresponding increase of cost [€], weight [kg] and volume [dm<sup>3</sup>], respectively. Above the figure are the fuel saving percentages, corresponding to the two driving cycles and the different fuel saving principles

Stop and 'BER' stands for Brake Energy Recovery) and combinations thereof. For each saving principle, the left (grey) bar indicates the weighted fuel saving for the urban cycle and the right (black) bar that for the highway cycle. Written on top of the bars is the corresponding increase of cost [€], weight [kg] and volume [dm<sup>3</sup>], respectively. Above the figure, the fuel saving percentages are listed, corresponding to the two driving cycles and the different fuel saving principles. The bars for 'E-line+SG' and 'SS+BER' are included because these are obvious combinations. Besides that, BER cannot exist on its own.

From Figure 3.12 it is seen that the mechanical system performs well on the urban cycle for all fuel saving principles, though to a lesser extent for E-line. SS+BER scores highest, because of the large fuel saving of 53.3%.

The situation is somewhat different on the highway cycle, where the use of SG becomes close to nil. E-line (and the combination E-line+SG) achieves the best value for this cycle. The same trends are seen for the electrical system (see Figure 3.13), but in no category can such a system perform nearly as well as its mechanical counterpart (note the different orders of magnitude of the ordinate values in both figures). At least for the urban cycle, the electrical system shows a preference for SG. Because the mechanical system is much cheaper than the electrical alternative (by a factor of ten), the difference between the two with respect to the normalized values is striking. However, the electrical system can be expected to be more flexible and easier to conceive.

The fact that the achievable fuel savings are systematically higher for the mechanical system, is due to higher efficiencies of the secondary path (in case of SS and SS+BER), and a

smaller increase of weight as compared to the electrical system (E-line and SG, in particular). The penalty on fuel consumption due to additional weight proved to be between 0.13 and 0.38% per % mass increase, or on average 1% fuel for every 4% additional weight. Notably, the fuel savings obtained by SS and SS+BER on the highway cycle drop towards the values for E-line in case of the mechanical system, and even below that for the electrical system. The latter is explained by the fact that on the highway cycle, the required powers below  $P_{ss}$  are still concentrated close to the sweet spot (unlike a ‘proper’ city cycle) where the best strategy is to use E-line and not SS. Also, the substantially increased weight (+122 [kg]) ruins part of the fuel saving. Averaging the results of the two driving cycles reveals that both the electrical and the mechanical system score well on the combination of E-line and SG, at least on their own scale, see Table 3.9. The mechanical variant scores even somewhat higher for SS+BER than for E-line+SG. As mentioned before, the electrical systems show about ten times lower

System	E-line	SG	E-line+SG	SS	SS+BER
mechanical	33	32	53	44	69
electrical	3.1	4.1	5.1	2.5	4.7

Table 3.9: Normalized innovation value (cost-specific fuel saving [%/k€]), averaged over the urban and highway cycle, for the mechanical and electrical system

normalized innovation values than the mechanical counterpart. On the other hand (less quantitative) aspects such as driveability, safety and developing efforts level out the two principles somewhat. For instance, realizing a mechanical system for SS+BER requires a CVT with an exceptionally large ratio coverage (more than 20), and a high energy flywheel with mechanical components like clutches and gear stages, see [van Druten, 2001]. This yields additional issues of driveability and safety. The severity of these issues is much smaller for E-line+SG than for SS+BER, because of lower energy contents of the flywheel. Electrical systems, on the other hand, require few mechanical adaptations, and are flexible with regard to the controls. An electrical E-line+SG hybrid may additionally be utilized to supply electrical power for several purposes (e.g., 42 Volt net). The robustness and predictability of batteries is still troublesome.

### ZI powertrain: mechanical mild hybrid

The combination of E-line and SG may be termed *mild hybrid* as opposed to *full hybrid* in case of SS+BER [van Druten *et al.*, 2001]. From this section, it is concluded that a mechanical hybrid is preferable above an electrical hybrid, with respect to cost especially. Furthermore, the mechanical full hybrid scores higher than the mechanical mild hybrid. Therefore, a mechanical full hybrid seems favourable for reducing fuel consumption in a passenger car. However, the development effort (engine and catalyst adaptations, control of intermittent engine operation, *etc.*) for a full hybrid, relative to its potential is large compared to that for a mild hybrid. In the EcoDrive project, after studying different concepts it was decided to develop a mechanical mild hybrid, using two new concepts, called ZI and ZI Stop-Go. Choosing for ZI and ZI Stop-Go, the project goal can largely be met using the available development time, research and engineering capacity. Furthermore, the two concepts can be designed, realized and tested separately enabling a step-by-step implementation and hence reducing development risks.

The fuel saving of E-line+SG, (here embodied as ZI Stop-Go), taking efficiency and increased weight into account, is estimated by computations similar to those conducted in Section 3.2.3. The estimated fuel saving of ZI Stop-Go on the NEDC with respect to OL<sub>15%</sub> is around 21%.

## Chapter 4

# The Zero Inertia Powertrain

This chapter presents the conceptual design of the Zero Inertia powertrain in a nutshell. Section 4.1 translates the findings from the previous chapter that are related to E-line tracking into a problem description. After that, the ZI solution is derived in Section 4.2. A brief description of the ZI Stop-Go transmission is given in Section 4.3.

### 4.1 Zero Inertia principle

In the previous chapter it was concluded that the use of E-line tracking as a fuel saving principle necessitates an additional power assist system. Electric power assist systems are able to supply the power needed to compensate for primary inertia effects in slow transient situations, and, when physical limits are not reached, even overcompensate. However, arbitrarily fast speed changes generally cannot be compensated for, due to power and torque limitations of the electric machine. A counteracting inertia, capable of supplying the power needed to overcome inertial effects would therefore be very interesting. This mechanical power assisting device, *i.e.*, a *flywheel*, should speed down when the primary inertia speeds up and vice versa, at a rate dictated by, among others, the ratio of flywheel inertia and primary inertia. To link the speed of the flywheel to that of the primary side of the powertrain, a component with a continuously variable transmission ratio is needed. Possible components to realize this are:

1. Continuously Variable Transmissions (CVTs)
2. Couplings
3. Torque converters
4. Planetary gears

#### **continuously variable transmissions**

Automotive CVTs can be mechanical, hydraulic, or electrical. Hydraulic CVTs are used especially in heavy vehicles (construction vehicles, trains, agricultural machinery), but have moderate efficiencies. So called electrical CVTs require an electric motor and an electric generator both of which are capable of handling the maximum power of the primary source of propulsion. Compared to an internal combustion engine with the same maximum power,



electric machines and their overhead (battery, inverter) are bulky and rather expensive, as well as rather inefficient, as was seen in the previous chapter. Modern mechanical CVTs are capable of transmitting the required power for almost every size of passenger car at efficiencies not much lower than that of conventional stepped transmissions (MT and AT). Commercially available CVTs are the Van Doorne metal V-belt CVT (*e.g.*, in the Nissan Primera), the Audi Multitronic chain belt CVT (*e.g.*, in the Audi A6), the Bando dry hybrid belt CVT (*e.g.*, in the Daihatsu Mira) and the dual cavity toroidal CVT (*e.g.*, in the Nissan Cedric).

### **couplings**

Couplings can transmit torque between two bodies with a continuously variable speed ratio. The torque ratio is always equal to 1. A coupling that transmits the torque hydraulically is known as a *fluid coupling* (or *fluid flywheel*), otherwise the term *clutch* is more common. The torque transmitted by a fluid coupling can be influenced by varying the amount of oil. In a clutch that transmits torque mechanically, the torque can be manipulated by changing the clutch engaging pressure, either hydraulically, mechanically or electro-magnetically. 'Intermediate' solutions such as electro-magnetic and electro-rheological clutches use electro-magnetic fields to change the viscosity of the torque transmitting medium. The latter still somewhat exotic clutch is in some ways comparable to the fluid coupling because of the viscous torque transmission. Current applications of this technology are found primarily in active engine mounts. The electro-magnetic powder clutch on the other hand, has been applied successfully, *e.g.*, in the Subaru CVT.

### **torque converters**

A torque converter basically is a fluid flywheel combined with a stator (or reactor) which is connected to the transmission casing by a one-way clutch. When the torque on the stator is such that the one-way clutch locks, this third torque transmitting member enables the amplification of input torque whenever the input speed exceeds the output speed. In effect, the torque converter acts as a hydrodynamical CVT with a quite moderate efficiency. Some torque converters have a (mechanical) lock-up clutch to enlarge the efficiency by eliminating the slip when the torque ratio approximates 1. The continuous variability is then obviously lost.

### **planetary gears**

Planetary gears are widely used, for instance in stepped automatic transmissions. A *basic* planetary gear has three main rotating members and three submembers, see Figure 4.1. The inner member is termed the *sun*, the outer member is the *annulus* or *ring*. The intermediate member carries the three *planets* (submembers) and is therefore called *carrier*. More complex epicyclic configurations can have several sun, annulus and carrier wheels or double planets with different teeth numbers connected to the same axis, for instance see Figure 4.2. Also, planets can run on opposing planets, instead of on an opposing sun or annulus. An example of this can be found in the DNR (Drive-Neutral-Reverse) set, see Figure 4.3. Epicyclic sets as seen in practice (*e.g.*, Simpson, Ravigneaux, see, *e.g.*, [Lechner and Naunheimer, 1999]), are composed of several basic planetary gears, possibly combined with alternative planet configurations. In most automotive applications, the planetary gear is used as a concentric reduction gear, where any rotating member can be connected to ground (*i.e.*, the transmission housing). Given the speed of one member, varying the speed of a second member in turn varies the speed of a third member. This creates two speed ratios which are both continuously variable.

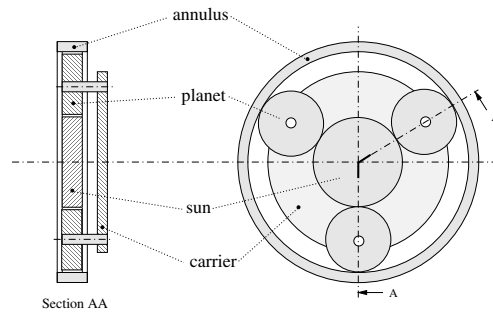


Figure 4.1: Basic planetary gear

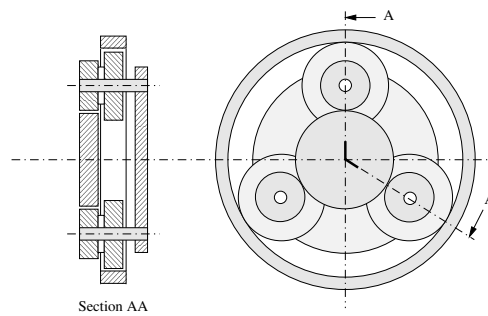


Figure 4.2: Planetary gear with stepped planet

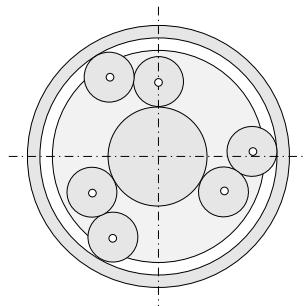


Figure 4.3: DNR (Drive Neutral Reverse) reversal stage

In this example, the speed of the second member must somehow be controllable. This is possible by active control of the torque applied to one of the members. For example, in the hybrid powertrain of the Toyota Prius [Riezenman, 1998], the speed of the members is controlled by an electric motor/generator connected to the sun. The engine is connected to the carrier and

the wheels to the annulus.

Summarizing, a number of components exists which in principle can transmit power between two rotating bodies at variable transmission ratios. In the following, further constraints will decide what solution is favourable for the intended application.

## 4.2 ZI Concept design

The drive train of the vehicle must be able to combine a given range of vehicle speeds with appropriate engine speeds and flywheel speeds. In general, the flywheel speeds should be high for low engine speeds and vice versa. Strictly speaking, this calls for two CVTs or similar power transmitting components. Obviously, the application of two CVTs, be it mechanical, electrical, or hydraulic, is unacceptably expensive and bulky. Furthermore, the required ratio coverage, needed to link all practical speed combinations, using a flywheel with an inertia comparable to the primary inertia, is by far larger (typically 30) than the ratio coverage of standard mechanical CVTs (typically 6). Hydraulic CVTs are not an option due to their moderate efficiencies, whereas an electrical layout would offer possibilities, although preferably not in a series hybrid configuration.

The use of a planetary gear arrangement as in the Toyota Prius is reasonably cost-effective, although the Prius uses two electric motors which renders this solution still rather expensive. An alternative solution, incorporating a planetary gear, does not control the speed of one rotational member electrically, but mechanically instead, through the use of a mechanical CVT. Such a solution would again be overexpensive, if the CVT could be used only for regulating the flywheel speed. However, if the CVT can also be used to control the engine speed, such a solution becomes increasingly interesting.

### 4.2.1 Resulting configuration

The easiest way to realize the suggested solution is to have a fictitious line connecting the engine and flywheel speed that rotates around a pivot in between, as illustrated in Figure 4.4. A sensible choice is to make the median speed the vehicle speed, hence the secondary speed

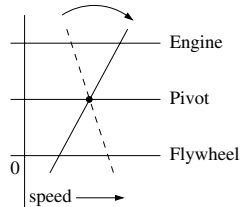


Figure 4.4: Pivot mechanism

of the CVT. By downshifting the CVT, it is seen that while the engine increases speed with respect to the vehicle speed, the flywheel speeds down, and vice versa. This is exactly the mechanism needed to create the energy exchange between engine and flywheel. In terms of a basic planetary gear, the sketched mechanism can be realized by connecting the secondary speed to the carrier, whereas the engine and flywheel are connected to the annulus and sun, respectively, or possibly, the other way around. The outlined topology (see Figure 4.5), which

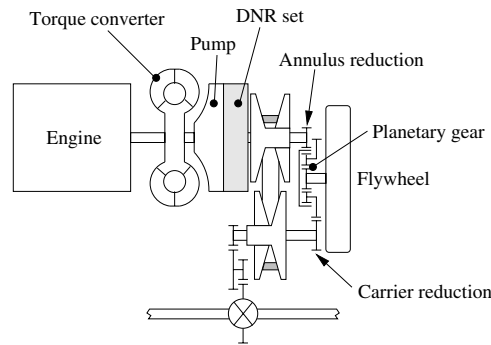


Figure 4.5: Resulting ZI powertrain concept layout

is just one possibility out of many, will serve as the layout to be used throughout this thesis, and will in fact prove to be a good starting point, see [van Druten, 2001].

### 4.3 ZI Stop-Go

The Stop-Go functionality (proposed in Section 2.4 to increase the fuel efficiency and evaluated as an interesting technology in Section 3.3) is investigated in combination with the Zero Inertia powertrain. Naturally, before vehicle launch, the energy contents of the flywheel must be sufficiently high. For this purpose, at least one additional clutch is needed in order to enable disengagement of the flywheel from the drive train at a flywheel speed high enough to facilitate a new vehicle launch. The flywheel preferably should be able to launch the vehicle and start the engine *at the same time*. Such a specification is certainly not trivial, since most commercially available Stop-Go systems *first* start the engine, *after* which the engine can start to propel the vehicle. As was mentioned in Section 3.3.2, cranking up the engine is conceivable as a *direct-start* or an *impulse-start*, for instance see [Reik, 1999]. The first strategy has one clutch only, positioned between the starter and the primary side of the transmission, as in a conventional driveline. The impulse-start strategy uses the inertia of the starting device, which can be disengaged from the engine by an additional clutch, see [Seiffert and Walzer, 1989]. Depending on the starter-clutch(es) configuration, and on the size of the electric starter motor, the combined time needed for restarting the engine and engaging the launching clutch may be more than the driver is willing to accept. This is the case in the former Volkswagen Eco-Golf/Ecomatic [Adcock, 1998; Greve and Liesner, 1993] and supposedly also in the current Volkswagen Lupo 3L [Healey, 1999]. In the Honda Insight with Integrated Motor Assist (IMA), the electric motor power is much larger, thus enabling a pleasant vehicle launch.

To enable the flywheel system to simultaneously speed up the engine and the vehicle, one additional clutch is needed to decouple the CVT from the driveline. To see this, it is crucial to understand that, while the flywheel contributes torque to the wheels (secondary side of the CVT) it drains (some) torque from the primary side of the CVT and hence the engine. Therefore, while launching the vehicle, the flywheel tends to speed up the engine in the wrong direction. To avoid this, the CVT has to be decoupled from the secondary shaft and the DNR set must be set in Reverse. In Figure 4.6 the ZI Stop-Go layout is depicted showing

the two additional clutches ( $C_f$  and  $C_s$ ) as well as the existing clutches ( $C_l$ ,  $C_d$  and  $C_r$ ) that will be operated differently. Part III of this thesis will elucidate the physical background, as well

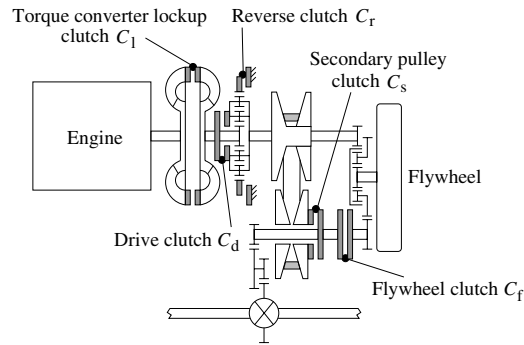


Figure 4.6: Resulting ZI Stop-Go powertrain concept layout

as the supervisory and clutch control strategies needed to operate the Stop-Go facility.

## 4.4 Further reading

Given the concepts of the ZI and ZI Stop-Go powertrain, an extensive though achievable list of development (or innovation) efforts has to be tackled. These efforts are reported in this thesis, in [van Druten, 2001] and in [Serrarens, 2001], also see Figure 1.3.

In [van Druten, 2001] the designs of the ZI and ZI Stop-Go concepts are illustrated as well as general ideas about flywheel usage in passenger cars. The control problem of generating appropriate setpoints for engine and CVT along with developing dynamic models for and testing of the ZI powertrain is the subject of [Serrarens, 2001].

## **Part II**

# **CVT Modeling and Control**



## Chapter 5

# The CVT in the ZI Powertrain

A Continuously Variable Transmission (CVT) is a stepless power transmission device with an infinite number of transmission ratios within a certain range, limited by constructional boundaries. As mentioned in Chapter 4, automotive CVTs can be mechanical, hydraulic or electrical. Various existing CVT concepts and their specific pros and cons are discussed, *e.g.*, in [Lechner and Naunheimer, 1999]. For the present application, mechanical CVTs are preferable for reasons of efficiency, size, weight, production cost and noise. Within the category of mechanical CVTs, three main types can be distinguished. The first of these uses a 'one-way crank' with variable stroke to transmit force, but is not relevant for modern automotive applications. Much more suited for high powers are the toroidal or *traction drive CVTs*, which use rolling elements to transmit torque. The transmission ratio is changed by shifting or turning the rolling element. The third category of mechanical CVTs is the *variable pulley transmission*. It adjusts the axial distance between the pulley halves to attain different transmission ratios.



Figure 5.1: Van Doorne's pushbelt CVT

At present, the variable pulley CVTs are commercially the most significant and can be subdivided into *rubber belt CVTs*, *chain CVTs* and *pushbelt CVTs*. Rubber belts were incorporated in the former *Variomatic*, and currently in the *dry hybrid belt* or *Bando CVT* [Takahashi *et al.*, 1999; Yuki *et al.*, 1995]. Both types of rubber belt CVTs are limited to small torques. Chain



CVTs have been in production for industrial applications by PIV/Reimers and more recently are used in Audi/LuK's Multitronic [Nowatschin *et al.*, 2001]. The largest market share is still occupied by the Van Doorne steel pushbelt CVT, see Figure 5.1. It is this type of CVT which is used in the ZI powertrain, and which is the focus of the present part.

Figure 5.2 depicts the CVT as used in the ZI powertrain, but without the flywheel and the planetary stage. One recognizes the torque converter, the pump, the Drive-Neutral-Reverse (DNR) set, the primary pulley, the pushbelt, the secondary pulley, the final reduction, the differential gear and the hydraulics to pressurize the pulleys. The total of these components and their housing is referred to as *CVT*. Throughout this thesis, besides *CVT* the term *variator* will be used. The *variator* is defined as the combination of the metal V-belt and the two pulleys.

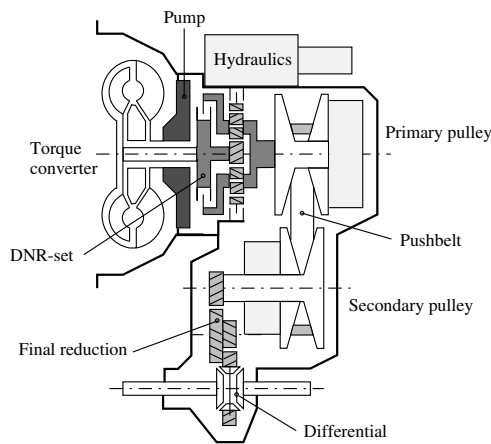


Figure 5.2: Schematic view of the CVT

## 5.1 The pushbelt variator

Figure 5.3 depicts the essentials of the pushbelt variator. The transmission ratio is obtained through two pairs of conical discs, and a belt with a V- or trapezoidal cross-section. Both pairs of discs consist of a fixed and a moveable disc, by which the running radius of the belt can be varied. The side of the variator which is directly connected to the engine is referred to as the *primary side*, whereas the side linked to the final reduction is referred to as the *secondary side*. In the left picture of Figure 5.3 a situation is depicted where the belt radius at primary side is minimal, and the radius at secondary side is maximal. This corresponds to the *underdrive (ud)* or *low* transmission ratio. The reverse situation, in the right of Figure 5.3 corresponds to the *overdrive (od)* transmission ratio. The moveable sheaves are positioned at opposing sides of the belt, meaning that the belt will keep running (approximately) perpendicular to the shafts, for all transmission ratios.

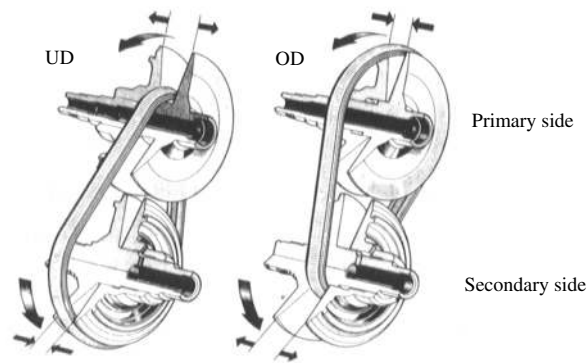


Figure 5.3: Variator operation

## 5.2 The pushbelt construction in detail

The pushbelt and its components are depicted in Figure 5.4. The belt consists of two sets of

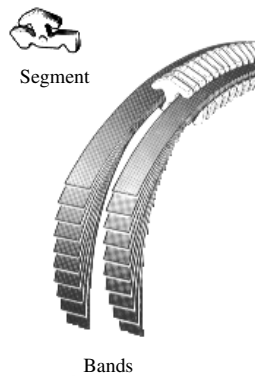


Figure 5.4: Pushbelt components

*bands* (also known as *rings* or *loops*) and a large number of *segments* (also known as *elements*, *blocks*, or *plates*). The two sets of bands each consist of 9 to 12 bands (14 for the *high power belt*, see [Brandsma *et al.*, 1999]), which fit without play, and form a nearly inextensible ring with a very low bending stiffness. The bands are made of *maraging-steel*, a chromium-nickel steel that was originally developed for aerospace applications. The circa 450 segments are kept together by the two sets of bands. The segments can tilt around their *rocking edge*, see Figure 5.5. The belt width evaluated at the rocking edge, can be 24 or 30 [mm] (33 [mm] under development [Brandsma *et al.*, 1999]), depending on the application. The pushbelt CVT can be reasonably compact due to the flexibility of the bands which permits a small running radius. The clamping force is divided over a large number of segments, yielding a relatively low surface pressure, which results in minimal wear and a long life-span. Because of the small

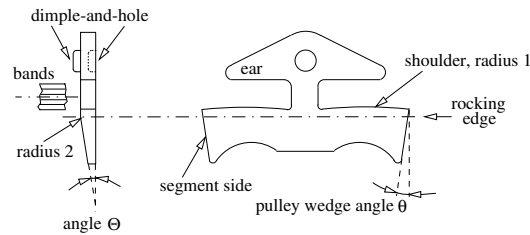


Figure 5.5: Segment terminology

segment thickness, the noise level is moderate and a polygon effect is barely present. The mass per unit length of the pushbelt is fairly low, which allows for high rotational speeds.

### 5.2.1 Segment design

A segment basically is a compressive member which is tapered in two directions. In one direction, the segment is V-shaped conform the pulley wedge angle  $\theta$ , see Figure 5.5. In the perpendicular direction, the segment is tapered (angle  $\Theta$ ) to allow the belt to run on the smallest radius. The contact areas between the bands and the segments are referred to as *shoulders* (also known as *saddles*). To prevent the segments from falling at the straight parts between the pulleys, they are equipped with *ears*. Finally, the so-called *dimple-and-hole* (also known as *peg-and-hole*) is present to prevent skewing from segments in the straight parts of the belt. Along the angle of wrap, dimple and hole open up, preventing an overdefined situation from establishing. The segment thickness is a compromise between noise (polygon effect) and axial strength, while the Hertzian stress at the rocking edge is lower for thinner segments [Hendriks *et al.*, 1988]. The width of the segments should be small for reasons of axial<sup>1</sup> stiffness (especially relevant at zero pushing force), though wider segments can support wider bands, and hence transmit higher torques without increasing the tensional stress in the bands. The segment shoulder is curved (radius 1 in Figure 5.5), so as to make the bands run at the top of the shoulder. This self-centering mechanism makes sure that the bands do not collide with the inner strut connected to the segment ears, or with the pulley surface. On the other hand, this curvature causes the bands to be curved along the entire belt, resulting in a preferred bending radius (in circumferential direction), known as synclastic bending. Consequently, a larger shoulder radius reduces the bending stress. The segment sides have an irregular profile aimed at breaking through the oil film in order to increase the friction coefficient. Besides, the thin metal projections may deform more easily than a continuous surface, hence adjusting for small deviations from the nominal size. The contact between the segments is through the rocking edge, which is slightly curved (radius 2 in Figure 5.5) to limit the Hertzian stress.

The distance between the rocking edge and the segment shoulder should be small to minimize the sliding speed between the inner band and the segment shoulder and between the individual bands, also see Section 6.7. The self-centering mechanism of the bands on a curved support is less effective for higher sliding speeds, *i.e.*, larger distance [Hendriks *et al.*, 1988]. However, a minimum value for this distance is needed to have some margin in manufacturing tolerance. The tolerances for the position of the segment shoulders and the segment sides with respect to the dimple-and-hole, as well as the tolerances for the dimensions of the dimple

<sup>1</sup>*i.e.*, the direction parallel to the pulley shaft.

and the hole and their relative position are quite narrow, to prevent large differences in the amount of force exerted on the inner bands and on the segment sides. Besides this, the segment form should be such that weight (and hence centrifugal force) and manufacturing costs are minimal.

### 5.2.2 Band design

Current bands have a thickness of approximately 0.2 [mm], whereas the width depends on the segment width (24 or 30 [mm]). The wider the bands are, the higher the torque that can be transmitted for a certain admissible tensional stress level, at least to some extent. Because the segments need to be upscaled along with the bands, the belt mass increases (and thus the centrifugal forces), which beyond a certain band width causes the tensile stress to increase again [Brandsma *et al.*, 1999]. The thickness of the bands is limited by the maximum bending stress. Given a certain band thickness, increasing the number of bands raises the allowable sum tensile force level. On the other hand, a higher number of bands also increases the number of inner-band friction surfaces, and hence the losses. In practice, the number of bands is chosen as an optimum between bending stress, ease of manufacturing, and transmission losses. The tolerances for the thickness and diameter of the bands are quite narrow since tensile stress should not differ substantially between different bands (which would diminish the effectiveness of multiple bands). In the production process, the bands are measured and then selected, aiming at a mean variation of zero. Due to manufacturing variations, increasing the number of bands lowers the tensional band stress less than linearly. Besides, the increased belt mass results in higher centrifugal forces. The inner sliding surface of the bands is equipped with a herring-bone pattern surface so as to wedge oil in between, thus minimizing inner band friction losses. Some friction is still needed though, to ensure that the bands are running at the top of the segment shoulders.

### 5.2.3 Pulley design

In commercially available pushbelt CVTs, half the pulley wedge angle  $\theta$  is  $11^\circ$ . For smaller angles, the risk of self-locking of the belt in radial direction becomes larger, especially at standstill of the pulleys. Nevertheless, pulley sheaves with an angle of  $7^\circ$  are under development, for high power applications [Brandsma *et al.*, 1999]. The reason for the increased torque capacity is that the radially outward pushing component of the normal force between pulley and segments decreases for descending  $\theta$ . The resulting tensile stress reduction for the  $7^\circ$  pulley amounts up to 12%, when compared to the  $11^\circ$  pulley [Brandsma *et al.*, 1999]. Additionally, a smaller pulley wedge angle decreases the oil flow demand due to axial movement of the moveable sheave. In effect, the pump displacement can be reduced.

The axial deformation of the pulleys, bending of the pulley shafts and backlash in the pulley bearings result in widening of the pulley wedge, causing the belt to vary its orbit radius. In effect, the belt will spiral its way along the pulley wrap angle, both inward and outward. Obviously, the spiraling movement causes the friction force between pulley and segments to have a radial component, which doesn't contribute in the torque transmission. For this reason, the stiffness of the pulleys and their bearings is of the utmost importance.

One geometrically inherent loss factor is the misalignment of the belt. Because only one sheave at each pulley is moveable, the belt will run perpendicular to the shafts at the utmost at two transmission ratios. Usually, one of these ratios is chosen to be the *top ratio*, *i.e.*, the variator ratio in which the vehicle reaches its maximum speed. The pushbelt has been shown to endure small misalignments, which in practice amount up to 0.5 [mm] [Robertson and Tawi,

1997]. A rather costly solution to counteract misalignment, is to apply bulged (or crowned) pulley profiles, as in the Audi Multitronic [Wagner *et al.*, 2001].

## Chapter 6

# CVT Modeling and Validation

### 6.1 Introduction

This chapter presents a model for the hydraulically actuated metal pushbelt CVT. The model has several purposes. It is used for gaining insight in the operation of the CVT, both of the hydraulic part and of the pushbelt. Models of the pushbelt variator seen in literature are mostly empirical, therefore a physically obtained model is desirable to value the available 'grey-box' models. Having decided on a model best suited for control purposes, this model can be used both for deriving a model-based controller, and for testing such a controller in a simulation environment. The CVT that is used in the experiments is a Van Doorne CVT type P920. In modeling the P920 CVT, a number of parameters are taken from the highly similar P884 CVT (courtesy of VDT). Various experiments were performed to identify those parameters which are highly transmission-specific.

Modeling of the variator is subject of the first part of this chapter. After obtaining a model and identifying some of its parameters, simulation results are compared to experimentally obtained data. Next, a model for the hydraulics is presented. This model comprises the roller vane pump, the two solenoid valves and the interaction within the hydraulic circuit and with the variator. The models of the variator and of the hydraulics are combined with models for the planetary stage and flywheel, to obtain a (low-complexity) model for the ZI powertrain. This model is especially useful for reconstructing the torques that are exerted on the pushbelt by the pulleys. Moreover, it gives insight in the effects of the additional flywheel inertia of the ZI powertrain on the variator behaviour and the resulting implications for control. These issues are discussed at the end of this chapter. Furthermore, a CVT efficiency model is presented and efficiency measurements are analyzed.

### 6.2 Description of the test platform

Validation of the various models that will be presented, requires an experimental platform. For this purpose, a test rig was designed and constructed, according to Figure 6.1. A detailed description of the test rig is included in Appendix A. Here the main features are briefly discussed. The electric motors at the two ends of the test rig are identical and have a maximum power rating of 81 [kW] from 2900 [rpm] to the maximum speed of 5000 [rpm], *i.e.*, in the field-weakened speed range. The maximum torque below 2900 [rpm] is 267 [Nm]. Between

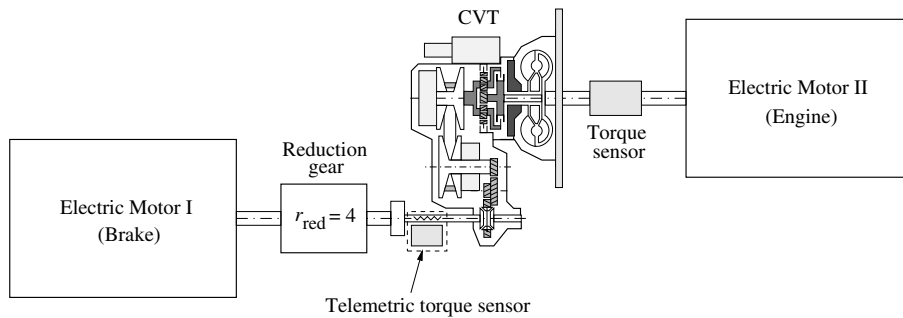


Figure 6.1: Schematic layout of the test platform

the two motors are the CVT and a (planetary) reduction gear, with gear ratio  $r_{\text{red}} = 4.00$ , *i.e.*, the speed of electric motor I ( $\omega_I$ ) is four times the speed of the drive shaft. The differential gear of the CVT is locked by a dismountable spline-shaft. The value of  $r_{\text{red}}$  is a trade-off between high-speed and high-torque testing. The maximum torque that motor I can exert at the drive shaft is 1067 [Nm], the maximum motor speed of 5000 [rpm] corresponds to a vehicle speed of 145 [km/h]. Presently, motor I is speed controlled, while motor II is torque controlled. Torque and speed control can easily be interchanged.

Among the available measurements are the torques at input and output shaft of the CVT. The input torque is measured between motor II and the torque converter, whereas the output torque is measured at the drive shaft, using telemetric signal transport. The speeds of the impeller, the turbine and the primary and secondary pulley are measured by Hall-effect sensors. Furthermore, various pressures are measured, the most important of which are the primary and secondary pressure. Temperature is monitored at a number of positions, mainly for diagnosis and for 'cooler management'. Besides the described test rig, a test vehicle equipped with the ZI transmission was used to conduct experiments. For details concerning this test vehicle, the reader is referred to [Serrarens, 2001].

### 6.3 Static variator models

The approaches in modeling of metal V-belt CVTs can be divided in two categories based on the friction models that are used to describe the phenomena in the segment-pulley contact, the segment-band contact and the contact between adjacent bands. The (rolling) friction between adjacent segments that occurs when the belt curves around a pulley is not taken into account. The majority of research assumes Coulomb friction [Gerbert, 1984; Becker, 1987; van Rooij and Schaerlaeckens, 1993; Sun, 1988; Asayama *et al.*, 1995]. In fact, the only work considering viscous shear is that done by [Mickle *et al.*, 1994]. While the latter type of modeling is still rarely seen, combinations of the two have so far never been investigated.

In the following, an overview of existing work is presented, and conclusions are drawn regarding the type of modeling best suited for practical application in a CVT controller.

### 6.3.1 Geometry and definitions

Figure 6.2 depicts the variator geometry for an arbitrary variator speed ratio  $r_{\text{cvt}} = \frac{\omega_s}{\omega_p}$ . The speed ratio  $r_{\text{cvt}}$  is lower bounded by the underdrive speed ratio  $r_{\text{ud}}$  (typically around 0.4) and upper bounded by the overdrive speed ratio  $r_{\text{od}}$  (typically around 2.5). It is assumed that

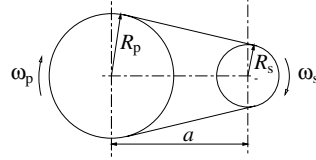


Figure 6.2: Variator geometry

no (gross) belt slip occurs (*i.e.*,  $\omega_s R_s = \omega_p R_p$ , so  $R_p = r_{\text{cvt}} R_s$ ), that the belt is inextensible and runs at perfect circles with radii  $R_p$  and  $R_s$  on the primary and secondary pulley, respectively. Defining the symmetrical ratio  $\lambda = \frac{r_{\text{cvt}} - 1}{r_{\text{cvt}} + 1}$ , the following implicit relationship between  $r_{\text{cvt}}$  and  $R_s$  can be derived using the variator geometry in Figure 6.2:

$$\frac{L}{2a} = \sqrt{1 - \rho^2 \lambda^2} + \frac{\pi}{2} \rho + \text{asin}(\rho \lambda) \rho \lambda \quad (6.1)$$

$$R_s = \rho \cdot \frac{a}{r_{\text{cvt}} + 1} ; R_p = r_{\text{cvt}} R_s \quad (6.2)$$

where  $L$  is the belt length and  $a$  the pulley center distance. A first order approximation for  $R_p$  with a maximum error of 5% can be obtained as follows. Set  $r_{\text{cvt}} = 1$ , so  $L = 2a + \pi(R_p + R_s)$ , and assume the latter expression to approximately hold for all  $r_{\text{cvt}}$ , then

$$R_p \approx \frac{r_{\text{cvt}}}{r_{\text{cvt}} + 1} \frac{L - 2a}{\pi} = \frac{L - 2a}{2\pi} (1 + \lambda) \quad (6.3)$$

The axial pulley position  $s_x$  ( $x = p$  for primary and  $x = s$  for secondary) is related to  $R_x$  by

$$s_x = 2 \tan \theta (R_x - R_{x,\text{min}}) \quad (6.4)$$

where  $R_{x,\text{min}}$  is the minimum belt radius at pulley  $x$ .

In order to describe several existing approaches, a basic model (termed *reference model*) is presented first, after which for each of these approaches the differences with this model are listed. The reference model is based on Coulomb friction. After describing viscous shear models in Section 6.3.3, it is decided what type of model is best suited for describing the variator behaviour.

Figure 6.3 defines the terminology relevant in describing the belt mechanics. The longitudinal direction for a segment coincides with the tangential (or circumferential) direction for a pulley when the segment is within the *angle of wrap*, *i.e.*, the circumferential angle for which the segment sides are in contact with the pulley. The lateral segment direction coincides with the pulley axial direction, and the segment transversal direction coincides with the pulley radial direction. Also shown in Figure 6.3 is the rocking edge, which was earlier defined as the contact line between adjacent segments, along which the segments tilt. The imaginary, longitudinal/tangential line through the rocking edges along the belt is called the *neutral line*. The



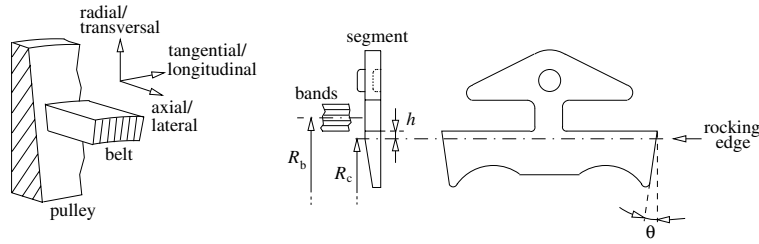


Figure 6.3: Definitions for bands and segments

distance between the rocking edge and the pulley center of rotation is called the segment orbit radius  $R_c$  (c for compression elements), whereas  $R_b$  is the distance between the pulley center and the centerline of the bands. Finally, the distance between rocking edge and segment shoulder is denoted by  $h$ .

### 6.3.2 Variator models based on Coulomb friction

In the reference model, the following assumptions are made:

1. the two packs of approximately 10 bands each, are treated as one solid pack without bending stiffness;
2. the belt is a continuous, homogeneous line of segments, that (for stationary states) runs at a radius which is constant for each pulley;
3. segments and bands are flexible in longitudinal direction and rigid in all other directions; deformations are always elastic and very small;
4. in deriving the kinematic relations and the equations of motion the undeformed geometry is used;
5. pulleys and pulley shafts are assumed to be rigid and pulley-skewness is neglected;
6. for stationary speed ratios, all contact friction is assumed to be of the Coulomb type. Viscous shear will be considered for changing speed ratios;
7. the radial position of the center of gravity of a segment coincides with that of the rocking edge (characterized by  $R_c$ ), while the center of gravity of a section of bands lies on the centerline (characterized by  $R_b$ ).

Depending on the purpose of the variator model, some of these assumptions may be rather restrictive. For instance, deformations resulting in the spiraling movement of the belt, are of great relevance for the transmission efficiency (to be treated in Section 6.7). Since the intention is to use the model for gaining insight into mechanisms concerning quantities such as the pulley clamping force and the load envelope of the pushbelt, the above assumptions are believed to be reasonable.

Consider the free body diagrams of infinitesimally small sections of bands and segments (Figure 6.4). In this representation  $Q$  denotes the compression force between segments,  $S$  is the tension force in the bands,  $dW_1$  and  $dW_2$  denote friction forces, and  $dN_1$  and  $dN_2$  normal

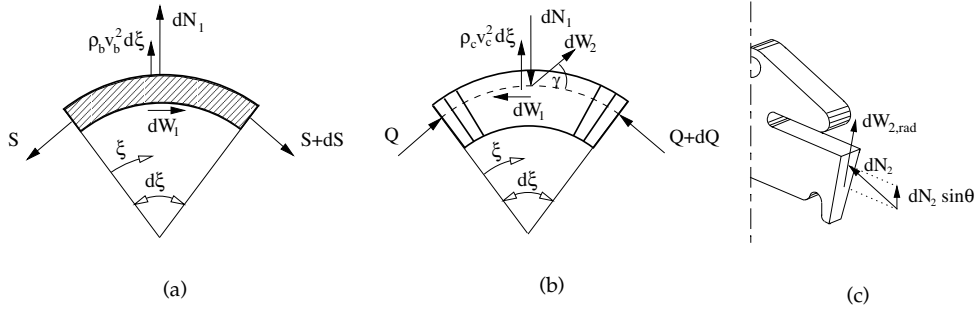


Figure 6.4: Forces acting on sections of bands (a) and segments (b), and segment side (c)

forces, acting between bands and segments, and segments and pulley, respectively. Because the two packs of bands are treated as one,  $dW_1$  and  $dN_1$  account for the combined forces of two packs, whereas  $dW_2$  and  $dN_2$  are forces per segment side. Finally,  $\rho_b v_b^2 / R_b$  and  $\rho_c v_c^2 / R_c$  are centrifugal forces per unit length of bands and segments, respectively. Here,  $\rho_b$  and  $\rho_c$  are the mass per unit length,  $R_b$  and  $R_c$  the orbit radii and  $v_b$  and  $v_c$  the tangential velocities of bands and segments, respectively.

The friction force  $dW_2$  can be decomposed into components  $dW_{2,rad}$  and  $dW_{2,tan}$ , acting in radial and tangential direction, respectively. With  $\gamma$  the angle between  $dW_2$  and the *neutral* line, we have

$$dW_{2,rad} = dW_2 \sin \gamma \quad (6.5)$$

$$dW_{2,tan} = dW_2 \cos \gamma \quad (6.6)$$

with

$$dW_2 = \chi_2 s_2 dN_2 \quad (6.7)$$

where  $s_2 = \text{sign}(v_u - v_c)$  with  $v_u$  the circumferential speed of the pulley evaluated at the rocking edge. The sign of  $s_2$  is related to the shape of the compression force along the angle of wrap, as will be become clear further on. Furthermore, the factor  $\chi_2$  is equal to the maximal coefficient of friction  $\mu_2$ , so  $\chi_2 = \mu_2$ , if there is a relative motion between the two surfaces<sup>1</sup>, *i.e.*, on the *active* arcs<sup>2</sup>. On the *idle* arcs  $\chi_2 < \mu_2$ .

The friction force  $dW_1$  between segments and bands is given by

$$dW_1 = \chi_1 s_1 dN_1 \quad (6.8)$$

where  $s_1 = \text{sign}(v_c - v_b)$ . Furthermore,  $\chi_1 = \mu_1$  if there is relative motion between segments and bands, and  $\chi_1 < \mu_1$  elsewhere. If the radius of the neutral line on the primary pulley

<sup>1</sup>A dynamical coefficient of friction, which would generally be smaller than the static one, is not considered here. Therefore,  $\vec{W} = \mu N \vec{v} / \|\vec{v}\|$  if the absolute value  $\|\vec{v}\|$  of the relative speed  $\vec{v}$  is unequal to zero, and  $|\vec{W}| = \chi N \leq \mu N$  if  $\vec{v} = 0$ .

<sup>2</sup>The terms *active* and *idle* arc will be defined in the following, also see Figures 6.5–6.7.

differs from the radius of this line on the secondary pulley, *i.e.*, if  $r_{cvt} \neq 1$ , then it is straightforward to see that the bands have to run ahead of the segments at the pulley with the larger belt radius and/or lag behind at the pulley with the smaller one. The sign  $s_1$  of  $dW_1$  depends on the relative speed between segments and bands. Choosing the path of least resistance, the bands will slip at the pulley with the smaller belt radius only. This causes the band tension to decrease in the pulley running direction at the smaller belt radius, and vice versa at the larger one (see Figure 6.5). This mechanism determines the direction of friction between bands and

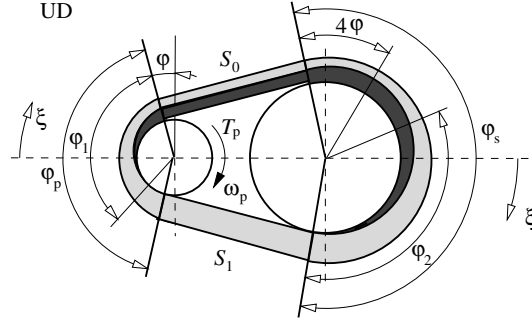


Figure 6.5: Tension (grey) and compression (black) forces for the UD case ( $r_{cvt} < 1$  and  $T_p$  'high');  $\varphi_p$  and  $\varphi_s$  are primary and secondary angles of wrap;  $\varphi_1$  and  $\varphi_2$  are primary and secondary active arcs;  $\varphi = (\pi - \varphi_p)/2$ ;  $S_0$  and  $S_1$  are, respectively, the low and high tension force in the straight parts of the belt;  $T_p$  and  $\omega_p$  are the primary torque and speed, respectively

segments. Furthermore, it enables the bands to transmit part of the input torque  $T_p$  for  $r_{cvt} < 1$ , whereas for  $r_{cvt} > 1$  the torque transmitted by the bands will counteract the torque transmitted by the segments. Hence, the compression force for  $r_{cvt} > 1$  must be in the upper straight part of the belt and should have some minimum value to compensate for the negative band torque, in order to transmit a net positive torque. On the other hand, for  $r_{cvt} < 1$ , the compression force can be in the upper straight part (for high input torques) as well as the lower straight part of the belt (for low input torques). The latter is possible if the torque transmitted by the bands is at least as large as the negative torque transmitted by the segments. These effects yield the various shapes of compression force, depicted in Figures 6.5–6.7.

The band tension mechanism results in a so called *idle arc* at primary pulley entry side ( $Q=0$ ), and at secondary pulley entry side ( $Q=\max(Q)$ ). In case the transmitted torque is small, band lag may cause segments to pile up at primary pulley exit side and to separate at secondary pulley entry side, resulting in a reversal of the torque transmitted by the segments. This situation will therefore be referred to as Underdrive Reversed compression (UR), see Figure 6.6, whereas the situation for relatively high torque  $T_p$  and  $r_{cvt} < 1$  is referred to as the UD (Underdrive) case. The reversal of compression does not happen for speed ratios between  $r_{cvt} = 1$  (*medium* transmission ratio) and OverDrive (OD), see Figure 6.7.

For  $\gamma = 0$  (see Figure 6.4), after some elaboration (see Appendix B) the primary and secondary pulley clamping force  $F_p$  and  $F_s$  can be shown to relate as follows

$$F_p = \Phi F_s + \frac{\int_{\varphi_p} D_p(\xi) d\xi - \Phi \int_{\varphi_s} D_s(\xi) d\xi}{2 \tan \theta} \quad (6.9)$$

where  $D(\xi) = S(\xi) - Q(\xi)$  and  $\Phi = \frac{\varphi_p}{\varphi_s}$ , with  $\varphi_p$  and  $\varphi_s$  the primary and secondary angles of wrap.

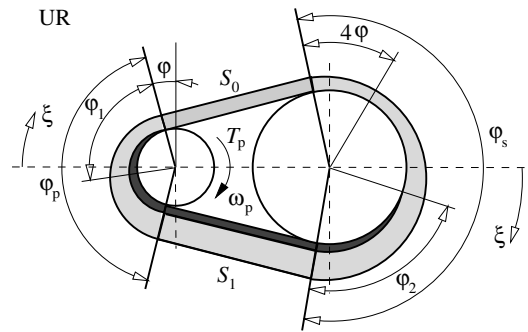


Figure 6.6: Tension (grey) and compression (black) forces for the UR (Underdrive Reversed compression) case ( $r_{cvt} < 1$  and  $T_p$  'low');  $\varphi_p$  and  $\varphi_s$  are primary and secondary angles of wrap;  $\varphi_1$  and  $\varphi_2$  are primary and secondary active arcs;  $\varphi = (\pi - \varphi_p)/2$ ;  $S_0$  and  $S_1$  are, respectively, the low and high tension force in the straight parts of the belt;  $T_p$  and  $\omega_p$  are the primary torque and speed, respectively

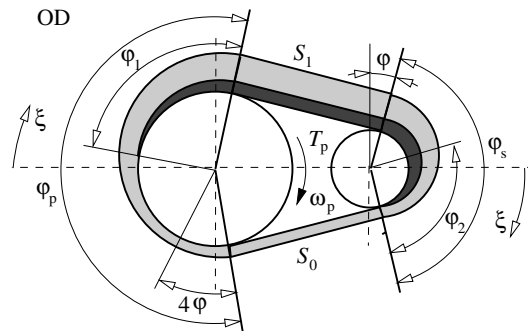


Figure 6.7: Tension (grey) and compression (black) forces for the OD case ( $r_{cvt} > 1$ );  $\varphi_p$  and  $\varphi_s$  are primary and secondary angles of wrap;  $\varphi_1$  and  $\varphi_2$  are primary and secondary active arcs;  $\varphi = (\pi - \varphi_p)/2$ ;  $S_0$  and  $S_1$  are, respectively, the low and high tension force in the straight parts of the belt;  $T_p$  and  $\omega_p$  are the primary torque and speed, respectively

### validation of the reference model

Using the calculation procedure described in Appendix B.1.1, results of the reference model are compared to experimental results, as a function of the speed ratio  $r_{cvt}$  and for various torque levels. The torque level is normalized using the *torque ratio*  $\tau'_s$ , defined in Appendix B as

$$\tau'_s = \frac{\cos \theta T_p}{2\mu_2 R_p F_s} \quad (6.10)$$

The torque ratio (normally between -1 and 1) can be interpreted as the transmitted torque relative to the torque that can be transmitted given the actual clamping forces (so  $|\tau'_s| = 1$  corresponds to the belt slip limit). Given a secondary pulley clamping force  $F_s$ , the force  $F_p^*$  is defined as the primary pulley clamping force needed to maintain a stationary CVT speed

ratio. The *pulley thrust ratio*  $\kappa$  is the ratio of  $F_p^*$  and  $F_s$ , i.e.,

$$\kappa = F_p^*/F_s \quad (6.11)$$

Figure 6.8 compares results from the reference model with  $\gamma = 0$ , to measurements  $\kappa(r_{cvt}, \tau_s')$  performed on the P920 transmission. It is chosen to depict  $\ln(\kappa)$  versus  $\ln(r_{cvt})$  in order to reveal symmetry around  $r_{cvt} = 1$ ,  $\kappa = 1$  and  $\tau_s' = 0$ . In this figure, the bold solid lines are

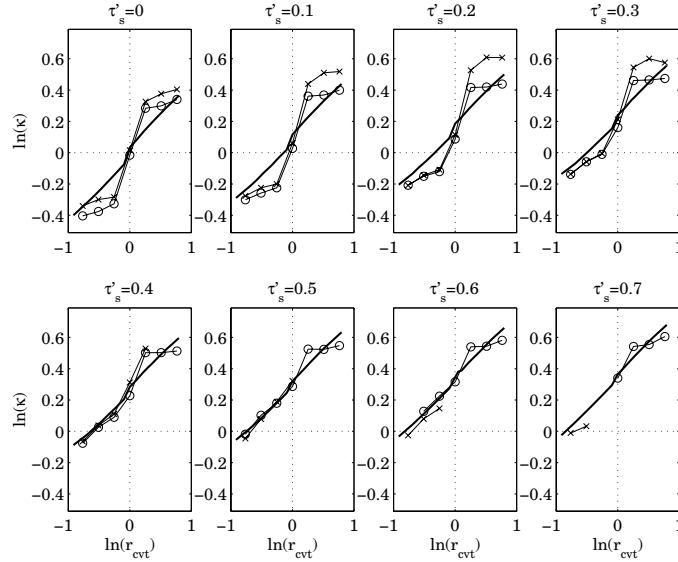


Figure 6.8: (Logarithms of) pulley thrust ratios  $\kappa = \frac{F_p^*}{F_s}$  versus speed ratio  $r_{cvt}$  for various  $\tau_s'$ . The bold solid lines are obtained using the reference model. The remaining two lines are measurements ('-o') and 'inverted' measurements ('-x'). The 'inverted' measurements  $\kappa(1/r_{cvt}, -\tau_s')$  are included as an indication of symmetry

obtained from the model. The remaining two lines are measurements ('-o') and 'inverted' measurements ('-x'). The 'inverted' measurements  $\kappa(1/r_{cvt}, -\tau_s')$  are included as an indication of symmetry. The underlying symmetry considerations are discussed in [Stouten, 2000]. The influence of  $\tau_s'$  on  $\kappa$  is well described by the model. However, the dependency of  $\kappa$  on  $r_{cvt}$  cannot accurately be predicted by the model. Also, the measurements and the inverted measurements show quite a difference, for  $r_{cvt} > 1$ . The very steep (almost discontinuous) part around  $r_{cvt} = 1$  is caused by the reversal of slip speed between bands and segments, which is more pronounced for larger  $\mu_1$ . In reality, the reversal of slip speed will probably occur over a certain ratio span, since the belt will not run at an exact circle, causing the slip speed direction to be evened out over both angles of wrap. The model obtained thus far (without the restriction  $\gamma = 0$ ) will be used as a reference for the following section.

#### literature on variator models based on Coulomb friction

The reference model in fact very much resembles the model used by [Becker, 1987], although Becker elaborates further on determining the angle  $\gamma$  for primary and secondary side. The

(iterative) process of determining  $\gamma$  is indeed very laborious. [van Rooij and Schaerlaeckens, 1993] take the simplified approach, *i.e.*,  $\gamma = 0$ . They also derive expressions for tension forces in the individual bands, and conclude their paper with a brief treatise on variator efficiency. Although this model is far less involving than that of Becker, computational demands are probably still unacceptable for on-line applications.

The model in [Asayama *et al.*, 1995] is very similar to the reference model (and hence Becker's model), only to differ in including segment and eventually pulley deformations. The latter deformations are considered in order to achieve better matching of their model results with the band tension forces as measured by strain gauges. They end up with a friction coefficient between segments and bands equal to 0.16 which is huge compared to the 0.07–0.09 generally used for the segment-pulley contact. Furthermore, this result is likely to contradict substantially with claims in [Hendriks *et al.*, 1988] stating that around 4% of the transmitted torque is due to the bands (also see the discussion still to come in Section 6.7.1). It must be said, though, that, *e.g.*, in [van Rooij and Schaerlaeckens, 1993], where  $\mu_1 = 0.03$  and  $\mu_2 = 0.07$ –0.09, the bands are found to account for as much as 40% of the total torque transmission. The latter numbers are supported by measurements in [Fujii *et al.*, 1993b], obtained in a way similar to Asayama's method. Fujii's measurements were performed at rotational speeds between 150 and 300 [rpm], whereas Asayama used speeds no higher than 10–20 [rpm]. The friction mechanisms acting at these speeds may be different from those present at practical speeds, *i.e.*, 1000–5000 [rpm].

Although Fujii's results will be of use in the following section, it must be stressed that some caution in using them seems appropriate, mainly because it is unclear whether or not the measured forces in their specially designed segments are fully representative for the forces in unmodified ones. The model Fujii *et al.* derive in Part 1 of their series of papers [Fujii *et al.*, 1993a] is very restrictive in that it, for one thing, neglects the role of centrifugal forces between bands and segments. Furthermore, the compression force does not appear in the radial segment force equilibrium, and the normal force between the segments and the pulley is assumed to be uniform over the angle of wrap. Part 4 of their series of papers [Kitagawa *et al.*, 1995] presents some interesting results regarding the forces acting on segments in case of ratio changes. Yet another modified segment is added, capable of measuring the friction force acting on the segment sides in radial direction. Their findings show, for one thing, that radial friction becomes very important, not only during shifting, but also in explaining some of the differences that are observed between measurements of pulley thrust ratios and model based values (as seen, *e.g.*, in Figure 6.8).

Sun's model [Sun, 1988] is in some ways similar to the reference model, except that it, among other things, assumes the friction force  $dW_2$  to be directed *either* radially *or* tangentially. At idle arcs and during ratio changes the direction is said to be radial only, whereas it is taken to be tangential otherwise. It is not clear why such an assumption should hold. Sun also considers deformations of segments and individual bands. He does not compare his model with experimental results, but concludes from calculations that bands contribute in transmitting torque for 1–20%, depending on friction coefficients.

Finally, the work by Gerbert [Gerbert, 1981, 1996] is mentioned. This very thorough work is rather restrictive in that it usually is related to the rubber V-belt, which is obviously essentially different, although some of its implications may well hold for the metal V-belt. The paper which *does* address the metal V-belt [Gerbert, 1984] only treats the case where  $r_{\text{cvt}} = 1$ . Interestingly though, it investigates the effect of pulley deflection as well as that of an initial gap between the segments.

### 6.3.3 Variator model based on viscous shear

Although in current metal V-belts the sides of the segments are prepared such as to prevent an oil film from being developed, work by Micklem and Guebeli [Micklem *et al.*, 1994; Guebeli *et al.*, 1993] suggests that an oil film nevertheless exists. This is supported by measurements of belt slip that are well in excess of what can be predicted by Coulomb friction models (see, *e.g.*, [Becker, 1987]). Also, in no case the slip velocity grows indefinitely, as would be expected with Coulomb friction. The model proposed in [Micklem *et al.*, 1994] differs from the reference model in a number of ways:

- first of all and most importantly,  $dW_{2,\text{rad}}$  no longer represents Coulomb friction but viscous shear, so

$$dW_{2,\text{rad}} = \tau_{\text{vs}} \cdot dA \quad (6.12)$$

where

$$\tau_{\text{vs}} = \frac{\eta_{\text{oil}}(v_u - v_c)}{h_f} \quad (6.13)$$

is the viscous shear stress. In this expression  $\eta_{\text{oil}}$  denotes the dynamic coefficient of viscosity for oil,  $v_u - v_c$  is the relative speed between pulley and segments, and  $h_f$  is the oil film thickness. It is assumed that the oil film is fully developed (no boundary lubrication), also for low speeds.

The infinitesimal area  $dA$  is given by (see Figure 6.9)

$$dA = b c \frac{R_c d\xi}{m} \quad (6.14)$$

where  $m$  is the thickness of one segment. The area  $b \cdot c$  in Figure 6.9 represents the

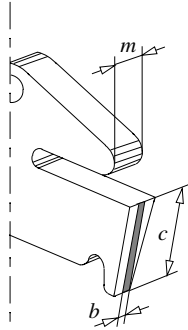


Figure 6.9: Dimensions of the Hertzian contact

Hertzian contact. In [Micklem *et al.*, 1994] expressions for  $b$  and  $h_f$  are taken from elastohydrodynamic lubrication theory, but these are omitted here;

- the second difference with the reference model lies in the fact that Micklem (correctly) treats all bands separately and determines viscous shear forces from relative velocities between adjacent bands.

In determining the pulley thrusts a number of restricting assumptions is made:

- the segment compression force ( $Q$ ) is assumed to increase linearly from 0 at pulley entry to some end value at pulley exit, hence there is no idle arc. This is a very restrictive assumption, since it results in a pulley thrust ratio that is independent of the torque to be transmitted;
- next, the normal force  $dN_1$  and hence the band tension  $S$  are assumed to be constant and equal at both pulleys. This implies that there is no friction between bands and segments, which actually contradicts with the viscous shear approach in determining the band tensions. The only justification for this may be found in Micklem's remark [Micklem *et al.*, 1994] that the bands apparently contribute negligibly in transmitting torque, although this very assumption was earlier mentioned to be rather disputable;
- except for ratio change situations,  $dW_{2,\text{rad}}$  is taken to be zero, which must of course be true if only viscous shear is considered.

Most likely, neither Coulomb friction nor viscous shear can fully describe the mechanisms in the actual contacts. A combination of the two might well characterize the situation better, where the contribution of each probably depends on the type of operation. It is from this point of view that it is suggested to use a particular kind of combination. Judging from experimental data collected by [Fujii *et al.*, 1993b], results from the Coulomb friction approach quite reasonably resemble actual measurements, *i.e.*, active and idle arcs indeed seem to be present. Although it was earlier mentioned that these experiments were all carried out at relatively low speeds, pulley thrust ratios most of the time rather well compare to computed data resulting from (6.9), whereas they would be load-independent under the assumption of zero idle arcs. Hence it is decided to use the Coulomb friction approach to determine stationary operating points.

## 6.4 Transient variator models

So far, the number of papers addressing the problem of modeling ratio change has been exceptionally small. Here, the models of three research groups are considered in some detail.

### Ide's model

The first is that of [Ide *et al.*, 1994]. This model uses a number of linear fits to arrive at a grey-box model. Ide *et al.* performed a vast number of ratio change experiments for various settings of pressures, primary speed, load and speed ratio and obtained the following expression for the rate of ratio change

$$\dot{r}_{\text{cvt}} = k_r(r_{\text{cvt}})(F_p - F_p^*)|\omega_p| \quad (6.15)$$

where  $k_r(r_{\text{cvt}})$  is an experimentally obtained function, and  $F_p^*$  is defined as in Section 6.3.2. Though in the paper where (6.15) is obtained the authors do not give physical explanations for any of their observations, a subsequent paper [Ide *et al.*, 1996] elucidates some of these findings. Further experiments—which were performed without load—suggest that the radius changes by a constant amount per revolution, hence that  $\dot{r}_{\text{cvt}}$  is linear in  $|\omega_p|$ . At least this is said to be true in what they call *creep mode*. The other mode they distinguish is termed *slip mode* and occurs for a rather small primary clamping force. It is not clear whether or not the latter mode will be present at all in practical situations, since according to the authors it might not be possible to transmit any torque during such operation.



### Guebeli's model

The second approach in modeling ratio change can be found in the viscous shear method. This was done by [Guebeli *et al.*, 1993], unfortunately leading to an erroneous result. In Appendix B the correct results are derived, yielding

$$\dot{r}_{\text{cvt}} = \cos^2 \theta \sin \theta \cdot \frac{k_h}{\eta_{\text{oil}}} \cdot \frac{r_{\text{cvt}} \Phi + 1}{R_s} \cdot \frac{F_p - F_p^*}{F_p + \Phi^2 F_s} \quad (6.16)$$

with  $\Phi$  as in Section 6.3.2. In this expression,  $\frac{k_h}{\eta_{\text{oil}}}$  is experimentally obtained from slip measurements, which were performed by [Micklem *et al.*, 1994; Guebeli *et al.*, 1993] and were fit to  $R_p$  according to

$$\frac{k_h}{\eta_{\text{oil}}} = c_{v0} + c_{v1} R_p \quad (6.17)$$

where  $c_{v0} \approx 2.7$  [m/s] and  $c_{v1} \approx 29$  [s<sup>-1</sup>].

### Shafai's model

The model in [Shafai *et al.*, 1995] has the form of a differential equation for the axial velocity  $\dot{s}_p$  of the primary pulley sheave:

$$m_s \ddot{s}_p = F_p - F_p^* - b_s \dot{s}_p \quad (6.18)$$

In this equation,  $s_p$  is related to the primary radius  $R_p$  according to (6.4),  $m_s$  is a 'representative' mass of sheave and belt, and  $b_s$  is a 'representative' damping coefficient. Values or physical backgrounds for these parameters are not given in [Shafai *et al.*, 1995]. However,  $m_s$  will be in the order of magnitude of 2 [kg], therefore  $m_s \ddot{s}_p$  is likely to be exceptionally small (also see [Luh, 1994]) compared to  $F_p - F_p^*$ , and can be neglected. Then Equation (6.18) simplifies to

$$b_s \dot{s}_p = F_p - F_p^* \quad (6.19)$$

or, equivalently (using Equations (6.3) and (6.4))

$$\dot{r}_{\text{cvt}} \approx \frac{\pi}{2 \tan \theta b_s (L - 2a)} (r_{\text{cvt}} + 1)^2 (F_p - F_p^*) \quad (6.20)$$

where  $b_s$  is taken to best match ratio change measurements.

### other models

Besides the mentioned models, some transient variator models exist which are not particularly suited for control application. One example is [Vanvuchelen, 1997], which describes the variator in terms of the moveable pulley positions (and their derivatives). The belt is modeled as a spring-damper. Like Shafai, Vanvuchelen takes the axial pulley accelerations into account. For his controller design, Vanvuchelen relies on the Ide model.

### 6.4.1 Validation of transient variator models

In this section, the three transient models of Ide, Guebeli and Shafai are compared with measurements obtained from the ZI transmission in the test vehicle. Because small variations in  $F_p^*$  due to model errors are to be expected, all three models may display low-frequency drift with respect to the measurements. Figure 6.10 depicts an arbitrary but fairly dynamic trajectory of  $r_{cvt}$ , both measured and simulated. The inputs for the simulation models are the clamping forces  $F_p$  and  $F_s$ , the primary belt torque  $T_p$ , and the secondary speed  $\omega_s$ . The clamping forces are reconstructed using pressure and speed measurements, whereas an estimate for  $T_p$  is obtained as will be outlined in Section 7.3. Shafai's model seems to outperform the other two,

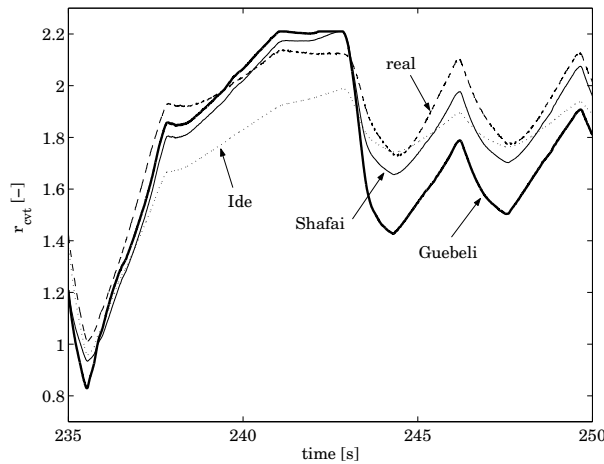


Figure 6.10: Comparison of CVT transient models

although most of the errors are due to drift. This drift is caused mainly by the fact that the pulley thrust ratio  $\kappa$  used in the model differs from the actual one, combined with the fact that the steady state CVT speed ratio is quite sensitive to those differences. The time-derivative of the measured  $r_{cvt}$  and the model errors in  $\dot{r}_{cvt}$  are shown in Figure 6.11. Guebeli's model generally produces the largest errors, whereas Ide's model and Shafai's model are quite competitive. The benefit of Ide's model is that it results in  $\dot{r}_{cvt} = 0$  for  $\omega_p = 0$ , which is correct. The other two models must explicitly set  $\dot{r}_{cvt}$  to zero for small  $|\omega_p|$  to circumvent the problem. Other than this, Shafai's model is easier to handle since effectively it only has one parameter. The Ide model is chosen to be used throughout the rest of this thesis.

## 6.5 Hydraulics

The variator is actuated by pressures acting on the moveable sheaves. The hydraulic circuit to control these pressures is schematically depicted in Figure 6.12. It essentially comprises a roller vane pump, and two proportional solenoid valves besides the undepicted accessories. The shaded pulley sheaves are axially fixed, the other two are moveable.

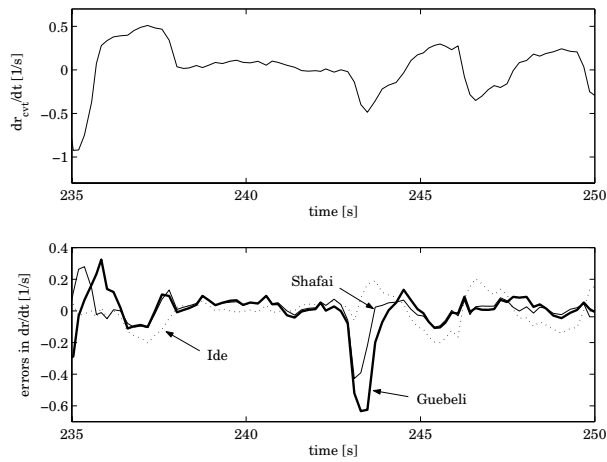


Figure 6.11: Comparison of model errors (lower plot) with respect to the measured  $\dot{r}_{cvt}$  (upper plot)

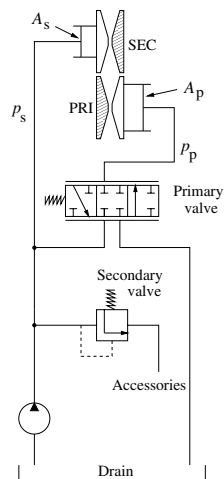


Figure 6.12: Hydraulic actuation system

### 6.5.1 Hydraulic circuit

The volume directly connected to the pump and the secondary cylinder is referred to as the *secondary circuit*; the volume connected to the primary cylinder as the *primary circuit*. Control of the secondary pressure is performed by the *secondary valve*, which bleeds off towards the accessories. The primary pressure is reduced from the secondary pressure by the *primary valve*. This valve can direct the flow from the secondary to the primary circuit, or from the primary circuit to the drain. All pressures are defined relative to the atmospheric pressure.

Both the primary and secondary pulley pressures are measured at channels connected to the oil supply that runs through the pulley shaft, so more or less at the center of the pulley cylinder. Therefore, centrifugal effects of the oil in the rotating cylinders are not measured by the pressure sensor. Hence, the primary pulley clamping force  $F_p$  is the sum of a direct pressure term  $A_p p_p$  and a centrifugal force term  $c_p \omega_p^2$ , *i.e.*,

$$F_p = A_p p_p + c_p \omega_p^2 \quad (6.21)$$

Here,  $A_p$  is the primary piston area,  $c_p$  a centrifugal coefficient and  $p_p$  the oil pressure in the primary circuit. Likewise, the secondary pulley clamping force  $F_s$  consists of a direct pressure term  $A_s p_s$  and a centrifugal force term  $c_s \omega_s^2$ , with  $A_s$  the secondary piston surface,  $c_s$  the centrifugal coefficient and  $p_s$  the secondary pressure. Moreover, in  $F_s$  there is a contribution of the secondary spring  $F_{spr}$  that has to warrant a minimal clamping force under all circumstances. Since the axial displacement  $s_s$  of the secondary moveable sheave is a linear function of the belt radius  $R_s$ , it follows that  $F_s$  is given by

$$F_s = A_s p_s + c_s \omega_s^2 + F_{spr}; \quad F_{spr} = k_{spr}(R_{s,max} - R_s) + F_{spr,0} \quad (6.22)$$

where  $k_{spr}$  is the spring constant,  $F_{spr,0}$  is the spring preload and  $R_{s,max}$  is the maximum secondary belt radius. Both the primary and secondary pulley pistons have O-ring seals that result in an axial friction force which is around 2% of the axial force  $A_x p_x$ , and is neglected in the model. In the LuK CVT that was mentioned in the previous chapter, teflon rings are inserted to reduce this friction, and hence minimize corresponding stick-slip problems.

The pressures  $p_p$  and  $p_s$  are regulated by controlling the throttling areas  $A_1$  and  $A_2$  of, respectively, the primary and secondary valve. The continuity equation, applied to the primary hydraulic circuit [Stouten, 2000], results in

$$k_{oil} V_p \dot{p}_p = -c_{pl} p_p - \dot{V}_p + \Phi_{sp} + \Phi_{pd} \quad (6.23)$$

where  $k_{oil}$  is the compressibility of the oil,  $V_p$  is the momentary volume of the primary circuit,  $c_{pl} p_p$  is the leak flow and  $\dot{V}_p = 2 \tan \theta A_p \dot{R}_p$  accounts for the volume change of the primary circuit, due to the displacement of the moveable sheave of the primary pulley. The compressibility  $k_{oil}$  actually depends on temperature, pressure and especially the air fraction in the oil, but is assumed constant for simplicity. Piston deformations can be substantial and are lumped into  $k_{oil} V_p$ . Finally, the terms  $\Phi_{sp}$  and  $\Phi_{pd}$  are the flow through the primary valve from the secondary to the primary circuit, and from the primary circuit to the drain, respectively. The definition of the throttling area  $A_1$  is such that an opening from the primary circuit to the drain is represented by  $A_1 < 0$ , whereas an opening from secondary to primary circuit is represented as  $A_1 > 0$ . In reality  $A_1 < 0$  and  $A_1 > 0$  correspond to two different orifices. The functions  $\Phi_{sp}$  and  $\Phi_{pd}$  are given by

$$\Phi_{sp} = \begin{cases} 0 & \text{if } A_1 \leq 0 \\ c_f A_1 \sqrt{\frac{2|p_s - p_p|}{\rho_{oil}}} \text{sign}(p_s - p_p) & \text{if } A_1 > 0 \end{cases} \quad (6.24)$$

$$\Phi_{pd} = \begin{cases} c_f A_1 \sqrt{\frac{2p_p}{\rho_{oil}}} & \text{if } A_1 \leq 0 \\ 0 & \text{if } A_1 > 0 \end{cases} \quad (6.25)$$

Here,  $\rho_{oil}$  represents the oil density, which is a function of oil temperature. For simplicity  $\rho_{oil}$  is assumed constant and the discharge coefficient  $c_f$  is taken equal for both orifices.

Application of the continuity equation to the secondary circuit yields

$$k_{\text{oil}} V_s \dot{p}_s = \Phi_{\text{pump}} - c_{\text{sl}} p_s - \dot{V}_s - \Phi_{\text{sp}} - \Phi_{\text{sa}} \quad (6.26)$$

where  $\Phi_{\text{pump}}$  is the pump flow,  $c_{\text{sl}} p_s$  is the leak flow and  $\dot{V}_s = 2 \tan \theta A_s \dot{R}_s$  accounts for the change of the volume  $V_s$  of the secondary circuit. Again,  $k_{\text{oil}} V_s$  may also include the effects of piston deformation. Besides,  $\Phi_{\text{sa}}$  is the oil flow through the secondary valve from the secondary circuit to the accessory circuit, *i.e.*,

$$\Phi_{\text{sa}} = c_f A_2 \sqrt{\frac{2|p_s - p_a|}{\rho_{\text{oil}}}} \text{sign}(p_s - p_a) \quad (6.27)$$

## 6.5.2 Proportional solenoid valves

### Secondary valve

The secondary valve is a pressure regulating valve (Figure 6.13) with a passive feedback of the upstream pressure  $p_s$ . The valve blows off towards the accessories ( $p_a$ ) through opening  $A_2$ . The accessories pressure  $p_a$  itself is controlled by a passive valve that bleeds off towards the lubrication circuit. The throttling orifice of this passive valve is the result of the balance between  $p_s$  and  $p_a$  acting on compensation areas similar to that in the secondary valve. Consequently,  $p_a$  relates approximately linearly to  $p_s$  according to

$$p_a = c_{a1} + c_{a2} p_s \quad (6.28)$$

where  $c_{a1} = 3.7$  [bar] and  $c_{a2} = 0.073$  [-]. This relation is valid only for  $p_s > c_{a1}/(1 - c_{a2}) = 4.0$  [bar]. If  $p_s$  drops below 4.0 [bar], flow is no longer supplied to the accessories, hence  $p_a \approx 0$ .

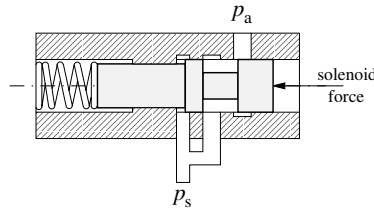


Figure 6.13: Secondary valve

Due to the pressure feedback in the secondary valve,  $p_s$  varies only moderately with  $\Phi_{\text{sa}}$ , see Figure 6.14. This figure depicts the secondary pressure as a function of the flow  $\Phi_{\text{sa}}$ , for various values of the solenoid current  $I_2$ . The resulting behaviour of the secondary valve is highly reproducible, even for a varying temperature, enabling a very effective feedforward for the secondary pressure control loop.

### Primary valve

The primary valve, shown in Figure 6.15, has two throttling orifices. These are the opening from secondary to primary circuit, and the opening from primary circuit to drain. An estimate of these throttling areas (represented by  $A_1$ ) as a function of the solenoid current  $I_1$  is depicted in Figure 6.16. The figure is constructed from static and dynamic experiments.

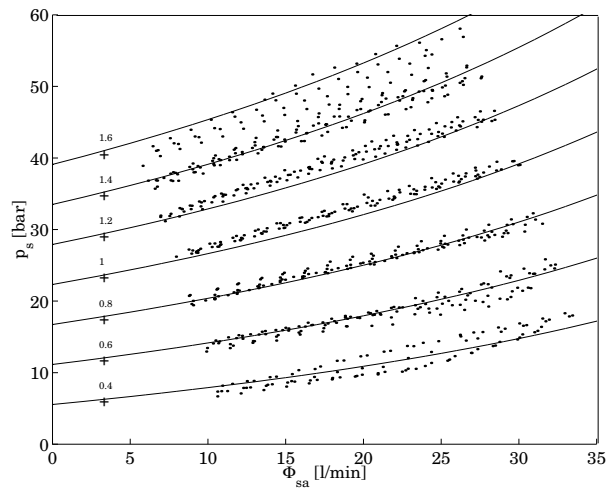


Figure 6.14: Characteristic of the secondary valve, depicted for secondary solenoid currents  $I_2 = \{0.4, 0.6, \dots, 1.6\}$  [A]

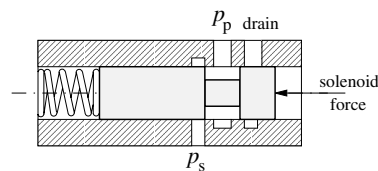


Figure 6.15: Primary valve

### static reconstruction

From Equations (6.24) and (6.25)  $A_1$  can be determined, provided the pressure differences over and flows through the valve are known. In the center region of the valve stem, the flows  $\Phi_{sp}$  and  $\Phi_{pd}$  are assumed to be equal ( $\Phi_{sp} = \Phi_{pd} =: \Phi_p$ ), since the throttling areas overlap, and leakflows are assumed to be negligible. The flow through the primary valve  $\Phi_p$  is determined as the difference of the pumpflow  $\Phi_{pump}$  and the flow through the secondary valve  $\Phi_{sa}$ , where  $\Phi_{pump}$  and  $\Phi_{sa}$  are reconstructed using the pump characteristic and the (inverted) secondary valve characteristic (Figure 6.14). The static reconstruction results are plotted in Figure 6.16 as dots, and show quite some noise. Furthermore, these results do not really connect to the results as they will be obtained in the dynamic reconstruction.

### dynamic reconstruction

Outside the region of orifice overlap, the throttling areas cannot be determined from static experiments, since then a static situation, fit for reconstruction purposes<sup>3</sup>, does not develop.

<sup>3</sup>That is, situations other than those where the pressure difference over the valve opening is approximately zero.

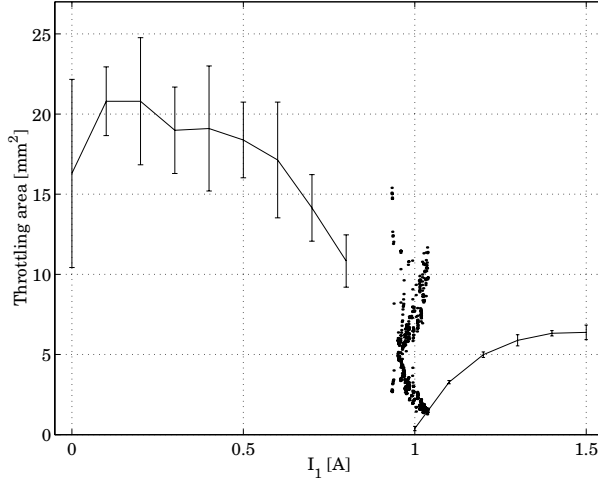


Figure 6.16: Characteristic of the primary valve; ‘dots’ are obtained with static reconstruction, solid lines with dynamic reconstruction; ‘bars’ indicate the standard deviation

Therefore, the mass conservation law (6.23) is used to derive the differential equation for the primary pressure:

$$k_{\text{oil}} V_p \dot{p}_p \approx \Phi_{\text{sp}} \quad \text{if } \dot{p}_p > 0 \quad (6.29)$$

$$\approx \Phi_{\text{pd}} \quad \text{if } \dot{p}_p < 0 \quad (6.30)$$

These approximations are valid under the assumption of no oil leakage and no axial pulley movement. In the proposed experiment where the variator is not running (so no significant axial pulley movement takes place) and  $p_s$  is kept constant, the primary solenoid current  $I_1$  is changed stepwise and remains constant after that, until the response of  $p_p$  settles. Define  $y = \sqrt{\Delta p}$  where  $\Delta p = p_s - p_p$  for  $\dot{p}_p > 0$  and  $\Delta p = p_p$  for  $\dot{p}_p < 0$ . Then for  $p_s$  constant, the following holds

$$|\dot{p}_p| = -2y \dot{y} \quad (6.31)$$

Substitution of (6.29), (6.30), (6.24) and (6.25) into (6.31) yields

$$y(t) = y(0) - \frac{c_f \sqrt{2/\rho_{\text{oil}}}}{2k_{\text{oil}} V_p} |A_1(I_1)| t \quad (6.32)$$

provided  $I_1$  is actually constant after the step, and  $A_1$  can be treated as a static function of  $I_1$ . Then,  $A_1$  can be determined as a function of  $I_1$  using (6.32).

In the experiment, the primary solenoid current  $I_1$  was changed stepwise<sup>4</sup>, either from 0 [A] to values between 1 and 1.5 [A] (rising stairs), or from 1.5 [A] to values between 0 and 0.9 [A] (falling stairs). Figure 6.16 shows the resulting mean values (solid line) and standard deviations (errorbars) for  $|A_1|$  as a function of  $I_1$ . The results for  $I_1 > 1$  [A] show a high reproducibility, while the results for  $I_1 < 0.9$  [A] do not. This may be due to any of the following reasons:

<sup>4</sup>As far as this is physically possible.

- since the electromagnetic solenoid can only exert positive forces, in the left part of Figure 6.16 (which was obtained from falling stairs) the dynamic system of valve stem and spring is limiting the rebound speed of the valve. Hence, the assumption that  $A_1$  is a static function of  $I_1$  is not valid here. In the right part of this figure though (obtained from rising stairs), the solenoid force is capable of moving the valve stem at a much higher rate than the spring can;
- all flows are assumed to be turbulent, hence  $\Phi \sim p^\alpha$ , where  $\alpha = 0.5$ . Especially, in the overlap region, where the flow is small, this assumption may not hold;
- the discharge coefficient  $c_f$  is assumed constant and equal to 0.6 [-];
- the oil density  $\rho_{oil}$  and compressibility  $k_{oil}$  are assumed constant and equal to, respectively,  $8.3 \cdot 10^2$  [kg/m<sup>3</sup>] and  $5 \cdot 10^{-9}$  [m<sup>2</sup>/N] (valid for ATF @ 80°C);
- for stationary situations (*i.e.*,  $\dot{p}_p \approx 0$ ), the overlap region is used. As mentioned before, the results for this part exhibit quite some noise, which is mainly due to model uncertainty. Besides, the primary valve displays severe hystereses, as can be seen from Figure 6.17. This figure gives a cross-section (of stationary points) of a number of experi-

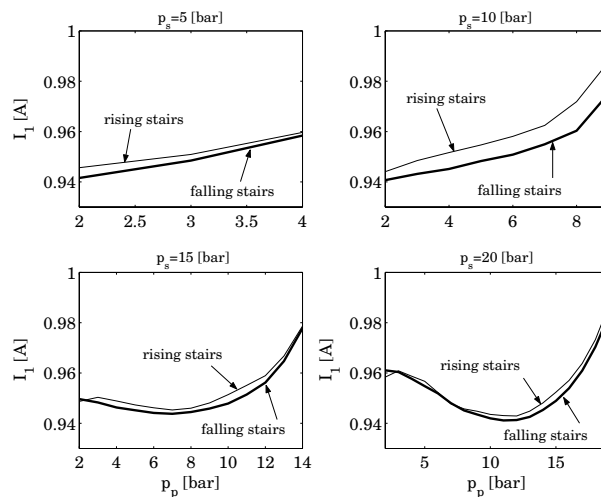


Figure 6.17: Primary solenoid current versus  $p_p$  and  $p_s$

ments where, for  $p_s = \{5, 10, 15, 20\}$  [bar],  $p_p$  was changed stepwise between 2 [bar] and  $p_s$ , along rising stairs followed by falling stairs. Although both pressure control currents have a dither signal, some remaining hysteresis is visible, especially for  $p_s = 10$  [bar]. Furthermore, for higher values of  $p_s$ , one value for the primary solenoid current  $I_1$  can result in two different pressures  $p_p$ . The primary pressure system is still controllable, since the situation shown is valid for stationary points only. However, it also demonstrates the impossibility of a feedforward in the primary pressure control loop. The reason for this may lie in the neglect of flow forces, the nature of which is insufficiently known. Also, the primary valve is designed as a flow control valve and not as a pressure control valve. In case  $p_p$  is to be controlled (which should at least be true if the primary



pulley is critical for belt slip), actually a *reducer valve* would be more appropriate than a flow control valve.

### 6.5.3 Roller vane pump

The pump in the P920 CVT is a roller vane pump of the binary displacement type. A fixed displacement pump designed to meet flow demands at low speeds, would generally deliver far too much flow at high rotational speeds. Therefore, (continuously) variable displacement pumps and binary pumps are seen to be used, attempting to better match the pump capacity to functional requirements across the expected operating speed range. Of course, variable displacement pumps will be better suited to match the actual demand than a binary pump, but are more complex and costly. In the P920 CVT, a pump with two modes, termed Double Sided (DS) and Single Sided (SS) mode, is used. The DS mode uses both outlets of the pump whereas in the SS mode one of the outlets is directly connected to the drain. The DS mode is used only at low pump speeds or at very high pressure demands, also see Appendix C. The pump is directly connected to the engine shaft. Apart from hydro-mechanical losses the pump flow is the product of the pump displacement and the pump speed. Figure 6.18 depicts the torque that is needed to drive the pump as a function of pump speed and pressure. Also shown are the practical operating regions for DS and SS mode. To obtain this figure, experiments were

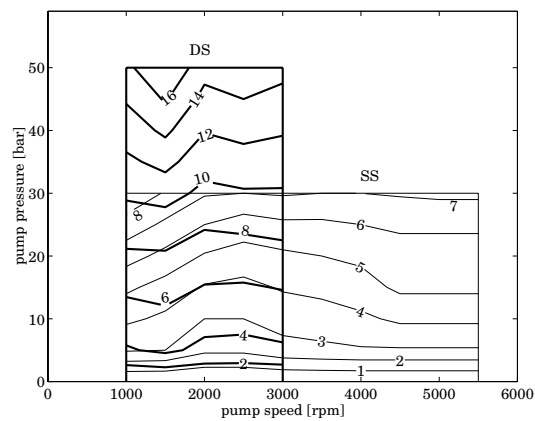


Figure 6.18: Contour plot of the torque needed to drive the pump as a function of pump pressure and speed; for DS (Double-Sided) and SS (Single-Sided) operation

performed on the P920 CVT at the test rig, where no clutches were engaged except from the torque converter lock-up clutch. The torques measured at the test rig also include additional losses from bearings and slipping clutches (Drive and Reverse).

### 6.5.4 Alternative hydraulic actuation

The overall dynamic behaviour of the CVT depends on the variator dynamics, on the CVT hydraulics and on the way the pressures are controlled. Before considering the controls, it is interesting to see how the topology of the hydraulic circuit with a given type and size of the pump imposes limitations on the CVT shift dynamics. Appendix C reports on such an

investigation which compares the potential of the hydraulic circuit depicted in Figure 6.19 with the original lay-out (Figure 6.12). The suggested alternative lay-out uses the secondary

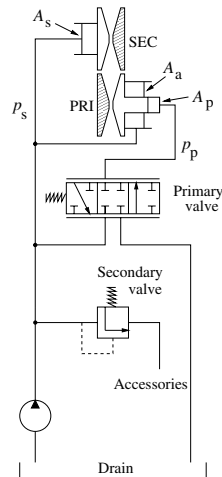


Figure 6.19: Alternative hydraulic system

pressure to generate a supplementary clamping force at primary side, by connecting it to an additional primary cylinder. Results show increased safety margins towards belt slip, while up- and downshifting times are substantially reduced. The suggested alternative hydraulic layout was not actually realized, hence the original hydraulic circuit is used throughout the remainder of this thesis. Nonetheless, the promising results presented in Appendix C argue for an experimental investigation into the potentials of the alternative hydraulic circuit.

Little information on structural design of hydraulic systems is found in literature. Most research is restricted to component sizing and matching [James and Vaughan, 1996] and the automation of this time-consuming task [Donne *et al.*, 1995].

## 6.6 ZI powertrain

In the ZI powertrain, the standard CVT is augmented with a flywheel that is linked to the variator by a planetary gear stage, see Figure 6.20. The two reductions to the planetary gear are the *annulus reduction*  $r_a$  from primary shaft to annulus, and the *carrier reduction*  $r_c$  from secondary shaft to carrier. Between the engine and the variator are the torque converter with lockup clutch  $C_l$ , and the DNR set with the reverse clutch  $C_r$  and the drive clutch  $C_d$ . When the DNR is in Drive position, only the drive clutch  $C_d$  is closed, whereas in the Reverse position,  $C_d$  is open and  $C_r$  is closed. The Neutral position is obtained by opening both clutches. A driveline model is needed to determine the torques that are exerted on the variator, and to analyze the consequences of the changed dynamics with regard to the CVT controller. For this purpose, models of the planetary gear and of the flywheel are required.

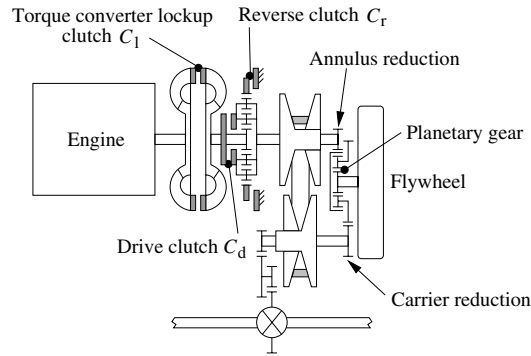


Figure 6.20: ZI drive train layout

### 6.6.1 Planetary gear

The flywheel is directly connected to the sun gear of the planetary set. The torque acting on the sun gear is indicated as  $T_f$ . Figure 6.21 schematically depicts the (helical) planetary gear set used in the ZI powertrain. The planetary gear set is kinematically characterized by the epicyclic gear ratio  $z$ , defined as the ratio of the number of teeth of the annulus and the sun gear. If the inertias of annulus, carrier and sun are neglected, and torque losses are assumed

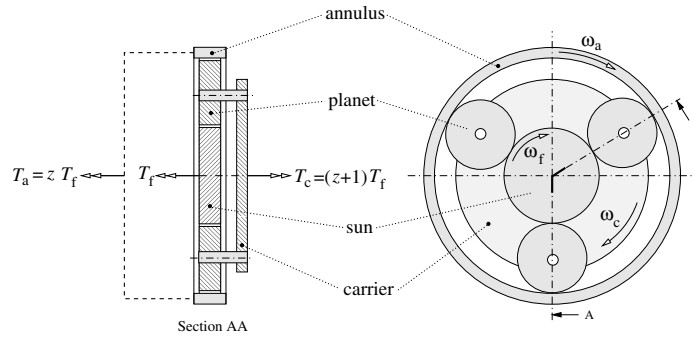


Figure 6.21: Planetary gear model

to be zero, the annulus torque  $T_a$  and carrier torque  $T_c$  are given by

$$T_a = z T_f \quad (6.33)$$

$$T_c = (z + 1) T_f \quad (6.34)$$

The speed of the sun gear  $\omega_f$  relates to the annulus speed  $\omega_a$  and the carrier speed  $\omega_c$  as

$$\omega_f = (z + 1)\omega_c - z\omega_a \quad (6.35)$$

With the reductions  $r_a = \omega_p/\omega_a$  and  $r_c = \omega_s/\omega_c$ , (6.35) can also be written as

$$\omega_f = \alpha_s \omega_s - \alpha_p \omega_p \quad (6.36)$$

where  $\alpha_s = (z + 1)/r_c$  and  $\alpha_p = z/r_a$ . Alternatively,  $\alpha_p$  and  $\alpha_s$  may be interpreted as the torque amplification factors from flywheel shaft to primary and to secondary shaft, respectively.

## 6.6.2 Flywheel

The flywheel is a steel disc with inertia  $J_f$ , running at subcritical speeds. Even without a vacuum system, the power losses due to air drag are small enough to neglect them [van Druten, 2001]. The flywheel is modeled as an inertia without any losses

$$T_f = J_f \dot{\omega}_f \quad (6.37)$$

## 6.6.3 Combined model for primary side of powertrain

For the analyses in the rest of this chapter, it can be assumed that the torque converter is locked and the DNR set is in Drive position. Consequently, when neglecting all compliances, the speeds of the engine, turbine and primary pulley are equal ( $\omega_e = \omega_t = \omega_p$ ) and the inertias of the engine ( $J_e$ ), turbine ( $J_t$ ) and primary pulley ( $J_p$ ) can be combined into one, resulting in Figure 6.22 (for the sign convention, refer to Figure 9.2). Then the torque  $T_p$ , exerted by the

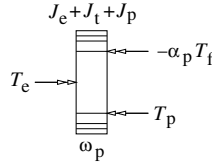


Figure 6.22: Model for determining  $T_p$

belt on the primary pulley, is determined as

$$T_p = T_e + \alpha_p T_f - (J_e + J_t + J_p) \dot{\omega}_p \quad (6.38)$$

## 6.7 CVT efficiency analysis and measurements

The power loss  $P_{\text{loss}}$  in a transmission T (see Figure 6.23) is the difference between the input power  $P_{\text{in}} = T_{\text{in}} \omega_{\text{in}}$  and the output power  $P_{\text{out}} = T_{\text{out}} \omega_{\text{out}}$ , i.e.,  $P_{\text{loss}} = P_{\text{in}} - P_{\text{out}} > 0$ .  $P_{\text{loss}}$  can be divided into *speed loss* and *torque loss*. Arithmetically, losses can be lumped into either of the two, though a torque loss description is usually preferable for modeling and simulation purposes. The practical definition of speed loss refers only to *integral slip*, i.e., slip which

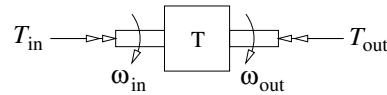


Figure 6.23: Torque and speed definitions for transmission T

accumulates with the number of shaft revolutions. Therefore, *momentary slip* can cause power loss, but all power loss will be attributed to torque loss if the integral slip is zero. This is the

case in all form-closed transmissions, such as toothed gear transmissions. Also, power losses at locations outside the transmission path to the output shaft (such as bearing losses, power-take-off), do not induce speed loss and are therefore treated as torque loss. In force-closed transmissions, both types of losses occur.

### 6.7.1 Power transmission in the variator

When analyzing the power transmission in the variator, it is useful to realize that in most cases (all except the UR mode, see Figure 6.6), the larger part of the power is transmitted by the compression force between the segments, but some power is also transmitted by the bands, because of the friction between the segments and bands and between adjacent bands. The free body diagram of the variator, assuming that the belt runs at perfect circles, is depicted in Figure 6.24, where  $R_p$  and  $R_s$  denote the orbit radii of the rocking edges of the segments at primary and secondary side, and  $\Delta R$  is the distance between the orbit radius of the bands and that of the rocking edges.  $S_{sl}$  and  $S_{ti}$  denote the tension forces, and  $Q_{sl}$ ,  $Q_{ti}$  the compression

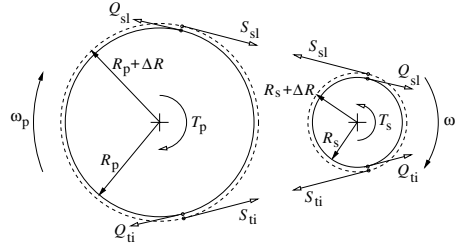


Figure 6.24: Free body diagram of the variator

forces at the slack and the tight side of the belt. Normally ( $\omega_p > 0$ ),  $Q_{ti} = 0$  except for very low torques and  $r_{cvt} < 1$  (UR, see Figure 6.6). Because of end play in the line of segments, either  $Q_{sl}$  or  $Q_{ti}$  must be zero. The resulting expressions for the torques  $T_p$  and  $T_s$  in the primary and secondary shaft, respectively, are

$$T_p = (Q_{sl} - Q_{ti})R_p + (S_{ti} - S_{sl})(R_p + \Delta R) \quad (6.39)$$

$$T_s = (Q_{sl} - Q_{ti})R_s + (S_{ti} - S_{sl})(R_s + \Delta R) \quad (6.40)$$

The angular speeds  $\omega_p$  and  $\omega_s$  of the primary and secondary pulley correspond to the angular speeds of the segments (assumed to run at perfect circles) if the segments do not slip with respect to the pulley. Then  $\omega_p R_p = \omega_s R_s$  and it is readily seen that the power loss due to slip between the bands and the segments is given by

$$P_{loss} = \omega_p (S_{ti} - S_{sl})(1 - r_{cvt})\Delta R \quad (6.41)$$

If  $S_{sl} = S_{ti}$  or if  $r_{cvt} = 1$  this power loss is zero. Otherwise, the signs of  $S_{ti} - S_{sl}$  and of  $1 - r_{cvt}$  are equal if  $\omega_p > 0$  (see Figures 6.5–6.7), so  $P_{loss} > 0$ . Actually, this slip occurs between the innermost band and the segment shoulder and between adjacent bands, on the pulley with the smaller orbit radius only (see Section 6.3.2). In the remainder of this (qualitative) analysis, the friction loss between adjacent bands, although not necessarily smaller, is neglected for simplicity. If this friction is to be included, the reasoning for the contact between the segments and the innermost band can easily be adopted for the contacts between the bands.

### 6.7.2 Speed and torque losses

Besides the slip between segments and bands, deformations—especially of the pulleys and the pulley shafts—contribute to the power losses in the variator. The slip between the segments and the pulleys due to deformations in circumferential direction, known as *micro-slip*, is small and neglected for now. Likewise, the micro-slip between segments and bands, and between adjacent bands is negligible, especially compared to the gross slip between segments and bands on the pulley with the smaller belt radius. Pulley tilting resulting from bearing play and -compliance has about the same effect as pulley deformation.

Figure 6.25 shows an abstraction of the overall situation, by actually having two parallel paths transmit the power. The left part of the (virtual) transmission can be seen as a pure pushbelt transmission, and reflects the power transmitted by the segments only. It is assumed that some frictionless construction holds the segments together. This part of the power transmission has losses due to deformations, mainly. The actual friction losses between the inner

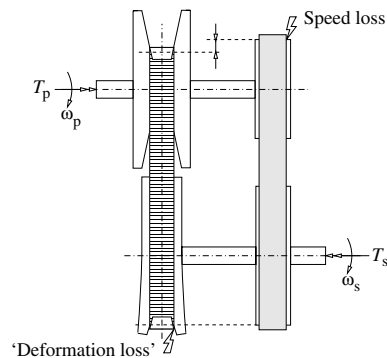


Figure 6.25: Intuitive representation of variator losses, depicted for  $r_{cvt} < 1$

bands and the segment shoulders on the pulley with the smaller belt radius, is accounted for by the right part of the virtual transmission, which is simply a flat belt transmission.

#### slip loss

In Figure 6.25, the slip between bands and segments is lumped to the primary side, by giving the flat belt transmission on the right side of the figure a larger pulley radius than the orbit radius of the segments on the pushbelt transmission on the left side. Therefore, the flat belt (bands) will lag behind the faster pulley. For this example, where  $r_{cvt} < 1$ , the direction of the slip is such that the bands transmit a positive torque. If  $r_{cvt} > 1$ , the bands counteract the torque transmission by the segments. In the latter case, the segments must transmit extra torque in order to compensate for the negative torque transmitted by the bands (known as *blind* torque or power). The power loss in the flat belt transmission can be expected to increase because of the increased normal force exerted on the bands and hence friction loss, on the one hand. On the other hand, the increased power transmitted by the segments, can be expected to be accompanied with increased losses. The magnitude of the slip speed between bands and

segments, relative to the segment speed  $v_c$ , can be determined as

$$\left| \frac{v_b - \omega_p(R_p + \Delta R)}{v_c} \right| = \frac{\Delta R |1 - r_{cvt}|}{R_p} \quad (6.42)$$

$$\approx \frac{\Delta R \pi}{L - 2a} \left| \frac{1}{r_{cvt}} - r_{cvt} \right| \quad (6.43)$$

where the approximate expression is obtained using (6.3). From (6.43) it is seen that the slip speed is symmetrical around  $r_{cvt} = 1$ . In practice, the maximum relative slip speed is in the order of 3%.

### losses due to deformation

The losses in the pushbelt transmission (left hand side of Figure 6.25) are mainly due to deformation and tilting of the pulleys, and bending of the shaft between the pulley halves. In the exaggerated situation depicted in the left of Figure 6.25, the losses due to deformation are attributed to the pulley with the larger belt radius. In practice both pulley sets (sheaves and shaft) will deform, although the deformations of the pulley set with the larger belt radius will be much larger, except for CVT speed ratios near  $r_{cvt} = 1$ . The ‘combined’ deformation of the two pulley sets will be at its smallest for  $r_{cvt} = 1$ , since the pulley sheave compliance—not the compliance associated with shaft bending—increases more than proportionally with the orbit radius.

Both deformation and tilting open up the pulley wedge, causing the belt to be pulled towards a smaller orbit radius. The wedge actually opens up because the resulting clamping force due to oil pressure in the hydraulic cylinders acts in the pulley’s center of rotation, while the normal forces between the segments and the pulley all act outside the pulley center. If these normal forces for simplicity are assumed to be uniform along the angle of wrap, the center of the combined normal forces will be somewhere near the point indicated by ‘Center of normal force’ in Figure 6.26. Therefore, the belt will be wedged in farthest halfway along the angle of wrap. In the situation in Figure 6.26 the actual path of the belt (*i.e.*, the neutral line, as defined in 6.3.2) is drawn as a solid line. The figure represents a stationary situation, *i.e.*,  $\dot{r}_{cvt} = 0$ , and is not to be mistaken for a transient one. The dotted circles correspond to the minimum and the maximum value that the orbit radius attains while negotiating the angle of wrap.

Along this path, five types of arrows are drawn. The deformation of the segments is neglected, so the magnitude of the longitudinal speed  $\|\vec{v}_c\|$  of the segments must be equal all along the belt path, and is indicated (at three points) by the bold solid arrows with closed pointers. The circumferential speed  $\vec{v}_u$  of the pulley is drawn in two points along the path, as dashed arrows. It is assumed that  $\|\vec{v}_u\| \geq \|\vec{v}_c\|$  everywhere on the angle of wrap, and that  $\vec{v}_u = \vec{v}_c$  at the smallest orbit radius. The speed difference  $\vec{v}_u - \vec{v}_c$  is depicted by the dotted arrows with closed pointers. The adopted Coulomb friction model states that the force, exerted on the segments in the contact area, will be directed along these dotted arrows. Finally,  $\vec{v}_u - \vec{v}_c$  can be decomposed into transversal and longitudinal (belt) components (as defined earlier in Figure 6.3). The transversal component is indicated by the bold solid arrows with open pointers. The longitudinal component is drawn at only one point as a dotted arrow with an open pointer.

From this representation, two types of losses can be identified. First, the friction force exerted on the segments in transversal direction is of no use for the transmission of torque. Still, these transversal components cause a moment about the pulley axis (all in a direction that

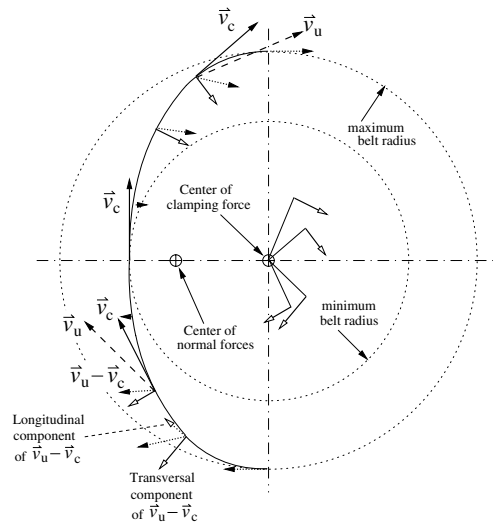


Figure 6.26: Power loss due to pulley deformation

must be balanced by a *positive* input torque), and hence a loss torque. Second, the friction force directed in longitudinal direction is useful for torque transmission but is also accompanied by slip. This constitutes an additional speed loss.

### 6.7.3 Efficiency measurements

Experiments were performed at the test rig, described in Appendix A. In these experiments the transmission temperature was kept between 78 and 82°C, the TC was locked, and the DNR was in Drive position. Torques and speeds were measured at the shaft of motor II and at the drive shaft. The pulley clamping forces were regulated in accordance with (B.34), whereas the pump pressure was restricted to a minimum of 6 [bar], although a minimum of 4 [bar] is feasible. This influences the pump torque, as well as the belt loss corresponding to (over)clamping at both pulleys. As a consequence, the measurements include power losses due to the pump, reverse clutch drag loss, several bearing losses, and final drive losses, besides the losses within the variator itself. Other than opening the drive clutch to (more or less) exclude the variator and final drive losses, no means were available to measure the losses of the various components separately.

The torque measured with the drive clutch open, was depicted in Figure 6.18, and can also be expressed as the *hydraulic efficiency*  $\eta_{\text{hydr}} = (T_e - T_{\text{pump}})/T_e$ . It is stressed that this efficiency definition disregards the fact that the pump torque is actually put to good use in supplying hydraulic power, and is therefore completely different from the *pump efficiency*, i.e., (flow  $\times$  pressure)/(speed  $\times$  torque). The hydraulic efficiency is depicted in Figure 6.27, as a function of  $T_e$  and  $r_{\text{cvt}}$ , and for vehicle velocities  $v_v = \{25, 60, 100, 150\}$  [km/h]. It is chosen to represent the pump loss in this form (besides Figure 6.18) to reveal the influence of the pump on the total CVT efficiency for clamping pressures corresponding to various input torques  $T_e$ , and for various vehicle speeds. The minimum and maximum engine (motor II) speed (800 and 5000 [rpm], respectively) impose limits for  $r_{\text{cvt}}$ , which is why not all CVT ratios can be



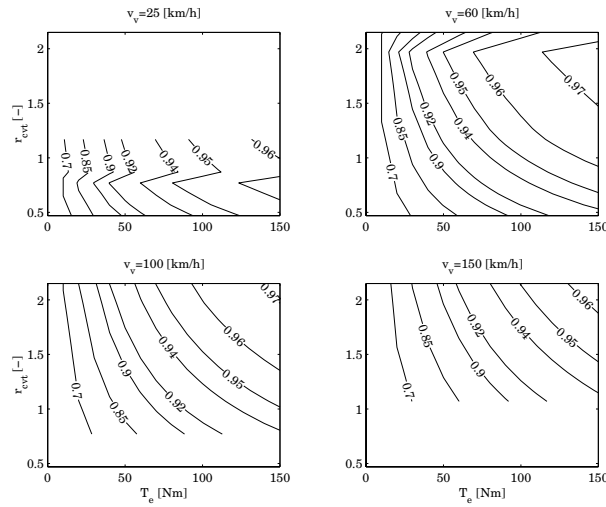


Figure 6.27: ‘Hydraulic efficiency’  $\eta_{\text{hydr}}$  as a function of  $T_e$  and  $r_{\text{cvt}}$ , for  $v_v = \{25, 60, 100, 150\}$  [km/h]

reached. The kink in the upper two plots corresponds to the point where the pump switches from single to double sided (where the pump speed is 1200 [rpm]) causing the pump efficiency to drop. The efficiency of the CVT including the final drive, with the DNR in Drive and the TC locked, is referred to as the *overall CVT efficiency*  $\eta_{\text{cvt}} = \frac{T_w \omega_w}{T_e \omega_e}$ . Deducting the pump losses from the overall CVT efficiency measurements, gives an indication of the efficiency of the rest of the CVT, *i.e.*, of the variator and the final drive, see Figure 6.28. The latter efficiency is referred to as the *mechanical efficiency*  $\eta_{\text{mech}}$ . Consequently,  $\eta_{\text{cvt}} = \eta_{\text{pump}} \cdot \eta_{\text{mech}}$ . This procedure is not entirely correct since the pump torque measurements (DNR in Neutral) include drag losses of both clutches whereas the overall measurements (DNR in Drive) include drag loss of the reverse clutch only, even though the slip speed of the reverse clutch in the latter case will be higher for a given  $\omega_e$ . Nevertheless, the clutch drag losses are always small compared to the other losses. Figure 6.28 depicts the mechanical efficiency  $\eta_{\text{mech}}$  versus the CVT speed ratio  $r_{\text{cvt}}$  and the turbine torque  $T_t$ , for various vehicle speeds  $v_v$ . The turbine torque  $T_t$  is used as input instead of  $T_e$ , since  $T_e$  is generally different from  $T_t$ .

As Figure 6.28 shows, the efficiency  $\eta_{\text{mech}}$  of the CVT without pump reaches values up to 98% for ‘medium’ torque ( $T_t = 90$  [Nm]), speed ( $v_v = 100$  [km/h]) and ratio ( $r_{\text{cvt}} = 1$ ). The variator efficiency is always highest for  $r_{\text{cvt}} = 1$ , which makes sense in light of the discussion in the previous section. However, depicting efficiency as a function of  $T_e$  and  $r_{\text{cvt}}$  gives a somewhat distorted view. For instance, consider a situation where  $v_v = 60$  [km/h],  $T_t = 40$  [Nm] and  $r_{\text{cvt}} = 2$ , resulting in a mechanical efficiency of around 88%. If instead of  $r_{\text{cvt}} = 2$ , it is chosen to operate the CVT at  $r_{\text{cvt}} = 1$ , the turbine torque  $T_t$  should be approximately halved to maintain the same output power. For  $r_{\text{cvt}} = 1$  and  $T_t = 20$  [Nm] the mechanical efficiency is again circa 88%.

For analysis and implementation purposes, it is therefore useful to represent the overall CVT efficiency as a function of  $r_{\text{cvt}}$  and the wheel power  $P_w$ , instead of the input torque  $T_t$ . Figure 6.29 depicts the overall efficiency  $\eta_{\text{cvt}}$  of the CVT, versus the *wheel power*  $P_w$ , for  $r_{\text{cvt}} =$

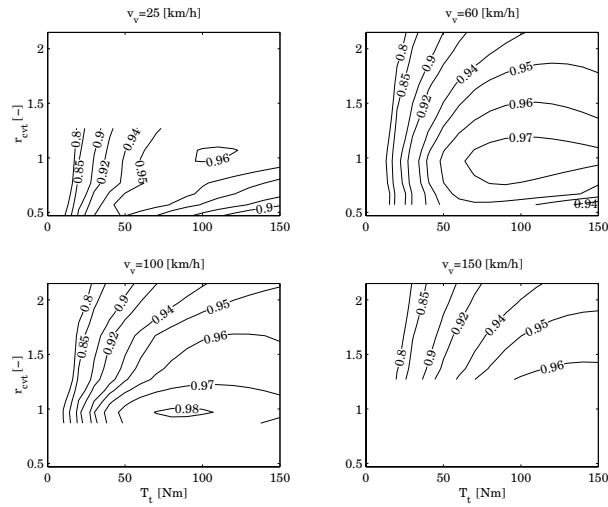


Figure 6.28: Mechanical efficiency  $\eta_{\text{mech}}$  as a function of  $T_t$  and  $r_{\text{cvt}}$ , for  $v_v = \{25, 60, 100, 150\}$  [km/h]

$\{r_{\text{cvt,min}}, r_{\text{cvt,max}}\}$ , and for various vehicles speeds  $v_v$ . The minimum and maximum value for

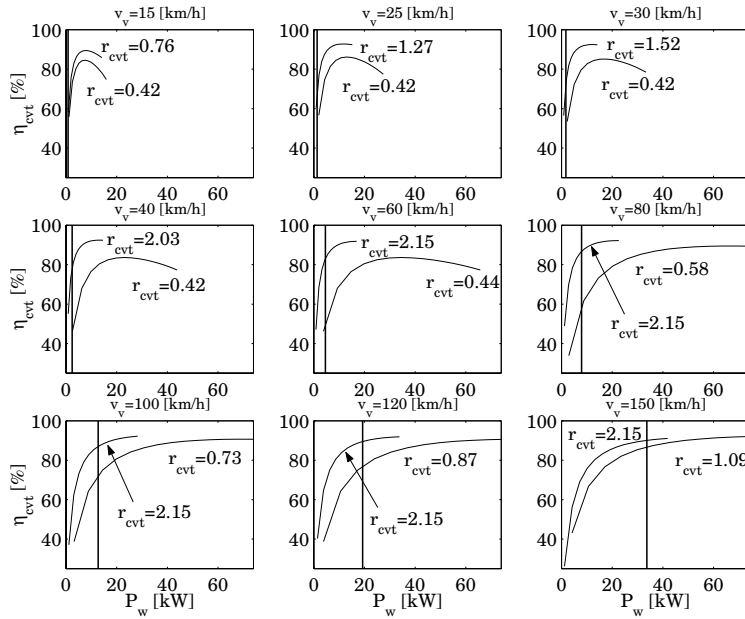


Figure 6.29: Overall transmission efficiency  $\eta_{\text{cvt}}$  versus  $P_w$ ,  $r_{\text{cvt}}$  and  $v_v$

$r_{\text{cvt}}$  are imposed by the maximum and minimum engine speed, and the ratio limitations of the CVT. The vertical bold lines indicate the power needed to maintain the vehicle speed (no hill climbing), written above the figure. Especially at lower vehicle speeds, the efficiency curves do not cover the entire power range, because the (emulated) engine can not reach maximum speed. From Figure 6.29 it is seen that efficiency rises with increasing CVT ratio. For vehicle speeds beyond 80 [km/h], the efficiency of the CVT also rises with increasing wheel power. Below 80 [km/h], the efficiencies increase with  $P_w$  up to some point, and then decrease again. The power level corresponding to a stationary vehicle speed (vertical line) is always below the power level where the efficiency is highest. Figure 6.30 illustrates the influence of  $r_{\text{cvt}}$  in more detail, for  $v_v = 80$  [km/h], and for various wheel power levels. The vertical lines indicate

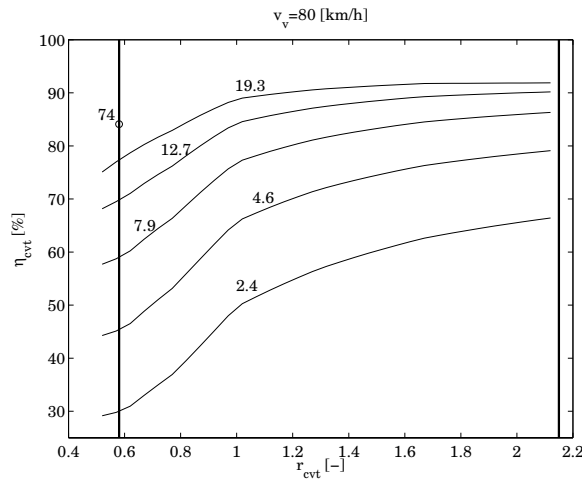


Figure 6.30: Transmission efficiency  $\eta_{\text{cvt}}$  versus speed ratio  $r_{\text{cvt}}$  at  $v_v=80$  [km/h] for  $P_w = \{2.4, 4.6, 7.9, 12.7, 19.3, 74\}$  [kW]

the minimum and maximum CVT ratio possible. The power level  $P_w = 7.9$  [kW] corresponds to a stationary vehicle speed  $v_v = 80$  [km/h]. The circle at the left vertical line, indicates the efficiency at  $P_w = 74$  [kW], *i.e.*, the maximum engine power of the test vehicle. The actual input power in this point must obviously be higher than this, due to losses, and can be realized at the test rig, but not in the vehicle. Furthermore, the maximum power can only be delivered in one CVT ratio, in this case  $r_{\text{cvt}} \approx 0.58$ . The upper curve relates to  $P_w = 19.3$  [kW] (corresponding to a stationary vehicle speed of 120 [km/h]), which is more or less the maximum power level that can be realized in all achievable CVT ratios, for  $v_v = 80$  [km/h]. It is seen that the influence of  $r_{\text{cvt}}$  on the efficiency is large for low values of  $P_w$ , but gets smaller with higher  $P_w$ , especially for  $r_{\text{cvt}} > 1$ . For instance, for  $P_w = 19.3$  [kW],  $\eta_{\text{cvt}}$  reduces from around 92 to 89%, when decreasing  $r_{\text{cvt}}$  from  $r_{\text{cvt}} = r_{\text{od}}$  to  $r_{\text{cvt}} = 1$ .

Especially the observation that for a certain vehicle speed  $v_v$  and wheel power  $P_w$ ,  $\eta_{\text{cvt}}$  increases with  $r_{\text{cvt}}$ , needs some elucidation. For example, compare two situations where for  $v_v = 80$  [km/h], the stationary wheel power  $P_w = 7.9$  [kW] is delivered in  $r_{\text{cvt}} = 1$  and  $r_{\text{cvt}} = 2$ , respectively. First of all, for both CVT ratios the secondary pulley will be critical with respect to belt slip. Therefore, the minimum pressure needed for torque transmission decides the pump pressure. Using the clamping strategy according to (B.34), the minimum clamping

force increases less than proportionally with the primary belt torque  $T_p$ . Even if the clamping strategy were proportional to  $T_p$ , the ratio  $T_p/R_p$  would increase with  $r_{cvt}$  approximately (using (6.3)) according to  $(r_{cvt} + 1)T_s\pi/(L - 2a)$ , which is less than proportional (since  $T_s$  is approximately constant).

On the other hand, for stationary vehicle speeds—where efficiency is most important—the pressures required for torque transmission are often so low that the secondary valve saturates at its maximum opening towards the accessories. For this opening the pressure drop over the valve and consequently the pump pressure, is determined mainly by the flow through the valve. For higher  $r_{cvt}$ , the pump speed and therefore the pump flow is lower, resulting in a slightly lower pump pressure. In the range below 6 [bar], the influence of pump speed on pump torque is small. Concluding, the pump torque will be comparable for  $r_{cvt} = 1$  and  $r_{cvt} = 2$ , but the *power loss* will be about twice as large for  $r_{cvt} = 1$ .

Because speeds and torques in the final drive are the same for  $r_{cvt} = 1$  and  $r_{cvt} = 2$ , power losses in the final drive will be no different. Except for the region near  $r_{cvt} = 1$  (where power losses due to slip between bands and segments as well as pulley deformations are minimal), the efficiency of the variator for a certain output power is hardly influenced by  $r_{cvt}$ , since most of the contour lines in Figure 6.28—at least above  $r_{cvt} = 1$ —move towards higher torques for higher  $r_{cvt}$ . All in all, the pump loss will be dominant and cause the overall efficiency of the CVT to be larger for higher  $r_{cvt}$ , at least for low to average  $P_w$ . Because the required pump pressure will become substantially larger than 6 [bar] for high  $P_w$ , the difference in efficiency for high and low  $r_{cvt}$  becomes smaller for increasing  $P_w$ .

#### 6.7.4 Empirical efficiency model

The efficiency of a transmission can be formulated in different ways. An *additive* power loss representation  $P_{out} = P_{in} - P_{loss}$ , with  $P_{loss} > 0$ ,  $P_{in} = T_{in}\omega_{in}$  and  $P_{out} = T_{out}\omega_{out}$  according to Figure 6.23, is preferable over a *multiplicative* representation, *i.e.*,  $P_{out} = \eta_T P_{in}$ , for the following reason.  $\eta_T$  is Although the multiplicative formulation may be more intuitive for a majority of situations (which is why it was used in presenting the experimental efficiency results), if the power flow reverses,  $\eta_T$  should also be reversed or else it loses all meaning.

Having decided on using the additive formulation, for implementation one must choose how to divide the power loss between torque loss and speed loss. In form-closed transmissions all losses are due to torque losses whereas in force-closed transmissions, such as the pulley type variator, both types of losses will generally exist. Hence, a combination of the two seems to be the most general, but also the least practical for implementation. Lumping the two types of losses into either one of them results in Figure 6.31, depicting both an additive torque and an additive speed loss model. In both representations, the transmission T is lossless. A similar formulation is presented in [Beccari and Cammalleri, 2001], though less general in that it applies only for a pushbelt CVT where the belt runs at perfect circles. In the torque loss model, all power losses are attributed to a torque loss  $T_{loss}$  that acts at a node without speed loss. In the speed loss model, all power losses are lumped into a speed loss  $\omega_{loss}$ , *i.e.*, a slip speed as in a clutch. For implementation, the torque loss model is best suited. Therefore the entirely empirical efficiency model used for simulations, is formulated in terms of a torque loss.  $T_{loss}$  is determined as the sum of the pump torque  $T_{pump}$  and the mechanical torque loss  $T_{mech}$ , or

$$T_{loss} = T_{pump}(p_s, \omega_e, i_{pump}) + T_{mech}(T_{in}, v_v, r_{cvt}) \quad (6.44)$$

The pump torque (with  $i_{pump}$  the pump mode, SS or DS) can be obtained from Figure 6.18, while the mechanical torque loss  $T_{mech}$  is obtained from the measurements presented in Sec-

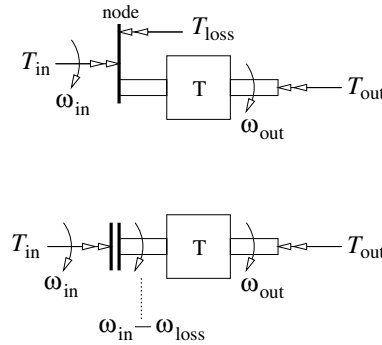


Figure 6.31: General torque and speed loss models

tion 6.7.3.  $T_{in}$  equals  $T_t$  in stationary situations and is to be corrected with inertia effects for in-stationary situations. In the implementation (in Part III of this thesis and in [Serrarens, 2001]),  $T_{in}$  is then corrected with the resulting loss torque  $T_{loss}$  and possibly combined with the torque stemming from the flywheel, to obtain the net input torque for the lossless transmission. Note that this input torque is generally different from the primary belt torque  $T_p$ .

## 6.8 ZI-CVT load envelope

This section evaluates the effects of the addition of the flywheel in the ZI powertrain on the torque that is exerted on the belt, on the one hand, and the measures that should be taken with regard to the powertrain controller in order to limit this torque, on the other (see Section 6.8.1). These insights can then be used for the design of the transmission and of the powertrain controller, treated in [van Druten, 2001] and [Serrarens, 2001], respectively. Section 6.8.2 discusses the influence of the flywheel inertia on the variator dynamics, and the resulting implications for local CVT control. The design of the local CVT controller will be discussed in the following chapter.

### 6.8.1 Impact on transmission and powertrain controller design

In the ZI powertrain, the flywheel functions as a torque assist in transient situations. As such, it drastically changes the dynamic properties of the driveline. In this section, an indicative analysis is performed into the effects of the load envelope on transmission design on the one hand and on the design of the CVT setpoint generator (as is treated in [Serrarens, 2001]) on the other. For this purpose, a load envelope was deduced from an arbitrary but fairly dynamic driving cycle, that was performed with the test vehicle on a test circuit, using (some of) the CVT and powertrain control strategies as they will be obtained in the following chapter and in [Serrarens, 2001], respectively. This makes it really an a posteriori investigation that is useful for validating some of the decisions that were made in the design process, as well as for formulating guidelines for further design iterations.

The drive cycle is depicted in the upper left plot of Figure 6.32. The other three plots show histograms of the CVT speed ratio, the engine speed and the accelerator pedal position, respectively. In the cycle, a number of semi- and full kickdowns was performed. Although

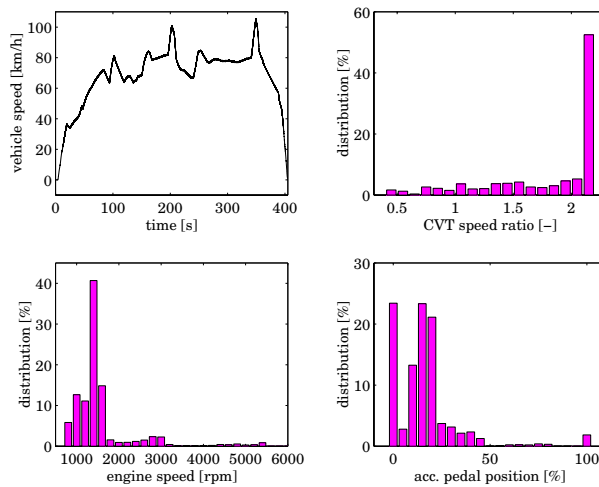


Figure 6.32: Vehicle speed (upper left) during an arbitrary driving cycle, and corresponding histograms of the CVT speed ratio (upper right), engine speed (lower left) and accelerator pedal position (lower right)

fairly dynamic, the CVT is in overdrive ratio half of the time. Also, the corresponding engine speeds are grouped in the vicinity of 1400 [rpm], though some excursions into the 5500 [rpm] range are visible. These high engine speeds are directly related to the full kickdowns, visible as 100% accelerator pedal position in the lower right plot. It is noted that most of the (stationary) driving is accomplished using less than 25% pedal depression while, except for an occasional kickdown, the accelerator pedal position hardly ever goes beyond 45%.

Important for the design of the variator and especially of the belt is the maximum torque that is to be exerted on the belt. Of course, it is the absolute value and not so much the direction of the torque that determines the belt requirements, although the belt itself is not symmetrical. The upper plot of Figure 6.33 shows histograms of the absolute belt torque acting at primary side, for three different situations. The left bar corresponds to the ZI powertrain and is indicated by 'ZI'. The middle bar, indicated by 'CVT' depicts the situation for the same powertrain but without the extra flywheel. The right bar, indicated by 'engine', shows the torque distribution in case the flywheel inertia and all the primary sided inertias are zero, and is included for comparison, only. The global picture is rather similar for all three situations, although the ZI powertrain displays some torques in the range from 150 to 180 [Nm], where the others do not. To get an idea of how disturbing the latter can be, a better indication of the force that is actually exerted on the belt in circumferential direction is given by  $F_b = \frac{|T_p|}{R_p}$ . Obviously, this net circumferential force can be composed of the compression force between segments and the tensile force in the bands, in numerous ways. Even without slip between the bands and the segments, *i.e.*,  $S_{sl} = S_{ti}$  *cf.* Figure 6.24, the tension in the bands can be arbitrarily large. Therefore,  $F_b$  is strictly a lower bound for the actual band tension. This lower bound is actually obtained if the band tension at the slack side of the belt exactly equals the compression force in the segments. In practical high torque situations, the band tension may exceed the compression force by a factor of 1.5 to 2 (values determined with the reference model from Section 6.3.2). Still, the trends in  $F_b$ , shown in the lower plot of Figure 6.33 and summarized in

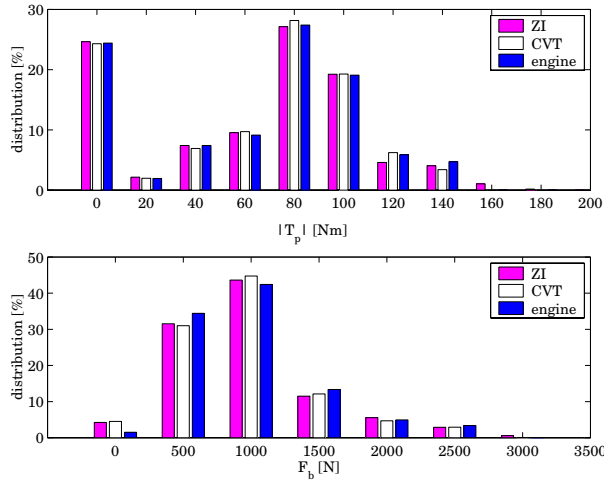


Figure 6.33: Load histograms for 'ZI', 'CVT' and 'engine', corresponding to Figure 6.32

Table 6.1, can be thought to be representative. Although the overall trends in  $F_b$  are similar for

	mean( $T_p$ ) [Nm]	min( $T_p$ ) [Nm]	max( $T_p$ ) [Nm]	mean( $F_b$ ) [kN]	max( $F_b$ ) [kN]
ZI	69.0	-161.3	196.1	0.92	3.42
CVT	68.3	-39.5	148.6	0.91	2.64
engine	69.2	-32.1	148.3	0.92	2.73

Table 6.1: Load envelope comparison, corresponding to Figure 6.32

'ZI', 'CVT' and 'engine', the extrema that occur during the driving cycle are quite a bit higher for the ZI powertrain. This can be explained when looking at the primary belt torque  $T_p$ , if the TC is closed and the DNR is in drive position. Using (6.36)–(6.38),  $T_p$  can be obtained as

$$T_p = T_e + \dot{r}_{\text{cvt}} \omega_s \frac{J_e + J_t + J_p + \alpha_p^2 J_f}{r_{\text{cvt}}^2} - \dot{\omega}_s \left( \frac{J_e + J_t + J_p + \alpha_p^2 J_f}{r_{\text{cvt}}} - \alpha_p \alpha_s J_f \right) \quad (6.45)$$

Besides the engine torque  $T_e$ , also the CVT shift rate and the vehicle acceleration (via  $\dot{\omega}_s$ ) influence the belt torque. The shift rate term generally is dominant over the  $\dot{\omega}_s$  term, mainly because  $\dot{r}_{\text{cvt}} \omega_s$  can easily be an order of magnitude higher than  $\dot{\omega}_s$ . Only when  $\dot{r}_{\text{cvt}} = 0$ , the influence of the  $\dot{\omega}_s$  term will become noticeable. For instance, in a full throttle acceleration from standstill, the belt torque will be lowered in both 'ZI' and 'CVT' although more substantially in the 'ZI' system (up to 9% lower belt torque with respect to 'CVT', for  $r_{\text{cvt}} = r_{\text{ud}}$ ).

Furthermore, both terms are a function of  $r_{\text{cvt}}$  and the  $\dot{\omega}_s$  term even changes sign for 'ZI', see Figure 6.34. Both in 'ZI' and 'CVT', upshifting increases the belt torque, especially for lower CVT ratios. For  $r_{\text{cvt}} = r_{\text{ud}}$ , this sensitivity is even 2.5 times higher for 'ZI' than for 'CVT'. Exactly the latter must be taken into account when performing an upshift starting at low CVT ratios. Such situations occur when after a kickdown acceleration, the accelerator pedal is

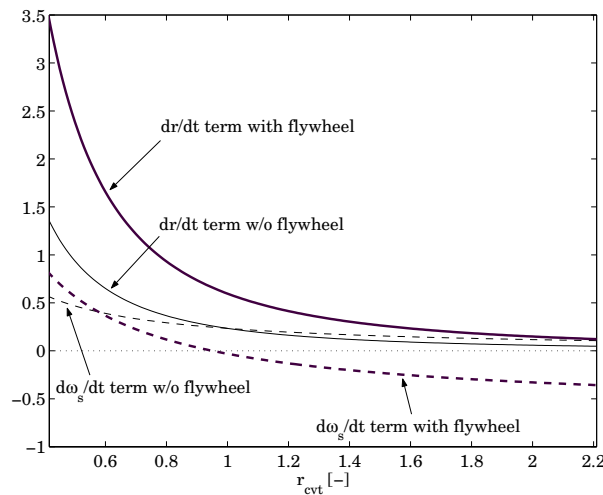


Figure 6.34: Terms corresponding to  $\dot{r}_{cvt}$  and  $\dot{\omega}_s$ , see Equation (6.45)

abruptly released. If the powertrain controller can limit the upshift speed on pedal backout, it is expected that the incidental higher loads can be entirely eliminated.

## 6.8.2 Impact on CVT controller design

The variator tends to shift down if the torque level increases. This was referred to as ‘ratio droop’ by [Vahabzadeh and Linzell, 1991]. Looking at Figure 6.8, this is easily explained since  $\kappa$  increases with both  $\tau'_s$  and  $r_{cvt}$ . Hence, if the actual ratio of  $F_p$  and  $F_s$  remains the same, an increase in torque will cause the variator to stabilize at a lower  $r_{cvt}$ .

The physical background for the dependency of  $\kappa$  on  $r_{cvt}$ , as it is also reflected by the first term in Equation (6.9), is rather intuitive. The dependency of  $\kappa$  on  $\tau'_s$  is a little more involving, therefore only a hint is given. Consider a situation where power is transmitted from the primary to the secondary pulley, and where subsequently the primary torque  $T_p$  is increased. This enlarges  $\tau'_s$ , if  $F_s$  is assumed to be (approximately) constant, as are the friction coefficients and the speeds. Then the compression force between the segments at the exit of the primary pulley, and hence the tension forces in the bands, will also increase. The increased tension force results in a higher normal force between bands and segments. This normal force is balanced by the radial components of the axial clamping force and those of the compression force between the segments (see Figure 6.4). In the idle arc at the primary pulley (no compression force), all of the balancing force must come from an increase in axial clamping force. At the secondary pulley, along the entire angle of wrap but especially on the idle arc, the compression force between segments contributes in balancing the normal force that acts on the segment shoulders. Therefore, the primary clamping force must rise relatively more than the secondary, and so  $\kappa$  rises. This effect diminishes, when the idle arc at primary side vanishes ( $\tau'_s \uparrow 1$ ), which in turn causes the slope of  $\kappa$  to decrease with increasing  $\tau'_s$ .

The ratio droop has a stabilizing effect on the variator ratio control system, because a downshift will cause the torque exerted on the belt to drop due to the inertia effect, as reflected by the  $\dot{r}_{cvt}$  term in Equation (6.45). In the ZI powertrain, the torque that acts on the belt is



generally different from that in a conventional CVT powertrain, *unless* the flywheel speed is constant. The latter is true when all speeds are stationary. As discussed earlier, the belt torque in the ZI powertrain will generally be lower during the downshift and higher during the upshift, as compared to the conventional CVT powertrain. The stabilizing effect resulting from the ratio droop is therefore even more prominent for the ZI powertrain. It also offers some degree of self-protection against high torques due to shifting, since an increased torque caused by upshifting tends to counteract the upshift and hence will somewhat limit the belt torque. Obviously, if the CVT ratio setpoint in combination with the CVT controller has a sufficiently high bandwidth, the belt torque may still attain high values, as was seen in the previous section. However, also in downshifts, where belt torque is usually not a limiting factor, the stabilizing effect of the variator-flywheel combination will limit the closed-loop bandwidth, given the limitations of the actuators. To quantify these effects, the differential equation (6.15) for  $r_{\text{cvt}}$  is combined with  $T_p$  according to (6.45).

The following approximations for  $\kappa(r_{\text{cvt}}, \tau'_s)$  and  $k_r(r_{\text{cvt}})$ , as appearing in (6.15), are introduced

$$k_r(r_{\text{cvt}}) \approx k r_{\text{cvt}}; \quad k = 4 \cdot 10^{-7} [1/(\text{Nrad})] \quad (6.46)$$

$$\kappa(r_{\text{cvt}}, \tau'_s) \approx c_\lambda \lambda + c_\tau \tau'_s + 1; \quad c_\lambda = 0.9; \quad c_\tau = 0.6 \quad (6.47)$$

with  $\lambda = \frac{r_{\text{cvt}} - 1}{r_{\text{cvt}} + 1}$  and  $\tau'_s$  according to (6.10). These rough approximations are based on empirical data (see *e.g.*, Figure 6.8), and are used for simplicity. The accuracy of the original parameters  $k_r$  and  $\kappa$  is already moderate. The variance of the approximations with respect to the measurements will be in the order of  $\pm 30\%$ . Equation (6.45) is substituted into (6.15), where  $\dot{\omega}_s$  can be neglected if  $|\dot{r}_{\text{cvt}}| \gg 0$ , yielding

$$\dot{\omega}_e = -k\omega_e^2 \frac{F_p - (1 + c_\lambda \lambda)F_s - \frac{c_\tau \cos \theta T_e}{2\mu_2 R_p}}{1 + k \frac{c_\tau \cos \theta}{2\mu_2 R_p} (J_e + J_t + J_p + \alpha_p^2 J_f)} \omega_e^2 \quad (6.48)$$

$$= a_\omega \left( F_p - (1 + c_\lambda \lambda)F_s - \frac{c_\tau \cos \theta T_e}{2\mu_2 R_p} \right) \quad (6.49)$$

where the *shift gain*  $a_\omega$  (in  $[\text{rad}/(\text{kN}\cdot\text{s}^2)]$ ) is introduced. This shift gain is shown in Figure 6.35 versus vehicle speed and speed ratio  $r_{\text{cvt}}$ , for the ZI and CVT powertrain. The ratio of these gains for CVT over ZI is depicted in Figure 6.36. Also depicted in both figures are the boundaries corresponding to minimum and maximum engine speed  $\omega_{e,\text{min}}$  and  $\omega_{e,\text{max}}$ . Especially for low speed ratios and high vehicle speeds, the shift gain of CVT relative to ZI is substantially higher, up to a factor 2.2, see Figure 6.36. The apparent problem in this is alleviated by three factors. First, for low speed ratios and high vehicle speeds, *i.e.*, high  $\omega_e$  (and hence a high pump speed), the hydraulic flow reserve is larger, enabling considerable actuation forces. Second, if the shift gain is 'sufficient' (again for high vehicle speeds), the fact that the CVT powertrain has an even higher gain is irrelevant. The third factor alleviating the shift problem requires the notion of the so-called ZI speed ratio  $r_{zi}$ . As is elucidated in [Serrarens, 2001], when shifting below this CVT ratio the flywheel inertia no longer boosts the acceleration but becomes a load instead, though still smaller than the load of the primary-sided inertias in a conventional CVT vehicle. Therefore, fast shifting below  $r_{\text{cvt}} = r_{zi} \approx 0.96$  is not desirable anyway (see [Serrarens, 2001]), in which case a limited shift gain may not be a real problem. The shaded area in Figure 6.36 depicts the region above  $r_{zi}$ , where the relative reduction in shift gain is larger than 1.2, and where the absolute shift gain is lower than -15. Although these values are somewhat arbitrary, the shaded area gives a rough indication of the operating range where shift problems may be encountered.

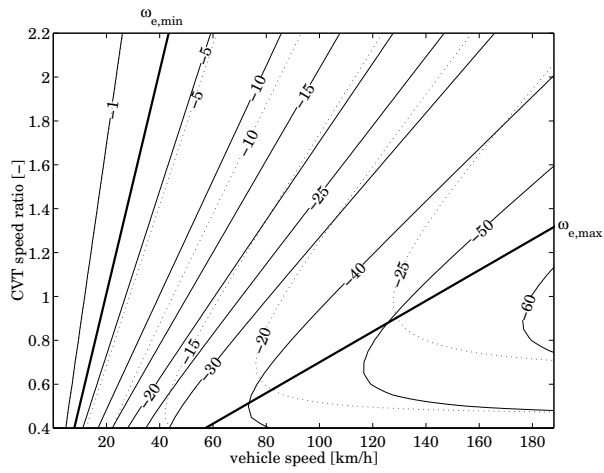


Figure 6.35: Shift gain  $a_\omega$  [ $\text{rad}/(\text{kN}\cdot\text{s}^2)$ ] versus vehicle speed [km/h] and speed ratio  $r_{\text{cvt}}$ , for CVT (solid) and ZI (dotted)

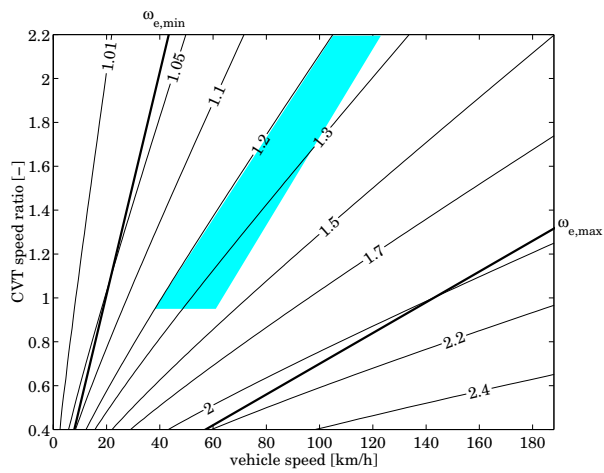


Figure 6.36: Ratio of shift gains (CVT over ZI) versus vehicle speed [km/h] and speed ratio  $r_{\text{cvt}}$

In the following chapter, the (transient) models for the mechanical and hydraulic part of the CVT are used to obtain a model-based CVT controller.



## Chapter 7

# Hydraulic CVT Control

The organization of this chapter is outlined using the general control system setup depicted in Figure 7.1. In this diagram,  $G$  is the system to be controlled,  $K$  is the controller,  $w$  are the exogenous variables,  $z$  the controlled variables,  $u$  the control actions (outputs of the controller) and  $y$  the measurements (inputs of the controller). The system  $G$  comprises the variator and

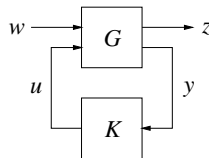


Figure 7.1: General control system

its hydraulics. Depending on the control strategy, the controller  $K$  may consist of different layers. The exogenous inputs  $w$  are the reference signal and the input torque of the transmission. The choice for the reference signal depends on the choice for the variable  $z$  to be controlled (e.g.,  $r_{cvt}$ ,  $\dot{r}_{cvt}$ ,  $\omega_e$ ). The choice for the to-be-controlled quantity is made in Section 7.1. After that, the control objectives can be formulated (Section 7.2). The inputs and outputs of the controller ( $y$  and  $u$ ) are listed in Section 7.3. The control actions  $u$  are limited between lower and upper constraints which may be state-dependent. Moreover, the speed ratio  $r_{cvt}$  is physically constrained whereas the pulley clamping pressures should be sufficient to prevent gross belt slip, while not exceeding their maximally allowed values. All these constraints have to be taken into account, especially in combination with integral controller action. This is treated in Section 7.4. The overall control strategy is presented in Section 7.5, and briefly compared to CVT control as seen in literature (Section 7.6). The actual controller design is presented in 7.7. The chapter concludes with simulation (Section 7.9) and experimental results (Section 7.8).

### 7.1 To-be-controlled quantity

Before formulating the control objectives it is important to realize what quantity actually needs to be controlled. This question is not trivial, since a number of candidates exist, all of which

are relevant from one viewpoint or another. The candidate to-be-controlled variables are the primary speed  $\omega_p$ , the speed ratio  $r_{cvt}$ , and the rate of ratio change  $\dot{r}_{cvt}$ . All of these signals are available from the powertrain controller [Serrarens, 2001]. It is assumed that the powertrain controller takes the engine speed constraints  $\omega_{e,\min}$  and  $\omega_{e,\max}$  and the CVT speed ratio constraints  $r_{ud}$  and  $r_{od}$  into account. Furthermore, the powertrain controller must see to it that the magnitude of the belt torque  $T_p$  that can be expected given the setpoints  $T_{e,d}$  and  $r_{cvt,d}$  (and hence  $\dot{r}_{cvt,d}$ ), does not exceed the maximally allowed value of 250 [Nm]. Moreover, in the ZI powertrain the desired flywheel speed pattern should not give rise to flywheel torques with a magnitude larger than 180 [Nm].

### primary speed control

The first option is to control the primary speed, which makes sense as it determines the engine operating point. However, at low vehicle speeds, the engine speed and the primary speed are decoupled (torque converter is still open), so trying to control the engine speed using the CVT controller no longer makes sense. Furthermore, the fact that the primary speed feedback signal becomes very small for very low vehicle speeds would seriously compromise the controller performance. Observing that the pump speed is generally low at low vehicle speeds, thereby limiting the maximum shift speed, and that the variator has more trouble shifting at low primary speeds (as is reflected by Ide's model, Equation (6.15)), it seems unwise to knowingly limit the controller performance for low vehicle speeds. Moreover, at zero and very low vehicle speeds it is the torque amplification factor of the transmission which is important above anything else. Especially this last observation argues for directly controlling the CVT speed ratio. Primary speed control is used, *e.g.*, in [Hirano *et al.*, 1991], but not for low speeds. Then either the CVT speed ratio  $r_{cvt}$  or the (secondary) clutch input speed is controlled.

### speed ratio control

When controlling the CVT speed ratio  $r_{cvt}$ , certain quantities at primary and secondary side of the transmission must be measured, to reconstruct the actual speed ratio. These quantities can be the speeds, the belt radii or the axial pulley positions. Measuring the speeds is the cheapest, easiest and most robust way, although for zero speeds  $r_{cvt}(= \omega_s/\omega_p)$  cannot be determined. The axial position of the primary pulley position is sometimes used as a passive feedback for the primary valve [Adachi *et al.*, 1999]. Measurement of the belt radii is applied only in experimental setups [Kim and Lee, 1994; Micklem *et al.*, 1994], usually to determine values for belt slip.

### rate of ratio change control

Because the flywheel torque assist depends heavily on the rate of ratio change  $\dot{r}_{cvt}$ , it is useful to consider controlling  $\dot{r}_{cvt}$ , as was also done in the flywheel hybrid vehicle treated in [Spijker, 1994]. To investigate the influence that (errors in)  $r_{cvt}$  and  $\dot{r}_{cvt}$  have on the net torque  $T_n$  that acts on the (lumped) secondary inertia, the partial derivatives  $\frac{\partial T_n}{\partial r_{cvt}}$  and  $\frac{\partial T_n}{\partial \dot{r}_{cvt}}$  are determined

for a range of operating points. When for simplicity assuming  $\eta_{\text{cvt}} = 100\%$ ,  $T_n$  is given by

$$\begin{aligned} T_n &= \frac{T_p}{r_{\text{cvt}}} - \alpha_s T_f \\ &= \frac{T_e}{r_{\text{cvt}}} + \frac{\dot{r}_{\text{cvt}} \omega_s}{r_{\text{cvt}}^3} [(\alpha_p - \alpha_s r_{\text{cvt}}) \alpha_p J_f + J_e + J_t + J_p] \\ &\quad - \frac{\dot{\omega}_s}{r_{\text{cvt}}^2} [(\alpha_p - \alpha_s r_{\text{cvt}})^2 J_f + J_e + J_t + J_p] \end{aligned} \quad (7.1)$$

where  $-\alpha_s T_f$  is the torque contribution of the flywheel at the secondary shaft and  $T_p$  is taken from (6.45). As can be seen from (7.1), the net torque at the secondary shaft depends on  $r_{\text{cvt}}$  directly via the engine torque  $T_e$ , and both on  $r_{\text{cvt}}$  and  $\dot{r}_{\text{cvt}}$  through the flywheel torque assist terms as well as the total primary inertia ( $J_e + J_t + J_p$ ).

The resulting partial derivatives are depicted in Figures 7.2 and 7.3, for  $\omega_{s,0} = 340$  [rad/s],  $\dot{\omega}_{s,0} = 10$  [rad/s<sup>2</sup>],  $T_{e,0} = 110$  [Nm], and a range  $r_0 = (0.4, \dots, 2.2)$ ,  $\dot{r}_{\text{cvt},0} = (-2, \dots, 1)$  (data taken from an actual semi-kickdown experiment). In Figure 7.2 the contour lines of  $\frac{\partial T_n}{\partial r_{\text{cvt}}}$

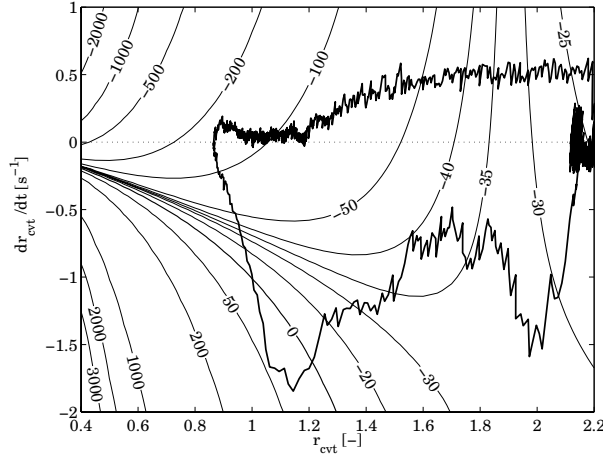


Figure 7.2: Sensitivity  $\frac{\partial T_n}{\partial r}$  [Nm] of  $T_n$  to errors in  $r_{\text{cvt}}$

are drawn versus  $r_{\text{cvt}}$  and  $\dot{r}_{\text{cvt}}$ . As an indication of the practical operating region, the path of  $\{r_{\text{cvt}}, \dot{r}_{\text{cvt}}\}$  during the kickdown transient is drawn. The contour lines are valid only in the linearization point, and of course not exactly along the entire transient. The actual values of the partial derivatives as a function of time in this kickdown transient will be depicted in Figure 7.4. Figure 7.3 shows  $\frac{\partial T_n}{\partial \dot{r}_{\text{cvt}}}$  as a function of  $r_{\text{cvt}}$ , for the CVT with flywheel (solid) and—for comparison—without (dashed). Obviously, the sensitivity of  $T_n$  to errors in  $\dot{r}_{\text{cvt}}$  is largest for  $r_{\text{cvt}} = r_{\text{ud}}$ , in both cases but more so for the system *with* flywheel. The sensitivity  $\frac{\partial T_n}{\partial \dot{r}_{\text{cvt}}}$  of the two systems is equal at the so-called *geared neutral* ratio  $r_{\text{gn}}$ . For  $r_{\text{cvt}} = r_{\text{gn}}$ , the flywheel speed is zero. At  $r_{\text{cvt}} = r_{\text{zi}}$ ,  $\frac{\partial T_n}{\partial \dot{r}_{\text{cvt}}}$  of the system with flywheel is zero. Also, the absolute value of  $\frac{\partial T_n}{\partial \dot{r}_{\text{cvt}}}$  at high  $r_{\text{cvt}}$  is larger for the system with flywheel than for the system without.

In the depicted semi-kickdown experiment the absolute value of the partial derivative  $\frac{\partial T_n}{\partial r}$  is at least as large as, but most of the time much larger than the absolute value of  $\frac{\partial T_n}{\partial \dot{r}_{\text{cvt}}}$ , see

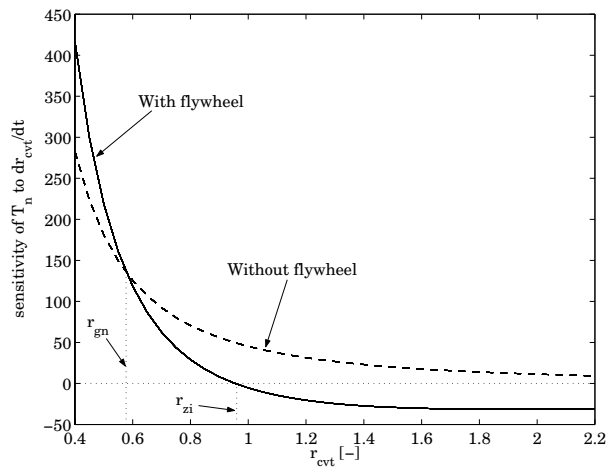


Figure 7.3: Sensitivity  $\frac{\partial T_n}{\partial \dot{r}_{cvt}}$  [Nms] of  $T_n$  to errors in  $\dot{r}_{cvt}$

Figure 7.4. These observations and the fact that the reconstruction of  $\dot{r}_{cvt}$  inherently exhibits a lot of noise (also see Figure 7.2), renders ratio control preferable over rate of ratio change control.

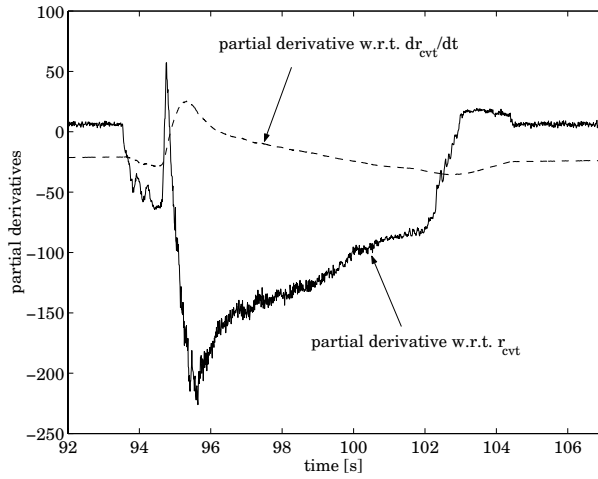


Figure 7.4: Partial derivatives  $\frac{\partial T_n}{\partial r}$  and  $\frac{\partial T_n}{\partial \dot{r}_{cvt}}$  versus time for a kickdown experiment

## 7.2 Control objectives

Having decided to use  $r_{\text{cvt}}$  as the variable to be controlled, the prime objective of the CVT controller is to track a desired speed ratio trajectory (*ratio control*), while maximizing the transmission efficiency. The efficiency is generally highest when both the pulley clamping forces (and hence the oil pressures) are minimal. The durability of the belt is also highest for minimum clamping forces, provided that no gross belt slip occurs. Preventing belt slip (*safety control*) under all partly unpredictable load conditions, is therefore the second control objective. In practice, most of the time one of the two pressures is controlled at its critical (belt slip) value, while the other is adjusted to minimize the ratio error. Moreover, the controller should be robust against external disturbances (*e.g.*, temperature change, air fraction, oil volume, operational faults, sensor/actuator malfunction), and model uncertainties, with respect to stability and performance.

## 7.3 Inputs and outputs of the controller

As detailed in Appendix A, a large number of measurements is available, but the controller only uses the pressures  $p_p$  and  $p_s$ , the speeds  $\omega_e$ ,  $\omega_t$ ,  $\omega_p$  and  $\omega_s$  and either the engine torque  $T_e$  (test rig), or the throttle valve angle  $\phi$  (test vehicle). In the car, the engine torque must be estimated using the engine map together with  $\omega_e$  and  $\phi$ . The (estimated) engine torque is then fed into the torque converter map together with inputs  $\omega_e$  and  $\omega_t$  and corrected with inertia effects (possibly including the flywheel) to arrive at  $T_p$ .  $T_p$  is used to derive the minimum clamping forces, and as an input to the model-based feedforward of the CVT controller. The speeds  $\omega_p$  and  $\omega_s$  are used to reconstruct the CVT speed ratio  $r_{\text{cvt}}$ . The measured pressures  $p_p$  and  $p_s$  are in the feedback part of the controllers and are used to monitor the safety margin towards belt slip.

The analogue controller outputs are the currents  $I_1$  and  $I_2$  to, respectively, the solenoids of the primary and secondary valve. The digital outputs are the pump mode  $i_{\text{pump}}$ , the TC lockup signal  $i_{\text{lockup}}$  and the ‘safety’ valve setting  $i_{\text{safety}}$  (see Appendix A).

## 7.4 Constraints and integral windup

Variator control is limited by some operational and physical constraints, being:

1. the CVT speed ratio  $r_{\text{cvt}}$  is bounded by  $r_{\text{ud}}$  and  $r_{\text{od}}$ ;
2.  $p_{p,\text{max}} = 25$  [bar] and  $p_{s,\text{max}} = 50$  [bar], to avoid damage to the pulley cylinders and pistons and to the pump;
3. the pressures needed for torque transmission  $p_{x,\tau}$  ( $x=p,s$ ):

$$p_{p,\tau} = \frac{F_{30\%}(T_p, r_{\text{cvt}}) - c_p \omega_p^2}{A_p} \quad (7.2)$$

$$p_{s,\tau} = \frac{F_{30\%}(T_p, r_{\text{cvt}}) - c_s \omega_s^2 - F_{\text{spr}}(r_{\text{cvt}})}{A_s} \quad (7.3)$$

with  $F_{30\%}$  according to (B.34), where  $T_p$  is given by (6.45) if the TC is closed and the DNR is in Drive position;



4. minimally controllable pressures:  $p_{p,\min} = 1$  [bar] and  $p_{s,\min} = p_{s,I_2,\min}(\omega_e, i_{\text{pump}})$ , where  $p_{s,I_2,\min}$  is the secondary pressure corresponding to  $I_2 = I_{2,\min} = 0.4$  [A] for a given pump speed  $\omega_e$ , and pump mode  $i_{\text{pump}}$ . A lower  $p_s$  is infeasible, hence desiring for a secondary pressure lower than  $p_{s,I_2,\min}$  would only give rise to integral windup, see the discussion in Section 7.4.1;
5.  $I_1 \in [0.4, 1.16]$  outside of which the throttling orifice no longer changes,  $I_2 \in [0.4, 1.5]$  outside of which the valve stem reaches its mechanical stop;
6.  $I_2 < I_{2,\max}(\omega_e, i_{\text{pump}})$  because otherwise the flow towards the accessories becomes too small.

Properly dealing with these constraints is vital for the performance of the implementation.

### 7.4.1 Conditional anti-windup

A common nonlinearity in control systems, is a saturating element in the actuator signal generation. If integral control is applied to such a system, an undesired side effect, known as *integrator windup*, may occur. To avoid this phenomenon, many different *anti-windup* strategies have been suggested, see, e.g., [Bohn and Atherton, 1995; Rundqwist, 1991]. Two strategies have been experimentally evaluated showing striking differences between the two. The first strategy is the ‘classical’ method to prevent integral windup, also known as *tracking anti-windup*. It uses the difference between the saturated and the unsaturated control signal to generate a feedback signal that reduces the input to the integrator. The second strategy, termed *conditional integration*, switches the integral action on or off depending on certain conditions. In the implementation, the integration is suspended when the control error is such that the actuator saturates and is not moving back towards the unsaturated (linear) range.

As Figure 7.5 illustrates, both strategies (with identical settings for proportional and integral gain) manage to prevent anti-windup, in that the solenoid currents do not display the dead-times common to saturated conventional integral-action controllers, when subjected to a control error changing sign. However, the classical method obviously leads to a very slow response compared to the conditional method. First of all, this is due to a very high initial controller output (caused by proportional action and possibly feedforward) which reduces the integral action such that the net output of the controller exactly equals the upper saturation limit. When the control error diminishes, the proportional (and possibly feedforward) action decreases again, leaving the integral action to ‘creep’ all the way back towards the upper saturation limit. This effect is not seen in the conditional integrator strategy, where the integral action is reset only when the control error wants to drive the control output back towards the unsaturated range.

Secondly, as was shown in Section 6.5.2, the primary pressure is quite sensitive with respect to changes in the solenoid current within a small region (approximately between 0.94 and 1.00 [A], see Figure 6.17), and moreover is corrupted with severe hysteresis. These nonlinearities cause small differences in the solenoid current to have a large effect on the pressure response. For systems less nonlinear, the differences between the anti-windup strategies are smaller. Nevertheless, similar observations were made in [Bohn and Atherton, 1995], upon which it was suggested to use a *modified tracking anti-windup* scheme that additionally limits the feedback signal which corrects the integrator input. In the following, for all integral controllers the conditional integrator anti-windup scheme is applied.

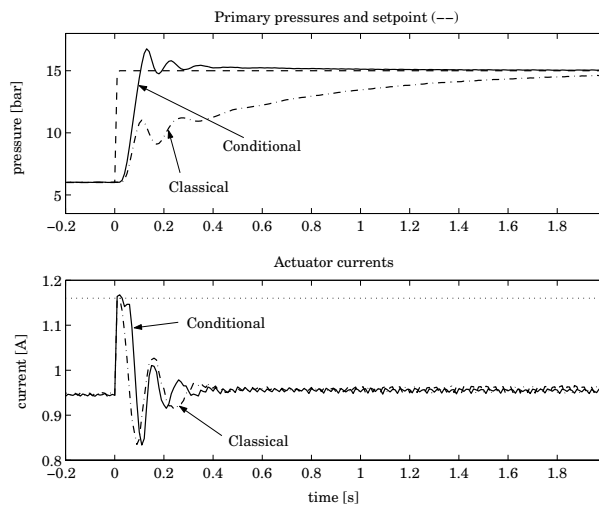


Figure 7.5: Pressure control experiment using Conditional (solid) and Classical anti-windup (dot-dashed)

## 7.5 Control strategy

Now that the to-be-controlled quantity, the objectives, the inputs and outputs of the controller and the constraints are defined, a strategy is devised to reach the objectives subject to the safety and operational constraints. It is proposed to use a cascade controller, consisting of one level which controls the primary and secondary pressure, and a second level that determines pressure setpoints based on the desired speed ratio, while taking into account the various constraints. Such a division of layers is justified if the operation of one layer can be described independently of the other. Although the closed-loop pressure controllers will be shown to have a higher bandwidth than the closed-loop ratio controller, the separation is not complete. The overall results will reveal that this causes no real problems.

It is chosen to use pressure control, instead of flow control [Spijker, 1994; Vanvuchelen, 1997], for a number of reasons:

1. the pulley pressures are directly measured, whereas flows have to be reconstructed from  $\dot{r}_{cvt}$ . As was seen in the previous section, reconstructing  $\dot{r}_{cvt}$  is not without problems. Also, flow control effectively is  $\dot{r}_{cvt}$  control, which was shown not to be preferable over  $r_{cvt}$  control;
2. among the reasons mentioned in literature to opt for flow control the only one remotely convincing is that pressure control becomes increasingly difficult as the flow through the pressure controlled volume approaches zero. In our application such reasoning would hold for the primary circuit only, which for stationary situations, *i.e.*,  $\dot{r}_{cvt} = 0$  can be pressure controlled merely by grace of oil leakage and oil compressibility. However, in such situations flow control based on reconstruction of  $\dot{r}_{cvt}$  is likely to be even more difficult because the leakflows are very small and moreover still need to be reconstructed from pressure measurements;

3. both circuit pressures should minimally be equal to the value  $p_{x,\tau}$  needed for torque transmission and should not exceed the maximum value  $p_{x,\max,\tau}$  as discussed in Section 7.4. [Spijker, 1994] partly circumvents this by allocating the pressure control to the pulley which is critical for belt slip.

## 7.6 Literature on CVT control

The number of publications concerning variator control on the hydraulic actuation level is exceptionally small. Even then, most papers from automotive industry are rather concealing (e.g., [Adachi *et al.*, 1999] from Nissan), whereas academic researchers often use benchmarks which are somewhat distant from practical applications [Kim *et al.*, 1996; Vanvuchelen, 1997] or have rather exotic applications in mind [Spijker, 1994].

Most of the approaches control the clamping pressure at the secondary pulley and control the CVT speed ratio by *steering* the oil flow into the primary pulley cylinder [Abromeit and Wilkinson, 1983; Sakai, 1990; Hirano *et al.*, 1991]. The approaches in [Spijker, 1994; Vanvuchelen, 1997] actually use flow *control*, whereas [Sakai, 1990] claims that the rate of ratio change is the most important control factor, but in the end does not feedback  $\dot{r}_{\text{cvt}}$ . The CVT control concept of [Wade, 1984] is different in that it controls both pulley pressures simultaneously. The pressure controllers are augmented by a ratio controller to achieve the desired ratio response. This setup will prove to be somewhat similar to the one that is suggested in the following section.

Among the encountered controllers are PI(D) [Hirano *et al.*, 1991; Kim *et al.*, 1996; Sato *et al.*, 1996], LQG [Kim *et al.*, 1996], fuzzy [Kim and Vachtsevanos, 2000; Kim *et al.*, 1996], robust control [Adachi *et al.*, 1999; Cheng and de Moor, 1994], model reference adaptive control [Spijker, 1994], feedback linearization [van der Laan and Luh, 1999; Vanvuchelen, 1997] and combinations thereof. Besides feedback, [Hirano *et al.*, 1991] uses a feedforward to increase the bandwidth of the secondary pressure controller. [van der Laan and Luh, 1999] uses Ide's model (see Section 6.4) to obtain an estimate for the primary pressure. Within the Eco-Drive project, [Stouten, 2000] investigated the use of several control strategies in simulations and partly in experiments. The method of input/output decoupling proved to work very well if perfect models were available, yielding decoupled linear-time-invariant relations between (virtual) inputs and the to-be-controlled variables (e.g., the primary and secondary pressure), so linear control theory could be applied for the remaining system. However, in the presence of modeling inaccuracies, the remaining dynamics were highly nonlinear, making it difficult to control the remaining system with linear control. Eventually it was decided to create a new input  $u = F_p - F_s$  and use it in combination with model-based feedforwards and PI control. Some of the ideas presented in [Stouten, 2000] were adopted in the controller design.

## 7.7 Controller design

In this section, the method of determining the pressure setpoints is elucidated. In short, the desired secondary pressure  $p_{s,d}$  is foremost determined by the minimum clamping pressure needed to prevent belt slip (*safety control*), besides guaranteeing sufficient flow supply for the primary circuit. The latter is particularly relevant when performing upshifts. The primary pressure setpoint  $p_{p,d}$  is essentially dedicated to controlling the variator speed ratio  $r_{\text{cvt}}$  (*ratio control*).

Besides these basic functions, the secondary pressure should take over the ratio control,

when the primary pressure reaches its belt-slip-critical value. Until the ratio control error changes sign, the primary pressure setpoint remains equal to this critical value.

### primary pressure feedforward

In controlling the speed ratio, use can be made of the variator model that is available in the form of (6.15), with (6.21), yielding a feedforward for the primary pressure  $p_{p,ff}$  given by

$$p_{p,ff} = \frac{1}{A_p} \left( \frac{\dot{r}_{cvt,d}}{k_r(r_{cvt})|\omega_p|} + F_p^*(r_{cvt}, \tau_s') - c_p \omega_p^2 \right) \quad (7.4)$$

Since the ratio controller is activated only if  $|\omega_p| > \varepsilon$  with  $\varepsilon$  a small positive constant, the division by  $|\omega_p|$  in (7.4) poses no problem.

### secondary pressure feedforward

The feedforward for the secondary pressure setpoint is based on the requirement that the secondary circuit supplies the primary circuit with flow. Given a desired speed ratio trajectory  $r_{cvt}(t)$ , the required flow into the primary cylinder can be calculated as

$$\Phi_{sp} = 2 \tan \theta A_p \max(0, \dot{R}_{p,d})$$

when neglecting oil compressibility and leakage. To enable this flow, a pressure difference  $\Delta p = p_s - p_p$  over the primary valve is needed, constrained by (see Equation (6.24))

$$\Delta p \geq \frac{\rho_{oil}}{2} \left( \frac{\Phi_{sp}}{c_f A_{1,max}} \right)^2 \quad (7.5)$$

where  $A_{1,max}$  is the maximum valve opening from the secondary to the primary circuit.  $A_{1,max}$  is used instead of  $A_1(I_1)$  because  $A_1$  cannot accurately be reconstructed. The resulting feedforward is then given by

$$p_{s,ff} = p_{p,d} + \frac{\rho_{oil}}{2} \left( \frac{2 \tan \theta A_p \max(0, \dot{R}_{p,d})}{c_f A_{1,max}} \right)^2 \quad (7.6)$$

where  $p_{p,d}$  is the (yet to be determined) desired value for  $p_p$ . This feedforward comes down to a flow steering based on  $\dot{R}_{p,d}$ , but will not be afflicted with the noise that would be introduced in case  $\dot{R}_p$  were fed back.

### pressure setpoints

Let  $p_{x,f} = p_{x,ff} + p_{x,fb}$  ( $x = p, s$ ), where  $p_{x,fb}$  represents the feedback part. Then the pressure setpoint  $p_{x,d}$  is determined as

$$p_{x,d} = \min(p_{x,max}, \max(p_{x,min}, p_{x,\tau}, p_{x,f})) \quad (7.7)$$

$p_{x,fb}$  is obtained from a conditional anti-windup PI controller, that feeds back the error  $e_r = \ln(r_{cvt,d}) - \ln(r_{cvt})$ . It is chosen to use logarithms in order to make the feedback signal symmetrical around  $r_{cvt} = 1$ . The feedback part is normally active at the primary side only. The secondary pressure setpoint  $p_{s,d}$  then equals the maximum of  $p_{s,min}$  and  $p_{s,\tau}$ . Only when  $p_{p,d}$  drops below its minimal value according to (7.7), the secondary feedback part is activated. More information on this can be found in [Vroemen *et al.*, 2000].

### 7.7.1 Pressure control

Both the pressures controllers are anti-windup PI controllers with feedforwards for the solenoid currents. As was argued in Section 6.5.2, a feedforward for the primary valve other than a constant value ( $\approx 0.94$  [A]) is useless, because of the large hysteresis. On the other hand, a feedforward current  $I_{2,ff}(\omega_e, p_{s,d}, i_{\text{pump}})$  for the secondary solenoid (see Figure 6.14) is quite effective.

## 7.8 Simulations

Figures 7.6, 7.7, and 7.8 show results of the controller with and without feedforward evaluated on a trajectory which is typical for the ZI powertrain in case of a kickdown acceleration. Such a situation combines a low initial pump speed with high downshift rates, followed by a moderate upshift and then a rather fast upshift, besides periods of (semi-) stationary operation, see the upper plot of Figure 7.6. For comparison, the actual speed ratio as measured in

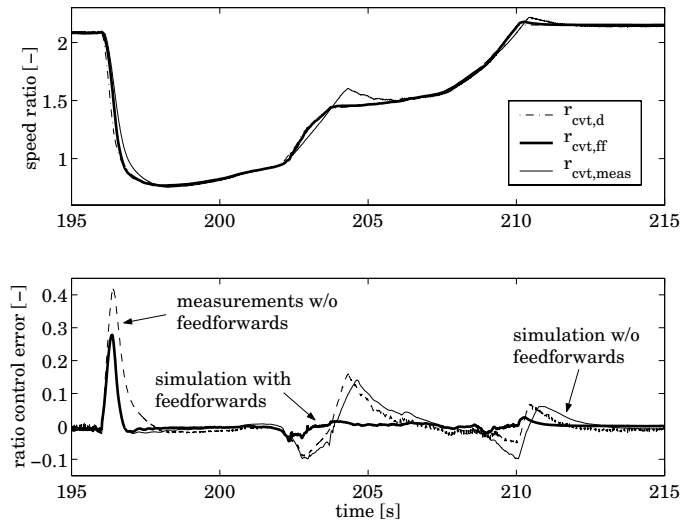


Figure 7.6: Desired speed ratio  $r_{\text{cvt},d}$ , realized speed ratio  $r_{\text{cvt},ff}$  with feedforwards (from simulation), measured speed ratio  $r_{\text{cvt},\text{meas}}$  (from experiment) and control errors, with and without feedforwards

the test vehicle, is also shown in Figure 7.6. As can be seen from the upper plot, the measured speed ratio  $r_{\text{cvt},\text{meas}}$  tracks the desired speed ratio  $r_{\text{cvt},d}$  reasonably well, except from a rather severe overshoot between  $t = 204$  and  $206$  [s]. This ratio control error is more disturbing than the error in the downshift around  $t = 196$  [s]. Hence, the effort should be directed towards decreasing the overshoot in the upshift more than at improving the downshift behaviour, that is thought to be acceptable as it is.

To see if the CVT model is able to predict the errors as they were measured, the kickdown was repeated using the same controller as in the experiment. In this controller the pressure feedforwards were not yet implemented. The result, indicated as *simulation w/o feedforwards*

compares fairly well to the measurement (indicated as *measurement w/o feedforwards*), especially around the overshoots between  $t = 204$  and  $206$  [s], and between  $t = 210$  and  $211$  [s].

Applying the pressure feedforwards, both the mentioned overshoots are decimated, and also the preceding undershoots (around  $t = 203$  and  $t = 210$  [s]) are reduced significantly. It is actually these undershoots that partly induce the overshoots. The pressure setpoints  $p_{x,d}$ , and some of their components are depicted in Figure 7.7. In the upper plot, the difference of

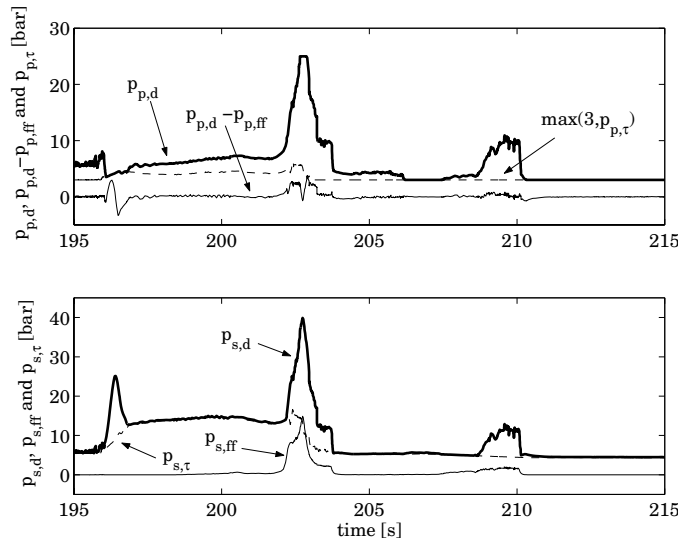


Figure 7.7: Setpoint and feedforward for the primary and secondary pressure

the primary pressure setpoint  $p_{p,d}$  and feedforward  $p_{p,ff}$  is depicted instead of the feedforward pressure itself, because the difference between the setpoint and the feedforward is quite small. This difference is partly the contribution of the feedback pressure  $p_{p,fb}$ , but is also caused by the minimum and maximum pressure constraints ( $p_{p,\tau}$  and  $p_{p,max} = 25$  [bar]), which are never violated by the pressure setpoint. Note that most of the time  $p_{p,d} > p_{p,\tau}$ , except around  $t = 206$  [s] and between  $t = 210$  and  $t = 215$  [s], where  $p_{p,min} = 3$  [bar] is reached. In those time intervals, the secondary pressure is controlling the ratio, and will therefore generally be higher than  $p_{s,\tau}$  (in this example only slightly, *i.e.*, 0.15–0.30 [bar]), see the lower plot of Figure 7.7. For the secondary pressure setpoint, always  $p_{s,\tau} > p_{s,min}$ . As can be expected, the secondary feedforward  $p_{s,ff}$  is active during upshifting only, and amounts up to 15 [bar] around  $t = 203$  [s]. Besides the fast transients,  $p_{s,d}$  mostly equals  $p_{s,\tau}$ , indicating efficient variator operation.

Finally, Figure 7.8 compares the pressure setpoints that are generated by the ratio controller with and without feedforwards. The setpoints with and without feedforwards during the downshift are indistinguishable. This is not so surprising in view of the fact that both primary pressure setpoints (with and without feedforward) come across the constraint  $p_{p,\tau}$ . The large differences arise during the subsequent upshifts, where  $p_{s,ff}$  successfully compensates for the pressure drop over the primary valve.

Enlarging the secondary pressure for an upshift might seem somewhat counterintuitive, since this directly increases  $F_p^* = \kappa F_s$  in Equation (6.15), which in itself decreases  $\dot{r}_{cvt}$ . However,

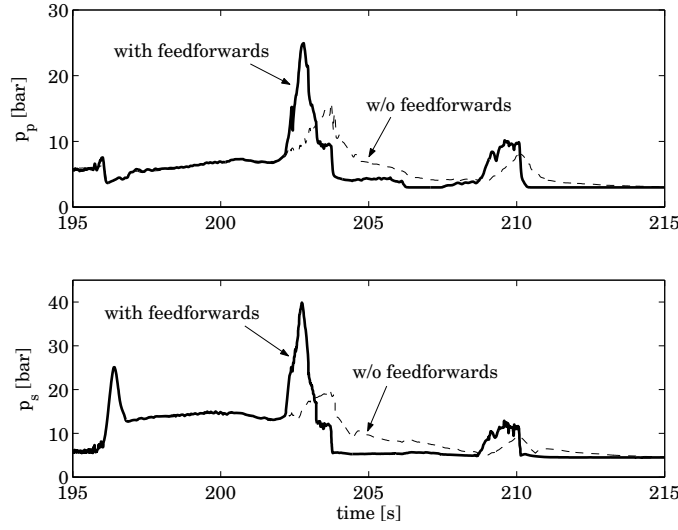


Figure 7.8: Comparison of realized primary and secondary pressures for controllers with and without feedforwards

if the larger secondary pressure enables a correspondingly larger primary pressure, then the upshift rate increases. For example, consider a situation where  $p_p = 10$  [bar],  $p_s = 15$  [bar] and  $\kappa = 1.3$ , roughly corresponding to the simulation without feedforwards around  $t = 203$  [s]. Then, if for simplicity centrifugal and secondary spring force are neglected,  $F_p \approx 26$  [kN] and  $F_p^* \approx 24$  [kN]. Increasing the secondary pressure to 30 [bar], and the primary pressure by an equal amount, *i.e.*,  $p_p = 25$  [bar], yields  $F_p \approx 65$  [kN] and  $F_p^* \approx 48$  [kN]. In this example the pulley thrust ratio  $F_p/F_s$  increases from 1.40 to 1.75, while  $F_p - F_p^*$  increases from 2 to 17 [kN], clearly enlarging the upshift rate. Even when the pulley thrust ratio doesn't change, but  $F_p - F_p^*$  does, the upshift rate gets larger (*e.g.*, increasing  $p_p$  from 10 to 20 [bar] and  $p_s$  from 15 to 30 [bar] raises  $F_p - F_p^*$  from 2 to 4 [kN]—hence doubles the shift rate—while  $F_p/F_s$  is unchanged). This observation can be quantified more precisely, when combining Equations (6.15), (7.6), (6.21), (6.22) and approximation (6.3), yielding

$$\dot{R}_p = v_R \left( -1 + \sqrt{1 + 2 \frac{p_p(A_p - \kappa A_s) + c_p \omega_p^2 - \kappa(c_s \omega_s^2 + F_{spr})}{v_R m_R}} \right) \quad (7.8)$$

with

$$m_R = \frac{\pi(r_{cvt} + 1)^2}{k_r(L - 2a)\omega_p}$$

$$v_R = \frac{m_R}{\kappa A_s \rho_{oil}} \left( \frac{c_f A_{1,max}}{2 \tan \theta A_p} \right)^2$$

Figure 7.9 shows the resulting  $\dot{R}_p$  for  $p_p \in (0 \dots 25)$ . Clearly, the shift speed increases for higher  $p_p$ , although the effectiveness decreases for higher pressures.

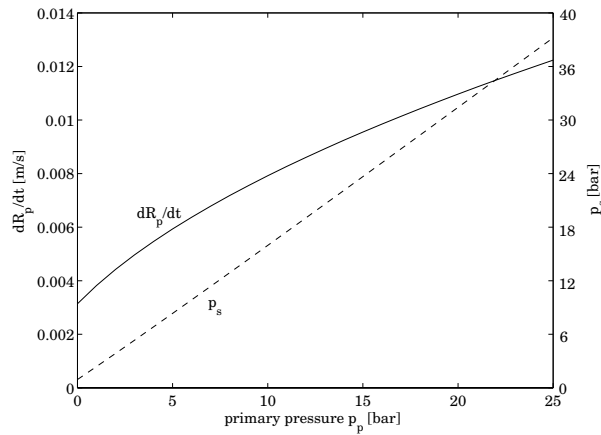


Figure 7.9: Upshift rate  $\dot{R}_p$  and corresponding secondary pressure  $p_s$  for  $p_p \in (0 \dots 25)$ ,  $\kappa = 1.29$ ,  $\omega_p = 371$  [rad/s],  $r_{cvt} = 1.155$  (data taken from the experiment depicted in Figure 7.6 at  $t = 203$  [s])

## 7.9 Experimental control results

The results depicted in this section are obtained from experiments performed with the test vehicle on a test track. Figures 7.10, 7.11 and 7.12 depict measurements and corresponding setpoints of the CVT speed ratio and of the primary and secondary pressure, respectively, for an experiment where the flywheel was not part of the transmission. The experiment concerns a fast downshift (kick-down), succeeded by a slow and a fast upshift, see Figure 7.10. The results are comparable with those depicted in Figures 7.6–7.8. In Figure 7.11 it is seen (around  $t = 157$  [s]) that the primary pressure controller has trouble following its (decreasing) setpoint because of the secondary pressure which rises nearly stepwise by circa 30 [bar], see Figure 7.12. The secondary pressure controller is quite fast, but cannot increase  $p_s$  beyond 40 [bar], because of the relatively low pump speed (around 1500 [rpm]) at the start of the transient. The subsequent upshift poses no problems, up to  $t \approx 167$  [s], where the desired upshift speed drastically increases, see Figure 7.10. Not surprisingly, the unrealistically high initial desired upshift speed ( $r_{cvt,d} \approx 3.3$ , or alternatively  $\dot{\omega}_{e,d} \approx -1600$  [rad/s<sup>2</sup>]) cannot nearly be tracked, even though the initial pump speed is high (around 5600 [rpm]). Instead, the CVT shifts up with a virtually constant shift rate of 0.45 [s<sup>-1</sup>]. Figure 7.11 suggests that the upshift speed could be improved if the primary pressure were able to follow its setpoint. Using the feedforward proposed in (7.6), a substantial improvement in this respect is expected. Moreover, because the primary pressure is below its setpoint all the while from  $t \approx 167$  to 169 [s], the primary valve saturates resulting in the overshoot in  $r_{cvt}$  between  $t = 169$  and 171 [s]. As was also shown in Section 7.8, the overshoot is likely to be eliminated using the (yet to be implemented) feedforward that compensates for the pressure drop over the primary valve.

The CVT speed ratio and pressures from another experiment—this one *with* flywheel—are depicted in Figures 7.13, 7.14 and 7.15. This experiment is included to show the response of the ratio controller to fluctuating inputs, such as those induced by *pedal jogging* [Serrarens, 2001]. As Figure 7.13 shows, the reference CVT speed ratio moves through its entire range,



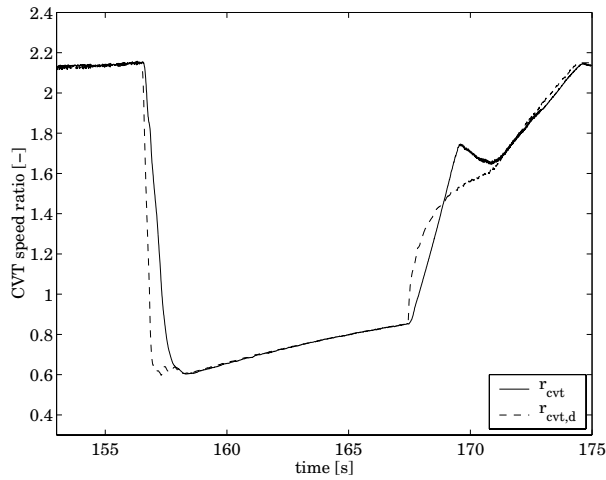


Figure 7.10: CVT speed ratio and setpoint

in a highly fluctuating manner. Most of the fluctuations are tracked reasonably well, except maybe the upshifts around  $t \approx 178$  and  $t \approx 187$  [s]. Figures 7.14 and 7.15 depict the corresponding pressures and their setpoints. Without going into much detail it is observed that the secondary pressure is perfectly able to track its setpoint, apart from a small peak towards 50 [bar] around  $t = 188$  [s], see Figure 7.15. The primary pressure has much more trouble following its setpoint, due to interaction with the secondary pressure (Figure 7.14). Again, the feedforward according to (7.6) can be expected to remove most of the errors during fast upshifting ( $p_{p,d} > p_p$ ). Practical implementation of this feedforward is still to be performed.

Summarizing, the developed CVT controller proved to perform well in practice, although some augmentations of the controller that worked well in simulations are still to be implemented. Furthermore, the CVT controller developed here has been adopted in the ZI Stop-Go transmission without modification. Even though the various system parameters of the CVT can be expected to be somewhat different, experimental experiences show that this CVT controller performs remarkably well. This gives some indication of the controller robustness with respect to model errors.

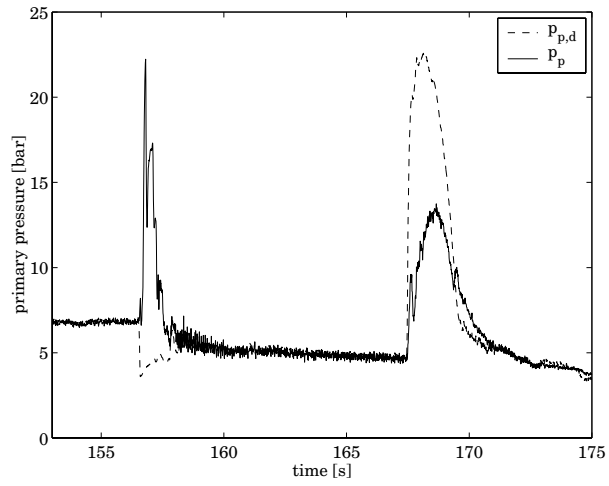


Figure 7.11: Primary pressure and setpoint

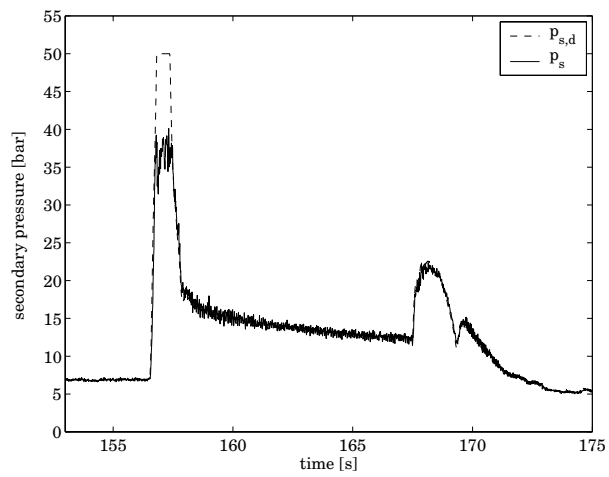


Figure 7.12: Secondary pressure and setpoint

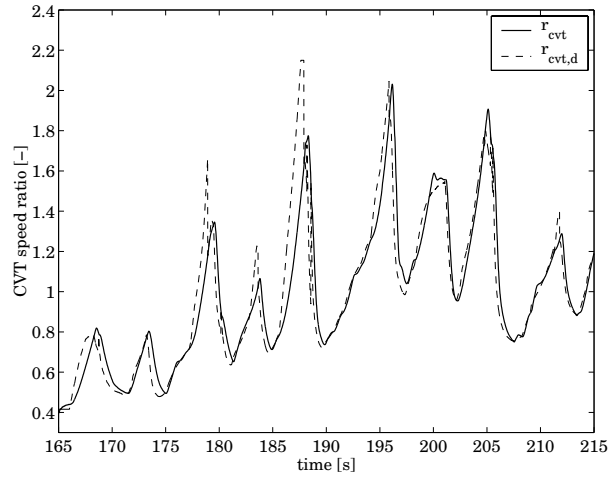


Figure 7.13: CVT speed ratio and setpoint

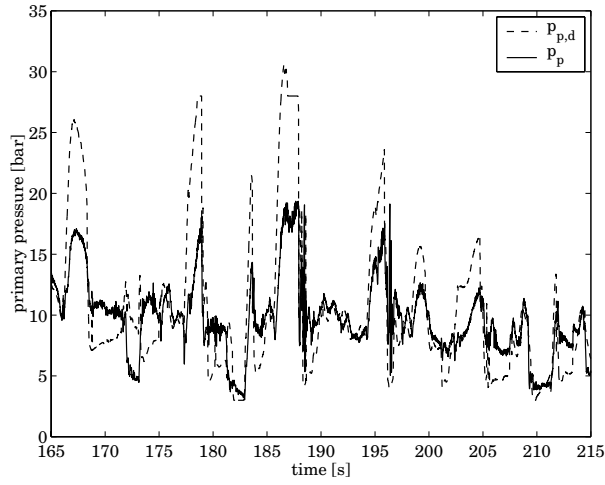


Figure 7.14: Primary pressure and setpoint

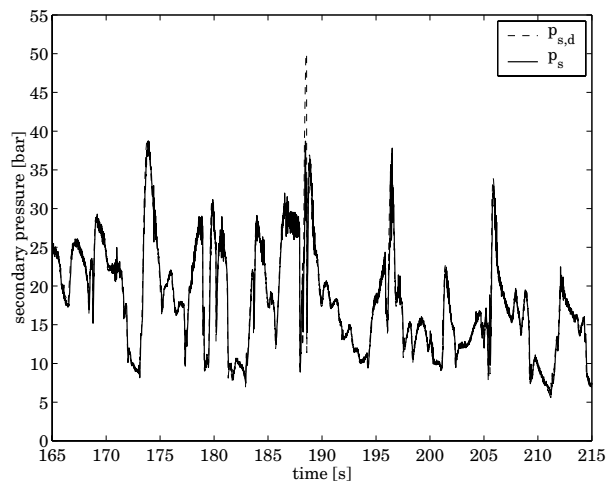


Figure 7.15: Secondary pressure and setpoint



**Part III**  
**ZI Stop-Go**



## Chapter 8

# Introduction to Stop-Go

As briefly introduced in Section 4.3, the remaining part of this thesis investigates the feasibility of a mechanical Stop-Go system, based on the ZI powertrain. After elucidating existing commercial Stop-Go concepts (Section 8.1), the mechanical ZI Stop-Go solution is introduced (Section 8.2) and a model for the ZI Stop-Go powertrain is presented (Chapter 9). The augmentation to the ZI powertrain introduces quite some additional complexity due to the fact that the various clutches may be open, slipping or closed.

Focus is on modeling and control of the vehicle launch. Besides, the transitions from Stop-Go to ZI operation and back are investigated. The engine, which is to be shutdown and re-ignited repeatedly, is modeled as an inertia with an external (possibly negative, *i.e.*, drag) torque to be determined from the stationary engine map, as used, *e.g.*, in Part I. The problems related to such intermittent engine operation with respect to emissions and heat treatment of the catalytic converter, are beyond the scope of the present treatise. The fuel savings associated with ZI Stop-Go operation are not determined experimentally. For the potential fuel savings the reader is referred to the discussion in Chapter 3.

Based on the derived ZI Stop-Go model, a control strategy is proposed for the five clutches in the system in conjunction with the engine and the CVT, see Chapter 10. This top-level controller is hybrid in the sense that it switches from one control scheme to another, depending on the current structure of the model. On a lower level, component controllers deal with the operation of the engine, the CVT and the clutches. The control strategy is first evaluated in simulations.

A prototype ZI Stop-Go transmission was developed to validate the concept and its controllers. For this purpose, the test rig as described in Appendix A was slightly modified to facilitate the actuation of the various clutches. Preliminary experiments performed on this test rig yield promising results.

### 8.1 Commercial Stop-Go concepts

In order to achieve the fuel savings predicted in Chapter 3, the fuel injection should be suspended whenever the desired engine power is non-positive. In modern cars, fuel cut-off while driving is common practice when the accelerator pedal is released and the engine speed is still above idle speed. At idle speed (or in fact at some margin above that) the engine must be decoupled from the transmission and the engine idle speed controller has to take over.



Hence fuel cut-off while driving introduces no additional problems. If during fuel cut-off, the engine is disengaged from the rest of the driveline, some strategy is required to—comfortably and quickly—re-engage the engine in case of a power demand. However, doing so is useful only in three situations.

The first situation arises when the driver demands for a negative power at the wheels (*coasting*) between zero and the engine drag power. Cutting-off fuel would be best for fuel economy, but can cause too much engine braking. To isolate the engine drag torque from the powertrain, the engine should be disengaged and the wheel brakes must be applied to control the wheel power. The fuel savings corresponding to engine shutdown during coasting are between 0.3 (highway) and 3.6% (rural), depending on the driving cycle. These numbers were obtained using the reference vehicle from Part I, and its reference engine operating line (called the  $OL_{15\%}$  line in Section 3.2). Such operation implies relatively low engine speeds for low wheel power demands. If on the other hand, engine speeds are consistently higher, the fuel savings from engine shutdown while coasting are larger.

A second, rather artificial type of vehicle operation, is discussed in [Bertram, 1996]. For instance, when approaching a traffic light, the fuel economy is best when the engine is shut-down and disengaged while the vehicle comes to a stop, using vehicle drag only. That way, the time during which the fuel is cut-off is maximized, simply because the time needed for stopping is longer, though of course a desired wheel power generally can no longer be realized. Such vehicle operation can never be pursued by a powertrain management system, but is totally up to the driver [Bernhardt and Heidemeyer, 1992]. Driving behaviour can be *stimulated* in the form of a driving support tool (such as a miles-per-gallon gauge or more advanced, see [van der Voort, 2001]), but not be *imposed*. Alternatively, in the near future, vehicle operation may be managed by some intelligent traffic guidance system [Breuer *et al.*, 2000].

The third reason for disengaging the engine is to maximize the amount of recoverable braking energy. It will be seen in Section 8.1.2 that not all Stop-Go configurations are capable of recovering the engine braking energy.

### 8.1.1 Stop-Go configurations

In this section, several Stop-Go configurations as seen in practice, are discussed. Full hybrids (see Part I), which are capable of a purely electrical vehicle launch are not discussed here, because in those systems restarting of the engine may be an issue not until some time after vehicle launch.

In the design of a Stop-Go system, a number of choices has to be made. It is to be decided whether to first start the engine or first launch the vehicle, or alternatively, both at the same time. Most systems known in literature start the engine first and then use the engine to accelerate the vehicle. The resulting delay between depressing the accelerator pedal and a noticeable vehicle acceleration is an obvious drawback.

Launching the vehicle before, or simultaneously with starting the engine, poses other problems depending on the applied strategy to restart the engine. If the engine is restarted by suddenly connecting it to the drive train, severe driveability penalties can be expected. If the strategy is to have the engine engaged to the driveline from the beginning, ignition and injection can commence around 800 [rpm], from where the engine is able to propel the vehicle. The resulting prerequisite is that the vehicle has to reach the speed corresponding to 800 [rpm] (referred to as  $v_{v,\text{idle}} \approx 8$  [km/h]) within a 'foreseeable' future. Furthermore, the torque and power requirements for launching the vehicle are highly dependent on the situation and can be much higher than the requirements for restarting the engine, especially with respect to *gradeability* demands. For example, climbing a slope of 30% using the reference

vehicle weighing 1360 [kg] and an engine drag torque of 15 [Nm], requires approximately 10 [kW] at  $v_v = v_{v,\text{idle}}$  and  $\dot{v}_v = 0$ . If additionally a reasonable minimum of  $\dot{v}_v = 0.5 \text{ [m/s}^2\text{]}$  is needed, an extra 2 [kW] (at  $v_v = v_{v,\text{idle}}$ ) is required. For prolonged driving on such a slope, the vehicle may not be able to reach  $v_{v,\text{idle}}$  quickly, demanding a sustained power rating of the starting device of at least 10 [kW]. Because of these relatively high power requirements, *electrical* vehicle launch is seen only in full hybrids which are capable of prolonged electrical propulsion. Using a *mechanical* starting device (*i.e.*, a flywheel) lowers the penalty on high power requirements, whereas the energy requirements for vehicle launch are generally quite low, in itself arguing for a flywheel solution, see Part I. Again, if the vehicle is to be driven at speeds below  $v_{v,\text{idle}}$  for some time, it should be guaranteed that the engine can take over.

If it is chosen to first restart the engine, one can still select between a *direct-start* and an *impulse-start*, see, *e.g.*, [Reik, 1999]. In a direct-start, the starting device is directly connected to the crank shaft as in a conventional vehicle, or possibly via a clutch. Such a device must obviously be able to deliver high torques from rest. In an impulse-start, an inertia—which may be the starter-rotor itself—is accelerated and subsequently engaged with the crank shaft. Using impulse-start lowers the requirements on the starter's maximum torque, even so that the starter may be smaller than a conventional one [Seiffert and Walzer, 1989]. That is, if the additional delay is thought to be acceptable. Even if the maximum torque of the starter is the same for the direct- and the impulse-start system, the combined time of speeding up the inertia of the starter (referred to as *phase 1*) and next closing the clutch between inertia and crankshaft (*phase 2*) may be longer than the time needed for a direct-start. If for simplicity it is assumed that the starter's torque changes stepwise from 0 to a constant  $T_{\text{st}}$ , and that the engine drag is constant and equal to  $T_{\text{e,drag}} > 0$ , the time needed to speed up towards the engine idle speed  $\omega_{\text{e,idle}}$  using direct-start, is given by

$$t_{\text{direct}} = \frac{\omega_{\text{e,idle}}(J_e + J_r)}{T_{\text{st}} - T_{\text{e,drag}}} \quad (8.1)$$

where  $J_e$  and  $J_r$  are the moments of inertia of the engine crankshaft and of the starter-rotor. Assuming that in phase 2 of the impulse-start, the clutch torque is changed stepwise from 0 to  $T_c$  and that the clutch actuation system is infinitely fast, the combined time needed to reach  $\omega_{\text{e,idle}}$  using impulse-start can be determined as

$$t_{\text{impulse}} = t_{\text{phase1}} + t_{\text{phase2}} \quad (8.2)$$

$$= \omega_{\text{e,idle}} \left( \frac{J_r}{T_{\text{st}}} + \left( 1 + \frac{T_c}{T_{\text{st}}} \right) \frac{J_e}{T_c - T_{\text{e,drag}}} \right) \quad (8.3)$$

$$(8.4)$$

For realistic values ( $n_{\text{e,idle}} = 800 \text{ [rpm]}$ ,  $J_e = 0.08 \text{ [kg m}^2\text{]}$ ,  $J_r = 0.17 \text{ [kg m}^2\text{]}$ ,  $T_{\text{st}} = 150 \text{ [Nm]}$ , and  $T_{\text{e,drag}} = 15 \text{ [Nm]}$ ) Figure 8.1 depicts these starting-times, and the speed  $\omega_{r0} = t_{\text{phase1}} T_{\text{st}} / J_r$  of the starter-rotor needed for the impulse-start, as a function of the clutch torque  $T_c$ . Of course, if somehow the starter-rotor was already (or still) running with a sufficiently high speed, the starting-time for an impulse-start only depends on the clutch torque, and can easily be reduced below 0.1 [s], see the curve corresponding to phase 2 in Figure 8.1. Such a method of operation is used in Section 8.2, and in the Volkswagen SNA system [Bernhardt and Heidemeyer, 1992]. Both the direct and the impulse start strategies still require some launching clutch, which sets the minimal number of clutches for impulse-start at two.

Figures 8.2 and 8.3 depict configurations as seen in commercial Stop-Go systems. The layout of Figure 8.2 is encountered, *e.g.*, in Honda Insight, BMW 3 and 7 Series, and only allows

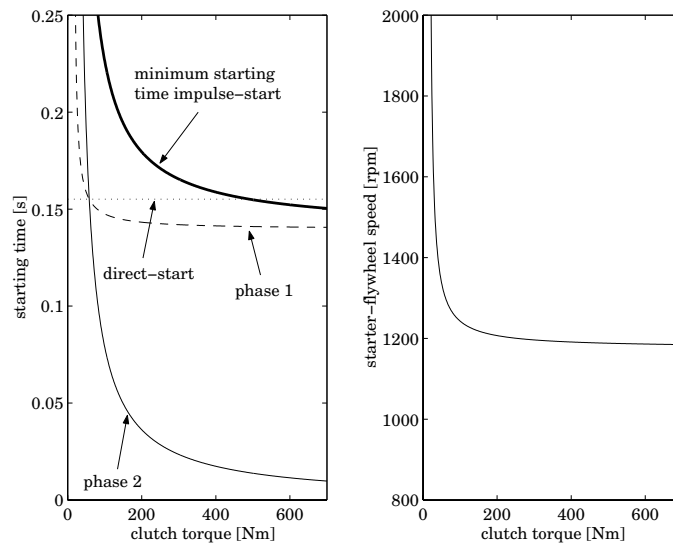


Figure 8.1: Starting times for direct-start and impulse-start

for a direct-start. BMW actually was the first one to use a combined starter-alternator (SA, also known as Integrated Starter-Generator, ISG) during the 1950s and '60s in their BMW 700 Dynastart. The current BMW system (called Crankshaft Starter-Alternator, CSA) is developed in cooperation with ISAD Systems (Cologne, Germany), Bosch and Siemens. In the Honda Insight the transmission can be a 5-speed manual transmission or, alternatively, a CVT, in which case the clutch is positioned at secondary side of the transmission. Surprisingly, the Honda is moreover equipped with a conventional backup starter motor.

The layout as shown in Figure 8.3 is seen, *e.g.*, in the Mitsubishi SUV Advance, in which case the transmission is a CVT. This type of configuration enables direct-start as well as impulse-start. The clutch at secondary side of the transmission may also be placed at primary side, between the transmission and the SA. Because an impulse-start is possible, the size of the starter may be reduced substantially, as seen in the VW Ecomatic of 1993 [Greve and Liesner, 1993].

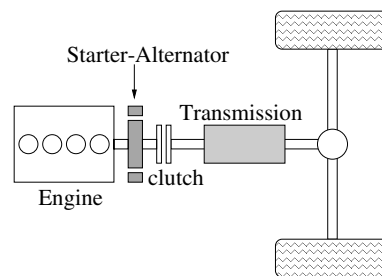


Figure 8.2: Stop-Go system as used in Honda Insight

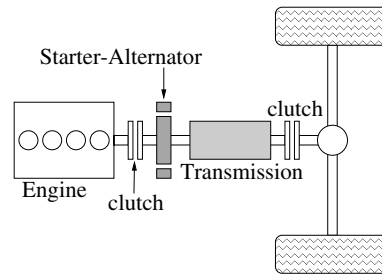


Figure 8.3: Stop-Go system as used in Mitsubishi SUW Advance

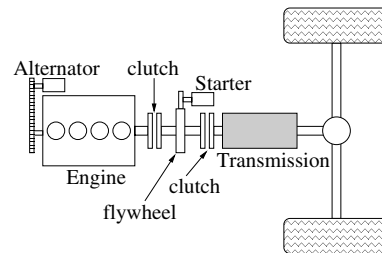


Figure 8.4: Stop-Go system with flywheel impulse start as seen in VW Golf Ecomatic

### 8.1.2 Additional functions of Stop-Go systems

Besides the possibility of saving fuel consumption, additional functions of SG systems are conceivable, especially for electrical SG systems, which are usually referred to as SA systems [Frisster and Henneberger, 1988; Bolenz, 1996; Caricchi *et al.*, 2000].

Among the possible additional functions of Stop-Go systems are:

1. high-efficiency power supply for the 42 Volt on-board net (see Part I);
2. brake energy recovery;
3. torque assist;
4. purely electrical propulsion;
5. torsional vibration damping;
6. active gear synchronization for Automated Manual Transmission (AMT);
7. elimination of torque interruption for gearshift in AMT.

Both the Honda and the Mitsubishi system have a starter-alternator well capable of supplying energy for the 42 Volt net. The former VW Golf could also have done so, but didn't aim at increasing the alternator power. Purely mechanical SG systems are obviously incapable of generating electric energy. All systems can charge the accumulator while standing still. Even in a mechanical SG system, the flywheel can be seen as the accumulator, and may be charged

during standstill. Brake energy recovery is pursued in both the Honda and the Mitsubishi system, though the potential fuel saving is much higher for the Mitsubishi than for the Honda, because the Mitsubishi can also recuperate the energy which is dissipated by engine braking in the Honda. Finally, both Honda and Mitsubishi use the SA to assist the engine during accelerations (torque assist), so that the engine can be downsized. The Honda Insight is most radical in this respect. It uses a 3 cylinder 1.0 ℓ VTEC engine, whereas the Mitsubishi uses a 1.5 ℓ GDI engine.

The last four functions (4 to 7) are not known to be pursued by either the Honda or the Mitsubishi system. Purely electrical propulsion is rather impractical if the sustained maximum power of the electric motor is lower than circa 15 [kW]. Torsional damping of engine vibrations is performed in the ISAD system (Integrated Starter-Alternator-Damper, see [Zeyen and Pels, 1997]), as used, *e.g.*, in BMW and Citroën [Adcock, 1998], and might even be combined with engine idle speed regulation [Zaremba and Davis, 2000]. The ISAD system, which was introduced in 1997 by the Continental Automotive Systems Group along with BMW and PSA provides electric damping of engine vibrations. This is realized by filling up the torque gaps between individual combustions in motor mode, while shaving the peaks of these torques in generator mode. Due to the conversions from electrical current to torque and vice versa, the efficiency of this type of torsional damping may be as low as 70%, which is rather poor when compared to a conventional engine flywheel, where the losses are close to zero. However, active damping is capable of more effective crankshaft speed pulsation attenuation than a flywheel, and can adapt to varying frequencies and amplitudes, which is impossible for a Dual-Mass-Flywheel [Albers, 1995; Sudau and Sasse, 1998].

Functions 6 and 7 are mentioned, *e.g.*, in [Reik, 1999; Fischer, 1999] and are increasingly important to widen the market for AMTs.

### 8.1.3 Ways to gain acceptance

Apart from situations where the driver explicitly turns off the engine by turning the key, shutdown of the engine is associated with unreliability, discomfort and even lack of safety. Previous attempts to develop Stop-Go systems using conventional starter motors—as tried by Fiat and by Volkswagen in its Eco Golf—literally stalled through lack of consumer confidence and the slowness of the starter to crank up the engine [Adcock, 1998; Bertram, 1996]. Even when a subsequent restart is guaranteed, engine shutdown poses psychological issues as also seen in hybrid vehicles that operate the engine intermittently. Ideally, the engine shutdown and restart should be unnoticeable. This implies that either the engine should be so silent that it is never heard, or else the engine sound should be imitated whenever the engine is off. In all cases, the operation should be predictable, noise-free, and without shocks. Additionally, a (conventional) backup system may be required to offer at least the predictability of conventional vehicles. Finally, the PTO (power steering, power brakes, heating/airconditioning, automated clutch actuation, *etc.*) supply should be taken over by some secondary power source, whenever the engine is shutdown.

Most of today's efforts aim at gaining acceptance by handing the controls to the driver whenever possible, so as to make the on-off operation predictable. Therefore, most commercial Stop-Go systems are *not* fully automated. For instance, in the Honda Insight (not the CVT version) and in the Citroën Xsara Dynalto, the transmission is an ordinary MT, forcing the driving to make some decisions (operating the clutch, choosing gear) which can then be used to derive the driver's intentions. More precisely, in the Honda Insight, the engine shuts down when *all* of the following criteria are met [Honda, 2001]:

1. the vehicle speed is below 30 [km/h] and the brake pedal is depressed;
2. the vehicle is stopped, declutched and shifted to neutral;
3. the accelerator pedal is not depressed;
4. the engine coolant is close to its normal operating temperature;
5. the battery charge is sufficient;
6. the airconditioner is off, or in 'ECON' mode (moderate power consumption);
7. the engine vacuum reserve is adequate for power braking.

The first two conditions are set by the driver, and demand quite some deliberate action. For example, if the driver forgets to shift the transmission into neutral, no idling fuel is saved. The first three conditions are meant to cut some slack for cranking up the engine, while the driver is operating the clutch and gear shift lever. The other conditions make sure that the overall system runs reliably and is always ready for another vehicle launch. If all conditions were met and hence the engine was shutdown, it restarts again when the clutch pedal is depressed and first gear is selected. Roughly the same manner of operation is applied in the Citroën Xsara Dynalfo.

The Volkswagen Lupo (and Audi A2 which is technically highly similar) is somewhat more automated in that the transmission is an AMT. This potentially reduces the time available for an engine restart, since the driver is not asked to depress the clutch. Therefore, the engine is shutdown only after the vehicle has come to a complete stop and the brake pedal is depressed for at least four seconds. If the brake pedal is released, the engine restarts. Furthermore, if the driver releases the accelerator pedal while driving, the engine is disengaged and idles. If subsequently the brakes are applied the engine is re-engaged to allow engine braking.

## 8.2 Mechanical solution: ZI Stop-Go

The mechanical Stop-Go facility as realized in the ZI driveline, as it was depicted in Chapter 4 is repeated in Figure 8.5. It augments the ZI powertrain with two clutches. The *secondary clutch* ( $C_s$ ) can disengage the secondary pulley from the shaft through that pulley, *i.e.*, the *secondary shaft*. The *flywheel clutch* ( $C_f$ ) can separate the secondary shaft from the gear which connects to the carrier of the planetary gear set, *i.e.*, the *secondary gear*. The usual clutches, *i.e.*, the *torque converter lockup clutch* ( $C_l$ ), the *drive clutch* ( $C_d$ ), and the *reverse clutch* ( $C_r$ ), are operated differently. As was mentioned in Section 4.3, the flywheel clutch is needed to enable disengagement of the flywheel from the drive train at some vehicle speed where the flywheel speed is sufficient for a restart of engine and vehicle. To enable the flywheel system to simultaneously speed up the engine and the vehicle, the secondary pulley clutch is needed to decouple the CVT from the driveline.

### 8.2.1 ZI Stop-Go operation

The four principal phases in the ZI Stop-Go launch sequence are sketched in Figure 8.6, where the clutch states can be closed (no slip), open (no transmitted torque) or slipping (slip and transmitted torque are both unequal to zero). Slipping refers to opening or closing of a clutch, and is never a permanent situation. Initially all five clutches are unpressurized, and therefore

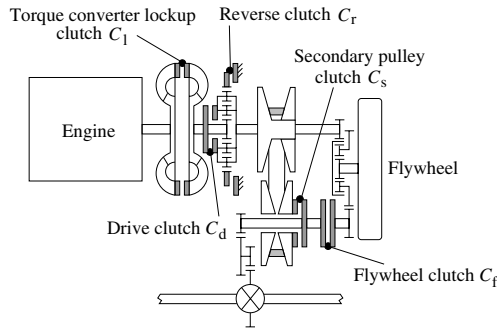


Figure 8.5: Schematic view of the mechanical Stop-Go system (torque converter is rigorously simplified)

	initial	Start	Brake	Sync	End
$C_f$					
$C_1$					
$C_r$					
$C_d$					
$C_s$					

= open   
 = slipping   
 = closed

Figure 8.6: Clutch states in ZI Stop-Go launch sequence

open, due to the release springs. The clutches  $C_1$  and  $C_r$  need to be closed at the beginning of the *Start* phase, *i.e.*, the first phase of the launch sequence. The clutch pressure is supplied by a hydraulic accumulator while the pump speed (*i.e.*,  $\omega_e$ ) is insufficient. In the *Start* phase,  $C_f$  starts closing to launch the vehicle and speed up the engine.  $C_r$  is closed to reverse the primary pulley speed, thus avoiding speeding up of the engine in the wrong direction. To enable negative pulley speeds,  $C_s$  is open in this phase.  $C_1$  is closed because the TC cannot transmit negative torque. When the engine has reached ignition speed, combustion is resumed. Then the *Start* phase is finished, and the *Brake* phase is initiated.

During the *Brake* phase  $C_d$  starts closing while  $C_r$  is still closed (or possibly opening but still transmitting torque), effectively braking the primary pulley speed to zero. This is necessary because in the *Start* phase the primary pulley speed has become negative. Simultaneously,  $C_1$  must be opened, in order not to brake the engine. As soon as the primary pulley speed is zero,  $C_r$  must be opened so the engine can start propelling the vehicle via the parallel planetary gear stage. This happens in the *Sync* phase.

While the engine speeds up the primary and the secondary pulley, the speed difference over  $C_s$  becomes smaller. When the speed difference is approximately zero,  $C_s$  can begin closing while  $C_f$  gradually disengages. The latter is done to make the transition smooth and

to prevent deceleration of the flywheel into the negative speed range. After  $C_s$  is fully closed, the *End* phase is entered. The drive train structure in the *End* phase is equal to that of the CVT driveline, with open TC. Naturally, the TC can be locked if the conditions for closing  $C_1$  are met (see, e.g., Appendix D.1.1). Moreover,  $C_f$  will be closed when the CVT speed ratio is such (i.e.,  $r_{cvt} > r_{gn}$ ) that  $\omega_f$  will be positive when re-engaged.





## Chapter 9

# ZI Stop-Go Modeling

### 9.1 Model of the ZI Stop-Go Powertrain

Figure 9.1 schematically depicts the ZI Stop-Go driveline model for controller design. Contrary to the model that will be used for simulations, the model in Figure 9.1 neglects all compliances, tire characteristics and component efficiencies. The DNR set is modeled as a two-

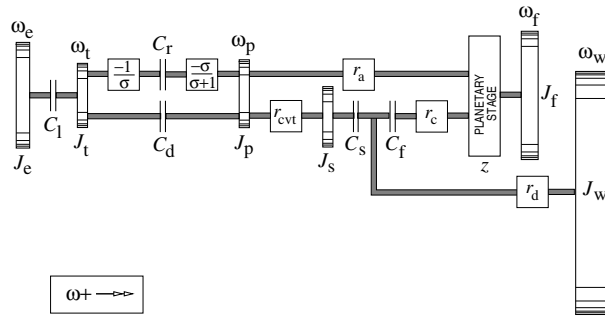


Figure 9.1: ZI Stop-Go model

channel connector, characterized by the epicyclic gear ratio  $\sigma = -2.13$ . If both  $C_d$  and  $C_r$  are open, the DNR is in Neutral. Closing  $C_d$ , while leaving  $C_r$  open results in the Drive position. On the other hand, opening  $C_d$  and closing  $C_r$  creates the Reverse position.

The relevant degrees of freedom for the ZI Stop-Go model are the engine speed  $\omega_e$  (inertia  $J_e$ ), the turbine speed  $\omega_t$  (inertia  $J_t$ ), the primary pulley speed  $\omega_p$  (inertia  $J_p$ ), the flywheel speed  $\omega_f$  (inertia  $J_f$ ) and the wheel speed  $\omega_w$  (inertia  $J_w$ ). The secondary pulley speed  $\omega_s$  is not considered as a separate degree of freedom, because its inertia  $J_s$  can always be lumped into either the primary inertia  $J_p$  (when the CVT ratio is constant) or into the wheel sided inertia  $J_w$  (when  $C_s$  is closed). The wheel sided inertia  $J_w$  comprises all inertias that are directly manifest at the output of the final reduction, *i.e.*, the vehicle mass, the inertia of all four wheels and the inertia of differential gearing and final drive. The epicyclic gear ratio of the planetary stage is denoted by  $z$  in Figure 9.1, as previously in Section 6.6.1. Besides the CVT reduction  $r_{cvt}$ , three additional reductions are depicted in this figure. The final reduction  $r_d$  is the ratio of wheel

speed (equal to drive-shaft speed in case of no compliance) over secondary shaft speed, *i.e.*,  $r_d = \omega_w / \omega_{ss}$ . The annulus reduction  $r_a$  is the ratio of primary pulley speed and annulus speed, *i.e.*,  $r_a = \omega_p / \omega_a$ . Finally, the carrier reduction is the ratio of secondary gear speed and carrier speed, *i.e.*,  $r_c = \omega_{sg} / \omega_c$ .

The relevant torques and their sign conventions are depicted in Figure 9.2. From left to right, these are the engine torque  $T_e$ , the impeller torque  $T_i$ , the torque converter lockup clutch torque  $T_{cl}$ , the turbine torque  $T_t$ , the reverse clutch torque  $T_{cr}$ , the drive clutch torque  $T_{cd}$ , the

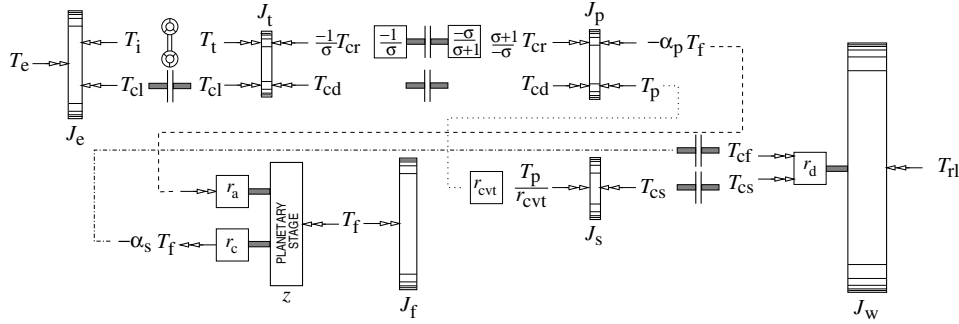


Figure 9.2: ZI Stop-Go definitions and sign conventions

flywheel torque  $T_f$ , the torque acting at the primary side of the belt  $T_p$ , the flywheel clutch torque  $T_{cf}$ , the secondary pulley clutch torque  $T_{cs}$  and the road load torque  $T_{rl}$ . From this depiction it is fairly straightforward to derive the corresponding differential equations for the various situations that may occur, depending on what clutches are closed, slipping or open.

### 9.1.1 Torque converter

In the ZI Stop-Go system, the torque converter model is operated in locked and in open (or *converter*) mode. A simple model for the converter mode in terms of the *torque ratio*  $\alpha_{tc}$ , the *capacity factor*  $b_{tc}$  and the *speed ratio*  $r_{tc}$ , is given by

$$r_{tc} = \frac{\omega_t}{\omega_i} \quad (9.1)$$

$$\alpha_{tc} = \frac{T_t}{T_i} \quad (9.2)$$

$$b_{tc} = \frac{T_i}{\omega_i^2} \quad (9.3)$$

with  $\omega_i$  ( $= \omega_e$ ) and  $\omega_t$  the speeds, and  $T_i$  and  $T_t$  the torques of impeller and turbine. Figure 9.3 gives  $\alpha_{tc}$  and  $b_{tc}$  as a function of  $r_{tc}$ .

### 9.1.2 Clutch model

Although in the remainder all clutch torques are assumed to be somehow realized by the corresponding clutch pressure, a basic clutch model is presented for completeness. Consider two inertias  $J_1$  and  $J_2$  with external torques  $T_1$  and  $T_2$ , and speeds  $\omega_1$  and  $\omega_2$ , respectively, which can be connected by a clutch with torque  $T_c$ , see Figure 9.4. The corresponding dynamics are

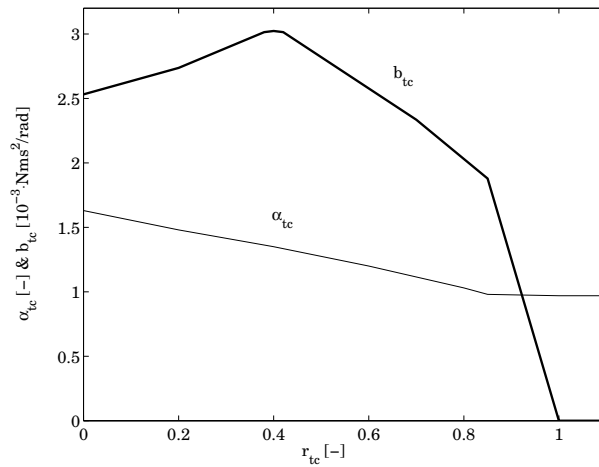


Figure 9.3: Torque converter characteristics

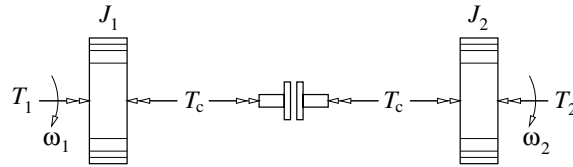


Figure 9.4: Clutch model

given by

$$J_1 \dot{\omega}_1 = T_1 - T_c \quad (9.4)$$

$$J_2 \dot{\omega}_2 = T_c - T_2 \quad (9.5)$$

The torque  $T_{\text{slip}}$  transmitted by a slipping clutch (*i.e.*,  $\omega_1 \neq \omega_2$ ) is given as

$$T_{\text{slip}} = c_c p_c \text{sign}(\omega_1 - \omega_2) \quad (9.6)$$

where  $c_c$  is a constant and  $p_c$  is the pressure applied on the clutch piston. The torque  $T_{\text{stick}}$  transmitted by the clutch in case of stick no longer relates to the pressure  $p_c$ . Instead, using (9.4) and (9.5), and  $\dot{\omega}_1 = \dot{\omega}_2$ , yields

$$T_{\text{stick}} = \frac{J_1 T_2 + J_2 T_1}{J_1 + J_2} \quad (9.7)$$

Implementing a clutch model as a submodel of a larger dynamic model requires proper handling of the changing number of degrees of freedom. One way is to incorporate a spring between the clutch halves that is active only when the clutch is closed. That way, the two degrees of freedom are always preserved. If the real system does not actually have a spring,

the stiffness of the ‘artificial’ spring should be large enough not to introduce additional dynamics in the frequency range of interest. This can result in an ill-conditioned model and in high computational demands. A preferable way to maintain two degrees of freedom is to use the method suggested in [Karnopp, 1985]. In that approach, (9.4) and (9.5) are always used, where

$$\begin{aligned} T_c &= T_{\text{slip}} & \text{if } |\omega_1 - \omega_2| > \varepsilon \\ T_c &= T_{\text{stick}} & \text{if } |\omega_1 - \omega_2| \leq \varepsilon \wedge T_{\text{slip}} \geq T_{\text{stick}} \end{aligned} \quad (9.8)$$

with  $\varepsilon$  some small positive value. In the implementation, the ‘Karnopp’ approach is adopted.

### 9.1.3 Abbreviations

Table 9.1 gives a number of abbreviations that will be used in the sequel. Note that  $\alpha_w$  is the torque amplification factor from flywheel to wheels, and  $r_r$  is the reverse gear ratio from  $\omega_t$  to  $\omega_p$ . The first index (e,t,w) in the subscripts of the various lumped inertias, indicates the shaft

SYMBOL	DEFINITION
$\alpha_w$	$\frac{\alpha_s}{r_d}$
$r_r$	$\frac{1}{\sigma+1}$
$J_{\text{cvt}}$	$J_p + r_{\text{cvt}}^2 J_s$
$J_{\text{t,r}}$	$J_t + r_r^2 J_{\text{cvt}}$
$J_{\text{e,r}}$	$J_e + J_{\text{t,r}}$
$J_{\text{t,d}}$	$J_t + J_{\text{cvt}}$
$J_{\text{t,gn}}$	$J_{\text{t,d}} + \frac{\alpha_p^2 J_f J_w}{J_w + \alpha_w^2 J_t}$
$J_{\text{w,gn}}$	$J_w + \frac{\alpha_w^2 J_f (J_t + J_{\text{cvt}})}{J_t + J_{\text{cvt}} + \alpha_p^2 J_f}$
$J_{\text{t,c}}$	$J_t + J_{\text{cvt}} + r_{\text{cvt}}^2 J_d^2 J_w$

Table 9.1: Various abbreviations and their definitions

where the inertia is evaluated (engine, turbine or wheels), the second index (r,d,gn,c) denotes respectively SG-Reverse, SG-Drive, geared neutral, or conventional.

### 9.1.4 Differential equations for the launch sequence

In the ZI Stop-Go powertrain five clutches are present, each of which can either be closed (no slip), open (no transmitted torque) or slipping. Consequently,  $2^5 = 32$  different modes exist. In practice, less than half of these modes is actually relevant. Using Figure 9.2, the differential equations corresponding to the modes that occur for the four phases in a typical launch sequence, as depicted in Figure 8.6, are presented next. Further modes will be analyzed as they present themselves, in Chapter 10.

#### Start phase

In the Start phase,  $C_f$  is closing,  $C_l$  and  $C_r$  are closed, and  $C_d$  and  $C_s$  are open. Hence, the turbine speed  $\omega_t$  is equal to the engine speed  $\omega_e$  whereas the primary pulley speed  $\omega_p$  is equal

to  $r_r\omega_e$ . The dynamics of the engine, flywheel and vehicle are governed by

$$J_{e,r}\dot{\omega}_e = T_e - \frac{r_r\alpha_p}{\alpha_s}T_{cf} - (1 - r_r)T_{cd} \quad (9.9)$$

$$J_f\dot{\omega}_f = -\frac{T_{cf}}{\alpha_s} \quad (9.10)$$

$$J_w\dot{\omega}_w = \frac{T_{cf}}{r_d} - T_{rl} \quad (9.11)$$

The term including  $T_{cd}$  is included for the convenience of general applicability (*e.g.*, in Section 10.3), although  $T_{cd} = 0$  in the Start phase. The state for this phase is  $\underline{x} = [\omega_e, \omega_f, \omega_w]'$ ; the only input in the Start phase is  $\underline{u} = T_{cf}$ . The engine torque  $T_e$  is a load, and not an input in this case. The slip speed over the flywheel clutch is given by

$$\omega_{cf} = \frac{\omega_f + r_r\alpha_p\omega_e}{\alpha_s} - \frac{\omega_w}{r_d} \quad (9.12)$$

$$(9.13)$$

### Brake phase

In the Brake phase,  $C_f$  is still closing,  $C_1$  and  $C_s$  are open,  $C_r$  is closed or releasing, and  $C_d$  is closing. Because  $C_1$  is open, the torque converter is transmitting torque in converter mode. The differential equation for  $\omega_e$  changes into

$$J_e\dot{\omega}_e = T_e - T_i; \quad T_i = b_{tc}\omega_e^2 \quad (9.14)$$

The behaviour of the flywheel and vehicle are still governed by Equations (9.10) and (9.11). While  $C_r$  is still closed,  $\omega_t$  is described by

$$J_{t,r}\dot{\omega}_t = T_t - \frac{r_r\alpha_p}{\alpha_s}T_{cf} - (1 - r_r)T_{cd}; \quad T_t = \alpha_{tc}T_i \quad (9.15)$$

and  $\omega_p = r_r\omega_t$ , whereas for  $C_r$  releasing, the differential equations for  $\omega_t$  and  $\omega_p$  are given by

$$J_t\dot{\omega}_t = T_t - T_{cd} + \frac{r_r}{1 - r_r}T_{cr} \quad (9.16)$$

$$J_{cvt}\dot{\omega}_p = T_{cd} - \frac{1}{1 - r_r}T_{cr} - \frac{\alpha_p}{\alpha_s}T_{cf} \quad (9.17)$$

The state is  $\underline{x} = [\omega_e, \omega_t, \omega_f, \omega_w, (\omega_p)]'$ ; the input is  $\underline{u} = [T_e, T_{cf}, T_{cd}, (T_{cr})]'$ .  $\omega_p$  and  $T_{cr}$  are between brackets because they are only present in  $\underline{x}$  and  $\underline{u}$  if  $C_r$  is releasing. The slip speeds for clutches  $C_d$  and  $C_r$  are given by

$$\omega_{cd} = \omega_t - \omega_p \quad (9.18)$$

$$\omega_{cr} = \frac{1}{1 - r_r}(\omega_p - r_r\omega_t) \quad (9.19)$$

### Sync phase

The Sync(hronize) phase comprises speeding up of the primary pulley until the slip speed  $\omega_{cs}$  over the secondary pulley clutch is very small, succeeded by closing  $C_s$ . Hence,  $C_s$  is open or closing,  $C_r$  and  $C_l$  are open,  $C_d$  is closed whereas  $C_f$  is first closed, and is then gradually disengaged. Equation (9.14) describes the engine dynamics. After some elaboration, the differential equations for  $\omega_t$  and  $\omega_w$ , provided  $C_f$  is closed, can be obtained as

$$J_{t,gn}\dot{\omega}_t = T_t - \frac{\alpha_p\alpha_w J_f}{J_w + \alpha_w^2 J_f} T_{rl} + \left( \frac{\alpha_p\alpha_w J_f / r_d}{J_w + \alpha_w^2 J_f} - r_{cvt} \right) T_{cs} \quad (9.20)$$

$$J_{w,gn}\dot{\omega}_w = \frac{\alpha_p\alpha_w J_f}{J_{t,d} + \alpha_p^2 J_f} T_t - T_{rl} + \left( \frac{1}{r_d} - \frac{r_{cvt}\alpha_p\alpha_w J_f}{J_{t,d} + \alpha_p^2 J_f} \right) T_{cs} \quad (9.21)$$

The primary pulley speed equals the turbine speed, *i.e.*,  $\omega_p = \omega_t$ . Since  $C_f$  is closed, the flywheel speed is kinematically determined by  $\omega_t$  and  $\omega_w$

$$\omega_f = \alpha_w\omega_w - \alpha_p\omega_t \quad (9.22)$$

The slip speed of clutch  $C_s$  is given by

$$\omega_{cs} = r_{cvt}\omega_t - \frac{\omega_w}{r_d} \quad (9.23)$$

For this mode, the state is  $\underline{x} = [\omega_e, \omega_t, \omega_w]^T$  while the input is  $\underline{u} = [T_e, T_{cs}]^T$ .

When the flywheel clutch opens, while  $C_s$  is closing, the turbine and wheel speed dynamics are described by

$$J_{t,d}\dot{\omega}_t = T_t - \frac{\alpha_p}{\alpha_s} T_{cf} - r_{cvt} T_{cs} \quad (9.24)$$

$$J_w\dot{\omega}_w = \frac{T_{cf} + T_{cs}}{r_d} - T_{rl} \quad (9.25)$$

Obviously,  $\underline{u}$  is now augmented with  $T_{cf}$ . In all phases up to and including the Sync phase, the desired CVT ratio is constant and equal to  $r_{ud}$ .

### End phase

The End phase constitutes the normal CVT driveline situation. It is reached when  $C_s$  is closed. Furthermore,  $C_f$ ,  $C_r$  and  $C_l$  are open and  $C_d$  is closed. If the conditions for torque converter lockup are met,  $C_l$  may also be closed. In practice, this will not happen before the End phase is started. In this phase  $r_{ud} \leq r_{cvt} \leq r_{od}$ .

Since the focus of Part III is not on this phase, the corresponding models for this phase (with or without the flywheel) are not stated here, but may be found in [Serrarens, 2001].

## 9.2 Minimum flywheel speed

In the present section, it is determined what flywheel speed is minimally needed to both launch the vehicle and speed up the engine, up to the point where the engine can take over propelling the vehicle. This means that the engine must be accelerated far *beyond* the speed

where combustion can be resumed ( $\omega_{e,\text{ign}}$ ), *i.e.*, to the idle speed  $\omega_{e,\text{idle}}$ . In the actual implementation, combustion will be resumed at  $\omega_{e,\text{ign}}$ , from where the engine speeds up itself (with open torque converter), while the closing drive clutch takes over from the drag torque. In the present analysis, the simplifying assumption is made that the engine is dragging until its speed reaches  $\omega_{e,\text{idle}}$ . Doing so, equation (9.9) for the engine dynamics in the first stage can be applied (with  $T_{\text{cd}} = 0$ ), yielding

$$J_{e,r}\dot{\omega}_e = \alpha_p r_r J_f \dot{\omega}_f - T_{e,\text{drag}} \quad (9.26)$$

Furthermore, Equation (9.11) with (9.9) and  $T_{\text{cd}} = 0$  gives

$$J_w \dot{\omega}_w = -\frac{\alpha_w}{\alpha_p r_r} (J_{e,r} \dot{\omega}_e + T_{e,\text{drag}}) - T_{r1} \quad (9.27)$$

Up to  $t = t_1$ , when the engine reaches idle speed, the flywheel must be able to drive the vehicle. If the flywheel clutch were closed before that time,  $\dot{\omega}_f = \alpha_w \dot{\omega}_w - r_r \alpha_p \dot{\omega}_e$  should be negative in order to exert a positive torque at the wheels and at the engine. Since both  $\dot{\omega}_w$  and  $\dot{\omega}_e$  should be positive at least until  $t = t_1$ , it is immediately seen that such a situation can never occur (since  $\alpha_w > 0$  and  $-r_r \alpha_p > 0$ ). Therefore, the flywheel clutch must remain slipping until  $t = t_1$ , so  $r_d \omega_{\text{sg}} > \omega_w$  should hold until then. The latter translates to

$$\omega_f(t_1) > \alpha_w \omega_w(t_1) - r_r \alpha_p \omega_{e,\text{idle}} \quad (9.28)$$

Integrating (9.26) and (9.27) from the starting time  $t_0$  until time  $t_1$ , in combination with (9.28), gives

$$\omega_f(t_0) > -\omega_{e,\text{idle}} \left( \frac{J_{e,r}(J_w + \alpha_w^2 J_f)}{\alpha_p r_r J_f J_w} + \alpha_p r_r \right) - \frac{J_w + \alpha_w^2 J_f}{\alpha_p r_r J_f J_w} \int_{t=t_0}^{t=t_1} T_{e,\text{drag}}(t) dt - \frac{\alpha_w}{J_w} \int_{t=t_0}^{t=t_1} T_{r1}(t) dt \quad (9.29)$$

The first term in the right-hand-side is entirely determined by fixed system parameters and by the idle speed  $\omega_{e,\text{idle}}$ . The two other terms depend on the course of  $T_{e,\text{drag}}$  and  $T_{r1}$  in time, hence indirectly on the way the flywheel clutch is closed, *i.e.*, on the course of  $T_{\text{cf}}$  in time.

Because the time interval between  $t_0$  and  $t_1$  will generally be small (as will also appear from the results), it seems realistic to assume that the position of the accelerator pedal and therefore the demanded wheel torque in this interval are constant. Consequently (when neglecting the dynamics of the closed-loop clutch controller)  $T_{\text{cf}}$  can be assumed constant. Moreover, since the vehicle speed  $\omega_w$  in this phase is small, air drag will be very small compared to rolling resistance  $T_r$  and a possible road slope contribution  $m_v g R_w \sin \varrho$  (with  $\varrho$  the road slope), and is therefore neglected, yielding

$$T_{r1} = T_r + m_v g R_w \sin \varrho \quad (9.30)$$

$T_{r1}$  is assumed to be constant in the interval  $t_0$  to  $t_1$ . The brake pedal is regarded as a driver input which increases the load on the wheels. The resulting (disc) brake torque may be lumped into the road load, but is assumed to be zero in this investigation. Finally, the engine drag torque  $T_{e,\text{drag}}$  is a function of engine speed  $\omega_e$ . For simplicity though, in the elaboration of (9.29)  $T_{e,\text{drag}}$  is assumed constant and equal to 15 [Nm].

The minimum initial flywheel speed  $\omega_f(t_0)$  and the (average) vehicle acceleration  $\dot{v}_v$  can be determined as a function of  $t_1$  and road slope  $\varrho$ , using (9.29) and the integral of (9.27), respectively. Since  $T_{\text{cf}}$  and  $T_{r1}$  were assumed constant, the average vehicle acceleration equals



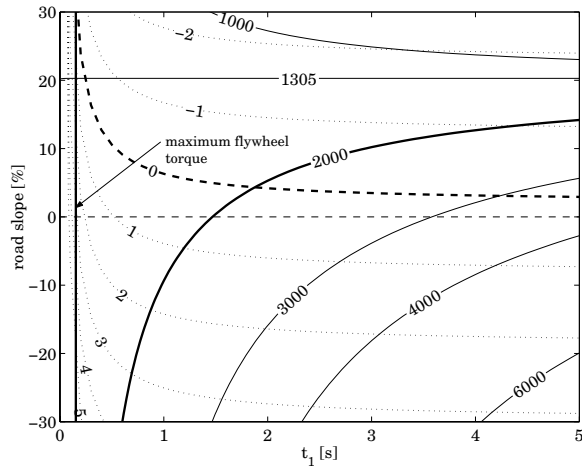


Figure 9.5: Minimally required flywheel speed and corresponding vehicle acceleration as a function of time  $t_1$  [s] and road slope  $\rho\%$

the momentary value for all  $t \in [t_0, t_1]$ . This yields Figure 9.5, which depicts the minimal initial flywheel speed (in [rpm], solid lines) and  $\dot{v}_v$  (in  $[m/s^2]$ , dashed lines) as a function of  $t_1$  and  $\rho$ . The bold flywheel speed contour line corresponds to 2000 [rpm], which is a realistic value for implementation. The bold-dashed contour line indicates  $\dot{v}_v = 0$  and forms a boundary for the practical operating region, since negative vehicle accelerations are prohibited if the gear lever is in Drive position. The bold vertical line (apparently coinciding with  $t_1 \approx 0.15$  [s]) corresponds to the maximum torque that the flywheel is allowed to exert on the sun gearing (180 [Nm]). From the figure it is seen that the minimal initial flywheel speed increases, and the vehicle acceleration decreases with  $t_1$ , at least for  $\rho < 20\%$ . For a road slope close to 20%, the minimal initial flywheel speed is independent of  $t_1$  and equals 1305 [rpm]. This speed is exactly the first term of the right-hand-side in (9.29). Actually, for  $t_1 = 0$  the contour line for 1305 [rpm] changes discontinuously from  $\rho \approx 20\%$  to  $\rho = 0$ . Finally, it is observed that the bold line corresponding to an initial flywheel speed of 2000 [rpm] imposes a minimal vehicle acceleration, which is larger than zero for  $\rho < 4.3\%$ .

The latter is illustrated more clearly in Figure 9.6, where the minimal initial flywheel speed is depicted versus the vehicle acceleration and the road slope. As is seen from this figure, two constraints—depicted as bold lines—limit the vehicle acceleration that can be achieved. The *maximum* vehicle acceleration is bounded by the maximum flywheel torque. For instance, on a flat road the maximum acceleration possible is 3.23  $[m/s^2]$ . Obviously, the maximum value increases for downhill and decreases for uphill driving. The *minimum* vehicle acceleration is imposed by the initial flywheel speed (in this case 2000 [rpm]). The explanation for this is twofold, and requires insight in the *final* vehicle speed, *i.e.*,  $v_v$  at  $t = t_1$ . This speed is shown in Figure 9.7, again as a function of vehicle acceleration and road slope.

First, consider a flat road situation, see Figure 9.7. For lower accelerations, the final vehicle speed slightly increases, and therefore also the final kinetic energy of the vehicle. Because the vehicle acceleration is lower,  $t_1$  is also larger. This increases the dissipated energy both at the engine and at the vehicle side, whereas the final kinetic energy of the engine remains the same. All in all, the required initial flywheel energy is larger. The second reason is a more

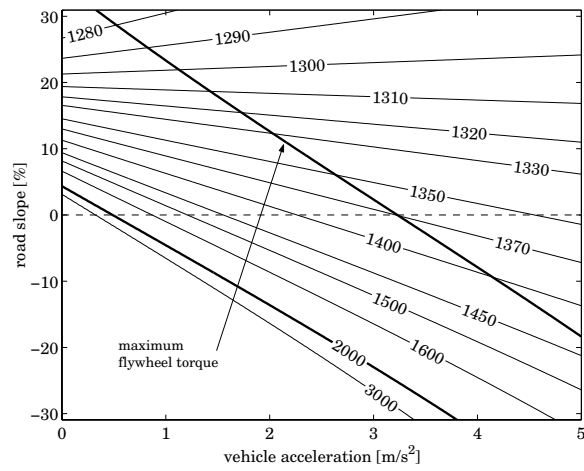


Figure 9.6: Minimally required flywheel speed [rpm] as a function of vehicle acceleration [ $\text{m/s}^2$ ] and road slope  $\rho\%$

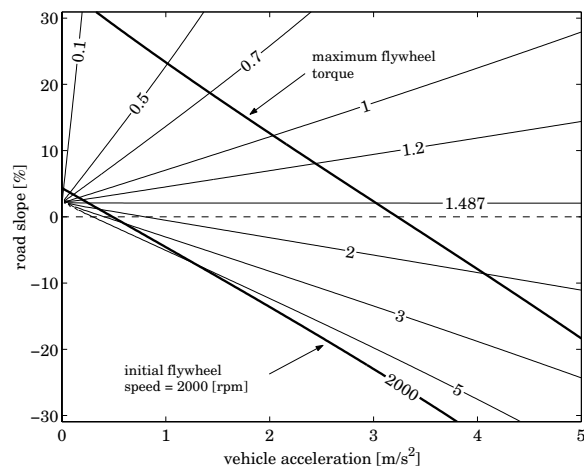


Figure 9.7: Vehicle speed [km/h] at  $t = t_1$ , versus vehicle acceleration [ $\text{m/s}^2$ ] and road slope  $\rho\%$

kinematic one, and stems from the requirement that a positive slip speed over the flywheel clutch is needed in order to exert a positive torque at the wheels. The consequence is that for downhill driving, where the vehicle speed tends to increase without propulsion, the initial flywheel speed needs to be systematically higher, whereas for hill climbing the necessary flywheel speed is relatively low, see Figure 9.6. Finally, it is stressed that in the previous analysis it was assumed that the initial flywheel speed equals the minimally needed value. In the eventual implementation, the initial flywheel speed will be fixed at 2000 [rpm], hence the final

vehicle speed for conditions between the two bold lines in Figure 9.7 will be generally higher than what is depicted, since the synchronization of the flywheel clutch happens later.

The minimum acceleration level (e.g.,  $0.48 \text{ [m/s}^2\text{]}$  for a flat road) requires special consideration, with respect to the translation of the accelerator and brake pedal into to-be-controlled variables.

### 9.3 Pedal interpretation

In this section, a translation of the normalized accelerator pedal position  $\delta \in (0 \dots 1)$ , and the brake pedal force  $\beta \geq 0 \text{ [N]}$  into setpoints for the various clutch torques as well as for the engine torque is presented. In the normal ZI driveline, a translation of pedal position into *wheel* power is used most of the time, except for low vehicle speeds. Then the accelerator pedal can be thought to be directly linked to the throttle valve, as in a conventional powertrain. An interpretation like that is appropriate in the ZI Stop-Go powertrain after the secondary pulley clutch is closed. Before that, a pedal to wheel power interpretation is problematic, because then the vehicle speed is zero or very low, meaning that only zero or very low wheel powers can be realized. Hence, demanding for a wheel power other than zero (or very low) is useless. Translating the accelerator pedal into a desired *engine* power in this situation is equally impractical since the TC torque versus speed curves for low vehicle speeds (hence low TC speed ratios  $r_{tc}$ ) make it impossible to reach maximum engine power, see Figure 9.8. Also, the relationship between engine power and resulting wheel torque may be rather untransparent.

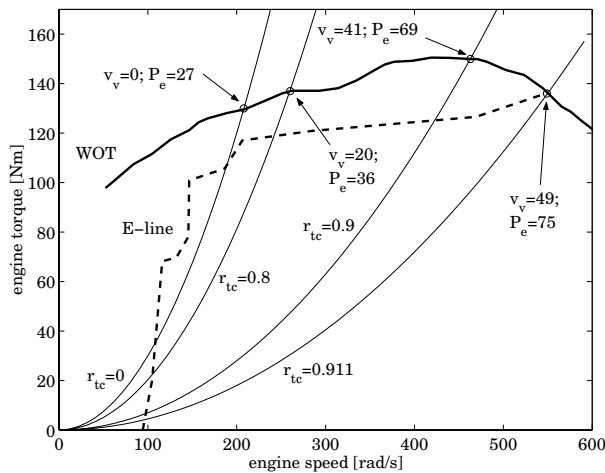


Figure 9.8: Engine torque  $T_e$  [Nm] versus engine speed  $\omega_e$  [rad/s] for various TC speed ratios  $r_{tc}$ ; at the intersections between the TC curves and the WOT line the corresponding engine power  $P_e$  [kW] and vehicle speed  $v_v$  [km/h] are shown, assuming a CVT ratio  $r_{cvt} = r_{ud}$

### 9.3.1 Torque interpretation

Translating the pedal position  $\delta$  into a desired wheel torque  $T_{w,d}$  seems to be the more intuitive choice, at least for the low vehicle speed regime. Let  $T_{w,d}$  as a function of  $\delta$  be given as

$$T_{w,d} = f(\delta)(T_{w,d}^{\max} - T_{w,d}^{\min}) + T_{w,d}^{\min} \quad (9.31)$$

where  $f(\delta)$  is a strictly increasing function, with  $f(0) = 0$  and  $f(1) = 1$ . Both the minimum and the maximum desired wheel torque ( $T_{w,d}^{\min}$  and  $T_{w,d}^{\max}$ ) can be a function of vehicle speed, engine speed, slope, etc.

For instance, for an AT with torque converter  $T_{w,d}^{\min}$  may be imposed by the *creep torque*, which can be significant. The torque converter used in the ZI (or for that matter, CVT, and further on indicated as ZI-CVT) transmission, qualifies as a rather 'soft' one (*i.e.*, the turbine torque for a certain impeller speed is relatively small, see [Lechner and Naunheimer, 1999]), having a creep torque at engine idle speed of  $T_w \approx 200$  [Nm]. Creep torques more than two times as high are not uncommon. Figure 9.9 compares the creep torque of the standard ZI-CVT transmission with the one that is needed for ZI Stop-Go, in order to guarantee an engine restart. At negative slopes, the torque needed for engine restart amounts up to circa 450 [Nm],

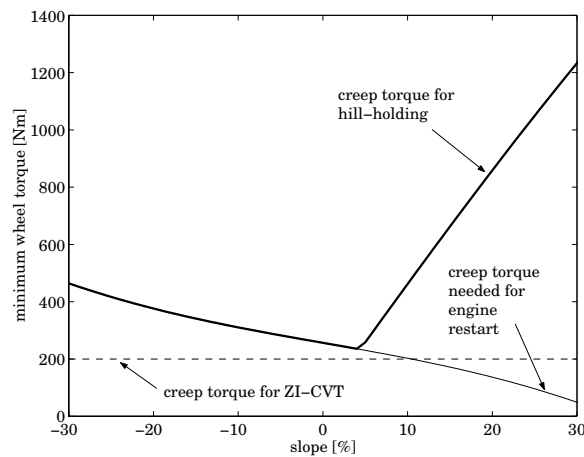


Figure 9.9: Initial creep torque [Nm] versus the slope  $\varrho\%$

while for positive slopes the minimally needed torque is much smaller than the wheel torque required to overcome the road load (gravity). To prevent roll-back of the vehicle (also known as *hill-holding*, see *e.g.*, [Vahabzadeh and Linzell, 1991]), it is chosen to use the creep torque depicted by the bold solid line, in Figure 9.9. Implementing such a strategy requires a procedure similar to the one used in the Volkswagen Lupo and Audi A2, recall Section 8.1.3. Restarting the engine when the brake pedal is released is not really a problem, apart from the fact that, in order to warrant an engine restart, the flywheel torque should at least equal the minimum creep torque (thin solid line in Figure 9.9) divided by  $\alpha_w$ . Hence, some knowledge is necessary about the actual slope. A simple inclinometer would be sufficient for this purpose, since the slope information is needed only at vehicle standstill.

Next, a realistic value for  $T_{w,d}^{\max}$  is determined. The maximum torque  $T_w^{\max}$  in a conventional driveline is limited by the maximum engine torque (which is a function of engine speed),

and by the maximum torque amplification by the transmission, possibly including the torque amplification of a torque converter. It is up to the manufacturer on the one hand and the driver on the other, whether or not the vehicle should be able to 'burn rubber,' *i.e.*, if the maximum wheel torque should be larger than the torque which can be transmitted by the driven tires on a dry road ( $\approx 1600$  [Nm] in this case). In the present investigation, the maximally transmittable torque is not treated as a limiting factor.

Taking a closer look at the combination of engine, torque converter and CVT in the ZI vehicle reveals that the maximum torque that can be delivered at vehicle standstill is approximately 2100 [Nm]. This value drops to circa 1350 [Nm] for  $v_v = 20$  [km/h]. If the ZI (or CVT) powertrain didn't have a torque converter but a launching clutch instead, the maximum wheel torque would be limited to 1500 [Nm], imposed by the maximum engine torque at the WOT-line at  $\omega_e \approx 400$  [rad/s]. In order to have the engine constantly operate at this speed, the launching clutch must slip until  $v_v \approx 40$  [km/h]. In the ZI Stop-Go driveline, matters are a bit more complex. In the beginning of the launch sequence, when  $C_f$  is closing, the maximum wheel torque is limited by the maximum flywheel torque and equals  $180\alpha_w\eta_g \approx 1400$  [Nm], where  $\eta_g$  is the efficiency of the geartrain from flywheel to driveshaft (assumed at 98 [%]). After that, the engine needs to take over, resulting in a maximum wheel torque of  $T_e\alpha_{tc}\alpha_w\eta_g/\alpha_p \approx 1300$  to 1100 [Nm], as the vehicle speed rises to about 20 [km/h]. The wheel torque drops because of the TC characteristic, and is generally lower than what can be delivered via the CVT, because the effective torque amplification factor through the parallel stage ( $\alpha_p/\alpha_s$ ) is lower than through the CVT ( $1/r_{ud}$ ).

### 9.3.2 Power interpretation

Interpreting the pedal position as a torque is not without problems. Obviously, for large vehicle speeds the lowest CVT speed ratio cannot be maintained, for otherwise the engine speed would exceed its maximum,  $\omega_{e,max}$ . Because the TC is not as efficient in amplifying torque as the CVT,  $T_w = T_{w,max}$  can no longer be realized from the point where  $\omega_e = \omega_{e,max}$ , since the CVT needs to shift up. This would result in an accelerator pedal which is ineffective for some part of its excursion. Therefore, a power interpretation appears more suitable from this point onward. As a consequence, the transition from torque to power interpretation must be given some attention, so as to make it continuous and, preferably, monotonic with respect to the realized wheel torque. The desired wheel power is given by

$$P_{w,d} = g(\delta)(P_{w,d}^{max} - P_{w,d}^{min}) + P_{w,d}^{min} \quad (9.32)$$

where  $g(\delta)$  is a strictly increasing function with  $g(0) = 0$  and  $g(1) = 1$ .  $P_{w,d}^{min}$  may be related to  $T_{w,d}^{min}$  (*e.g.*,  $P_{w,d}^{min} = T_{w,d}^{min}\omega_w$ ), while for  $P_{w,d}^{max}$  it makes sense to take the maximum wheel power, *i.e.*,  $\eta_{cvt}P_{e,max} \approx 68$  [kW].

### 9.3.3 Transition between torque and power interpretation

In order to make the change in interpretation from power to torque and vice versa a continuous one,  $P_{w,d}$  and  $T_{w,d}\omega_w$  should be equal at the point of transition, so the switching speed  $\omega_{w,sw}$  is given by

$$\omega_{w,sw} = \frac{g(\delta)P_{w,d}^{max}}{f(\delta)T_{w,d}^{max} + (g(\delta) - f(\delta))T_{w,d}^{min}} \quad (9.33)$$

$$(9.34)$$

which is undefined for  $\delta = 0$ . If  $f(\delta) \equiv g(\delta)$ ,  $\omega_{w,sw} = P_{w,d}^{\max} / T_{w,d}^{\max}$ . For example, when taking a constant  $T_{w,d,\max} = 1600$  [Nm] and  $P_{w,d}^{\max} = 68$  [kW], then  $\omega_{w,sw} \approx 42$  [rad/s] (circa 46 [km/h]), independent from  $\delta$ . In the remainder it is chosen to take  $g(\delta) = f(\delta) = \delta$ , simply because no good reasons exist to use a more complex function.

### 9.3.4 CVT and TC operation

The setpoint generation for the CVT ratio and for the TC lockup clutch after the secondary clutch is closed, is needed in the End phase only and is detailed in Appendix D. During all other phases the desired CVT ratio  $r_{cvt,d}$  is equal to  $r_{ud}$ , whereas the TC lockup clutch state is determined by the supervisory controller.



# Chapter 10

## ZI Stop-Go Control

As is apparent from the previous chapter, the Stop-Go powertrain has different modes, due to the various clutches which can be open, closed or slipping. Consequently, the system is *hybrid*, since it combines continuous and discrete states. These hybrid characteristics obviously necessitate a hybrid controller, *i.e.*, different modes require different control laws. Even during one mode, the control laws might switch due to the fact that some criteria issue discrete events. This chapter concentrates on deriving and analyzing the appropriate control strategies for the four phases of the launch sequence. In deriving the control laws, it is assumed that no torque measurements are available. Consequently, if any torque signals are needed in the control laws, these signals should be reconstructed from speeds, possibly in combination with component characteristics (such as engine and TC map).

### 10.1 General ideas for controlling ZI Stop-Go

Before deriving the control strategies for managing the Stop-Go launch sequence, it is useful to illustrate some of the mechanisms that should be taken into account. This is done using a graphical representation of the speed relations, known as a *nomograph*. For instance, consider Figure 10.1. In this representation three speed axes are drawn as horizontal lines, whereas the vertical axis is the zero speed (*base*) line. The upper axis holds the primary speed ( $n_p$ , in [rpm] for convenience), and possibly the turbine speed and the engine speed, depending on what clutches are actually engaged. The middle axis holds the secondary gear speed ( $n_{sg}$  in [rpm]), and possibly the secondary shaft speed and pulley speed. The vehicle speed  $v_v$ , which is directly linked to  $n_{ss}$ , may also be depicted along the middle axis. The lower axis holds the flywheel speed ( $n_f$  in [rpm]). The primary speed, the secondary gear speed and the flywheel speed can always be connected by a straight line, which represents the planetary gear relation. Also, the forces (torques) acting on the corresponding inertias (depicted as spheres with size proportional to the moment of inertia) can be drawn in the nomograph.

#### Start phase

The nomograph of Figure 10.1 is used to illustrate the Start phase of the launch sequence. The starting point is represented by the dashed line, so  $n_p (= n_e = n_t) = 0$  [rpm],  $n_f = 2000$  [rpm], and  $n_{sg} \approx 1200$  [rpm]. Upon engaging  $C_i$ , the torque  $T_{cf}$  hoists up the vehicle inertia (large



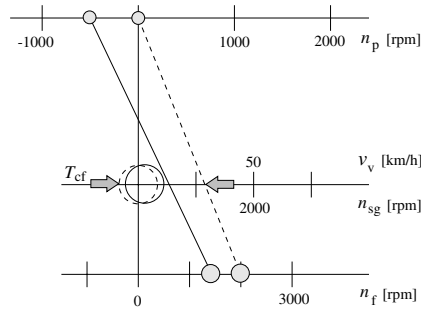


Figure 10.1: Nomograph for Start phase

transparent sphere), slowing down  $n_{sg}$  and the primary and flywheel inertias ‘attached’ to it via the dashed line. At the end of the Start phase  $n_p \approx -500$  [rpm], which corresponds to an engine speed around 600 [rpm] (DNR is in reverse), *i.e.*, ignition speed. In this example, the flywheel speed has dropped to circa 1400 [rpm], and the vehicle speed is between 1 and 2 [km/h]. The transition between the dashed and the solid line can take between 0.15 and 1.5 [s] (recall Figure 9.7), depending on the actual flywheel clutch torque  $T_{cf}$ .

### Brake phase

Next is the Brake phase, illustrated in Figure 10.2. By engaging  $C_d$  a torque  $T_{cd}$  is exerted

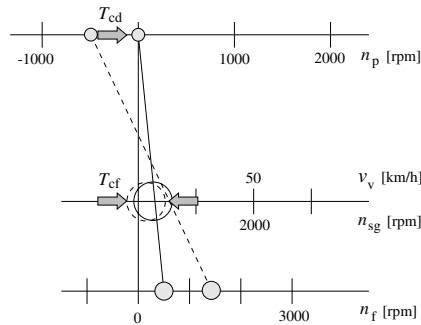


Figure 10.2: Nomograph for Brake phase

on the primary pulley, braking it to zero. At the same time,  $C_1$  is opened (not shown) to avoid braking of the engine, while enabling the engine to further accelerate itself towards idle speed. Because the DNR is still in reverse, care should be taken not to apply too much engine torque, because it will tend to decelerate the primary pulley towards more negative speeds, and consequently lower  $n_{sg}$  and therefore the slip over the flywheel clutch. This devaluates the use of any flywheel speed, no matter how high. Meanwhile,  $T_{cf}$  is still accelerating the vehicle and ‘moving the dashed line’ towards the vehicle inertia. Both  $T_{cd}$  and  $T_{cf}$  lower the flywheel speed. When  $n_p = 0$  [rpm], the vehicle speed has reached circa 5 [km/h], and the flywheel speed is down to approximately 500 [rpm]. Around this point, the slipping speed

over the flywheel clutch will be close to zero, hence  $C_f$  can be closed. Moreover, the engine will have reached idle speed from where it may propel the vehicle.

### Sync phase

As soon as  $n_p = 0$  [rpm], the reverse clutch is released, and the engine has to accelerate the turbine and the primary pulley. Therefore, the torque driving the primary pulley is  $T_t$ , see Figure 10.3. In this figure the primary and secondary pulley speed can be connected by a straight line, representing the CVT. If the CVT is not shifting, like in the launch sequence, where  $r_{cvt} = r_{ud}$ , the CVT ratio can be depicted as a pivot located on the base line. During

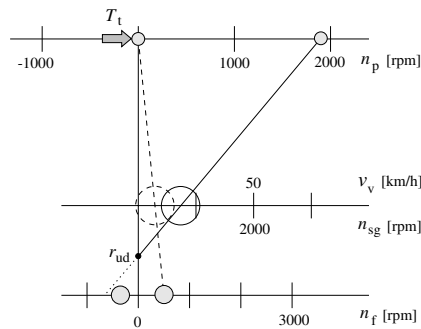


Figure 10.3: Nomograph for Sync phase

the transition towards the depicted end situation ( $n_p \approx 1900$  [rpm],  $v_v \approx 20$  [km/h],  $C_s$  closed) the flywheel speed decreases from 500 [rpm] towards negative speeds. Once  $C_s$  can actually be engaged, speeding down the flywheel below zero makes no sense, because it increases the flywheel energy in a situation where all energy should be directed towards accelerating the vehicle. It is therefore decided to gradually disengage the flywheel while  $C_s$  is closing, which is also useful to make the transition towards the End phase a smooth one. The implications for control will become clear in Section 10.4.

Figure 10.4 illustrates the resulting synchronization process in more detail, where the sphere corresponding to the vehicle inertia is omitted for clarity. In this depiction, three consecutive situations are shown. The initial situation is indicated by the two dashed lines, the second by the dot-dashed line, and the third and final situation by the two solid lines. For each situation, one line runs through the primary and the flywheel speed (corresponding to the planetary gear) and a second line runs through the pivotal point of the CVT, for which  $r_{cvt} = r_{ud}$ . For the dot-dashed situation these two lines (deliberately) coincide. Initially, the primary pulley speed is a little above zero (circa 100 [rpm]), whereas the flywheel speed is around 400 [rpm], so  $n_{sg} \approx 300$  [rpm]. Because  $C_f$  is closed,  $n_{ss} = n_{sg}$ . The speed of the secondary pulley  $n_s$  can be constructed by drawing a line through  $n_p$  and the pivotal point, corresponding to  $r_{cvt} = r_{ud}$ , and is slightly above zero (circa 50 [rpm]). Closing  $C_s$  at this point would result in a severe torque recession at the wheels, and is therefore postponed until  $n_s \approx n_{ss} = n_{sg}$ . The exact moment when this happens, is depicted by the dot-dashed line. As explained in the above,  $C_f$  is opened while  $C_s$  is closing, so henceforth  $n_s = n_{ss}$  and  $T_{cf} = 0$ . If flywheel losses are neglected, this implies that  $n_f$  no longer changes. Accelerating the primary pulley (and thus the vehicle) further, introduces an increasing speed difference between  $n_{sg}$  and  $n_{ss} = n_s$ .

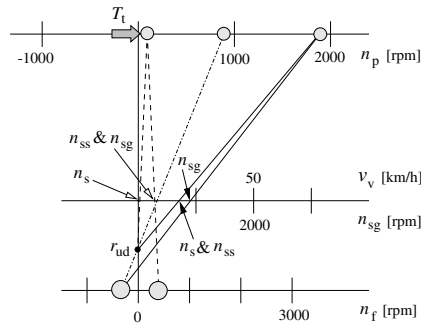


Figure 10.4: Nomograph for the actual synchronization process of the secondary pulley clutch  $C_s$

At some point later when (the CVT speed ratio is such that)  $n_{ss} \approx n_{sg}$  the flywheel clutch can be (gradually) re-engaged.

### End phase

The final state of the Sync phase constitutes a special case of the End phase. Figure 10.5 depicts a typical situation that arises when the vehicle is (mildly) accelerated from a stationary speed situation. In the depicted example, the engine speeds up from 1300 to 2300 [rpm],

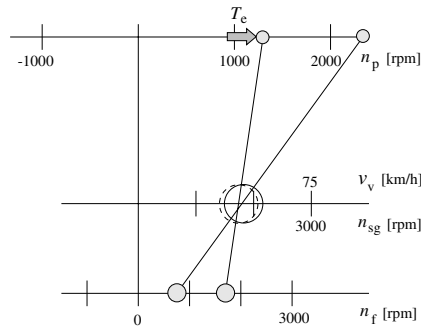


Figure 10.5: Nomograph for ZI Stop-Go powertrain in End phase;  $C_f$  closed

for  $v_v \approx 45$  [km/h], resulting in the flywheel decelerating from 1700 to 750 [rpm]. In this particular example, the energy that the flywheel emits to the driveline is slightly higher than what is needed to increase the engine's kinetic energy. The operation of the driveline in ZI mode is treated extensively in [Serrarens, 2001], and therefore not treated here.

An important issue in deriving the control strategies for the various stages is to prevent driveline oscillations due to discontinuities in the clutch torques, both in closing and opening of a clutch. In short, the basic strategy aims to:

- open a clutch when the transmitted torque is zero;

- fully engage a clutch when the torque corresponding to the applied clutch pressure equals the stick torque.

Both these strategies require the reconstruction of the torque transmitted by the clutch. This may be undesirable in practice, though the strategies themselves are useful as a starting point for deriving the control laws.

## 10.2 Control strategy for the Start phase

In the Start phase,  $C_f$  is closing in order to start the engine and launch the vehicle at the same time. Although it is vital to ensure that the engine can always restart, the exact trajectory along which the engine speed increases is not of particular interest, besides possible issues related to noise. The main control target for the flywheel clutch is therefore to realize the desired wheel torque as it is interpreted from the accelerator (and brake) pedal (see Section 9.3). As a result, the desired flywheel clutch torque is simply given by

$$T_{cf,d0} = r_d T_{w,d} \quad (10.1)$$

where  $T_{w,d}$  is the desired wheel torque. Differentiation of Equation (9.12), using Equations (9.9)–(9.11), yields a relation for the flywheel clutch slip speed

$$\dot{\omega}_{cf} = \frac{r_r \alpha_p}{\alpha_s} \frac{T_e}{J_{e,r}} + \frac{T_{rl}}{r_d J_w} - \left( \frac{1}{\alpha_s^2 J_f} + \frac{r_r^2 \alpha_p^2}{\alpha_s^2 J_{e,r}} + \frac{1}{r_d^2 J_w} \right) T_{cf} \quad (10.2)$$

The engine drag torque ( $T_e = -T_{e,drag} < 0$ ) tends to increase the slip speed, while  $T_{cf} > 0$  obviously lowers  $\omega_{cf}$  to zero. Normally  $T_{cf} > 0$ , though it will change sign if the slip speed itself becomes negative, so either way the slip will eventually vanish, if the flywheel clutch pressure is positive. The road load  $T_{rl}$ , will increase the slip speed if  $T_{rl} > 0$ . When going downhill  $T_{rl}$  may be well below zero and then tends to synchronize the flywheel clutch, as was discussed from an other viewpoint in Section 9.2. The Start phase terminates when the engine speed has reached  $\omega_{e,ign}$ .

## 10.3 Control strategy for the Brake phase

During the Brake phase, the following targets are to be accomplished:

- the engine speed must be raised from ignition speed  $\omega_{e,ign}$  to idle speed  $\omega_{e,idle}$ , from which point onward the engine can deliver a substantial torque;
- the lockup clutch must be disengaged;
- the primary pulley must be braked to zero and the drive clutch must be fully closed;
- the reverse clutch must be released.

### 10.3.1 Unlocking the torque converter

Opening the TC lockup clutch  $C_1$  could introduce driveline oscillations if  $C_1$  was still transmitting torque at the moment of disengagement. Therefore, the aim is to steer  $T_{cl}$  to zero (by controlling  $T_e$ ), while  $T_{cd}$  takes over the role of balancing  $T_{cf}$ . Meanwhile,  $C_f$  is still controlled to realize a desired wheel torque, cf. Equation (10.1). When the torque transmitted by  $C_1$  is zero,  $C_1$  can open. Summarizing, the engine torque control should be directed towards achieving  $\omega_e = \omega_{e,idle}$  and  $T_e = 0$  (i.e., the engine delivers only the torque needed to overcome its own losses and to drive the accessories (PTO)). Hence, the following control laws for the desired engine torque  $T_{e,d1}$  and drive clutch torque  $T_{cd,d1}$  are proposed

$$T_{e,d1} = -T_{e,drag} + k_1(\omega_{e,ign} - \omega_e) + k_2 \int (\omega_{e,idle} - \omega_e) dt \quad (10.3)$$

$$T_{cd,d1} = T_{cd,ff1} + k_3(\omega_{e,idle} - \omega_e) \quad (10.4)$$

In (10.3) an offset equal to  $-T_{e,drag} - k_1(\omega_{e,idle} - \omega_{e,ign})$  is introduced to make the change from the engine drag torque to  $T_{e,d1}$  cf. (10.3) a continuous one. On the other hand, the integral action makes sure that the offset is gradually removed, so  $T_{cl}$  can become zero eventually (even before  $\omega_e = \omega_{e,idle}$  as will be shown further on).

The control law for  $T_{cd,d1}$  has a feedforward term  $T_{cd,ff1}$  and a feedback term  $k_3(\omega_{e,idle} - \omega_e)$ . The feedforward term is obtained from Equation (9.9) by setting  $\dot{\omega}_e = 0$ ,  $\omega_e = \omega_{e,idle}$  and  $T_{e,d1} = 0$ , yielding

$$T_{cd,ff1} = \frac{-r_r}{1-r_r} \frac{\alpha_p}{\alpha_s} T_{cf} \quad (10.5)$$

In order to have  $T_{cd,d1} = 0$  when entering the Brake phase,  $k_3$  is determined as

$$k_3 = \frac{T_{cf}}{\omega_{e,idle} - \omega_{e,ign}} \frac{\alpha_p r_r}{\alpha_s (1-r_r)} \quad (10.6)$$

Define the speed control error as  $e = \omega_{e,idle} - \omega_e$ . Combining Equations (9.9), and (10.3)–(10.6), the error dynamics are obtained as

$$\dot{e} = \frac{1}{J_{e,r}} \left[ T_{e,drag} + k_1(\omega_{e,idle} - \omega_{e,ign}) - \left( k_1 - \frac{T_{cf}}{\omega_{e,idle} - \omega_{e,ign}} \frac{\alpha_p r_r}{\alpha_s} \right) e - k_2 \int e dt \right] \quad (10.7)$$

which is stable if

$$k_1 > \frac{T_{cf}}{\omega_{e,idle} - \omega_{e,ign}} \frac{\alpha_p r_r}{\alpha_s} < 0 \quad \wedge \quad k_2 > 0 \quad (10.8)$$

The first condition can be accomplished simply by taking  $k_1 > 0$ .

The torque converter clutch should be opened when  $T_{cl} = 0$ . Therefore, it is important to show that  $T_{cl}$  will in fact become zero when  $\omega_e \leq \omega_{e,idle}$ . The torque transmitted by  $C_1$  when this clutch is closed is given by

$$T_{cl} = \frac{J_e \left[ \frac{r_r \alpha_p}{\alpha_s} T_{cf} + (1-r_r) T_{cd} \right] + J_{t,r} T_e}{J_{e,r}} \quad (10.9)$$

Substituting  $T_{cd} = T_{cd,d1}$  and  $T_e = T_{e,d1}$  gives

$$T_{cl} = \begin{cases} \frac{J_e T_{cf} \frac{r_r \alpha_p}{\alpha_s}}{J_{e,r}} - J_{t,r} T_{e,drag} < 0 & \text{for } \omega_e = \omega_{e,ign} \\ J_{t,r} \dot{\omega}_e & \text{for } \omega_e = \omega_{e,idle} \end{cases} \quad (10.10)$$

and practically,  $\dot{\omega}_e > 0$  for  $\omega_e = \omega_{e,\text{idle}}$ , so  $T_{\text{cl}}$  must have been zero somewhere in between  $\omega_e = \omega_{e,\text{ign}}$  and  $\omega_e = \omega_{e,\text{idle}}$ . Consequently,  $\omega_{e,\text{ign}} < \omega_e \leq \omega_{e,\text{idle}}$  when  $C_1$  is opened. Detecting the exact moment when  $T_{\text{cl}} = 0$  is done by evaluating Equation (10.9), where it is assumed that  $T_{\text{cd}} = T_{\text{cd},\text{d1}}$ ,  $T_e = T_{e,\text{d1}}$  and where  $T_{\text{cf}}$  is reconstructed using the time-derivative of  $\omega_t(t)$ . The disengagement of  $C_1$  may be speeded up by preliminarily reducing the clutch pressure to a value which is just sufficient for transmitting the torque. Once  $C_1$  is released, Equation (9.9) with  $T_e$  replaced by  $T_t$ , describes the turbine speed dynamics.  $T_{\text{cf}}$  still tends to increase the turbine speed  $\omega_t$ , which may result in  $\omega_t > \omega_e$  since the engine is being controlled near  $\omega_{e,\text{idle}}$ . Meanwhile,  $T_{\text{cd}}$  is still rising towards  $T_{\text{cd},\text{ff1}} > 0$  and will eventually balance the torque exerted by the flywheel, implying the primary pulley stops decelerating.

### 10.3.2 Braking the primary pulley

While braking the primary pulley speed to zero (*i.e.*,  $\dot{\omega}_p > 0$ ), some strategy should take care of releasing the reverse clutch  $C_r$  at a sensible moment. If anything,  $C_r$  should be completely opened once  $\omega_p = 0$ . In order to allow for possible system delays, starting to release  $C_r$  beforehand seems reasonable. The torque that is transmitted by the closed reverse clutch is readily determined as

$$T_{\text{cr}} = (r_r - 1) \frac{\left( \frac{\alpha_p}{\alpha_s} T_{\text{cf}} - T_{\text{cd}} \right) J_t + r_r (T_t - T_{\text{cd}}) J_{\text{cvt}}}{J_{t,r}} \quad (10.11)$$

From Equations (9.16) and (9.17) it is seen that a positive  $T_{\text{cr}}$  is a braking torque for  $\omega_t$  and  $\omega_p$ , while it is a driving torque if it is negative. So, if  $T_{\text{cr}}$  was positive before disengagement, both the turbine and the primary pulley speed can be expected to increase, whereas if  $T_{\text{cr}}$  was negative, both speeds will tend to decrease, if  $C_r$  is opened. Since deceleration of the primary pulley is undesirable, disengaging  $C_r$  should not commence before  $T_{\text{cr}}$  cf. (10.11) is positive. Opening  $C_r$  at the exact moment when  $T_{\text{cr}} = 0$  seems preferable, because having  $C_r$  still closed while  $T_{\text{cr}} > 0$  actually prevents the primary pulley from speeding up, which is undesirable. In order not to require a reconstruction of  $T_{\text{cr}}$ , it is proposed to open  $C_r$  when  $\omega_t = \omega_{t,\text{d2}}$  ( $\omega_{t,\text{d2}}$  still to be determined) in combination with the following control law for the desired drive clutch torque  $T_{\text{cd},\text{d2}}$

$$T_{\text{cd},\text{d2}} = T_{\text{cd},\text{ff2}} + k_4(\omega_{t,\text{d2}} - \omega_t) \quad (10.12)$$

where  $T_{\text{cd},\text{ff2}} = \frac{\alpha_p}{\alpha_s} T_{\text{cf}}$ , so that  $\dot{\omega}_p$  cf. (9.17) equals zero when  $T_{\text{cr}} = 0$ .

Suppose the engine torque  $T_e$  equals some setpoint  $T_{e,\text{d2}}$ , yet to be determined, then substitution of  $T_{e,\text{d2}}$  and  $T_{\text{cd},\text{d2}}$  into Equations (9.14) and (9.15) gives

$$\begin{bmatrix} \dot{\omega}_e \\ \dot{\omega}_t \end{bmatrix} = \begin{bmatrix} -\frac{b_{\text{tc}}}{J_e} \omega_e^2 \\ \frac{\alpha_{\text{tc}} b_{\text{tc}}}{J_{t,r}} \omega_e^2 \end{bmatrix} + \begin{bmatrix} \frac{T_{e,\text{d2}}}{J_e} \\ -\frac{\alpha_p}{\alpha_s} \frac{T_{\text{cf}}}{J_{t,r}} \end{bmatrix} - \begin{bmatrix} 0 \\ \frac{k_4(1-r_r)}{J_{t,r}} \end{bmatrix} [\omega_{t,\text{d2}} - \omega_t] \quad (10.13)$$

In the equilibrium point, the following should hold

$$\begin{aligned} T_{e,\text{d2}} &= b_{\text{tc}}(r_{\text{tc},\text{d2}}) \cdot \omega_{e,\text{d2}}^2 \\ \frac{\alpha_p}{\alpha_s} T_{\text{cf}} &= \alpha_{\text{tc}}(r_{\text{tc},\text{d2}}) \cdot b_{\text{tc}}(r_{\text{tc},\text{d2}}) \cdot \omega_{e,\text{d2}}^2 \end{aligned} \quad (10.14)$$

where  $r_{\text{tc},\text{d2}} = \frac{\omega_{t,\text{d2}}}{\omega_{e,\text{d2}}}$ . Given  $T_{\text{cf}}$ , choosing some  $\omega_{t,\text{d2}}$  determines  $\omega_{e,\text{d2}}$  and  $T_{e,\text{d2}}$ . It is suggested to choose  $\omega_{t,\text{d2}}$  such that  $\omega_{t,\text{d2}} > 0 \wedge \omega_{e,\text{d2}} > \omega_{e,\text{idle}}$ .

To evaluate the stability of system (10.13), it is linearized around  $(\omega_{e,d2}, \omega_{t,d2})$  yielding

$$\begin{bmatrix} \delta \dot{\omega}_e \\ \delta \dot{\omega}_t \end{bmatrix} = \omega_{e,d2} \begin{bmatrix} \frac{-1}{J_e} \left( 2b_{tc} - \frac{db_{tc}}{dr_{tc}} r_{tc,d2} \right) & \frac{-1}{J_e} \frac{db_{tc}}{dr_{tc}} \\ \frac{1}{J_{t,r}} (2\alpha_{tc} b_{tc} - \zeta r_{tc,d2}) & \frac{1}{J_{t,r}} \left( \zeta + \frac{k_4(1-r_r)}{\omega_{e,d2}} \right) \end{bmatrix} \begin{bmatrix} \delta \omega_e \\ \delta \omega_t \end{bmatrix} \quad (10.15)$$

where

$$\zeta = b_{tc} \frac{d\alpha_{tc}}{dr_{tc}} + \alpha_{tc} \frac{db_{tc}}{dr_{tc}} \quad (10.16)$$

System (10.15) with (10.14), (10.16) and with  $k_4 = 0$  is stable, at least if  $\frac{d\alpha_{tc}}{dr_{tc}} < 0$  and  $\frac{db_{tc}}{dr_{tc}} < 0$ , which is true for  $r_{tc} > 0.4$ , as can be seen in Figure 9.3. For  $r_{tc} < 0.4$ , where  $\frac{db_{tc}}{dr_{tc}} > 0$ , the mentioned system is stable if

$$\frac{db_{tc}}{dr_{tc}} < \frac{b_{tc} \left( \frac{J_{t,r}}{J_e} - \frac{d\alpha_{tc}}{dr_{tc}} \right)}{\alpha_{tc} + \frac{J_{t,r}}{J_e} r_{tc}} \quad (10.17)$$

which is always true in practice (see Figure 10.6). Hence, if  $k_4 < 0$  the system remains stable. Similar to opening  $C_l$ , it may be wise to lower the reverse clutch pressure in advance, to a

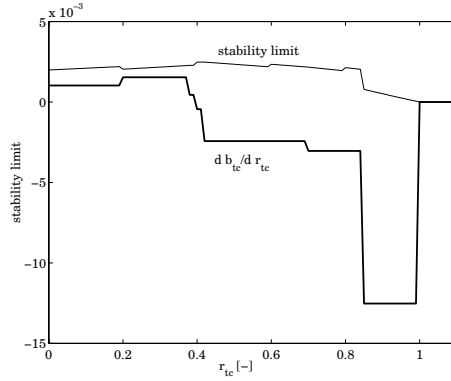


Figure 10.6: Stability limit for  $\frac{db_{tc}}{dr_{tc}}$

value corresponding with the transmitted torque, in order to speed up the response.

### 10.3.3 Synchronizing the drive clutch

After  $C_r$  is opened, the drive clutch may still be closing. A priori it is not known at what primary pulley speed synchronization will happen. Therefore, the control strategy in this stage aims at increasing  $\omega_p$  to a level where the secondary pulley speed and the secondary shaft speed are equal, *i.e.*,  $\omega_{p,d3} = \frac{\omega_{ss}}{r_{ud}}$ . The fact that synchronization of  $C_d$  may occur before that is unimportant. Other than this, the engine torque should be regulated such that some desired engine speed  $\omega_{e,d3}$ , which is yet to be determined, is realized. The following control laws for  $T_e$  and  $T_{cd}$  are suggested

$$T_{e,d3} = T_{e,ff3} + k_5(\omega_{e,d3} - \omega_e) \quad (10.18)$$

$$T_{cd,d3} = T_{cd,ff3} + k_6(\omega_{p,d3} - \omega_p) \quad (10.19)$$

where  $T_{e,ff3}$  and  $T_{cd,ff3}$  are determined from the equilibrium point for the combined system that results when substituting (10.18) and (10.19) into (9.14), (9.16) and (9.17) with  $T_{cr} = 0$ , yielding

$$\begin{bmatrix} \dot{\omega}_e \\ \dot{\omega}_t \\ \dot{\omega}_p \end{bmatrix} = \begin{bmatrix} -\frac{b_{tc}}{J_e} \omega_e^2 \\ \frac{\alpha_{tc} b_{tc}}{J_t} \omega_e^2 \\ 0 \end{bmatrix} + \begin{bmatrix} \frac{T_{e,ff3}}{J_e} \\ -\frac{T_{cd,ff3}}{J_t} \\ \frac{T_{cd,ff3} - \frac{\alpha_P}{\alpha_s} T_{cf}}{J_{cvt}} \end{bmatrix} + \begin{bmatrix} \frac{k_5}{J_e} & 0 \\ 0 & -\frac{k_6}{J_t} \\ 0 & \frac{k_6}{J_{cvt}} \end{bmatrix} \begin{bmatrix} \omega_{e,d3} - \omega_e \\ \omega_{p,d3} - \omega_p \end{bmatrix} \quad (10.20)$$

The equilibrium point is obtained when

$$\begin{aligned} T_{e,ff3} &= b_{tc}(r_{tc,d3}) \cdot \omega_{e,d3}^2 \\ T_{cd,ff3} &= \alpha_{tc}(r_{tc,d3}) \cdot b_{tc}(r_{tc,d3}) \cdot \omega_{e,d3}^2 \\ &= \frac{\alpha_P}{\alpha_s} T_{cf} \end{aligned} \quad (10.21)$$

where  $r_{tc,d3} = \frac{\omega_{p,d3}}{\omega_{e,d3}}$ . Again, given  $T_{cf}$ , choosing  $\omega_{p,d3}$  determines  $\omega_{e,d3}$ ,  $T_{e,ff3}$  and  $T_{cd,ff3}$ . Linearization of the set of differential equations (10.20), again yields the stability requirements, in this case  $k_5 > 0$ ,  $k_6 > 0$ .

## 10.4 Control strategy for the Sync phase

During the Sync phase, the secondary pulley clutch  $C_s$  must be synchronized and then closed.

### 10.4.1 Accelerating the secondary pulley

If  $\omega_p r_{ud}$  is still lower than  $\omega_{ss}$ , first the primary pulley must be further accelerated, before closing of  $C_s$  can commence. The flywheel clutch  $C_f$  is likely to be closed at this time. The appropriate system equations are given by (9.20)–(9.23). The following control law for  $T_e$  is suggested

$$T_{e,d4} = \frac{T_{t,ff4} + k_7 \omega_{cs}}{\alpha_{tc}(r_{tc})} \quad (10.22)$$

$$(10.23)$$

where  $T_{t,ff4}$  is obtained by assuming a stationary situation:

$$T_{t,ff4} = r_{ud} r_d T_{w,d} \quad (10.24)$$

### 10.4.2 Synchronizing the secondary pulley clutch

Once the secondary pulley speed  $\omega_s$  has caught up with the secondary shaft speed  $\omega_{ss}$ , it is time to engage  $C_s$ . As was explained in Section 10.1, it is decided to release  $C_f$  while  $C_s$  is closing. Consequently, the final value for  $T_{cs}$  in this phase will be equal to  $r_d T_{w,d}$ , which is therefore used as a feedforward, *i.e.*,

$$T_{cs,ff5} = r_d T_{w,d} \quad (10.25)$$

Because  $T_{cs}$  and  $T_{cf}$  combined make up the torque at the final drive, an obvious setpoint for  $T_{cf}$  is

$$T_{cf,d5} = T_{cs,ff5} - T_{cs} \quad (10.26)$$



Since  $\omega_{cs} \approx 0$ ,  $\omega_t \approx \frac{\omega_w}{r_d r_{ud}}$ , therefore a setpoint for  $\omega_e$  can be determined, if  $T_{t,d5}$  is given by

$$T_{t,d5} = r_d r_{ud} T_{w,d} + J_{t,d} \dot{\omega}_p \quad (10.27)$$

where  $\dot{\omega}_p$  must be estimated from  $\omega_p(t)$ . The resulting setpoint for  $\omega_e$  is then implicitly given by

$$b_{tc}(r_{tc,d5}) \cdot \omega_{e,d5}^2 = \frac{T_{t,d5}}{\alpha_{tc}} + J_e \dot{\omega}_e \quad (10.28)$$

where  $r_{tc,d5} = \frac{\omega_w}{r_d r_{ud} \omega_{e,d5}}$ . The right-hand side of (10.28) is used as a feedforward  $T_{e,ff5}$ . The total control scheme then looks like

$$T_{e,d5} = T_{e,ff5} + k_9(\omega_{e,d5} - \omega_e) \quad (10.29)$$

$$T_{cs,d5} = T_{cs,ff5} + k_{10}\omega_{cs} \quad (10.30)$$

When eventually  $C_s$  closes completely, while  $C_f$  is completely open,  $T_{cs}$  should be continuous in the transition from slip to stick. Consequently, the desired torque according to (10.30) should equal the stick torque which is then given by

$$T_{cs,stick} = r_d \frac{J_{t,d} T_{rl} + r_{ud} r_d J_w T_t}{J_{t,c}} \quad (10.31)$$

so

$$T_{cs,d5} - T_{cs,stick} = k_{10}\omega_{cs} + \frac{r_d^2 r_{ud} J_w}{J_{t,c}} \left( \frac{J_{t,c} T_{w,d} - J_{t,d} T_{rl}}{r_d r_{ud} J_w} - T_t \right) \quad (10.32)$$

which can be shown (using (10.27), (9.25) and (10.25)–(10.26)) to be equivalent to

$$T_{cs,d5} - T_{cs,stick} = k_{10}\omega_{cs} + \frac{r_d^2 r_{ud} J_w}{J_{t,c}} (T_{t,d5} - T_t) \quad (10.33)$$

provided  $r_d r_{ud} \dot{\omega}_p = \dot{\omega}_w$ , which is true if  $\omega_{cs} = 0$ . Hence,  $T_{cs,d5} - T_{cs,stick} = 0$  when eventually the slip reduces to zero.

## 10.5 Control strategy for the End phase

In the End phase, the flywheel clutch is initially open, so then the powertrain is identical to that of a conventional CVT vehicle. Once the flywheel clutch re-engages (which will usually happen when  $r_{cvt}$  is around  $r_{gn}$ ), the ZI drive train configuration is re-established. In both cases (CVT and ZI), the CVT ratio  $r_{cvt}$  and the engine torque  $T_e$  are manipulated to control the power at the wheels. Strategies for controlling a conventional CVT powertrain are well covered in literature (see *e.g.*, [Liu and Paden, 1997] and references therein), whereas control of the ZI powertrain is reported in [Serrarens, 2001; Vroemen *et al.*, 2001].

## 10.6 Controller implementation

Implementation of the hybrid model and controller requires programming of the criteria that govern the transitions from one model, *c.q.* controller to the other. MATLAB STATEFLOW is a very powerful tool for dealing with such problems and is therefore used to design and evaluate the controllers. Without elaborating on its exact contents, the STATEFLOW diagram of the supervisory controller is depicted in Figure 10.7. The diagram gives an indication of the complexity that a multi-clutch system constitutes with respect to its controls.

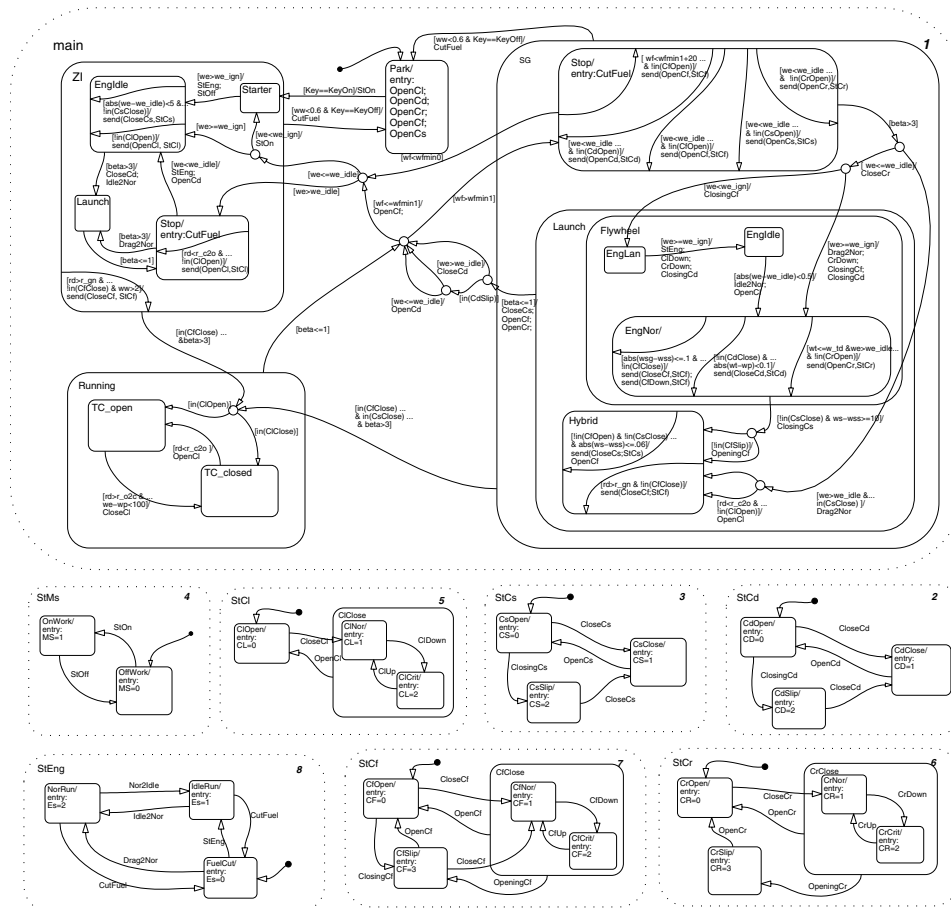


Figure 10.7: STATEFLOW diagram of the supervisory controller

## 10.7 Simulation results

In this section, some simulations results are presented. The simulation model is more detailed than the control model (Figure 9.1) in that it includes compliances for the TC spring and the drive shaft as well as a tire slip model. Furthermore, the torque losses in the pump and CVT are taken into account (as was treated in Section 6.7.4). The hydraulics of the CVT and the clutch actuation system are represented by second order transfer functions.

Figures 10.8–10.11 give results for a kickdown vehicle launch, starting at time  $t = 1$  [s]. The resulting vehicle acceleration and speed are depicted versus time (indicated by 'ZI Stop-Go') in Figure 10.8, and compared to measurements that were performed in the test vehicle without flywheel ('CVT'). The initial vehicle acceleration for ZI Stop-Go reaches circa  $2.2 \text{ [m/s}^2\text{]}$  within  $0.05$  [s]. The time needed to reach this level depends on the time-constant of the hydraulic system, and may be longer in practice, since the time needed to open the accumulator load

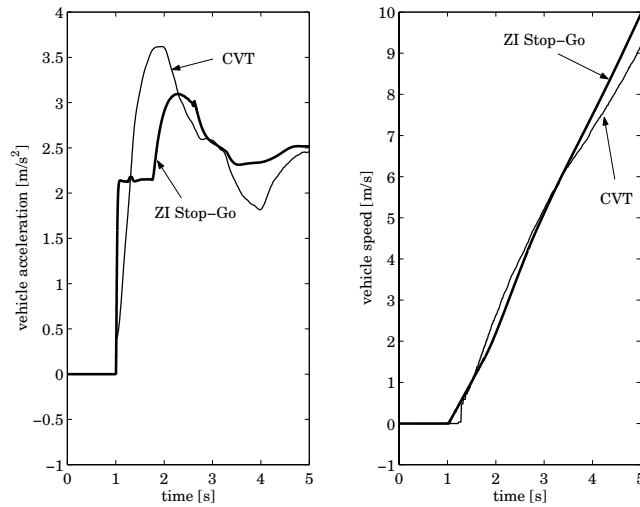


Figure 10.8: Vehicle speed [m/s] and acceleration [m/s<sup>2</sup>] versus time [s] for a kickdown vehicle launch; ZI Stop-Go compared to a conventional CVT vehicle

valve (see Section A.5) is not modeled. The combined time is nevertheless expected to be less than 0.1 [s]. The acceleration of the CVT vehicle rises less steeply, which is due to the primary-sided inertias that must be accelerated. The peak-value of the acceleration for the CVT vehicle is higher than that for ZI Stop-Go, which will be explained further on. The initial level of acceleration for ZI Stop-Go is *not* limited by the maximum flywheel clutch torque ( $T_{cf,max} = \alpha_s \cdot 180 = 299$  [Nm]), but by the fact that the engine needs to be able to balance the flywheel torque by the time the engine is delivering torque. Therefore, the initial acceleration could actually be higher, but would then fall back once the engine was balancing the flywheel torque on its own. Taking the maximum engine torque into account, the maximum wheel torque is moreover determined by the torque amplification factor  $\alpha_{tc}\alpha_s/\alpha_p$  through the TC and the planetary stage, by the pump and variator torque losses and by the driveline inertias up to the drive shaft (given some vehicle acceleration). Because the torque amplification for ZI Stop-Go is lower than for the conventional CVT, the peak acceleration level of CVT is not attained by ZI Stop-Go.

Around  $t = 1.8$  [s], the acceleration for ZI Stop-Go increases further when the secondary pulley clutch  $C_s$  starts closing. Because the control strategy for  $C_s$  is such that it starts closing after the slip speed  $\omega_{cs}$  is positive (*i.e.*,  $\omega_s > \omega_{ss}$ ), the clutch torque  $T_{cs}$  increases due to the fact that the driveline inertias cease to accelerate at the high rate seen prior to  $t \approx 1.8$  [s] (as will be shown in Figure 10.9). After  $C_s$  is synchronized, it completely closes and the wheel torque is basically equal to that of a conventional CVT powertrain. The fluctuations in the remainder of the vehicle acceleration are caused by the declining TC torque amplification and the maximum engine torque that depends on the (increasing) engine speed. The difference between ZI Stop-Go and the CVT vehicle between  $t \approx 3$  and 5 [s] remains to be explained.

Figures 10.9 and 10.10 depict the corresponding driveline speeds and clutch torques, respectively. Figure 10.11 is an enlarged view of Figure 10.10, where moreover the various events and phases are indicated. As seen in these Figures,  $\omega_f$  and  $\omega_{sg}$  start decreasing (approximately



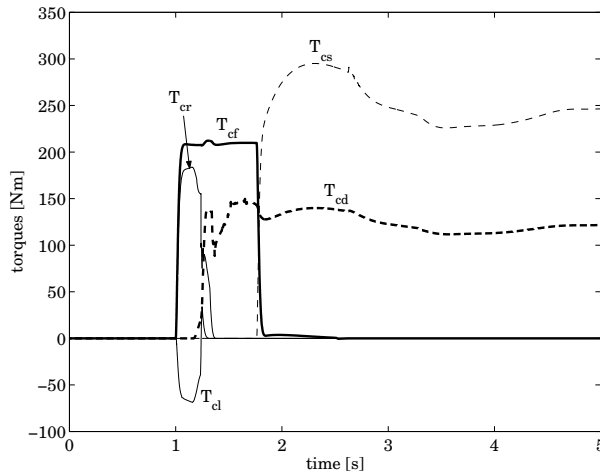


Figure 10.10: Clutch torques [Nm] versus time [s] for a kickdown launch sequence

## 10.8 Preliminary experimental results

This section shows first results obtained with the ZI Stop-Go transmission on the test rig. More extensive testing is needed to evaluate the concept and its controllers.

Figure 10.12 depicts a measurement of the flywheel speed which was accelerated towards circa 2000 [rpm] ( $\approx 215$  [rad/s]), and then disengaged from the rest of the driveline, by opening the flywheel clutch. In this experiment which was performed to evaluate the flywheel and clutch drag losses, it is seen that it takes about 270 [s] for the flywheel to come to a standstill. Notably, the gradient of the speed trajectory changes distinctly at around 190 [rad/s] and again around 90 [rad/s]. The reason for the change of slope is unclear, though may be related to system resonances. The corresponding drag torque, when subscribed to the flywheel clutch is between 0.4 and 0.5 [Nm], for the interval where  $\omega_f > 90$  [rad/s]. After that the drag is torque is closer to 0.8 [Nm]. A drag torque around 0.4 [Nm] can actually be expected for the wet-plate clutch used in the ZI Stop-Go transmission. Since the drag torque increases for a lower flywheel speed, air drag losses of the flywheel are thought to be insignificant for these speeds (also see [van Druuten, 2001]).

A first step towards a vehicle launch is shown in Figure 10.13. In this experiment, the flywheel was speeded up to a mere 820 [rpm] ( $\approx 86$  [rad/s]) and subsequently the flywheel clutch was (open-loop) engaged at  $t = 0$  [s] and disengaged again at  $t \approx 0.4$  [s]. The attained wheel torque was not controlled, so the considered situation does not relate to a desired wheel torque as in the earlier depicted kickdown acceleration. Figure 10.13 depicts the measured drive shaft torque  $T_w$  and impeller torque  $T_i$  ( $\times 10$ ), and the corresponding flywheel and engine speeds  $\omega_f$  and  $\omega_e$  and vehicle speed  $v_v$  [km/h] ( $\times 10$ ). It is seen that the wheel torque starts to increase around  $t = 0.15$  [s] and reaches 600 [Nm]. Simultaneously, the (negative) impeller torque starts to accelerate the engine. The engine and vehicle dynamics were emulated at the test rig using realistic drag models. While the flywheel speeds down from 86 to 55 [rad/s], the engine is accelerated towards 65 [rad/s] around  $t = 0.55$  [s], whereas the vehicle speed increases up to circa 1.3 [km/h].

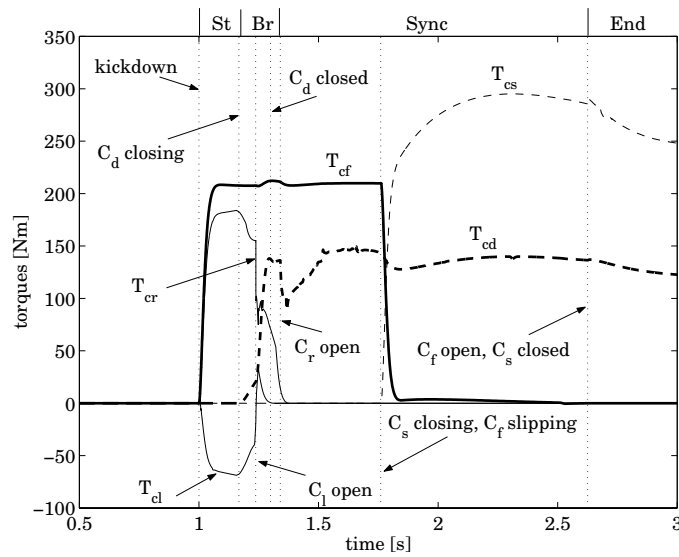


Figure 10.11: Clutch timing for a kickdown vehicle launch

The response time in the depicted experiment (around 0.15 [s]) can probably be reduced, since in the open-loop steering the flywheel clutch pressure did not make any use of model information, especially regarding the minimal amount of pressure that is needed for first engagement.

In the experimental implementation of the controllers for ZI Stop-Go, the CVT controller developed in Chapter 7 was adopted without modification. Remarkably, the CVT controller performed well and stable, even though the various system parameters of the CVT can be expected to be somewhat different. This can be regarded as an indication of robustness with respect to model errors.

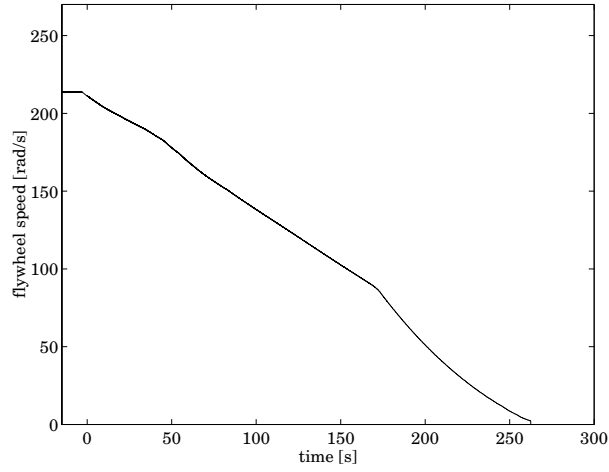


Figure 10.12: Flywheel free run at a transmission temperature of 50°C

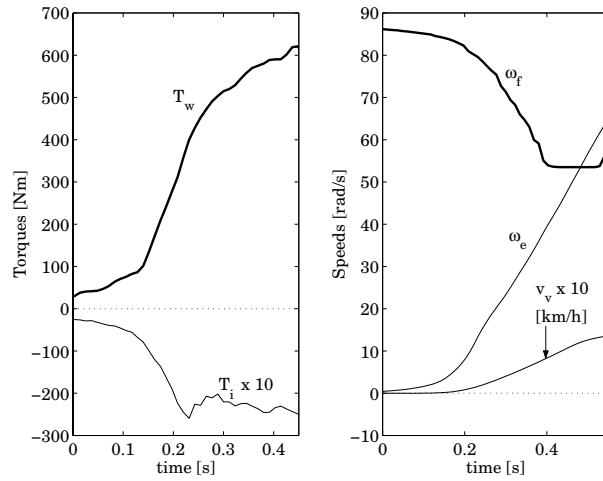


Figure 10.13: Start phase of the launch sequence, measured on the test rig

**Part IV**  
**Closure**





# Chapter 11

## Conclusions

This chapter gives conclusions based on the research covered in this thesis, and on the EcoDrive project as a whole. The chapter organization is as follows. In Section 11.1, overall conclusions regarding the EcoDrive project are presented. The conclusions which are specifically related to this thesis, are given in Section 11.2. The last section gives directions for future research based on this thesis, and more general directions based on the combined outcome this thesis, [van Druten, 2001] and [Serrarens, 2001].

### 11.1 Overall conclusions

A novel automotive transmission, called the 'Zero Inertia' (ZI) powertrain, has been proposed. This powertrain combines a Continuously Variable Transmission (CVT), a low-speed flywheel and a planetary gear stage, enabling a substantial reduction of fuel consumption while maintaining a high level of 'driveability', *i.e.*, longitudinal vehicle response and comfort. The improvement in fuel economy is obtained by operating the engine at very low speeds, where the engine efficiency is generally high. The sluggish vehicle behaviour, that would normally result from such engine operation, is effectively counteracted by the flywheel which acts as a power-dense mechanical power assist source.

Augmenting the ZI concept with two clutches created the 'ZI Stop-Go' powertrain which makes it possible to shutdown the engine during vehicle standstill, and hence save an additional amount of fuel. The challenge in that was to guarantee a simultaneous restart of vehicle and engine without a noticeable delay. To show the potential of the ZI and ZI Stop-Go concepts as means to save fuel, an overview of fuel saving principles and associated efforts (development, costs, packaging, etc) has been presented. The fuel savings for ZI Stop-Go on the NEDC driving cycle were predicted to amount up to 21%.

The target of the EcoDrive ZI project was set at saving 25% fuel consumption on the NEDC driving cycle, with respect to a 4-speed automatic transmission (4-AT) vehicle, and without loss of driveability. As predicted in Part I, achieving this target was deemed nearly possible, *i.e.*, a fuel saving of 21% was thought to be feasible. The actually obtained fuel savings on the NEDC using only ZI were measured at 9.0% and 11.0% with respect to 4-AT and CVT in 'performance mode', respectively, as reported in [Serrarens, 2001]. The theoretically derived fuel saving for Stop-Go gives an additional 8%. Consequently, the combined fuel saving for ZI Stop-Go is around 18%. This value is reasonably close to the theoretically predicted

fuel saving of 21%, but somewhat below the initial target. In the overview of fuel saving principles, other methods were shown to have more fuel saving potential, but also to be far more complex. It is therefore believed that the chosen solution offers a fair trade-off between achieving the initial targets and the objective to actually realize the ZI and ZI Stop-Go powertrains in a test vehicle and on a test rig, respectively, within a time-frame of less than four years.

Apart from the research outcome described in this thesis (see the following section), the EcoDrive project yielded a lot of knowledge on driveability notions, powertrain modeling, coordinated powertrain control, and controller implementation [Serrarens, 2001], as well as insights regarding the use and specification of flywheel energy exchange systems in passenger cars, an intuitive design tool for analyzing power-split transmissions, and obviously the realization of two transmissions used to prove the concepts [van Druten, 2001].

## 11.2 Modeling and control of powertrain components

The ZI transmission relies on a CVT that enables matching of the engine operating points to the desired wheel power on the one hand, and the smooth exchange of energy between the flywheel and the engine and vehicle on the other. Consequently, the CVT controller must realize the desired (semi-)stationary engine speeds accurately and, moreover, should accomplish smooth transitions in transient operation. The setpoints for the CVT controller are generated by the coordinated powertrain controller derived in [Serrarens, 2001]. In order to make the development of the total powertrain control hierarchy transparent, it was chosen to separate the local CVT controller from the setpoint generation. The coordinated powertrain controller should therefore supply setpoints that take the powertrain and (longitudinal) vehicle dynamics into account. Subsequently, the local CVT controller must realize those setpoints and meanwhile maximize the CVT efficiency. Since the applied pushbelt CVT is hydraulically actuated, maximizing the transmission efficiency basically comes down to reducing the oil pressures as far as possible, though preventing the belt from slipping. The slip constraint, the pressure constraints and valve solenoid current constraints make up the operating region of the CVT actuators. The ratio of the input and output speed of the CVT, *i.e.*, the *CVT speed ratio* is limited between *underdrive* and *overdrive*. All of the mentioned constraints must be explicitly taken into account by the CVT controller.

For several purposes, a model of the CVT is derived. It is used for gaining insight in the behaviour of the hydraulic part and of the pushbelt. For instance, the measured power losses in the CVT are analyzed and the loss mechanisms are represented in a way that is believed to give an increased understanding. Furthermore, a physical model is desirable to value the mostly empirical CVT models seen in literature. Having decided on which model is best suited for control purposes, this model is used for deriving a model-based controller and for testing the controller in a simulation environment. The proposed model-based speed ratio controller pays special attention to dealing with operational constraints. The CVT controller was validated in simulations and experiments. The experiments were conducted on a fully programmable test rig and in a test vehicle, both developed within the EcoDrive ZI project. The CVT controller, in conjunction with the coordinated powertrain controller, has been shown to perform well. Highly dynamic transients were performed with acceptable tracking errors and without gross belt slip, whereas the CVT losses were minimized in stationary situations.

Besides designing the CVT controller for maximum transmission efficiency, an alternative layout for the hydraulic actuation of the CVT has been suggested, that enables faster shifting

accompanied by an increased robustness with regard to gross belt slip. If one chooses to install a smaller pump, transmission losses can be reduced without impairing the maximum shift speed of the CVT, for most of the practical operating range.

The second part of the research concentrates on the modeling and control of the ZI Stop-Go powertrain. Several existing Stop-Go solutions are presented, showing the increased technical as well as commercial interest in this method to reduce fuel consumption. Although most of the mentioned systems are relatively easy to conceive and fairly cost-effective, gaining public acceptance of Stop-Go systems is still somewhat puzzling, especially if restarting the engine is accompanied by a noticeable delay. To prevent the latter problem, a mechanical Stop-Go solution, referred to as ZI Stop-Go is proposed, that enables a direct vehicle launch and a simultaneous restart of the engine. A hybrid model of the powertrain including clutches, engine and CVT is derived. This model is used to develop a hybrid controller, which is evaluated using a more elaborate version of the mentioned model. Simulation results reveal a kickdown vehicle launch response which is comparable to that of a conventional CVT vehicle. The ZI Stop-Go transmission was realized and the CVT hydraulics were modified to enable the actuation of the clutches, also during engine shutdown. This transmission was mounted on the aforementioned test rig and first experimental results are promising.

### 11.3 Directions for future research

In Chapter 1, the EcoDrive project organization was outlined in Figure 1.1. EcoDrive consisted of two parts, the results of which can in principle be combined to some extent. The part of EcoDrive not described in this thesis, termed EcoDrive SI, resulted in a number of design and control modifications aiming at improvement of the CVT and engine efficiency, [Veenhuizen and van Spijk, 2000]. The most important improvement was due to the integration of a so-called *torque fuse* in the CVT. This torque fuse allows a very small slip speed in the (secondarily positioned) drive clutch and as such safeguards the pushbelt of the CVT during torque shocks. Hence, the pulley clamping force can be substantially reduced, improving the CVT efficiency in part load especially. Given the layout of the ZI Stop-Go transmission, see Figure 4.6, the ‘secondary pulley clutch’ may be used as a torque fuse. Furthermore, in EcoDrive SI a CVT with a ratio coverage of 6.55 was developed, which is large, even compared to the ratio coverage of 5.17 of the CVT used in the ZI transmission. Incorporating this transmission into the ZI configuration can reduce the engine speed even more with apparent fuel economy benefits. Additionally, a chain driven binary displacement pump was designed for the EcoDrive SI transmission, to enable a simultaneous high pressure oil supply (for pulley clamping and clutches) and low pressure oil supply (for the torque converter, lubrication and cooling). Integration of the EcoDrive SI transmission modifications into the ZI design can be expected to improve the fuel economy by about 5%. To further increase the efficiency of the CVT, one can think of implementing the hydraulic circuit design as suggested in Chapter 6. Alternatively, one may choose to leave out the hydraulics partly or even entirely. In [van Tilborg, 2001], it is shown that the pump losses can be reduced by applying part of the pulley clamping force electro-mechanically.

In order to validate the functionality and performance of the ZI Stop-Go transmission, further implementation and validation of the controllers on the test rig is required. After that, ZI Stop-Go may be implemented in a test vehicle to demonstrate the driveability and fuel economy. In the latter case, extensive modifications to the engine management must be undertaken in order to adapt fuel injection and ignition without increasing the emissions. Also the emission control for normal ZI operation should be optimized for the operation at

very low engine speeds.

Further improvement of the overall control and powertrain performance might require a reconsideration of the setpoint generation for CVT and engine, by taking their dynamics into account more explicitly. This could also eliminate occasional high belt loads that occur in the ZI transmission on pedal back-out after a kickdown acceleration. Coordinated and component control, respectively described in [Serrarens, 2001] and this thesis, would be more intertwined then. On the component control level, the development and implementation of alternative model based CVT controllers may be given more attention. Especially the augmentations suggested at the end of Chapter 7 should be implemented and evaluated.

Finally, a number of research topics is proposed, involving more rigorous adaptations to the current ZI and ZI Stop-Go powertrains. The increasing popularity of the diesel engine in Europe, combined with its appreciable fuel economy, argues for investigating the combination of this engine with the ZI (and ZI Stop-Go) concept. Because the diesel engine has different torque and speed characteristics than the petrol engine, this would involve a modification of transmission parameters. Next, the torque converter which is normally used to facilitate vehicle launch, might be omitted from the ZI Stop-Go powertrain if the flywheel indeed proves to enable an acceptable vehicle launch. Probably the most rigorous future research topic is to conceive and develop a mechanical full hybrid powertrain. From Chapter 3, it was concluded that such a hybrid powertrain has a large fuel saving potential combined with relatively low manufacturing costs. On the other hand, research efforts are quite challenging. In fact, a few solutions in this direction were already proposed, see [Kok, 1999] and [Dietrich *et al.*, 1999]. Searching for a combination of such concepts and the ZI functionality to solve driveability issues, while always aiming for minimal fuel consumption, weight and complexity, seems well worth the investigation.

# Bibliography

- Abromeit, G. and Wilkinson, A. C. N. "An electronic control concept for a continuously variable transmission". In Proc. of ISATA, vol. 1, pp. 31–45. Croydon, UK, 1983.
- Adachi, K., Wakahara, T., Shimanaka, S., Yamamoto, M., and Oshidari, T. "Robust control system for continuously variable belt transmission". *JSAE Review*, vol. 20, pp. 49–54, 1999.
- Adcock, I. "Stop-go systems get the green light". *European Automotive Design*, pp. 24–26, 1998.
- Albers, A. "Selbsteinstellende Kupplung (SAC) und Zweimassenschwungrad (ZMS) zur Verbesserung des Antriebsstrangkomforts". *VDI Berichte 1175*, pp. 153–168, 1995.
- An, F. and Ross, M. "Model of fuel economy with applications to driving cycles and traffic management". *Transportation Research Record*, no. 1416, pp. 105–114, 1993.
- Asayama, H., Kawai, J., Tonohata, A., and Adachi, M. "Mechanism of metal pushing belt". *JSAE Review 9532209*, vol. 16, pp. 137–143, 1995.
- Baumann, B., Rizzoni, G., and Washington, G. "Intelligent control of the Ohio State University hybrid-electric vehicle". In Proc. of the 2<sup>nd</sup> IFAC Workshop on Advances in Automotive Control, pp. 123–128. Mohican State Park (OH), 1998.
- Beccari, A. and Cammalleri, M. "Implicit regulation for automotive variators". *Proc. IMechE*, vol. 215, pp. 697–708, 2001.
- Becker, H.-J. "Mechanik des Van-Doorne-Schubgliederbandes". *Antriebstechnik*, vol. 8, pp. 47–53, 1987.
- Bernhardt, W. and Heidemeyer, P. "Innovative Triebstrangsysteme für das Aggregatemanagement". *VDI Berichte 977*, pp. 545–578, 1992.
- Bertram, M. "Antrieb mit intermittierendem Motorbetrieb". *Automobiltechnische Zeitschrift (ATZ)*, vol. 98, no. 6, pp. 312–320, 1996.
- Bohn, C. and Atherton, D. P. "An analysis package comparing PID anti-windup strategies". *IEEE Control Systems*, pp. 34–40, 1995.
- Bolenz, K. "Design modifications of the electrical system to use intermittent engine operation". In IEE Colloquium on Machines for Automotive Applications, pp. 2/1–7. London, 1996.

- Brandsma, A., van Lith, J., and Hendriks, E. "Push belt CVT developments for high power applications". In Proc. of the Internat. Congress on Continuously Variable Power Transmission (CVT'99), pp. 142–147. Eindhoven, The Netherlands, 1999.
- Breuer, B., Dausend, U., and Fecher, N. "Global mobility on roads on the 21<sup>st</sup> century". In Proc. of FISITA'00, F2000 P413. Seoul, Korea, 2000.
- Bürger, K. G., Gröter, H. P., Lutz, H. J., Meyer, F., and Schleuter, W. "Alternators in automotive applications—State of the art and development trends (in German)". In Proc. Symposium Nebenaggregate im Fahrzeug. Haus der Technik Essen, 1994.
- Carbone, G., Mangialardi, L., and Mantriota, G. "Shifting dynamics of metal pushing V-belt—Rapid speed ratio variations". In N. D. Vaughan, editor, *Integrated powertrains and their control*, pp. 47–65. Professional Engineering Publishing, 2000.
- Caricchi, F., Crescimbin, F., Santini, E., and Solero, L. "High-efficiency low-volume starter/alternator for automotive applications". In Proc. of the 2000 IEEE Industry Applications Conf., vol. 1, pp. 215–222. 2000.
- Cheng, Y. and de Moor, B. L. R. "Robustness analysis and control system design for a hydraulic servo system". *IEEE Trans. on Control Systems Technology*, vol. 2, no. 3, pp. 183–197, 1994.
- Delsey, J. "How to reduce fuel consumption of road vehicle". In Proc. OECD/IEA Informal Expert Panel on Low Consumption Low Emission Automobile. Rome, 1991.
- Dietrich, P., Eberle, M. K., and Hörler, H. U. "Results of the ETH-hybrid III—Vehicle project and outlook". *SAE Technical Paper Series*, no. 1999-01-0920, 1999.
- Dietrich, Th. "Ultracapacitors—Power for innovative automotive applications (in German)". *VDI Berichte 1565*, pp. 731–735, 2000.
- DOE and EPA. "Energy Technology and Fuel Economy". U. S. Department of Energy, U. S. Environmental Protection Agency, <http://www.fueleconomy.gov/feg/atv.shtml>, 2001.
- Donne, M. S., Tilley, D. G., and Richards, W. "The use of multi-objective parallel genetic algorithms to aid fluid power system design". *Proc. IMechE*, vol. 209, pp. 53–61, 1995.
- DoT. "Transport statistics Great Britain 1994". Department of Transport, HMSO, London, 1994.
- van Druten, R. M. "Transmission design of the Zero Inertia powertrain". Ph.D. thesis, Technische Universiteit Eindhoven, Eindhoven, The Netherlands, 2001.
- van Druten, R. M., Mussaeus, M. A., Vroemen, B. G., Serrarens, A. F. A., and Veenhuizen, P. A. "Transmission system, especially for a motor vehicle (patent WO9956039A2)". World Intellectual Property Organization, 2000a.
- van Druten, R. M., Mussaeus, M. A., Vroemen, B. G., Serrarens, A. F. A., and Veenhuizen, P. A. "Vehicle drive assembly (patent WO995549A1)". World Intellectual Property Organization, 2000b.
- van Druten, R. M., Serrarens, A. F. A., Vroemen, B. G., van den Tillaart, E., and de Haas, J. "Mild hybrids with CVT: Comparison of electrical and mechanical torque assist". *VDI Berichte 1610*, pp. 331–345, 2001.

- dSPACE. Real-time interface (RTI and RTI-MP). Implementation Guide, 1999.
- Evans, L. "Driver behavior effects on fuel consumption in urban driving". *Human Factors*, vol. 21, no. 4, pp. 389–398, 1979.
- Fischer, R. "Integration automatisierter Schaltgetriebe mit E-Maschine". In LuK Fachtagung: E-Maschine im Antriebsstrang, pp. 65–85. 1999.
- Frister, M. and Henneberger, G. "New concepts for vehicle electrical systems". In IEE Colloquium on Vehicle Electric Power Management and Smart Alternators, pp. 6/1–4. Digest no. 53, London, 1988.
- Fujii, T., Kurokawa, T., and Kanehara, S. "A study of a metal pushing V-belt CVT—Part 1: Relation between transmitted torque and pulley thrust". *SAE Technical Paper Series*, no. 930666, 1993a.
- Fujii, T., Kurokawa, T., and Kanehara, S. "A study of a metal pushing V-belt CVT—Part 2: Compression force between metal blocks and ring tension". *SAE Technical Paper Series*, no. 930667, 1993b.
- Fushimi, Y., Fujii, T., and Kanehara, S. "A numerical approach to analyze the power transmitting mechanisms of a metal pushing V-belt CVT". *SAE Technical Paper Series*, no. 960720, 1996.
- Gerbert, B. G. "Some notes on V-belt drives". *Trans. of the ASME, Jrnl. of Mechanical Design*, vol. 103, no. 1, pp. 8–18, 1981.
- Gerbert, G. "Metal-V-belt mechanics". *ASME Paper*, no. 84-DET-227, 1984.
- Gerbert, G. "Skew V-belt pulleys". *SAE Technical Paper Series*, no. 9636259, 1996.
- Greve, P. and Liesner, W. P. "Der neue VW Golf Ecomatic". *Automobiltechnische Zeitschrift (ATZ)*, vol. 95, no. 9, pp. 438–446, 1993.
- Guebeli, M., Micklem, J. D., and Burrows, C. R. "Maximum transmission efficiency of a steel belt continuously variable transmission". *Trans. of the ASME, Jrnl. of Mechanical Design*, vol. 115, pp. 1044–1048, 1993.
- Guo, Z. Y., Yang, X. C., Yang, D., and Frank, A. A. "On obtaining the best fuel economy and performance for vehicles with engine-CVT transmissions". *SAE Technical Paper Series*, no. 881735, 1988.
- Healey, J. R. "VW Lupo: Rough road to fuel economy". *USA Today*, 1999.
- Heavenrich, R. M., Murrell, J. D., and Hellman, K. H. "Light-duty automotive technology and fuel economy trends through 1991". Tech. rep., Control Technology and Applications Branch, EPA/AA/CTAB/91-02, Ann Arbor (MI): U. S. Environmental Protection Agency, 1991.
- Hendriks, E., ter Heegde, P., and van Prooijen, T. "Aspects of a metal pushing V-belt for automotive Cut application". *SAE Technical Paper Series*, no. 881734, 1988.
- Hirano, S., Miller, A. L., and Schneider, K. F. "SCVT—A state of the art electronically controlled continuously variable transmission". *SAE Technical Paper Series*, no. 910410, 1991.



## Bibliography

---

- Hofmann, L., Petersen, R., Adamis, P., and Brunner, H. "Improvement of CVTs for light passenger cars—Fuel economy versus driveability—a solveable conflict? (in German)". *VDI Berichte 1418*, pp. 549–567, 1998.
- Höhn, B.-R. "Konzepte weit gespreitzter stufenloser Getriebe". *Konstruktion*, vol. 46, pp. 359–364, 1994.
- Höhn, B.-R. "Alternative Getriebesysteme". *VDI Berichte 1610*, 2001.
- Honda. "Honda Insight: Owner's manual highlights". <http://www.insightman.com>, 2001.
- Ide, T., Uchiyama, H., and Kataoka, R. "Experimental investigation on shift-speed characteristics of a metal V-belt CVT". *SAE Technical Paper Series*, no. 9636330, 1996.
- Ide, T., Udagawa, A., and Kataoka, R. "A dynamic response analysis of a vehicle with a metal V-belt CVT". In Proc. of the 2<sup>nd</sup> Internat. Symp. on Advanced Vehicle Control (AVEC'94), vol. 1, pp. 230–235. Tsukuba, Japan, 1994.
- James, I. B. and Vaughan, N. D. "Design and component matching of a pressure control circuit". *SAE Technical Paper Series*, no. 961854, 1996.
- Junio, M., Roesgen, A., and Corvasce, F. "Rolling resistance of tires". *VDI Berichte 1505*, pp. 255–298, 1999.
- Kanehara, S., Fujii, T., and Fujimura, O. "Characterization of a CVT using a metal V-belt at transitional states". In Proc. of the Internat. Congress on Continuously Variable Power Transmission (CVT'99), pp. 58–64. Eindhoven, The Netherlands, 1999.
- Karam, A. and Play, D. "A discrete analysis of metal V-belt drive (DE-Vol.43-1)". In Internat. Power Transmission and Gearing Conf. ASME, pp. 319–327. 1992.
- Karnopp, D. "Computer simulation of stick-slip in mechanical dynamic systems". *Trans. of the ASME, Jrnl. of Dynamic Systems, Measurement, and Control*, vol. 107, pp. 100–103, 1985.
- Kim, H. and Lee, J. "Analysis of belt behavior and slip characteristics for a metal V-belt CVT". *Mech. Mach. Theory*, vol. 29, no. 6, pp. 865–875, 1994.
- Kim, H., Song, H., Kim, T., and Kim, J. "Metal belt CVT and engine optimal operation by PWM electro-hydraulic control". *SAE Technical Paper Series*, no. 9636501, 1996.
- Kim, W. and Vachtsevanos, G. "Fuzzy logic ratio control for a CVT hydraulic module". In Proc. of the 15<sup>th</sup> IEEE Internat. Symp. on Intelligent Control, pp. 151–156. 2000.
- Kitagawa, T., Fujii, T., and Kanehara, S. "A study of metal pushing V-belt CVT (Part 4: Forces act on metal blocks when the speed ratio is changing)". *SAE Technical Paper Series*, no. 950671, 1995.
- Kluger, M. A. and Long, D. M. "An overview of current automatic, manual and continuously variable transmission efficiencies and their projected future improvements". *SAE Technical Paper Series*, no. 1999-01-1259, 1999.
- Kobayashi, D., Mabuchi, Y., and Katoh, Y. "A study on the torque capacity of a metal pushing V-belt for CVTs". *SAE Technical Paper Series*, no. 980822, 1998.

- Kok, D. B. "Design optimisation of a flywheel hybrid vehicle". Ph.D. thesis, Technische Universiteit Eindhoven, Eindhoven, The Netherlands, 1999.
- Kuwabara, S., Fujii, T., and Kanehara, S. "Study on a metal V-belt type CVT: Band tension and load distribution in steel rings". *JSAE Review*, pp. 55–60, 1999.
- Kuwabara, S., Fushimi, Y., Fujii, T., and Kanehara, S. "Study on a metal V-belt type CVT: Numerical analysis of forces acting on a belt at steady state". *JSAE Review*, pp. 117–122, 1998.
- van der Laan, M. and Luh, J. "Model-based variator control applied to a belt type CVT". In Proc. of the Internat. Congress on Continuously Variable Power Transmission (CVT'99), pp. 105–110. Eindhoven, The Netherlands, 1999.
- Lechner, G. and Naunheimer, H. *Automotive transmissions*, pp. 135–136. Springer, 1999.
- Lehna, M. "Audi Duo, ein Hybridfahrzeug für die City-Logistik". *VDI Berichte 1378*, pp. 119–128, 1998.
- Liu, S. and Paden, B. "A survey of today's CVT controls (FP08-4)". In Proc. of the 36<sup>th</sup> IEEE Conf. on Decision and Control. San Diego (CA), 1997.
- Luh, J. "Model of a belt drive CVT for the power train (in German)". *VDI Berichte 1153*, pp. 625–639, 1994.
- Machida, H. "Traction drive CVT up to date". In Proc. of the Internat. Congress on Continuously Variable Power Transmission (CVT'99), pp. 71–769. Eindhoven, The Netherlands, 1999.
- Matsuo, I., Nakazawa, S., Maeda, H., and Inada, E. "Entwicklung eines Hybridantriebsystems mit CVT". In Proc. of the Aachener Kolloquium Fahrzeug- und Motorentechnik, VDI, pp. 1299–1312. Aachen, Germany, 1999.
- Micklem, J. D., Longmore, D. K., and Burrows, C. R. "Modelling of the steel pushing V-belt continuously variable transmission". *Proc. IMechE, Part C, Jrnal. of Mech. Eng. Science*, vol. 208, no. C1, pp. 13–27, 1994.
- MITI. "Changes in fuel efficiency of Japanese passenger cars (10 mode fuel efficiency)". <http://www.eccj.or.jp/databook/1998e/p95.html>, source: Ministry of International Trade and Industry, Japan, 1996.
- Müller, F. and Köhle, S. "Hybrid electric vehicles—Discussion of different configurations". In Proc. of the 2000 Global Powertrain Congress, pp. 54–63. Detroit (MI), 2000.
- Mussaeus, M. A., Serrarens, A. F. A., and Veldpaus, F. E. "CVT ratio optimization for minimal system losses in passenger cars". In Proc. of the 2<sup>nd</sup> IFAC Workshop on Advances in Automotive Control, pp. 129–134. Mohican State Park (OH), 1998.
- Nowatschin, K., Hommes, G., and Deimel, A. "Wie erlebt der Fahrer die neue Getriebe-generation multitronic von Audi?" *VDI Berichte 1610*, pp. 763–783, 2001.
- Office of Technology Assessment. "Advanced automotive technology: Visions of a super-efficient family car". Tech. rep., DOE, 1995.

- Oppenheim, A. K., Maxson, J. A., and Shahed, S. M. "Can the maximization of fuel economy be compatible with the minimization of pollutant emissions". *SAE Technical Paper Series*, no. 940479, 1994.
- Paefgen, F.-J. and Lehna, M. "Der Audi Duo—das erste serienmässige Hybridfahrzeug". *Automobiltechnische Zeitschrift (ATZ)*, vol. 99, pp. 316–320, 1997.
- Reik, W. "Startergenerator im Antriebsstrang". In *LuK Fachtagung: E-Maschine im Antriebsstrang*, pp. 37–64. 1999.
- Riezenman, M. J. "Engineering the EV future". *IEEE Spectrum*, vol. 35, no. 11, pp. 18–20, 1998.
- Robertson, A. J. and Tawi, K. B. "Misalignment equation for the Van Doorne metal V-belt continuously variable transmission". *Proc. of IMechE Part D*, vol. 211, pp. 121–128, 1997.
- van Rooij, J. and Schaerlaeckens, W. "Kräfte und Wirkungsgrad beim Schubgliederband Teil I: Allgemeine Kräftebetrachtungen, Teil II: Im Band auftretende Kräfte, Teil III: Leistungsverluste im Schubgliederband und CVT-Getriebe". *Antriebstechnik*, vol. 32, no. 8, pp. 55–86, 1993.
- Rundqwist, L. "Anti-reset windup for PID controllers". Ph.D. thesis, Lund Institute of Technology, Lund, Sweden, 1991.
- Sakai, Y. "The 'ECVT' continuously variable transmission". *VDI Berichte 803*, pp. 235–261, 1990.
- Sato, K., Sakakiyama, R., and Nakamura, H. "Development of electronically controlled CVT system equipped with CVTip". *SAE Technical Paper Series*, no. 9636321, 1996.
- Seiffert, U. and Walzer, P. *Automobiltechnik der Zukunft*, pp. 146–147. VDI Verlag, 1989.
- Serrarens, A. F. A. "Coordinated control of the Zero Inertia powertrain". Ph.D. thesis, Technische Universiteit Eindhoven, Eindhoven, The Netherlands, 2001.
- Serrarens, A. F. A. and Veldpaus, F. E. "A management system for a flywheel hybrid driveline". In *Proc. of the 4th International Symposium on Advanced Vehicle Control*, pp. 159–164. Nagoya, Japan, 1998.
- Shafai, E., Simons, M., Neff, U., and Geering, H. P. "Model of a continuously variable transmission". In *Proc. of the 1<sup>st</sup> IFAC Workshop on Advances in Automotive Control*, pp. 99–107. 1995.
- Spijker, E. "Steering and control of a CVT based hybrid transmission for a passenger car". Ph.D. thesis, Technische Universiteit Eindhoven, Eindhoven, The Netherlands, 1994.
- Stouten, B. "Modeling and control of a CVT. WFW-report 2000.10". Master's thesis, Technische Universiteit Eindhoven, Eindhoven, The Netherlands, 2000.
- Sudau, J. and Sasse, Chr. "ZMSIIi—Ein neues, im Drehmomentenwandler integriertes Schwingungsdämpfungs-konzept für Automatgetriebe". *VDI Berichte 1393*, pp. 613–626, 1998.

- Sun, D. C. "Performance analysis of a variable speed-ratio metal V-belt drive". *Trans. of the ASME, Jnl. of Mechanisms, Transmissions, and Automation in Design*, vol. 110, pp. 472–481, 1988.
- Takahashi, M., Kido, R., Nonaka, K., Takayama, M., and Fujii, T. "Design and development of a dry hybrid belt (BANDO AVANCE) for CVT vehicles". In Proc. of the Internat. Congress on Continuously Variable Power Transmission (CVT'99), pp. 254–259. Eindhoven, The Netherlands, 1999.
- Tenberge, P. "E-Automat: Automatikgetriebe mit Esprit". *VDI Berichte 1610*, pp. 455–479, 2001.
- Thoolen, F. J. M. "Development of an advanced high speed flywheel energy storage system". Ph.D. thesis, Technische Universiteit Eindhoven, Eindhoven, The Netherlands, 1993.
- van Tilborg, P. "Development of a concept electromechanical clamping system for a Van Doorne pushbelt variator". Master's thesis, Technische Universiteit Eindhoven, Eindhoven, The Netherlands, 2001.
- Vahabzadeh, H. and Linzell, S. M. "Modeling, simulation, and control implementation for a split-torque, geared neutral, infinitely variable transmission". *SAE Technical Paper Series*, no. 910409, 1991.
- Vanvuchelen, P. "Virtual engineering for design and control of continuously variable transmissions". Ph.D. thesis, Katholieke Universiteit Leuven, Leuven, Belgium, 1997.
- Veenhuizen, P. A. and van Spijk, G. "General background of the application of the CVT by example of the VDT EcoDrive transmission". In Proc. CVT-Tagung 2000. Haus der Technik, Essen, 2000.
- van der Voort, M. C. "Design and evaluation of a new fuel-efficiency support tool". Ph.D. thesis, Universiteit Twente, Enschede, The Netherlands, 2001.
- van der Voort, M. C., Dougherty, M. S., and van Maarseveen, M. "A new generation fuel-efficiency support tool". *Transportation Research Part C*, vol. 9, no. 4, pp. 279–296, 2001.
- Vroemen, B., Serrarens, A., and Veldpaus, F. "Hierarchical control of the Zero Inertia powertrain". *JSAE Review*, 2001.
- Vroemen, B. G., van der Laan, M., and Veldpaus, F. E. "Alternative concepts for hydraulic CVT Control". In Proc. of the 4<sup>th</sup> Internat. Symp. on Advanced Vehicle Control (AVEC'98), pp. 153–158. Nagoya, Japan, 1998.
- Vroemen, B. G., Serrarens, A. F. A., and Veldpaus, F. E. "CVT control: A hierarchical approach". In Proc. of the 5<sup>th</sup> Internat. Symp. on Advanced Vehicle Control (AVEC'00). Ann Arbor (MI), 2000.
- Wade, J. M. A. "An integrated electronic control system for a CVT based powertrain (84006)". In Proc. of ISATA, vol. 1. 1984.
- Wagner, U., Teubert, A., and Endler, T. "Entwicklung von CVT-Ketten für Pkw-Anwendungen bis 400 Nm". *VDI Berichte 1610*, pp. 223–243, 2001.

- Waters, M. H. L. and Laker, I. B. "Research on fuel conservation for cars". Tech. Rep. 921, Transport and Road Research Laboratory, Crownthorpe, England, 1980.
- Yamamoto, K. and Aoki, T. "Analysis of the influence on fuel economy by transmission type and the estimation of fuel economy". In Proc. of FISITA'00, F2000 A148. 2000.
- Yoshida, H. "A study of forces acting on rings for metal V-belt type CVT". *SAE Technical Paper Series*, no. 970686, 1995.
- Yuki, T., Takayama, M., and Kato, H. "Development of dry hybrid belt CVT". *JSAE Review*, vol. 16, pp. 251–256, 1995.
- Zaremba, A. T. and Davis, R. I. "Control design for active engine damping using a starter/alternator". In Proc. of the American Control Conf., pp. 2043–2047. 2000.
- Zeyen, K.-P. and Pels, Th. "ISAD—A computer controlled integrated Starter-Alternator-Damper-System". *SAE Technical Paper Series*, no. 972660, 1997.

# Appendix A

## Test Rig Description

The test rig used for model validation and controller implementation is depicted in Figure A. The main components in the test rig are two identical electric motors, a transmission to be tested, and a reduction gear, basically to invert the final reduction of the transmission (if indeed present). Actually, if the speeds and torques of the two electric motors are to be matched

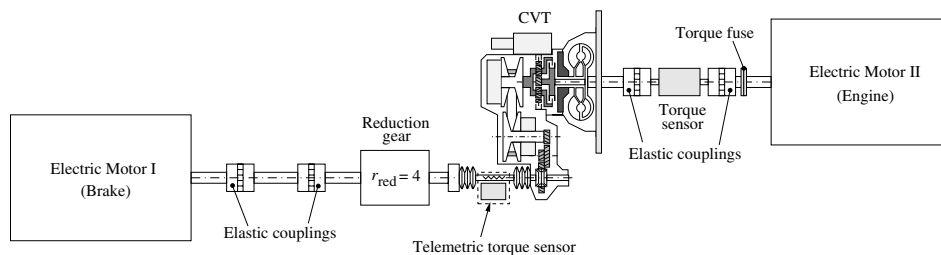


Figure A.1: Schematic depiction of the test rig (top view)

in all situations, the additional reduction gear should have a ratio coverage equal to that of the transmission to be tested and ideally be continuously variable. For most practical operating conditions, though, a reduction gear with speed ratio  $r_{\text{red}} = 4.00$  [-] is satisfactory.

Electric motor II represents the engine and is connected to the primary side of the CVT through a series connection of a torque fuse, two elastic couplings and a torque sensor. The elastic couplings allow for misalignment (shift and tilt), but have a reasonably high torsional stiffness in the direction of shaft rotation. The torque fuse is incorporated to protect the torque sensor in the input shaft against overload. Electric motor I represents the vehicle and its external load. The depiction shows the CVT (without flywheel). When necessary, the flywheel can be mounted in situ and within five minutes. The differential gearing is locked by a dismountable spline-shaft construction so the load can be applied at one drive shaft only. It is to be taken into account that this one shaft endures twice the torque that it normally would. The maximum torque exerted on the drive shaft should not exceed 1200 [Nm]. Furthermore, since normally the output torque of the CVT is balanced by two drive shafts, the stiffness of this end of the driveline is effectively halved, and eigenfrequencies due to the drive shaft elasticity can be expected to drop roughly by a factor  $\sqrt{2}$ . Moreover, the inertia of one electric motor is

0.5 [kgm<sup>2</sup>] and is therefore quite different from the inertias that would normally be present in a vehicle. At the output side the total inertia is about 16 times smaller than normal, whereas at the input side the inertia is around 2.8 times too large. While an inertia which is too small is no problem, the hefty input side proves to be somewhat problematic when highly dynamic transients are required.

The drive shaft is a homokinetic connection, therefore no additional elastic connectors are needed between transmission and reduction gear. At the drive shaft, strain gauges measure the torque and a telemetric receiver acquires the torque signal. The reduction gear is a one-stage planetary set, which is very compact, efficient and noise-free. Finally, the reduction gear is connected to motor I through two flexible connectors. Figure A.2 shows a picture of the actual test rig, whereas Figure A.3 zooms in on the ZI transmission. More information on the test rig components is presented in the following section.

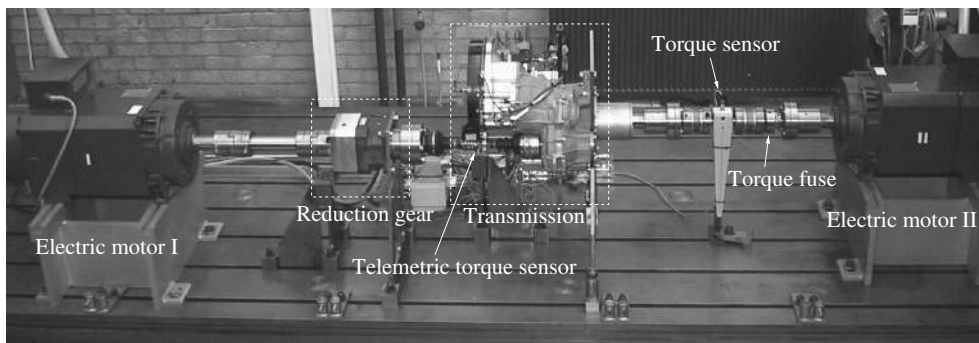


Figure A.2: The test rig (side view)

Besides the torque sensors, the transmission is equipped with various speed, pressure, temperature and acceleration sensors. These sensors will be described in more detail in Section A.3. The actuator and sensor signals are processed by a dSPACE workstation, detailed in Section A.4.

## A.1 Electric motors

At the heart of the test rig are two SIEMENS asynchronous three-phase squirrel-cage electric motors (type 1PA6184-4NL00-0GA03) with a maximum power rating of 81 [kW] and a maximum speed of 5000 [rpm]. The maximum power level is reached at the field-weakening speed of 2900 [rpm] and can be maintained until 5000 [rpm]. Up to the field-weakening speed, the maximum torque of 267 [Nm] can be supplied. Both motors are vector controlled by a SIEMENS MOTION CONTROL system. Motor I is speed controlled and motor II is torque controlled. During normal operation, motor II acts as a motor and motor I as a generator. The MOTION CONTROL feeds the power that is generated by one motor back to the other. The setpoints for the electric motors are supplied to the SIEMENS unit as analogue signals between -10 and +10 [V]. Both motors return a speed and torque (current) measurement, but these measurements are insufficiently accurate for the intended use.

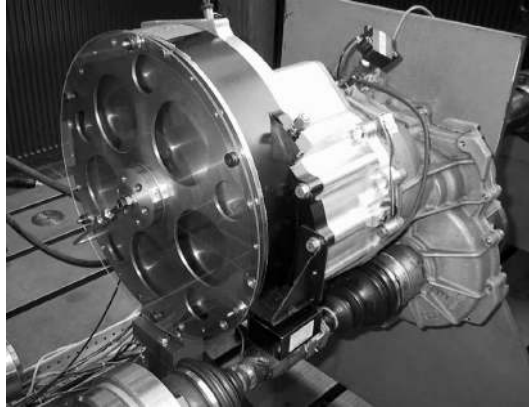


Figure A.3: ZI transmission mounted on the test rig

## A.2 Miscellaneous components

### reduction gear

The reduction gear is a NEUGART PLS 190-04 one-stage planetary reduction. The maximum allowable speed at the side of motor I is 6000 [rpm] (nominal speed 2500 [rpm]), the maximum allowable torque at the drive shaft side is 1200 [Nm]. At full load, the transmission efficiency of the reduction gear is 98%. The reduction gear is equipped with lifetime-grease lubrication, guaranteed in a temperature range from -25 to 100°C (shortly 120°C). The torsional stiffness, backlash and inertia measured at the (high-speed) side of motor I are  $2.16 \cdot 10^6$  [Nm/rad],  $< 3$  [arcmin] and  $2.97 \cdot 10^{-3}$  [kgm<sup>2</sup>], respectively. The noise level measured at a distance of 1 [m], running at 3000 [rpm] (at motor I side) is 70 dB(A), when no load is applied.

### flexible couplings

The two elastic couplings at the side of motor I are GERWAH ADS 500 with a maximum torque of 525 [Nm], and a maximum speed of 5600 [rpm]. Inertia and static (dynamic) torsional stiffness are  $1.06 \cdot 10^{-2}$  [kgm<sup>2</sup>], and  $5.59(2.24) \cdot 10^4$  [Nm/rad], respectively.

The two couplings at motor II side are KTR ROTEX 28 combined with a RUFLEX torque fuse. The maximum speed equals 5600 [rpm], the torsional stiffness is  $1.01 \cdot 10^4$  [Nm/rad].

## A.3 Sensors and actuators

### input torque sensor

For measuring the impeller torque  $T_i$ , two HBM T20WN torque sensors are available, one with a nominal range up to 50 [Nm], the other with a nominal range up to 200 [Nm]. The 50 [Nm] sensor is used for spin-loss measurements only. Most experiments are performed using the 200 [Nm] torque sensor. The outside dimensions of both sensors are identical facilitating easy interchange. The sensors can also measure speed ( $\omega_e$ ) and direction of motion, up to 6000 [rpm]. The torsional stiffness of the 50 and 200 [Nm] sensors are  $1.4 \cdot 10^4$  [Nm/rad]



and  $3.26 \cdot 10^4$  [Nm/rad], respectively. Moments of inertia are, respectively,  $5.37 \cdot 10^{-6}$  [kgm<sup>2</sup>] and  $5.72 \cdot 10^{-6}$  [kgm<sup>2</sup>]. Besides, for both sensors the following applies:

- characteristic tolerance:  $\pm 0.2\%$  of nominal torque;
- cut-off frequency (-3 dB) 200 [Hz];
- temperature influence  $\pm 0.2\%$  of nominal torque per 10 [K] deviation from nominal temperature range;
- characteristic curve deviation related to the nominal sensitivity  $< \pm 0.2\%$  (typical  $< \pm 0.1\%$ ).

### telemetric output torque measurement

The wheel torque  $T_w$  is measured using strain gauges and transported telemetrically using VOLLAND TELEMETRY MICRODAS B1, type BW2 (transmitter) and BS 2.2 (receiver). The same method is used in the test vehicle.

### miscellaneous sensors

The oil pressures  $p_p$  and  $p_s$  are measured using KULITE piezo resistive pressure transducers, type HKM-136-375M-70BAR-SG, with a range of 0–70 [bar]. All speeds except  $\omega_e$  are measured using PHILIPS KMI 10/1 magneto resistive transducers.

### CVT actuators

The actuators for the CVT are the primary valve solenoid (current  $I_1$ ), the secondary valve solenoid (current  $I_2$ ) and the drive clutch valve solenoid (current  $I_{cd}$ ). Furthermore, there are three on-off valves, *viz.* the TC lockup clutch valve (state  $i_{lockup}$ ), the pump mode valve (state  $i_{pump}$ ) and the safety valve (state  $i_{safety}$ )).

## A.4 DSPACE

The DSPACE data-acquisition system consists of a number of boards (hardware) and dedicated software.

### hardware

- DS1003 processor board: 512 kWord local RAM, 256 kWord global RAM;
- DS2002 multi-channel A/D board: Read access of 32 channels of 2 multiplexed A/D converters. Resolution: 4/8/10/12/13/14/15 or 16 Bits selectable for each of the two converters (presently set to 16);
- DS2003 multi-channel A/D board: Same as DS2002, except that channels are distributed automatically to the two converters. Resolution: 4/8/10/12/13/14/15 or 16 Bits selectable for each of the two converters (presently not used);
- DS2103 multi-channel D/A board: Provides multiplexed write access to 32 D/A channels. Output  $\pm 5$  [V] or  $\pm 10$  [V], selectable for each channel. Resolution 14 Bits;

- DS3001 incremental encoder interface board: Each of the 5 channels has a flank detection plus 24-bit counter with a resolution of 200 [ns];
- DS4002 Bit board: Provides read access to 8 Bits and write access to 8 (other) Bits.

### software

The DSP program is written on a PC in MATLAB/SIMULINK 2.2. The SIMULINK model is translated into C and subsequently compiled for and downloaded to the Texas Instruments processor on the DS1003 processor board.

A graphical interface to the DSP program is provided by the COCKPIT program. It allows the user to change parameters in real-time and to visualize the variables that are used in the SIMULINK model. Besides, SIMULINK variables can be monitored and stored to disk for (off-line) evaluation purposes, using TRACE. Both COCKPIT and TRACE run on the PC and communicate with the processor board by service routines.

### multiple timer task mode

For high-frequency analysis purposes and to avoid analogue filters, sensor signals are acquired at 4 [kHz]. Because the dSPACE processor is insufficiently fast to run the entire SIMULINK program at 4 [kHz], the 'multiple timer task mode' is used instead of the default 'single timer task mode'. The multiple timer task mode allows different parts of the program to run at different sample frequencies. By assigning a lower sample frequency to time consuming parts, more time will be available for the parts that have to operate at high sample frequencies. Currently, three sample frequencies are present in the program. Acquisition of sensor signals and digital downsampling is performed at 4 [kHz] (Task 1). The program parts concerned with pressure control are performed at 500 [Hz] (Task 2) to enable a desired closed-loop pressure control bandwidth of around 50 [Hz]. All other calculations are executed at 100 [Hz] (Task 3), which is sufficient for the slower processes, *e.g.*, ratio control at circa 10 [Hz]. Task 1 has the highest, Task 3 the lowest priority. For more information on the multiple timer task mode, see [dSPACE, 1999].

## A.5 Hydraulics

### CVT hydraulics

The hydraulic scheme of the conventional CVT is depicted in Figure A.4, for reference mostly.

### ZI Stop-Go hydraulics

Figure A.5 depicts the essentials of the ZI Stop-Go hydraulics. As compared to the conventional hydraulics, the following modifications are visible:

- two proportional pressure control valves are added, referred to as the *secondary clutch valve* and the *flywheel clutch valve*. Both are REXROTH DRE 4 K-31/18G24-10NK4M valves, and are controlled using a DC current ( $I_{\max} = 1.0$  [A]);
- a hydraulic accumulator is positioned in parallel to the (original) pump, as a pressure supply for the valves when the engine is shutdown. The accumulator (or *accu* for short)

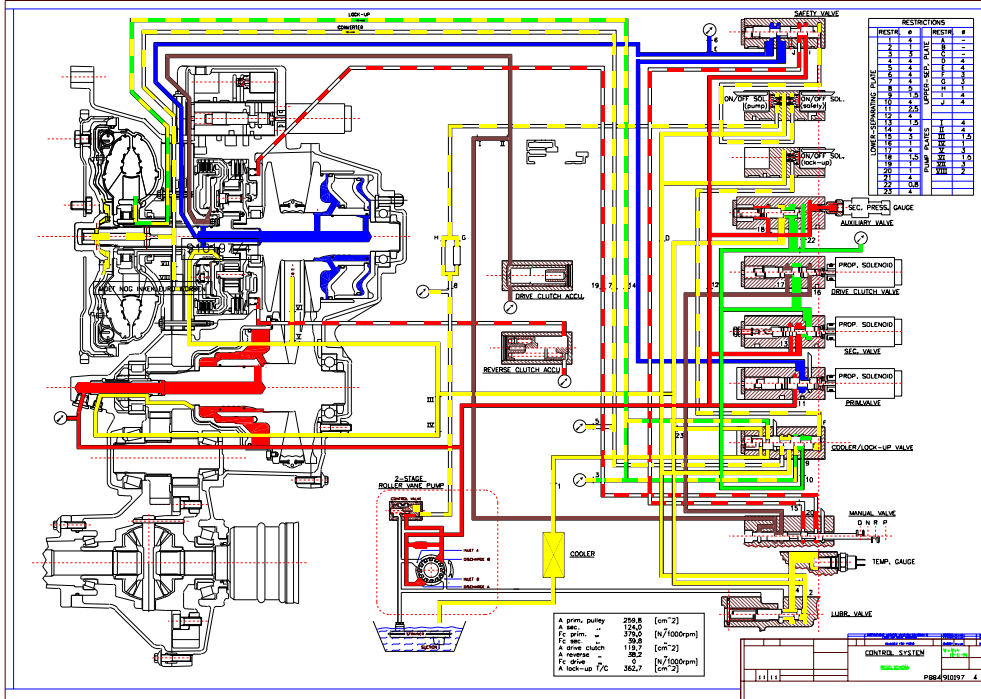


Figure A.4: The P884 hydraulics (courtesy of VDT), which are identical to the hydraulics of the P920 CVT in the ZI powertrain

is of the diaphragm type BOSCH 0 531 601 546. The accu is pre-charged with nitrogen ( $N_2$ ) at a pressure of 6 [bar], and has an effective volume of 0.35  $l$ . The maximum allowable pressure is 24 [bar]. The minimum operating pressure should not drop below the pre-charge pressure frequently, in order not to have the bladder continually knock against the internal valve (wear);

- the *accu load valve* is a leakproof on-off valve, type BOSCH 0 810 040 958, which is included to control the accumulator's state of charge. It is normally closed and opens for charging and when pressure is needed in the Start phase of ZI Stop-Go;
- a one-way valve (or, check valve) is placed in the pressure side of the pump to prevent oil leaking through the pump when it is not running;
- the *reverse clutch valve* is a modified version of the conventional 'manual valve'. The latter valve owes its name to the fact that it is manually operated by the driver's shift lever, switching between Drive, Neutral, Reverse and Park position. In the ZI Stop-Go transmission, though,  $C_d$  and  $C_r$  must be operated simultaneously. Therefore, the pressure to the drive clutch which is normally switched by the manual valve, bypasses

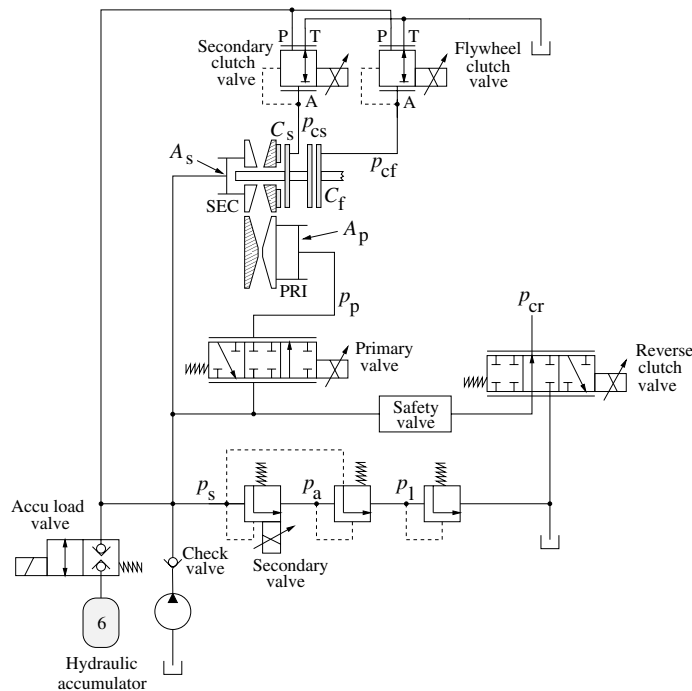


Figure A.5: Essentials of ZI Stop-Go hydraulics

this valve in the ZI Stop-Go transmission, and is only controlled by the (proportional) *drive clutch valve* (not shown in Figure A.5);

- the *safety valve* (shown, but not detailed in Figure A.5) should also be operated differently. Normally, in the 'on' position, the safety valve disconnects the line pressure from the manual valve (the reverse clutch valve, in case of ZI Stop-Go) and connects (not shown) the primary pressure to the primary valve, and vice versa in the 'off' position. The 'off' position is normally used for driving in reverse, and also for the fail-safe/limp-home mode. In the ZI Stop-Go system, the safety valve should be set to 'off' in order to operate the reverse clutch. Fortunately, in situations where  $C_r$  is transmitting torque, no substantial primary pressure is needed, because the CVT is not transmitting any torque ( $C_s$  is open), or alternatively, the clamping force is delivered by  $p_s$  and by the UD mechanical stop of the primary pulley (when driving in reverse,  $r_{cvt} = r_{ud}$ , same as conventional).

## A.6 Additional ZI Stop-Go clutches

The flywheel clutch  $C_f$  and the secondary clutch  $C_s$  in the ZI Stop-Go transmission were designed to fit within the confinements of the ZI transmission.  $C_f$  and  $C_s$  are multi-plate wet clutches with a BELLEVILLE release spring and both have centrifugal compensation. For details concerning the design of these clutches, the reader is referred to [van Druten, 2001].



# Appendix B

## Metal V-belt Model

In this appendix the variator models presented in Chapter 6 are elaborated and expressions for the minimal pulley clamping force are presented.

### B.1 Elaboration of the Coulomb model

Equilibrium in tangential and radial direction of forces acting on a piece of band (see Chapter 6 for the accompanying figures), yields

$$dS = -dW_1 \quad (\text{B.1})$$

and

$$(S - B)d\xi = dN_1; \quad B = \rho_b v_b^2 \quad (\text{B.2})$$

respectively. Using (6.8), (B.1) and (B.2) it is straightforward to see that

$$dS = -\chi_1 s_1 (S - B)d\xi \quad (\text{B.3})$$

and if  $B$ ,  $s_1$  and  $\chi_1$  are constant

$$S(\xi) = K_S e^{-\chi_1 s_1 \xi} + B \quad (\text{B.4})$$

where  $K_S$  is an integration constant. The assumption that  $\chi_1$  is constant implies either a smaller friction coefficient  $\chi_1$ , or an 'idle tension arc', at the pulley with the larger belt radius. In the paragraph succeeding Equation (B.10), it will be argued to use the latter assumption.

Similarly, tangential and radial equilibrium for a piece of segment yields

$$2dW_{2,\text{tan}} + dD = 0 \quad (\text{B.5})$$

and

$$(B + C - D)d\xi + 2dN_2 \sin \theta + 2dW_{2,\text{rad}} \cos \theta = 0 \quad (\text{B.6})$$

where  $D(\xi) = S(\xi) - Q(\xi)$  and  $C = \rho_c v_c^2$ . Using (6.5)–(6.7), (B.5) and (B.6), the following differential equation for  $D$  results

$$\frac{1}{\chi_3} \frac{dD}{d\xi} + D = B + C \quad (\text{B.7})$$

where

$$\chi_3 = \frac{\chi_2 s_2 \cos \gamma}{\sin \theta + \chi_2 s_2 \sin \gamma \cos \theta} \quad (\text{B.8})$$

### active and idle arcs

In equation (B.5),  $dQ \neq 0$  and hence  $Q = Q(\xi)$  at the active (compression) arcs, *i.e.*, the arcs at which  $Q$  is varying ( $dQ = 0$  at the idle arcs). At these active arcs creep motion results in  $\chi_2 = \mu_2$ , so that (B.8) can be readily replaced by

$$\chi_{3a} = \frac{\mu_2 s_2 \cos \gamma}{\sin \theta + \mu_2 s_2 \sin \gamma \cos \theta} \quad (\text{B.9})$$

For the active arcs, the solution to differential equation (B.7) is given by

$$D(\xi) = -K_Q e^{-\chi_{3a} \xi} + B + C \quad (\text{B.10})$$

where  $K_Q$  is an integration constant.

Similarly, in equations (B.1) and (B.2),  $dS \neq 0$  (and  $S = S(\xi)$ ) at what might be termed the ‘active tension arc’ (and, correspondingly, ‘idle tension arc’ for the remainder of the angle of wrap). However, the terms *active* and *idle* are generally seen to be reserved for compression forces. Furthermore, it is not totally clear whether an ‘idle tension arc’ exists at all, although it is often assumed to. Work by Fujii *et al.* [Fujii *et al.*, 1993b], in which they measured tension forces acting on a piece of band while running along the pulleys, does not seem to support such an assumption. In the following the mentioned assumption is made, mainly because the effect of excluding an idle tension arc (which calls for a friction coefficient that is smaller at the larger belt radius) was found to be small. Therefore,  $\chi_1 = \mu_1$  all along the smallest wrap angle and  $\chi_1 = 0$  for the remaining part at the larger wrap angle. Figure B.1 clarifies some of the terminology. Substituting  $dQ = 0$  into equations (B.5) and (B.6), yields the idle arc equations

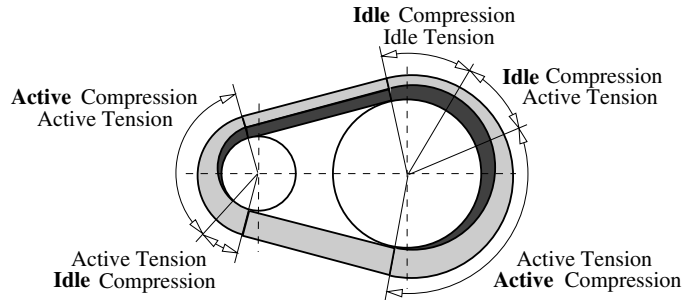


Figure B.1: Definition of active and idle arcs. Bold words indicate conventional terminology

$$2dW_{2,\tan} + dS = 0 \quad (\text{B.11})$$

$$\chi_2 s_2 = \frac{\sin \theta}{\cos \gamma} \cdot \frac{\chi_1 s_1 K_S}{K_S - (Q_i + C)e^{\chi_1 s_1 \xi} - \chi_1 s_1 \tan \gamma \cos \theta K_S} \quad (\text{B.12})$$

Table B.1: Boundary conditions

Model		Boundary conditions		$s_1$	$s_2$
UD	primary	$S(\varphi_p/2) = S_0$	$Q(\varphi_p/2 - \varphi_1) = 0$	+1	+1
	secondary	$S(\varphi_s/2 - \varphi_p) = S_0$	$Q(\varphi_s/2) = 0$	-1	-1
UR	primary	$S(\varphi_p/2) = S_0$	$Q(\varphi_p/2) = 0$	+1	-1
	secondary	$S(\varphi_s/2 - \varphi_p) = S_0$	$Q(\varphi_s/2 - \varphi_2) = 0$	-1	+1
OD	primary	$S(\varphi_p/2 - \varphi_s) = S_0$	$Q(\varphi_p/2 - \varphi_1) = 0$	-1	+1
	secondary	$S(\varphi_s/2) = S_0$	$Q(\varphi_s/2) = 0$	+1	-1

Table B.2: Integration constants

Model		$K_S$	$K_Q$
UD	primary	$(S_0 - B)e^{\chi_1 \varphi_p/2}$	$(C - K_S e^{-\chi_1(\varphi_p/2 - \varphi_1)}) \cdot e^{\chi_{3a}(\varphi_p/2 - \varphi_1)}$
	secondary	$(S_0 - B)e^{-\chi_1(\varphi_s/2 - \varphi_p)}$	$(C - K_S e^{\chi_1 \varphi_s/2}) \cdot e^{\chi_{3a} \varphi_s/2}$
UR	primary	$(S_0 - B)e^{\chi_1 \varphi_p/2}$	$(C - K_S e^{-\chi_1 \varphi_p/2}) \cdot e^{\chi_{3a} \varphi_p/2}$
	secondary	$(S_0 - B)e^{-\chi_1(\varphi_s/2 - \varphi_p)}$	$(C - K_S e^{\chi_1(\varphi_s/2 - \varphi_2)}) \cdot e^{\chi_{3a}(\varphi_s/2 - \varphi_2)}$
OD	primary	$(S_0 - B)e^{-\chi_1(\varphi_p/2 - \varphi_s)}$	$(C - K_S e^{\chi_1(\varphi_p/2 - \varphi_1)}) \cdot e^{\chi_{3a}(\varphi_p/2 - \varphi_1)}$
	secondary	$(S_0 - B)e^{\chi_1 \varphi_s/2}$	$(C - K_S e^{-\chi_1 \varphi_s/2}) \cdot e^{\chi_{3a} \varphi_s/2}$

where  $Q_i$  is the constant value for  $Q$  at the *idle* arc. Note that  $\chi_2$  is a function of  $\xi$ .

Finally, at the 'larger' pulley, a remaining arc exists where both  $dQ = 0$  and  $dS = 0$ , or  $\chi_1 = 0$ . Table B.2 lists  $K_S$  and  $K_Q$ , determined from boundary conditions for the various models, see Table B.1. Next, we wish to determine the primary and secondary pulley thrusts needed to maintain a stationary speed ratio for otherwise constant conditions. From Figure B.2, it is seen that

$$dF = dN_2 \cos \theta - dW_{2,\text{rad}} \sin \theta \quad (\text{B.13})$$

with  $F$  the axial pulley clamping force. Using (6.5) and (6.7) to obtain  $\frac{dN_2}{d\xi}$  from (B.6), (B.13) translates to

$$\frac{dF}{d\xi} = \frac{\cos \theta - \chi_2 s_2 \sin \gamma \sin \theta}{2(\sin \theta + \chi_2 s_2 \sin \gamma \cos \theta)} (D(\xi) - B - C) \quad (\text{B.14})$$

If, in equation (B.14),  $\gamma$  is taken to be zero (*i.e.*, there is no radial friction force between segments and pulley) the expression simplifies to

$$\frac{dF}{d\xi} = \frac{D(\xi) - B - C}{2 \tan \theta} \quad (\text{B.15})$$

$F_p$  and  $F_s$  can then be obtained by integrating (B.15), or

$$F_p = \int_{\varphi_p} \frac{dF_p}{d\xi} d\xi \quad (\text{B.16})$$

and

$$F_s = \int_{\varphi_s} \frac{dF_s}{d\xi} d\xi \quad (\text{B.17})$$



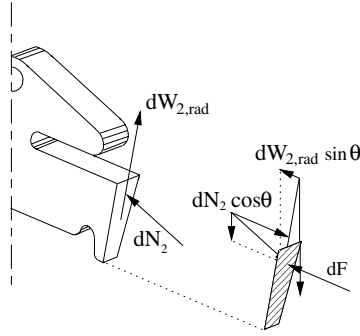


Figure B.2: (Axial) forces acting in segment-pulley contact

Combining (B.16) and (B.17) gives

$$F_p = \Phi F_s + \frac{\int_{\varphi_p} D_p(\xi) d\xi - \Phi \int_{\varphi_s} D_s(\xi) d\xi}{2 \tan \theta} \quad (\text{B.18})$$

where  $\Phi = \frac{\varphi_p}{\varphi_s}$  is introduced. At first sight, equation (B.18) may suggest that the centrifugal forces at primary side and secondary side cancel out. Of course,  $B$  and  $C$  still appear in determining  $K_S$  and  $K_Q$ , which themselves determine the 'shape' of  $S(\xi)$  and  $Q(\xi)$  and hence of  $\int D(\xi) d\xi$ .

### B.1.1 Calculation procedure

Using the above model, calculation of the various quantities is possible given the value of three input variables. Assuming that the input torque  $T_p$ , the speed ratio  $r_{cvt}$  and the secondary axial pulley clamping force  $F_s$  are known, the following procedure is used:

1. as a starting point, assume a value for the lowest band tension  $S_0$  (see Figures 6.5–6.7). Then  $S_1$  is obtained as

$$S_1 = (S_0 - B)e^{\mu_1 \min(\varphi_p, \varphi_s)} + B$$

where the angles of wrap  $\varphi_p$  and  $\varphi_s$  follow directly from  $r_{cvt}$ ;

2. since  $S_0$  and  $S_1$  are known, using (6.39) the compression force  $Q_{\max} = \max(Q_{sl}, Q_{ti})$  in the straight part of the belt can be determined, as well as the model (UD, UR or OD) that is actually applicable. For UD and OD  $Q_{\max} = Q_{sl}$ , whereas for UR  $Q_{\max} = Q_{ti}$  (terminology according to Figure 6.24);
3. assuming  $\gamma = 0$ , the secondary active arc  $\varphi_2$  that yields  $\max(Q) = Q_{\max}$  can be obtained. Subsequently, the integration constants  $K_S$  and  $K_Q$  can be determined and, through the integration of (B.15),  $F_s$ ;
4. vary  $S_0$  until the resulting  $F_s$  equals the secondary clamping force that was given at the start of the calculation;

5. when the final value of  $S_0$  is fixed, the primary active arc  $\varphi_1$ , the primary clamping force  $F_p$  and  $\kappa$  according to (6.11) can be obtained, in a way similar to that for the secondary side.

The friction coefficient  $\chi_2$  at the idle arcs (which is smaller than  $\mu_2$ ) can be determined using (B.12).

## B.2 Elaboration of the viscous shear model

Recall equations (6.12) and (6.13). Substituting  $v_u - v_c = \frac{-\dot{R}}{\cos\theta}$  in (6.13) yields

$$dW_{2,\text{rad}} = \frac{-\eta_{\text{oil}} \dot{R}}{h_f \cos\theta} \cdot \frac{bcR}{m} d\xi \quad (\text{B.19})$$

For simplicity, the oil film thickness  $h_f$  is assumed to be constant along each angle of wrap  $\varphi_x$  ( $x = p, s$ ) and, according to [Micklem *et al.*, 1994], equal to

$$h_f = \frac{k_h}{p_{\text{mean}}} \quad (\text{B.20})$$

where  $k_h$  is determined experimentally and where  $p_{\text{mean}}$  is the mean pressure in the Hertzian contact between pulley and segment:

$$p_{\text{mean}} = \frac{F}{bc \cos\theta} \cdot \frac{m}{R\varphi_x} \quad (\text{B.21})$$

with  $bc \cos\theta$  the flank surface of one segment projected in the plane perpendicular to  $F$ .

Using Equation (B.13) and substituting  $\frac{dN_2}{d\xi}$  as obtained from (B.6) results in

$$\frac{dF}{d\xi} = \frac{1}{2 \tan\theta} \left( D(\xi) - B - C - \frac{2}{\cos\theta} \frac{dW_{2,\text{rad}}}{d\xi} \right) \quad (\text{B.22})$$

Integrating  $\frac{dF}{d\xi}$  at primary and secondary side while substituting (B.19), yields

$$\frac{\eta_{\text{oil}} 2bc\varphi_p}{m \cos^2\theta} \cdot \dot{R}_p \left( \frac{R_p}{h_{f,p}} + \Phi \frac{R_s}{h_{f,s}} \right) = - \int_{\varphi_p} D_p(\xi) d\xi + \Phi \int_{\varphi_s} D_s(\xi) d\xi + 2 \tan\theta (F_p - \Phi F_s) \quad (\text{B.23})$$

where  $\dot{R}_s = -\Phi \dot{R}_p$  was used. Combining (B.23) with (B.20) and (B.21) gives

$$\dot{R}_p = \frac{- \int_{\varphi_p} D_p(\xi) d\xi + \Phi \int_{\varphi_s} D_s(\xi) d\xi + 2 \tan\theta (F_p - \Phi F_s)}{F_p + \Phi^2 F_s} \cdot \frac{k_h}{\eta_{\text{oil}}} \cdot \frac{\cos^3\theta}{2} \quad (\text{B.24})$$

Substitution of  $\dot{R}_p = 0$  results in a relation for the primary clamping force  $F_p^*$ , needed to maintain a stationary speed ratio. This force  $F_p^*$  is exactly equal to  $F_p$  as given by (B.18). Then (B.24) transforms into

$$\dot{R}_p = \cos^2\theta \sin\theta \cdot \frac{k_h}{\eta_{\text{oil}}} \cdot \frac{F_p - F_p^*}{F_p + \Phi^2 F_s} \quad (\text{B.25})$$

or, using

$$\dot{r}_{\text{cvt}} = \frac{\dot{R}_p}{R_s} \cdot (r_{\text{cvt}} \Phi + 1) \quad (\text{B.26})$$

equivalently into

$$\dot{r}_{\text{cvt}} = \cos^2 \theta \sin \theta \cdot \frac{k_h}{\eta_{\text{oil}}} \cdot \frac{r_{\text{cvt}} \Phi + 1}{R_s} \cdot \frac{F_p - F_p^*}{F_p + \Phi^2 F_s} \quad (\text{B.27})$$

In this expression,  $\frac{k_h}{\eta_{\text{oil}}}$  is experimentally obtained from slip measurements, which were performed by [Micklem *et al.*, 1994; Guebeli *et al.*, 1993] and fit to  $R_p$  according to

$$\frac{k_h}{\eta_{\text{oil}}} = c_{v0} + c_{v1} R_p \quad (\text{B.28})$$

where  $c_{v0} \approx 2.7$  [m/s] and  $c_{v1} \approx 29$  [s<sup>-1</sup>].

### B.2.1 Minimal pulley clamping force

For practical implementation, to prevent belt slip a minimal value for the pulley clamping forces is needed. The determination of this minimal value is based on the Coulomb friction model. When neglecting the radial friction force between segments and pulley, the normal force between the pulley and segments should balance the total axial pulley force  $F_x$  on the moveable pulley sheave  $x$  ( $x = p, s$ ), conform Equation (B.13), or

$$F_x = \cos \theta \int dN_{2,x}(\xi) \quad (\text{B.29})$$

The torque  $T_x$  transmitted between the belt and the pulley, is equal to the summed tangential friction force ( $2\mu_2 \int dN_{2,x}(\xi)$  for two friction surfaces), and multiplied by the radius  $R_x$

$$T_x = R_x 2\mu_2 \int dN_{2,x}(\xi) \quad (\text{B.30})$$

Hence, the minimum pulley clamping force needed to transmit a torque  $T_x$  equals

$$F_{x,\text{min}} = \frac{\cos \theta |T_x|}{2\mu_2 R_x} \quad (\text{B.31})$$

where  $\mu_2$  is the maximum friction coefficient. The ratio of the actually transmitted torque over the torque which can maximally be transmitted using clamping force  $F_x$ , is denoted by

$$\tau_x = \frac{\cos \theta T_x}{2\mu_2 R_x F_x} \quad (\text{B.32})$$

In commercial Van Doorne CVTs,  $F_p$  is difficult to reconstruct, because the pressure  $p_p$  in the hydraulic cylinder on the primary pulley is not measured. On the other hand, a measurement of the secondary pressure  $p_s$  is available. Also, in a commercial vehicle no torques are measured, though an estimate for the primary torque  $T_p$  is available from the engine map (with engine speed and throttle valve opening as inputs), combined with the torque converter map

(with engine speed and turbine speed as inputs). To determine the secondary torque  $T_s$ , the efficiency of the CVT needs to be taken in to account. Therefore, it may be hard to determine  $\tau_p$  and  $\tau_s$  from the actual measurements. For this reason, a modified torque ratio  $\tau'_s$  is introduced:

$$\tau'_s = \frac{\cos \theta T_p}{2\mu_2 R_p F_s} \quad (\text{B.33})$$

In practice, a safety margin is applied. For this purpose, in determining the minimum clamping force, the actual torque is increased with 30% of the maximal primary torque  $T_{p,\max}$ . The minimum clamping force then is determined from

$$F_{30\%} = \frac{\cos \theta (|T_p| + 0.3T_{p,\max})}{2\mu_2 R_p} \quad (\text{B.34})$$

where  $T_{p,\max}$  is taken equal to the maximum engine torque.



## Appendix C

# Alternative Hydraulic Actuation

In practice, the rate of ratio change is bounded by a number of physical limitations, like the maximum pump pressure and the maximum oil flow. In this respect, the effect of the hydraulic circuit layout should not be underestimated. Because there is only one pump, both the primary and secondary pressure have to be derived from the pump pressure. This requires a number of dedicated valves, which can be arranged in various configurations. Based on a comparison of four configurations [Vroemen *et al.*, 1998], an alternative layout is suggested, which should improve on ratio control without impairing safety control (as defined in Chapter 7). Throughout this appendix, focus is on the design of a hydraulic circuit to realize the primary and secondary pressure. Additional hydraulics (generally operating at lower pressures) are referred to as *accessories* and their design is outside the scope of the present investigation.

### C.1 Hydraulic circuit design

When designing a hydraulic circuit for controlling two pressures with minimal interaction, two independent pumps would be ideal. Because this is unacceptably costly and bulky, one pump must supply oil flow to both circuits, and valves should be chosen and positioned such as to minimize interaction. To reduce costs and complexity, the number of valves should be as small as possible, and the valves should be simple, and robust against disturbances such as contamination and wear. Furthermore, valves cause resistance and should therefore not be positioned upstream of the primary or secondary cylinder, unless absolutely necessary.

#### C.1.1 VDT layout

The VDT hydraulic circuit is repeated in Figure C.1. The primary pressure surface ( $A_p$ ) is larger than the secondary one ( $A_s$ ), since otherwise it would not be possible to obtain primary axial pulley forces  $F_p$  exceeding<sup>1</sup> the secondary pulley forces  $F_s$ , since always  $p_p \leq p_s$ .

The VDT hydraulic design exhibits a number of compromises between manufacturing and operating costs on the one hand, and ease of control (ratio as well as safety) on the other.

---

<sup>1</sup>The quotient of axial pulley forces at primary and secondary side needed to maintain a stationary CVT ratio, varies somewhere between 0.6 and 1.7. To achieve (sudden) changes in ratio the required interval is larger.

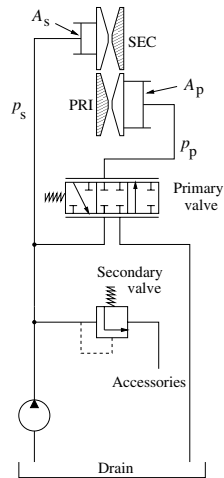


Figure C.1: VDT hydraulic system

For instance, the number of valves (besides those needed for the accessories) is kept to the minimum of two, needed to enable independent control of  $p_p$  and  $p_s$ , given the fact that there is only one pump. The valves themselves are a compromise between ease of manufacturing and performance, whereas their position in the hydraulic circuit aims at keeping hydraulic losses as low as possible. In this design the pump pressure equals the secondary pressure.

The way the variator is operated, *i.e.*, using  $p_s$  to maintain a certain level of safety towards belt slip and changing the speed ratio by manipulating  $p_p$ , is reason for concern when it comes to belt slip at primary side. Belt slip may occur if  $p_p$  is lowered quickly, in order to reach a lower speed ratio. The clamping force at primary side should always be large enough to guarantee slip free operation. However, for economical reasons, pressure is measured only at secondary side, and therefore a minimum primary clamping force cannot really be guaranteed.

## C.1.2 Alternative layout

The suggested alternative lay-out uses the secondary pressure to generate a supplementary clamping force at primary side, by connecting it to an additional primary cylinder. The resulting hydraulic layout, referred to as Double Primary Cylinder (DPC), is depicted in Figure C.2, where the additional pressure surface is indicated by  $A_a$ . A first glance comparison reveals some of the benefits that are to be expected:

- for the DPC system, there is a primary clamping force even when  $p_p = 0$ . This might solve primary belt slip problems that arise in the VDT configuration when  $p_p$  drops dramatically;
- in the VDT layout, flow from the secondary side can be used at primary side when shifting towards OD. DPC has the same benefit, whereas part of the flow does not have to overcome the restriction that the primary valve constitutes, thus potentially improving upshifting;

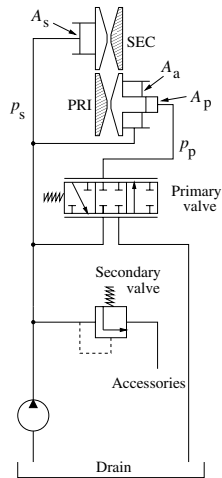


Figure C.2: DPC hydraulic system

- when shifting towards UD, the VDT setup offers no possibility for the primary flow to reenter the secondary circuit. This disadvantage is partly canceled in DPC through the connection of the secondary circuit and the additional cylinder. Also, the primary flow that must blow off towards the drain is smaller than for the VDT layout, implying that the restriction towards the drain becomes less of a limitation for downshifting (see Section C.2.2). Both mechanisms are likely to improve upon shifting towards UD.

Apart from these benefits there are some points of concern with respect to the alternative layout:

- the VDT layout needs to be equipped with an extra rotating flow connection. Still, modifications to the VDT design are small, *i.e.*, there is no need for additional or different valves, no extra pump is needed, and the second cylinder surface at primary side is in fact already present in current designs, though it should be resized, see Figure C.3;

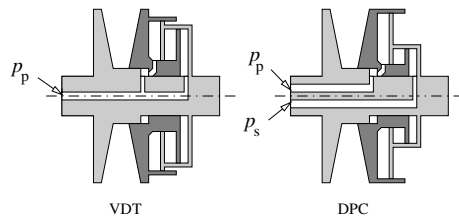


Figure C.3: Schematic VDT primary pulley construction and suggested DPC construction; pressure surface ratios are taken from Section C.1.3

- the cylinder pressure surfaces at primary side probably need to be resized, and may cause the cylinder outside diameter to increase (also see Figure C.3);



- the minimum ratio of  $F_p$  over  $F_s$  which can be realized is substantially larger for DPC than for the VDT layout, where it is approximately zero. Downshifting would be impaired by this effect, especially when *coasting*, *i.e.*,  $T_p < 0$ , where the required pulley thrust ratios are smallest.

Furthermore, the hydraulically realized  $F_p$  and  $F_s$  are more closely related for DPC than they are for VDT. Without further analysis, it is not clear whether this will be advantageous or not.

### C.1.3 Cylinder dimensioning

The pressure surface ratios  $A_p/A_s$  and  $A_a/A_s$  are constrained by the pulley thrust ratios needed to attain all possible speed ratios and, moreover, all required shift speeds. It is assumed that the pulley thrust ratio has to cover the entire empirically obtained interval (0.4 . . . 2). Extending (6.21) to include the contribution of the additional cylinder at primary side yields

$$F_p = A_p p_p + A_a p_s + c_p \omega_p^2 \quad (C.1)$$

Substitution of (C.1) and (6.22) into the constraints

$$\left( \frac{F_p}{F_s} \right)_{\min} \leq 0.4 \quad ; \quad \left( \frac{F_p}{F_s} \right)_{\max} \geq 2.0, \quad (C.2)$$

neglecting the centrifugal forces as well as the spring force, and using  $0 \leq p_p \leq p_s$ , gives

$$\frac{A_a}{A_s} \leq 0.4 \quad ; \quad \frac{A_a}{A_s} + \frac{A_p}{A_s} \geq 2.0 \quad (C.3)$$

For reasons of compactness of the construction it is preferable to make the ratio  $\frac{A_p}{A_s}$  as small as possible. In the following, it is chosen to take  $\frac{A_a}{A_s} = 0.4$ ,  $\frac{A_p}{A_s} = 1.6$ , *i.e.*, at their boundaries, in order to maximally reveal the differences between DPC and VDT. With this choice, the outside diameter of the primary cylinder will increase by circa 25 % as compared to the VDT system where the primary cylinder pressure surface is composed of two parallel cylinders with an outside diameter approximately equal to that of the secondary cylinder.

## C.2 Simulation results

The two hydraulic configurations are evaluated in this section, based on safety margins and shift speeds. It is chosen to use time-domain instead of frequency-domain [Vroemen *et al.*, 1998] comparisons, to avoid questionable linearizations. In the evaluating simulations it is chosen to operate the pump single-sided only. This means that whenever the attainable shift speed is dictated by the maximum pump flow, double sided operation is likely to increase the maximum shift speed.

### C.2.1 Safety in case of pressure breakdown

Using (C.1), (6.22), (B.32) and (B.34), taking  $p_p = 0$ , results in

$$\tau_p = \frac{\cos \theta T_p}{2\mu_2 R_p} \frac{1}{c_p \omega_p^2 + \frac{A_a}{A_s} \left( \frac{\cos \theta (T_p + 0.3 T_{p,\max})}{2\mu_2 R_p} - c_s \omega_s^2 - F_{\text{spr}} \right)} \quad (C.4)$$

where it is assumed that  $F_s$  equals  $F_{30\%}$  according to (B.34). If primary belt slip is to be prevented, then  $\tau_p \leq 1$  must hold. Assuming  $\tau_p = 1$ , the transmittable primary torque in case of primary pressure breakdown ( $p_p = 0$  [bar]) for  $r_{cvt}$  close to  $r_{ud}$  (*i.e.*, the pulley sheave has not reached its stop) can be determined. Figure C.4 shows the maximally transmittable primary torque for both the hydraulic layouts. Clearly, DPC has an inherently higher resistance

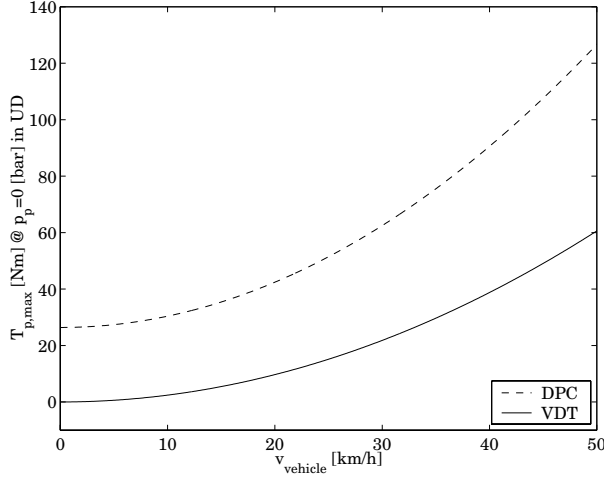


Figure C.4: Maximally transmittable primary torque in case of primary pressure breakdown towards belt slip over the entire vehicle speed region where  $r_{ud}$  can be maintained.

## C.2.2 Shifting speed

In order to evaluate shifting performance, the speed ratio is made to track a skewed sinusoidal reference signal which varies from the initial speed ratio down to  $\max(r_{ud}, \frac{\omega_s}{\omega_{e,max}})$  and back to  $\min(r_{od}, \frac{\omega_s}{\omega_{e,min}})$ , see Figure C.5. For every vehicle speed, the initial speed ratio is determined such that the engine initially operates at the E-line. In all simulations, both the vehicle speed and the road load torque are taken to be constant, *i.e.*,  $T_s$  is constant. Figures C.6 and C.7 show

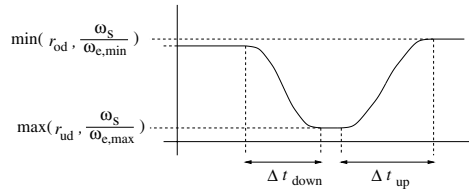


Figure C.5: Reference signal

some results, in the form of logarithmic shift speeds  $\Sigma$ , where  $\Sigma$  is defined by

$$\Sigma = \frac{1}{\Delta t} \left| \ln \frac{r_1}{r_0} \right| \quad (C.5)$$

Here  $r_0$  and  $r_1$  are initial and final speed ratio, and  $\Delta t$  is the time interval needed for the up- or downshift. The advantage in this shift speed definition lies in the fact that upshifting and downshifting are symmetrical around  $r_{\text{cvt}} = 1$ . Figure C.8 depicts the relative increase of  $\Sigma$  of

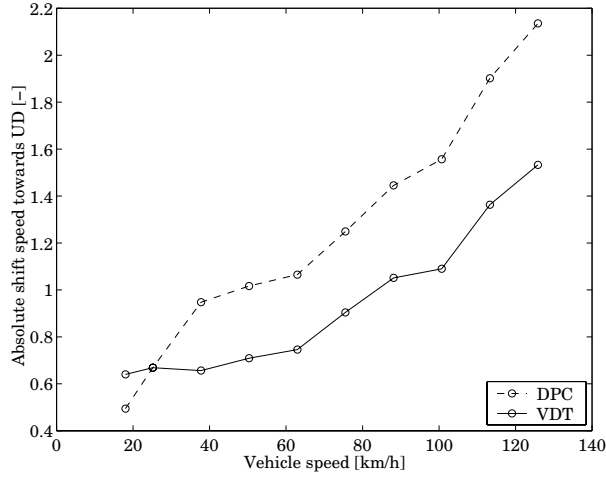


Figure C.6: Shifting towards UD

DPC over VDT. The factors limiting  $\Sigma$  in these simulations (also see Table C.1) are:

Table C.1: Shift speed limiting factors

$v_v$ [km/h]	to UD		to OD	
	DPC	VDT	DPC	VDT
18	B	D	A	A
25	D	D	A	A
> 38	D	D	C	C

- A. insufficient pump flow; this is a limiting factor when pump speed is low, causing the pump flow to be small;
- B.  $p_{s,\text{max}}=50$  [bar]; the limit is occasionally reached when  $\omega_p$  is low, forcing  $|F_p - F_p^*|$  in equation (6.15) to be high in order to compensate for low  $\omega_p$ ;
- C.  $p_{p,\text{max}}=25$  [bar]; when shifting towards OD with sufficiently high  $\omega_p$ , this is the limiting factor;
- D. shifting towards UD is usually limited because the combination of a low primary pressure  $p_p$  and a maximum valve opening towards the drain makes it impossible to remove sufficient excessive oil from the primary circuit.

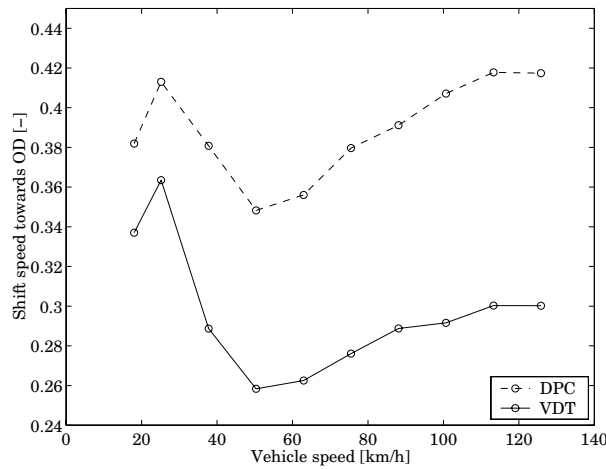


Figure C.7: Shifting towards OD

Mechanism B is the limiting factor which causes DPC to be slightly slower than VDT for speeds below circa 20 [km/h]. In situations where A is the limiting factor, double-sided operation of the pump can increase shifting speeds. So, for low vehicle speeds upshifting can be improved for both systems, by as much as 65% (not depicted). The fact that the pump flow is restricting the shift speed for both systems also implies that the pump size cannot be reduced without impairing overall shifting performance.

### C.2.3 Shifting while coasting

As mentioned in Section C.1.2, shifting while coasting might be reason for concern. The pulley thrust ratio  $\kappa$  conform (6.11), is smallest for negative primary torques, implying that downshifting in these situations will be hampered, whereas upshifting will be made easier. For DPC, the first is especially true, since the minimum pulley thrust ratio that can be realized is substantially larger than that for the VDT system. Provided the pressure surfaces are chosen sensibly, there are still no problems during coasting, as Table C.2 shows. This table lists

$T_p$ [Nm]	to UD		to OD	
	DPC	VDT	DPC	VDT
normal	0.73	0.59	0.36	0.26
-25	0.61	0.49	0.36	0.26
-50	0.61	0.49	0.39	0.28

Table C.2: Shift speeds cf. (C.5), coasting from 63 [km/h]

the absolute shift speeds  $\Sigma$  for up- and downshifting, given a ‘normal’ primary torque (*i.e.*,  $T_p$  corresponds to a stationary road load) and two negative torques. In fact, the DPC layout still outperforms the VDT layout. Also, as Table C.2 shows, downshifting is indeed worsened while upshifting is improved, as compared to the ‘normal’ situation.

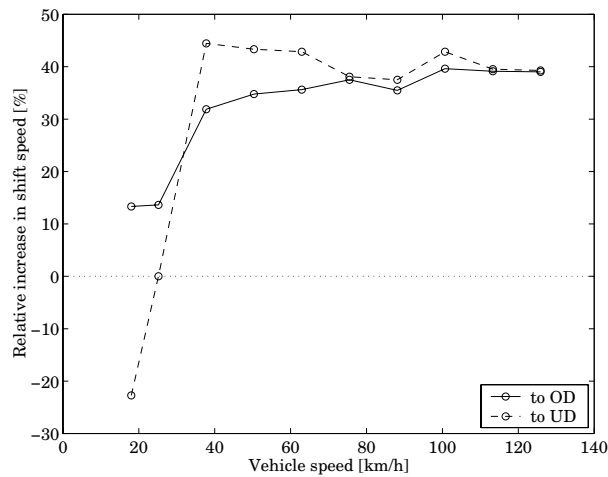


Figure C.8: Relative increase in shift speed, DPC over VDT

### conclusions

Summarizing, the DPC hydraulic layout increases the margins towards gross belt slip. Furthermore, the maximum shift speed towards UD and towards OD can be raised by around 30% without modifying the oil pump. This is true for all vehicle speeds, except for those below 20 [km/h]. At those speeds, downshifting with the DPC system is somewhat impaired with respect to the VDT layout, due to the secondary pressure reaching its upper constraint in order to compensate for the low primary speed. Finally, coasting situations prove to be no problem even though the minimum pulley thrust ratio that can be realized with the DPC layout is higher than that of the VDT layout. Based on these evaluations, it seems worthwhile to investigate the potential of the alternative layout experimentally.

# Appendix D

## CVT and TC Operation

The subject of this appendix shows similarities with some of the work covered in [Serrarens, 2001]. It is included here to facilitate the translation of the accelerator pedal position during the ZI Stop-Go End phase of the launch sequence into setpoints for the supervisory controller of the ZI Stop-Go powertrain, treated in Part III.

### D.1 Efficient driveline operation

The wheel power should preferably be delivered by the engine and transmitted by the transmission as efficiently as possible. Optimization of the integral driveline efficiency, *i.e.*, the combined efficiency of engine, TC and CVT, is a rather complex problem as was reported, *e.g.*, in [Mussaesus *et al.*, 1998]. For the present investigation, a simplified approach is used where

1. the TC clutch is engaged as soon as possible;
2. the engine operating points are chosen along the E-line, taking CVT ratio constraints ( $r_{\text{cvt}} \in [r_{\text{ud}}, r_{\text{od}}]$ ) and engine speed constraints ( $\omega_e \in [\omega_{e,\text{min}}, \omega_{e,\text{max}}]$ ) into account;
3. the CVT efficiency  $\eta_{\text{cvt}}$  is assumed to be constant.

#### D.1.1 Torque converter logic

Operation of the TC lockup is governed by several constraints. For best efficiency, the lockup should be engaged as early as possible. However, closing this clutch, which is operated by switch control, shouldn't lead to uncomfortable driveline oscillations. The speed difference between the impeller and the turbine must therefore be small when closing. Also, engaging the lockup at low CVT speed ratios, can cause driveline oscillations. Opening the lockup clutch is of no real concern, because the initial slip speed will always be zero. For closing the lockup, it is chosen to wait for the CVT speed ratio to exceed some predetermined value (in practice between  $r_{\text{cvt}} = 1$  and  $r_{\text{od}}$ ). Opening of the TC clutch is delayed until the point where the desired speed ratio  $r_{\text{cvt,d}}$ , assuming the TC to be closed, is smaller than  $r_{\text{ud}}$ .

## D.1.2 E-line operation

In order to operate the engine at the E-line when possible within the limited CVT range, at least when the TC is locked, a desired power  $P_{w,d}$  is needed, given by

$$P_{w,d} = \begin{cases} \text{Equation (9.31)} \cdot \omega_w & \text{for } \omega_w < \omega_{w,sw} \\ \text{Equation (9.32)} & \text{for } \omega_w \geq \omega_{w,sw} \end{cases} \quad (\text{D.1})$$

where the switching speed  $\omega_{w,sw}$  is given by (9.34). Let the E-line be characterized by  $\omega_e = \Omega(P_w)$ .  $P_{w,d}$  can be delivered at operating point  $\{\omega_e, T_e\}$  obtained from

$$\omega_{p,c} = \max\left(\frac{\omega_s}{r_{od}}, \Omega(P_{w,d})\right) \quad (\text{D.2})$$

$$\omega_{e,c} = \min\left(\frac{\omega_s}{r_{ud}}, \omega_{p,c}\right) \quad (\text{D.3})$$

$$r_{cvt,d} = \max\left(r_{ud}, \frac{\omega_s}{\omega_{p,c}}\right) \quad (\text{D.4})$$

$$T_{e,d,c} = \frac{P_{w,d}}{\eta_{CVT}\omega_{e,c}} \quad (\text{D.5})$$

where the index 'c' refers to the closed TC.

For an unlocked TC, the engine operating point cannot be chosen freely. Instead, it is entirely determined by the desired wheel torque, according to

$$T_{w,d} = \frac{\alpha_{tc}(r_{tc})b_{tc}(r_{tc})\omega_{e,o}^2\eta_{CVT}}{r_d r_{cvt,d}} \quad (\text{D.6})$$

where the index 'o' refers to the open TC. Given  $T_{w,d}$  and  $r_{cvt,d}$  this relationship is implicit in  $\omega_e$  since  $r_{tc} = \frac{\omega_s}{\omega_e}$ , and must be solved numerically, subject to the engine lower and upper speed constraints. The solution  $\omega_{e,o}$  then determines the desired engine torque

$$T_{e,d,o} = b_{tc}(r_{tc})\omega_{e,o}^2 \quad (\text{D.7})$$

This combination of engine speed  $\omega_{e,o}$  and engine torque  $T_{e,d,o}$  will generally not be on the E-line.

Once the TC is locked, the strategy is to keep it closed as long as  $r_{ud}\omega_{p,c} < \omega_s$ , with  $\omega_{p,c}$  according to (D.2). Below this speed ratio, the desired CVT ratio is set to  $r_{cvt,d} = r_{ud}$  and the engine speed and torque are computed in the same way as (D.6)–(D.7). More precisely, the TC is opened when the following holds

$$\frac{\omega_s}{r_{ud}} < \min\left(\omega_{e,max}, \max\left(\omega_{e,min}, \frac{\omega_s}{r_{od}}, \Omega(P_{w,d})\right)\right) \quad (\text{D.8})$$

In effect two regimes exist, that are different with respect to the TC mode. The two regimes are termed 'open-to-closed' and 'closed-to-open', respectively. The actual regime depends on history. The switch between these regimes is characterized by a hysteresis, since the conditions for 'open-to-closed' and 'closed-to-open' are different. Note that, though discontinuous in the engine speed, the CVT speed ratio is in fact continuous, guaranteed by always using  $r_{cvt,d}$  from (D.4).

For linear torque and power interpretations, *i.e.*,  $f(\delta) = g(\delta) = \delta$  (see Section 9.3), Figure D.1 depicts the resulting  $r_{cvt,d}$ , as a function of pedal position  $\delta$  and vehicle speed  $v_v \in \{0,10,20,\dots,180\}$  [km/h]. As could be expected,  $r_{cvt,d}$  decreases with decreasing vehicle speed and increasing  $\delta$ , and vice versa.

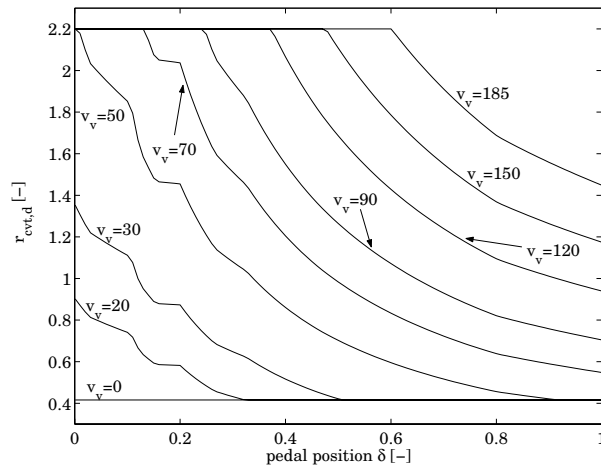


Figure D.1: Desired CVT ratio  $r_{cvt,d}$  [-] as a function of pedal position  $\delta$  [-], for various vehicle speeds  $v_v \in \{0,10,20,\dots,180\}$  [km/h]





# Nomenclature and Acronyms

In this appendix, the acronyms and symbols as used throughout this thesis are explained. Regarding the symbols it is tried to be as complete as possible, Only those sub- and superscripts which are frequently encountered and which can not be misinterpreted are listed at the end of this appendix.

## Acronyms

SYMBOL	DESCRIPTION
A	Accumulator
AMT	Automated Manual Transmission
AT	Automatic Transmission
ATF	Automatic Transmission Fluid
BER	Brake Energy Recovery
BSFC	Brake Specific Fuel Consumption [g/kWh]
CSA	Crankshaft Starter Alternator
CVT	Continuously Variable Transmission
DC	Direct Current
DNR	Drive-Neutral-Reverse
DPC	Double Primary Cylinder
DSFC	Distance-Specific Fuel Consumption [g/km]
E	primary power source (engine)
E-line	collection of fuel-optimal engine operating points
EM	Electric Motor
FESS	Flywheel Energy Storage System
FHD-III	Flywheel Hybrid Driveline III
G	Generator
GDI	Gasoline Direct Injection
GN	Geared Neutral
HY	HYbrid driveline project
HYZEM	HYbrid technology approaching efficient Zero Emission Mobility
IMA	Integrated Motor Assist
ISAD	Integrated Starter Alternator Damper
ISG	Integrated Starter Generator
Li-ion	Lithium ion

## Nomenclature

---

M	Motor
MT	Manual Transmission
NEDC	New European Driving Cycle
NiMH	Nickel Metal Hydride
OD	OverDrive
$OL_{x\%}$	operating line with $x\%$ higher BSFC than E-line
PM	Permanent Magnet
PTO	Power Take-Off
SA	Starter Alternator
SG	Stop-Go
SI	System Integrated
SOC	State Of Charge
SS	Start-Stop
SS, DS	Single-Sided, Double Sided (pump mode)
T	Transmission
TC	Torque Converter
TSFC	Time-Specific Fuel Consumption [g/s]
UD	UnderDrive
UR	UnderDrive Reversed compression
W	Wheels
WOT	Wide Open Throttle
ZI	Zero Inertia
ZI-SG	Mechanical Stop-Go system, based on ZI

## Symbols

SYMBOL	DESCRIPTION	VALUE [UNIT]
$a$	pulley center distance	0.178 [m]
$a_w$	shift gain	[rad/(kN)·s <sup>2</sup> ]
$dA$	infinitesimal area of Hertzian segment-pulley contact	[m <sup>2</sup> ]
$A_a$	additional (DPC) pulley cylinder surface	[m <sup>2</sup> ]
$A_p$	primary pulley cylinder surface	$2.60 \cdot 10^{-2}$ [m <sup>2</sup> ]
$A_s$	secondary pulley cylinder surface	$1.24 \cdot 10^{-2}$ [m <sup>2</sup> ]
$A_1, A_2$	throttling areas of primary, secondary valve	[m <sup>2</sup> ]
$\alpha_{tc}$	torque converter torque amplification factor	[-]
$\alpha_s$	$(z + 1)/r_c$ , torque amplification factor from flywheel to secondary shaft	1.661 [-]
$\alpha_p$	$z/r_a$ , torque amplification factor from flywheel to primary shaft	0.960 [-]
$\alpha_w$	$(z + 1)/r_c/r_d$ , torque amplification factor from flywheel to wheel shaft	7.81 [-]
$b, c$	width, height of Hertzian segment-pulley contact	[m]
$b_s$	'representative' damping coefficient (Shafai's model)	$1.5 \cdot 10^6$ [Ns/m]
$b_{tc}$	torque converter capacity factor	[Nms <sup>2</sup> /rad <sup>2</sup> ]
$B$	centrifugal force per unit angle of bands	[N/rad]

$\beta$	brake pedal force	[N]
$c_{a1}$	constant in relationship between $p_a$ and $p_s$	3.7 [bar]
$c_{a2}$	constant in relationship between $p_a$ and $p_s$	0.073 [-]
$c_c$	clutch constant	[m <sup>3</sup> ]
$c_d$	air drag coefficient	0.3 [-]
$c_f$	discharge coefficient	0.6 [-]
$c_\lambda$	coefficient in approximation for $\kappa$	0.9 [-]
$c_r$	coefficient in approximation for $\kappa$	0.6 [-]
$c_p$	primary centrifugal coefficient	$3.46 \cdot 10^{-2}$ [Ns <sup>2</sup> /rad <sup>2</sup> ]
$c_s$	secondary centrifugal coefficient	$3.63 \cdot 10^{-3}$ [Ns <sup>2</sup> /rad <sup>2</sup> ]
$c_{pl}, c_{sl}$	primary, secondary leak coefficient	$3.4 \cdot 10^{-12}$ [m <sup>3</sup> /(Pa s)]
$c_{v0}$	coefficient in Guebeli's viscous shear model	2.7 [m/s]
$c_{v1}$	coefficient in Guebeli's viscous shear model	29 [s <sup>-1</sup> ]
$C$	centrifugal force per unit angle of segments	[N/rad]
$C_l, C_d, C_r$	lockup clutch, drive clutch, reverse clutch	
$C_s, C_f$	secondary pulley clutch, flywheel clutch	
$\chi_3, \chi_{3a}$	combined friction coefficients	[-]
$D(\xi)$	$S(\xi) - Q(\xi)$ , net longitudinal belt force	[N]
$\delta$	accelerator pedal position	(0...1) [-]
$e$	control error	
$e_r$	$\ln(r_{cvt,d}) - \ln(r_{cvt})$ , speed ratio control error	[-]
$E_E$	energy from primary energy source	[J]
$E_{BER}$	energy recovered using BER	[J]
$E_{cyc}$	$E_{cyc}^+ - E_{cyc}^-$ , energy needed just for road load	[J]
$E_{cyc}^+$	total drive cycle energy	[J]
$E_{cyc}^-$	recoverable drive cycle energy	[J]
$\varepsilon$	small positive constant	
$f(\delta)$	torque shape function	[-]
$f$	fuel consumption	[g]
$f_{OL15\%}$	fuel consumption using OL <sub>15%</sub>	[g]
$(dF), F$	(infinitesimal) axial pulley clamping force	[N]
$F_b$	$ T_p /R_p$ , net belt force	[N]
$F_p, F_s$	primary, secondary axial pulley clamping force	[N]
$F_{spr}$	secondary spring force	[N]
$F_{spr0}$	secondary spring force preload	807 [N]
$F_p^*$	$\kappa F_s, F_p$ needed for maintaining a constant $r_{cvt}$	[N]
$F_{30\%}$	minimum pulley clamping force cf. 30% safety margin	[N]
$\mathcal{F}(\Psi)$	$f/f_{OL15\%}$ , normalized fuel consumption	[-]
$g$	gravity constant	9.81 [m/s <sup>2</sup> ]
$g(\delta)$	power shape function	[-]
$\gamma$	angle between $dW_2$ and neutral line	[rad]
$h$	distance between rocking edge and segment shoulder	[m]
$h_f$	oil film thickness	[m]
$\eta_{cvt}$	overall CVT efficiency	[-]
$\eta_g$	efficiency of the geartrain parallel to the CVT	[-]
$\eta_{hydr}, \eta_{mech}$	hydraulic, mechanical efficiency	[-]
$\eta_{oil}$	dynamic coefficient of viscosity, ATF @ 80°C	$10^{-2}$ [Ns/m <sup>2</sup> ]
$\eta_T$	transmission efficiency	[-]
$\eta_A$	accumulator efficiency	[-]

## Nomenclature

---

$\eta_G$	generator efficiency	[-]
$\eta_M$	motor efficiency	[-]
$\eta_{A \rightarrow M}$	efficiency from A to M	[-]
$\eta_{E \rightarrow G}$	efficiency from E to G	[-]
$\eta_{G \rightarrow A}$	efficiency from G to A	[-]
$\eta_{M \rightarrow W}$	efficiency from M to W	[-]
$\eta_{W \rightarrow G}$	efficiency from W to G	[-]
$\eta_{II}$	efficiency of secondary power path	[-]
$i_{\text{lockup}}$	lockup clutch state	{0, 1} [-]
$i_{\text{pump}}$	pump mode state	{0, 1} [-]
$i_{\text{safety}}$	safety valve state	{0, 1} [-]
$I_{cd}$	drive clutch solenoid current	[A]
$I_1, I_2$	primary, secondary solenoid current	[A]
$J_e$	engine inertia	0.156 [kgm <sup>2</sup> ]
$J_p$	primary inertia	0.042 [kgm <sup>2</sup> ]
$J_s$	secondary inertia	0.030 [kgm <sup>2</sup> ]
$J_t$	turbine inertia	0.036 [kgm <sup>2</sup> ]
$J_f$	flywheel inertia	0.393 [kgm <sup>2</sup> ]
$J_r$	rotor inertia	[kgm <sup>2</sup> ]
$J_w$	lumped inertia of vehicle and four wheels	129 [kgm <sup>2</sup> ]
$J_{\text{cvt}}, J_{\text{t,r}}, J_{\text{e,r}}$	lumped inertias, defined in Table 9.1	[kgm <sup>2</sup> ]
$J_{\text{t,d}}, J_{\text{t,gn}}, J_{\text{w,gn}}$	lumped inertias, defined in Table 9.1	[kgm <sup>2</sup> ]
$J_{\text{t,c}}$	lumped inertia, defined in Table 9.1	[kgm <sup>2</sup> ]
$k$	coefficient in approximation for $k_r$	$4 \cdot 10^{-7}$ [1/(N rad)]
$k_h$	viscous shear constant	[N/m]
$k_{\text{oil}}$	oil compressibility	$5 \cdot 10^{-9}$ [m <sup>2</sup> /N]
$k_r$	rate of ratio change parameter in Ide's model	[1/(N rad)]
$k_1, \dots, k_{10}$	control parameters	
$k_{\text{spr}}$	secondary spring constant	$1.92 \cdot 10^4$ [N/m]
$K_S, K_Q$	integration constants for $S(\xi)$ and $Q(\xi)$	[N]
$\kappa$	$F_p^*/F_s$ , pulley thrust ratio	[-]
$L$	belt length evaluated at the neutral line	0.748 [m]
$\lambda$	$(r_{\text{cvt}} - 1)/(r_{\text{cvt}} + 1)$ , symmetrical CVT ratio	[-]
$m$	segment thickness	[m]
$m_s$	'representative' mass of sheave and belt (Shafai's model)	2 [kg]
$m_v$	vehicle mass	1360 [kg]
$(\mu_1), \chi_1$	(maximum) friction coefficient between bands and segments	[-]
$(\mu_2), \chi_2$	(maximum) friction coefficient between segments and pulley	[-]
$n_x$	rotational speed of component $x$ , see $\omega_x$	[rpm]
$(dN_1), N_1$	(infinitesimal) normal force between segments and bands	[N]
$(dN_2), N_2$	(infinitesimal) normal force between segments and pulley	[N]
$\Delta p$	pressure difference	[bar]
$p_{\text{mean}}$	mean pressure in Hertzian segment-pulley contact	[N/m <sup>2</sup> ]
$p_p, p_s, p_a$	primary, secondary, accessories circuit pressure	[bar]

$p_c$	clutch piston pressure	[bar]
$p_{p,\tau}, p_{s,\tau}$	primary, secondary pressures needed for torque transmission	[bar]
$P_{assist}$	power from additional power assist source	[kW]
$P_{combustion}$	engine combustion power	[kW]
$P_{cyc}$	required wheel power on certain drive cycle	[kW]
$P_{desired}$	desired (engine) power	[kW]
$P_e$	engine power	[kW]
$P_{e,total}$	$P_{combustion} + P_{inertia}$ , total engine power	[kW]
$P_{in}, P_{out}$	input and output power	[kW]
$P_{inertia}$	power from primary-sided inertias	[kW]
$P_{loss}$	power loss	[kW]
$P_{th}$	threshold power for Start-Stop (and BER) operation	[kW]
$P_{ss}$	power level in the sweet spot	32 [kW]
$P_w$	wheel power	[kW]
$P_E$	power of primary source	[kW]
$P_M$	power of secondary motor	[kW]
$P_G$	power of secondary generator	[kW]
$P_W$	power at wheels	[kW]
$(dQ), Q$	(infinitesimal) compression force between segments	[N]
$Q_i$	compression force $Q$ at idle arc	[N]
$Q_{sl}, Q_{ti}$	compression force at slack and tight part of belt	[N]
$\theta$	half the pulley wedge angle	$11^\circ$
$\Theta$	segment wedge angle conform the minimum belt orbit radius	
$r_a$	$\omega_p/\omega_a$ , speed ratio of annulus reduction	2.94 [-]
$r_c$	$\omega_{sg}/\omega_c$ , speed ratio of carrier reduction	2.30 [-]
$r_{cvt}$	$\omega_s/\omega_p$ , CVT speed ratio	[-]
$r_{cvt,meas}$	measured $r_{cvt}$	[-]
$r_{cvt,ff}$	$r_{cvt}$ resulting from controller with feedforwards	[-]
$r_d$	$\omega_d/\omega_{ss}$ , speed ratio of final drive reduction	0.213 [-]
$r_{gn}$	Geared Neutral ratio	0.577 [-]
$r_{ud}$	UD speed ratio	0.416 [-]
$r_{od}$	OD speed ratio	2.150 [-]
$r_r$	speed ratio of reverse gear	-0.885 [-]
$r_{red}$	$\omega_{II}/\omega_w$ reduction gear speed ratio	4.00 [-]
$r_{tc}$	$\omega_t/\omega_e$ , torque converter speed ratio	[-]
$r_{zi}$	Zero Inertia ratio	0.96 [-]
$r_0, r_1$	initial and final value of speed ratio $r_{cvt}$	[-]
$R_b$	orbit radius of centerline of bands	[m]
$R_c$	segment orbit radius (at neutral line)	[m]
$R_p, R_s$	primary, secondary belt radius (at neutral line)	[m]
$R_w$	(dynamic) wheel radius	0.307 [m]
$\Delta R$	$R_b - R_c$	[m]
$\rho$	$(r_{cvt} + 1)R_s/a$ , dimensionless secondary radius	[-]
$\rho_b$	bands mass per unit length	[kg/m]
$\rho_c$	segment mass per unit length	[kg/m]
$\rho_{oil}$	oil density, ATF @ 80°C	$8.3 \cdot 10^2$ [kg/m <sup>3</sup> ]
$\varrho$	road slope	

## Nomenclature

---

$s_p, s_s$	primary and secondary axial pulley sheave position	[m]
$s_1, s_2$	$\text{sign}(v_c - v_b), \text{sign}(v_u - v_c)$	[-]
$(dS), S$	(infinitesimal) tension force in bands	[N]
$S_{sl}, S_{ti}$	tension force at slack and tight part of belt	[N]
$S_0, S_1$	lower and upper tension in bands	[N]
$\sigma$	epicyclic gear ratio of DNR set	-2.13 [-]
$\Sigma$	absolute logarithmic shift speed	[s <sup>-1</sup> ]
$t$	time	[s]
$t_{\text{direct}}$	time needed for direct-start	[s]
$t_{\text{impulse}}$	time needed for impulse-start	[s]
$t_{\text{phase1}}$	time needed for phase 1 of impulse-start	[s]
$t_{\text{phase2}}$	time needed for phase 2 of impulse-start	[s]
$\Delta t_{\text{up}}, \Delta t_{\text{down}}$	up-, downshift time interval	[s]
$t_0$	start time	[s]
$t_1$	time instant when $\omega_e = \omega_{e,\text{idle}}$	[s]
$t_f$	end time of drive cycle	[s]
$T_a, T_c, T_f$	annulus, carrier, flywheel torque	[Nm]
$T_c$	clutch torque	[Nm]
$T_{cl}, T_{cd}, T_{cr}$	lockup clutch, drive clutch, reverse clutch torque	[Nm]
$T_{cs}, T_{cf}$	secondary pulley clutch, flywheel clutch torque	[Nm]
$T_e$	engine torque	[Nm]
$T_{e,d,c}$	desired engine torque for TC closed	[Nm]
$T_{e,d,o}$	desired engine torque for TC open	[Nm]
$T_{e,\text{drag}}$	engine drag torque	[Nm]
$T_i, T_t$	impeller, turbine torque	[Nm]
$T_{in}, T_{out}$	input and output torque	[Nm]
$T_{\text{loss}}$	torque loss	[Nm]
$T_{\text{mech}}$	mechanical torque loss	[Nm]
$T_n$	net torque acting on secondary lumped inertia	[Nm]
$T_p, T_s$	primary, secondary belt torque	[Nm]
$T_{\text{pump}}$	pump torque	[Nm]
$T_r$	vehicle rolling resistance torque	55 [Nm]
$T_{rl}$	road load torque	[Nm]
$T_{\text{slip}}$	(clutch) slip torque	[Nm]
$T_{st}$	starter torque	[Nm]
$T_{\text{stick}}$	(clutch) stick torque	[Nm]
$T_w$	wheel torque	[Nm]
$\tau_p, \tau_s, \tau'_s$	primary, secondary, practical torque ratio	[-]
$\tau_{vs}$	viscous shear stress	[N/m <sup>2</sup> ]
$\underline{u}$	input vector	
$\vec{v}_b$	longitudinal velocity of bands	[m/s]
$\vec{v}_c$	longitudinal velocity of segments	[m/s]
$\vec{v}_u$	longitudinal velocity of pulley at neutral line	[m/s]
$v_v$	vehicle speed	[km/h]
$v_{v,\text{idle}}$	vehicle speed corresponding to $\omega_{e,\text{idle}}$ for $r_{cvt} = r_{ud}$ , TC and drive clutch closed	8 [km/h]
$V_p, V_s$	primary, secondary circuit volume	[m <sup>3</sup> ]
$\phi$	throttle valve angle	
$\varphi$	$(\pi - \varphi_p)/2$	[rad]

$\varphi_p, \varphi_s$	primary, secondary angle of wrap	[rad]
$\varphi_1, \varphi_2$	primary, secondary active arc angle	[rad]
$\Phi$	$\varphi_p / \varphi_s$ , ratio of angles of wrap	[-]
$\Phi_{sp}, \Phi_{pd}$	oil flow from secondary to primary, primary to drain	[m <sup>3</sup> /s]
$\Phi_{sa}, \Phi_{pump}$	oil flow from secondary to accessories, pump	[m <sup>3</sup> /s]
$(dW_1), W_1$	(infinitesimal) friction force between segments and bands	[N]
$(dW_2), W_2$	(infinitesimal) friction force between segments and pulley	[N]
$dW_{2,rad}, dW_{2,tan}$	radial and tangential component of $dW_2$	[N]
$\omega_a$	annulus angular speed	[rad/s]
$\omega_c$	carrier angular speed	[rad/s]
$\omega_{cd}$	slip speed over drive clutch	[rad/s]
$\omega_{cf}$	slip speed over flywheel clutch	[rad/s]
$\omega_{cl}$	slip speed over lockup clutch	[rad/s]
$\omega_{cr}$	slip speed over reverse clutch	[rad/s]
$\omega_{cs}$	slip speed over secondary pulley clutch	[rad/s]
$\omega_d$	differential cage angular speed	[rad/s]
$\omega_e$	engine angular speed	[rad/s]
$\omega_{e,c}$	desired engine speed for TC closed	[rad/s]
$\omega_{e,o}$	desired engine speed for TC open	[rad/s]
$\omega_{e,idle}$	engine idle speed	84 [rad/s]
$\omega_{e,ign}$	engine ignition speed	63 [rad/s]
$\omega_f$	flywheel angular speed	[rad/s]
$\omega_{in}, \omega_{out}$	input, output angular speed	[rad/s]
$\omega_{loss}$	speed loss	[rad/s]
$\omega_p$	primary pulley angular speed	[rad/s]
$\omega_{p,c}$	desired primary speed for TC closed	[rad/s]
$\omega_r$	rotor angular speed	[rad/s]
$\omega_s$	secondary pulley angular speed	[rad/s]
$\omega_{ss}$	secondary shaft angular speed	[rad/s]
$\omega_{sg}$	secondary gear angular speed	[rad/s]
$\omega_t$	turbine angular speed	[rad/s]
$\omega_w$	angular wheel speed	[rad/s]
$\omega_{w,sw}$	$\omega_w$ at switch between torque and power interpretation	[rad/s]
$\omega_I$	angular speed of electric motor I ('load')	[rad/s]
$\omega_{II}$	angular speed of electric motor II ('engine')	[rad/s]
$\Omega(P_w)$	engine speed as a function of power at the E-line	[rad/s]
$x$	state	
$\dot{x}$	time derivative of $x$	
$(d\xi), \xi$	(infinitesimal) circumf. coordinate along angle of wrap	[rad]
$\Psi$	hybridization factor	[-]
$\Psi_{min}$	minimum hybridization factor	[-]
$z$	epicyclic gear ratio of planetary gear	2.82 [-]
$\zeta$	derivative of $\alpha_{tc} b_{tc}$ to $r_{tc}$	[Nms <sup>2</sup> /rad <sup>2</sup> ]



## Subscripts and superscripts

SYMBOL	DESCRIPTION
d	desired
fb	feedback
ff	feedforward
min	minimum
max	maximum

# Samenvatting

Het brandstofverbruik van personenvoertuigen kan op vele manieren worden verminderd. Zo kan men bijvoorbeeld de externe voertuigbelasting reduceren door gewicht of luchtweerstand te verlagen. Een andere mogelijkheid is het verbeteren van het totale aandrijfsysteem, ofwel de *aandrijflijn*. Het verhogen van het rendement van de diverse aandrijflijn componenten is een manier. Een andere benaderingswijze is het verbeteren van het gebruik van de aandrijflijn als geheel om zo minder brandstof te verbruiken. Met name het werkpunt van de motor is van cruciaal belang voor het brandstofverbruik. De moderne verbrandingsmotor lijkt weinig ruimte meer te bieden voor rendementsverbetering. Daarentegen is het alternatief gebruik van de aandrijflijn nog een grotendeels onontgonnen gebied.

In het EcoDrive project dat ten grondslag ligt aan dit proefschrift werd daarom besloten de aandacht te richten op technologieën op het gebied van alternatief aandrijflijn gebruik. Na het verrichten van een onderzoek naar besparingsprincipes op het genoemde gebied, zijn twee methoden gekozen op grond van hun brandstofbesparings potentieel in combinatie met een relatief beperkte toevoeging van gewicht, kosten en complexiteit, ten opzichte van een conventioneel voertuig. Met de eerste van deze methoden, genaamd *E-line tracking*, kan brandstof bespaard worden door de gewenste stationaire vermogens steeds in brandstof-optimale werkpunten van de motor te leveren. Bij de tweede methode, genaamd *Stop-Go*, wordt brandstof bespaard door de motor niet onnodig stationair te laten draaien tijdens stilstand van het voertuig. De moeilijkheid bij beide methoden is om de brandstofbesparing te realiseren zonder de responsie (*driveability*) van het voertuig op het gaspedaal te verslechteren. Het project werd daarom gericht op 25% brandstofbesparing ten opzichte van een 4-traps automatische transmissie op de 'NEDC' cyclus, met behoud van 'driveability'.

Daartoe is een transmissie ontwikkeld met daarin een vliegwiel dat parallel met de transmissie verbonden is via een planetair tandwielstelsel. In het geval van *E-line tracking* dient het vliegwiel als vermogensbron om de motor te assisteren tijdens acceleraties vanuit een brandstofzuinig en dus typisch laag motortoerental. Omdat het bij de resulterende voertuigresponsie lijkt alsof de motor geen massa-traagheid meer heeft, wordt de aandrijflijn aangeduid als de *Zero Inertia (ZI)* aandrijflijn. Bij *Stop-Go* kan het vliegwiel daarnaast gebruikt worden om het voertuig aan te drijven vanuit stilstand, aangenomen dat het nog draaiende vliegwiel afgekoppeld werd enige tijd voor stilstand. In het voorgestelde ontwerp, genaamd *ZI Stop-Go*, worden het voertuig en de motor *gelijktijdig* versneld, zodat wegrijden zonder merkbare vertraging mogelijk is.

De gedoseerde uitwisseling van energie tussen het vliegwiel en de rest van de aandrijflijn is mogelijk dankzij de toepassing van een Continu Variabele Transmissie (CVT). Daarnaast stelt de CVT de motor in staat om exact in de brandstof-optimale werkpunten te draaien. In dit proefschrift is de aandacht gericht op de ontwikkeling van de (duwband) CVT regeling en de daartoe benodigde modellen. De beschouwde modellen lenen zich tevens voor het

vergaren van inzicht in de werking van de CVT en voor het verklaren van in de praktijk waargenomen fenomenen, zoals vermogensverlies in de transmissie. Speciale aandacht gaat uit naar het omgaan met actuator en systeem begrenzingen. De CVT regeling is experimenteel getest op een proefstand en in een testvoertuig, in combinatie met de overkoepelende regeling zoals die is afgeleid in [Serrarens, 2001]. In stationaire situaties slaagt de CVT regeling erin de transmissieverliezen tot een minimum te beperken, terwijl hoogdynamische trajectories gevolgd worden binnen een acceptabele marge, en zonder slip van de duwband.

Het tweede gedeelte van dit proefschrift wijdt uit over de ZI Stop-Go aandrijflijn. Als eerste wordt een aantal bestaande Stop-Go systemen behandeld, waaruit reeds de potenties maar ook de mogelijke problemen van dergelijke systemen naar voren komen. In de voorgestelde ZI Stop-Go oplossing zijn twee extra koppelingen benodigd. Ofschoon het ZI Stop-Go systeem mechanisch vrij eenvoudig is, is de werking en besturing complex. Zware eisen worden gesteld aan de regelingen, zowel op overkoepelend als op lokaal niveau. Daarom zijn eerst (hybride) modellen en op basis daarvan, (hybride) regelaars ontwikkeld. De regelaars zijn vervolgens geëvalueerd, gebruikmakend van een uitgebreide versie van het eerder genoemde model. Simulaties van een vol gas acceleratie vanuit stilstand tonen een voertuigresponsie die vergelijkbaar is met die van een conventioneel CVT voertuig. De ZI Stop-Go transmissie is gerealiseerd en het hydraulisch systeem van de CVT is aangepast om de bekrachtiging van de diverse koppelingen mogelijk te maken, ook als de motor uitstaat. De eerste experimenten met de ZI Stop-Go transmissie op de proefstand zijn veelbelovend.

De resultaten van het werk beschreven in dit proefschrift hebben bijgedragen aan het grotere behalen van het projectdoel, d.w.z. een brandstofbesparing van 18% is gerealiseerd, terwijl de *driveability* zelfs verbeterd is.

# Acknowledgments

EcoDrive was a joint research project of Van Doorne's Transmissie (VDT) in Tilburg, TNO Automotive in Delft and the Technische Universiteit Eindhoven (TU/e). The project was subsidized by the Dutch governmental program EET (Economy, Ecology and Technology). All of these partners are gratefully acknowledged for their support.

On a personal level, my gratitude is indebted to a number of people for their contributions to this thesis and to the EcoDrive project as a whole. First of all, I would like to thank my co-promotor Frans Veldpauw, for the numerous discussions and for reading through three theses carefully in a very short time. I thank my promotor Maarten Steinbuch for never letting off the pressure. The entire committee is acknowledged for their consideration in what proved to be a very tight time-frame.

A special 'thank you' goes to Shuiwen Shen, who contributed tremendously in Part III of this thesis, concerning *Stop-Go*. Shuiwen, I look forward to writing the long awaited paper with you.

Needless to say, I thank my two co-workers and friends Alex Serrarens and Roëll van Druten for the pleasant cooperation, the endless discussions (usually outside working-hours), and for DTI. Erwin Meinders, literally our 'manusje-van-alles' (Jack-of-all-trades), proved invaluable to the project in handling the contacts with the workshops of VDT and of the GTD, in assembling the test rig and the transmissions and generally in 'tying loose ends'. For that and for the good laughs (WSV Simon Stevin will not easily forget us two representing the EcoDrive team) I am grateful.

Besides Erwin, the workshops of VDT, the GTD (TU/e) and of Mechanical Engineering worked wonders in the realization of the hardware. In particular, gratitude goes to Toon van Gils and Karel Koekkoek for their contributions in setting up the test rig and vehicle and Harrie van de Loo for preparing the Stop-Go control unit, also known as 'the microwave'.

Regarding the EcoDrive organization, I am grateful to Dick Landheer, also for managing the 'Máxima event'. On that subject, I thank Willem-Alexander and Máxima for choosing for the Zero Inertia vehicle, despite the objections of the BVD. Bram Veenhuizen from VDT initiated the EcoDrive project. I thank Bram for that, and also for letting us in on the art of planning. Many more people at VDT are acknowledged for their contribution to this project, though in particular Maaïke van der Laan for introducing me to CVT control, and Marc Mus-saeus for brainstorming with us at the beginning of the project.

Furthermore, a number of students helped in solving various problems emerging during the project. I wish to express my gratitude to all of them, but especially to Bart Stouten, who contributed in the modeling and control of the CVT. Bart, good luck in your own PhD project.

Dirk and Nanne, thank you for the wonderful cover designs.

Finally, I thank my parents, my two brothers and two sisters for their love and support,

and for listening to stories, that I myself probably liked to listen to the most.

Bas Vroemen, October 2001

# Curriculum Vitae

Bas Vroemen was born June 2<sup>nd</sup>, 1973 in Breda, the Netherlands. He received his MSc degree in Mechanical Engineering in 1997 from the Technische Universiteit Eindhoven. During the Master studies, subjects of interest included:

- model based reduction techniques applied to active suspension with preview;
- survey of multi-objective control;
- design of a Model Predictive Controller for a laboratory gas turbine installation.

A paper on the last subject, presented at the 1998 Turbo Expo, won the 1998 ASME best paper award. From 1997 to 2001, he has been working towards his PhD degree at the Technische Universiteit Eindhoven, in the EcoDrive project. This project was a cooperation of the Technische Universiteit Eindhoven, Van Doorne's Transmissie (VDT) in Tilburg and TNO Automotive in Delft. The fuel-efficient hybrid drive train and its controls, designed in the project, received the Novem Energy Conversion Award and two patents were granted.

Medio 2001, Bas Vroemen, Roëll van Druten and Alex Serrarens have started a company called Drive Train Innovations (DTI) to support the automotive industry with innovative ideas and fundamental knowledge regarding hybrid powertrains.

